



ΔΙΠΛΩΜΑΤΙΚΗ ΕΡΓΑΣΙΑ

Διάγνωση σφαλμάτων σε direct drive γεννήτριες μονίμων
μαγνητών για υπεράκτιες ανεμογεννήτριες.

Συγγραφέας:
Αλέξανδρος Σεργάκης

Εξεταστική επιτροπή:
Αναπληρωτής Καθηγητής Κωνσταντίνος Γυφτάκης
Καθηγητής Μιχαήλ Ζερβάκης
Δόκτωρ Ελευθερία Σεργάκη

Φεβρουάριος 2024



DIPLOMA THESIS

Fault diagnosis in direct drive permanent magnet
generators for offshore wind turbines

Author:

Alexandros Sergakis

Committee:

Associate Professor Konstantinos Gyftakis

Professor Michail Zervakis

Doctor Eleftheria Sergaki

February 2024

Περίληψη

Στον τομέα των ανανεώσιμων πηγών ενέργειας, η υπεράκτια αιολική ενέργεια είναι σημαντική για την ουδετερότητα της Ελλάδας ως προς τις εκπομπές διοξειδίου του άνθρακα έως το 2050. Μελέτη του ΕΛΙΑΜΕΠ αναδεικνύει την κοινωνικοοικονομική αξία των υπεράκτιων αιολικών πάρκων. Το πλαίσιο ανάλυσης κόστους-ωφέλειας (CBA) εξετάζει τις παγκόσμιες και τοπικές επιπτώσεις, εστιάζοντας στη μείωση των εκπομπών CO₂ και την ανάγκη αποζημίωσης των τοπικών κοινοτήτων που πλήττονται από τις υπεράκτιες ανεμογεννήτριες. Αυτές οι ανεμογεννήτριες, συχνά χρησιμοποιούν γεννήτριες μόνιμων μαγνητών άμεσης κίνησης (PMSG), παίζουν κρίσιμο ρόλο στην αποτελεσματική αξιοποίηση της αιολικής ενέργειας. Η αξιοπιστία και η απόδοση αυτών των γεννητριών είναι σημαντική για την αδιάκοπη παραγωγή ενέργειας.

Η παρούσα διπλωματική εργασία μελετά την διάγνωση σφαλμάτων σε γεννήτριες μόνιμων μαγνητών άμεσης κίνησης, με ιδιαίτερη έμφαση στις γεννήτριες C-Gen, με στόχο τη βελτίωση της συντήρησης και της λειτουργίας των υπεράκτιων ανεμογεννητριών. Η έρευνά μας εξετάζει διαφορετικές προηγμένες τεχνικές ανίχνευσης σφαλμάτων σε περιπτώσεις απομαγνητισμού (σφάλμα δρομέα), συμπεριλαμβανομένης της προσέγγισης διανύσματος Park (PVA), της εκτεταμένης προσέγγισης διανύσματος Park (EPVA), της ανάλυσης σημάτων ρεύματος κινητήρα (MCSA) και της παρακολούθησης ροής μέσω των τάσεων των αισθητήρων. Αυτές οι προηγμένες διαγνωστικές μέθοδοι συμβάλλουν στη συνολική αποδοτικότητα και διάρκεια ζωής των υπεράκτιων ανεμογεννητριών, εξασφαλίζοντας τη βιωσιμότητα της παραγωγής ενέργειας.

Διάφορα ποσοστά απομαγνήτισης για 1 ή 2 (μη προσκείμενοι) μαγνήτες δοκιμάζονται με διαφορετικά ομικά φορτία, τα οποία προσομοιώνονται μέσω του Simcenter MAGNET για κάθε περίπτωση μόνιμης κατάστασης της C-gen γεννήτριας. Οι μετρήσεις τάσης, ρεύματος και ροπής από τη προσομοίωση δειγματοληπτούνται (6kHz) και επεξεργάζονται εκ των υστέρων με τη χρήση του MATLAB για τη διάγνωση κάθε περίπτωσης απομαγνήτισης.

Μετά την ανάλυση του επεξεργασμένου σήματος, μπορούμε να εντοπίσουμε τις διαφορές παρατηρώντας τα σήματα των υγιών και των ελαττωματικών περιπτώσεων στο πεδίο του χρόνου και της συχνότητας, συγκεκριμένα μελετώντας τις αρμονικές συχνότητες.

Abstract

In the field of renewable energy, Offshore wind energy is important for Greece's carbon neutrality by 2050. A study by ELIAMEP highlights the socio-economic value of offshore wind farms. The Cost Benefit Analysis (CBA) framework considers global and local impacts, focusing on reducing CO₂ emissions and the need for compensation to local communities affected by offshore wind turbines. These turbines, often employing direct drive permanent magnet generators (PMSGs), play a crucial role in harnessing wind power efficiently. The reliability and performance of these generators are important for uninterrupted energy production.

This thesis studies fault diagnosis in direct drive permanent magnet generators, with a particular focus on C-GEN generators, aiming to enhance the maintenance and operation of offshore wind turbines. Our research explores various fault detection techniques in case of demagnetization (rotor fault), including Park's Vector Approach (PVA), Extended Park's Vector Approach (EPVA), Motor Current Signature Analysis (MCSA) and flux monitoring through the voltage of the sensors. These advanced diagnostic methods contribute to the overall efficiency and lifespan of offshore wind turbines, ensuring the sustainability of energy production.

Various demagnetization percentages for 1 or 2 (non-adjacent at 22.5° apart) magnets are tested with different ohmic loads, which are simulated via SimcenterMAGNET for each of the steady-state cases of the C-gen generator. The voltage, current and torque measurements from the simulation are then sampled (at 6kHz) and post-processed using MATLAB to diagnose each case of demagnetization.

After analyzing the signal processing output, we can detect the differences by observing the signals of healthy and faulty cases in time and frequency domain, specifically looking at harmonic frequencies.

Acknowledgements

I would like to express my sincere gratitude to Associate Professor Konstantinos Gyftakis for his invaluable guidance, support, and expertise throughout the development of my diploma thesis. His commitment to academic excellence and unwavering encouragement have been instrumental in shaping the quality of this work.

I am also deeply thankful Doctor Georgios Skarmoutsos, Doctor Sergaki Eleftheria (EDIP) and Professor Michail Zervakis for their insightful feedback and valuable suggestions that significantly contributed to the improvement of my research. Their dedication to support me through my research has been truly inspiring.

To my friends and family, whose unwavering support sustained me through the highs and lows of this academic journey, I extend my heartfelt appreciation. Your encouragement and understanding provided the motivation I needed to overcome challenges and persevere in the pursuit of knowledge. This achievement is as much yours as it is mine, and I am grateful for the encouragement and support you have showered upon me.

Thank you all for being an integral part of this significant milestone in my academic endeavors.

Alexandros Sergakis
February 2024

Contents

List of Figures	iii
1 Introduction	1
1.1 Background[1]	1
1.2 Objectives and Methodology of Work	2
1.3 Outline	2
1.4 Related Work[2–11]	3
1.4.1 Demagnetization in Permanent Magnet Machines	3
1.4.2 Partial Irreversible Demagnetization in Large-Scale PM Wind Generators	3
1.4.3 Machine Learning for Fault Diagnosis in permanent magnet generators	3
1.4.4 New method for demagnetization fault diagnosis in axial flux permanent magnet synchronous generators	3
1.4.5 Temperature Rise Analysis of Permanent Magnet Generators with Demagnetization Faults	3
1.4.6 Fault Detection in Axial Flux Coreless Permanent Magnet Synchronous Generators	3
1.4.7 The Demagnetization Harmonics Generation Mechanism in PM Machines	4
2 Theoretical Background	5
2.1 Synchronous Generator [12, 13]	5
2.1.1 Permanent Magnet Synchronous Generator	5
2.2 C-GEN Technology [11, 14–18]	5
2.2.1 Constructional Features of C-GEN	6
2.3 Electrical Testing [19–24]	9
2.4 Fault Diagnosis Methods [25–31]	9
2.4.1 Park’s Vector Approach	9
2.4.2 Extended Park Vector Approach	11
2.4.3 MCSA	12
2.5 Torque Monitoring [32, 33]	13
2.5.1 Methods of Torque Measurement	13
2.6 Flux Monitoring [19, 34–40]	13
2.7 Demagnetization [10, 41–58]	13
2.7.1 Demagnetization Principles	14
2.7.2 Demagnetization Harmonics in PM Machines With Concentrated Windings	17
2.8 False Negative Diagnosis [3]	22
2.9 Finite Element Analysis [59, 60]	24
2.9.1 Introduction	24
2.9.2 Equations Used in FEA	24
2.9.3 Application of FEA in SimcenterMagnet	25
3 Simulation Setup	26
3.1 Model Description	27
3.1.1 AutoCAD	27
3.1.2 Model Creation in SimcenterMagnet	28
4 Case Study and Results	34
4.1 Voltage and Current Analysis for All Cases	34
4.1.1 Demagnetization 25%	34
4.1.2 Demagnetization 50%	41
4.1.3 Demagnetization 25% 50 %	47
4.1.4 Demagnetization 25% Both	54

4.1.5	Demagnetization 50% Both	61
4.2	Torque Monitoring All Cases	67
4.2.1	Demagnetization 25%	67
4.2.2	Demagnetization 50%	70
4.2.3	Demagnetization 25% 50%	71
4.2.4	Demagnetization 25% Both	73
4.2.5	Demagnetization 50% Both	75
4.3	Flux Monitoring via Sensor Voltage for All Cases	78
4.3.1	Demagnetization 25%	78
4.3.2	Demagnetization 50%	81
4.3.3	Demagnetization 25% 50%	82
4.3.4	Demagnetization 25% Both	84
4.3.5	Demagnetization 50% Both	86
4.4	PVA and EPVA	88
4.4.1	Demagnetization 25%	88
4.4.2	Demagnetization 50%	89
4.4.3	Demagnetization 25% 50%	90
4.4.4	Demagnetization 25% Both	91
4.4.5	Demagnetization 50% Both	92
5	Conclusions and Future Works	94
5.1	Discussion	94
5.2	Conclusion [10, 61]	99
5.3	Future work	99
	Bibliography	101
6	Appendix A	105

List of Figures

2.1	Electromagnetic Modeling where a Intermodule flux path, b Intramodule flux path, c Linear generator intramodule flux path, d Reluctance network for three C-Core modules seen end on, e Intramodule reluctance network seen side on, the common point labeled A The appendix of Figure 2.1 reluctances are, ag air gap reluctance, pm permanent magnet reluctance, sp spacer reluctance for inter-pole flux, web web steel reluctance, l fringing path reluctance. [14]	7
2.2	C-core under Magnet Load [14]	8
2.3	Structural Modeling of C-GEN Machine where a Main heat flow paths, b Cooling curves for rotating and steady state for radial flux machine. [14]	9
2.4	The Characteristic Fault Frequency Components Produced by Faults in Induction and Synchronous Motors [19]	10
2.5	Three phase current Park's Vector where a Park's vector healthy condition, b Park's vector faulty condition.[27]	11
2.6	(a) Demagnetization Curve and Recoil Lines of the Permanent Magnet and (b) Major and minor B-H curve[42]	14
2.7	The Effect of Temperature on the B-H curve of the PMs (a) Ferrite and Alnico (b) NdFeB and SmCo [41]	15
2.8	(a) The Effect of Armature Reaction on ID (b) The Effect of Temperature on the Required External DF for the NdFeB Magnet.[41]	16
2.9	The Effect of Load Line on the ID[41]	16
3.1	Outline of C-GEN with layers of airgap and sensors	28
3.2	Properties of Copper A used in Coils of Phase 1	28
3.3	Properties of Copper B used in Coils of Phase 2	29
3.4	Properties of Copper C used in Coils of Phase 3	29
3.5	Inner and Outer Rotor made by Rotor Steel (Gray color)	30
3.6	Airtooth	30
3.7	N42 south	31
3.8	N42 north	31
3.9	Inner and outer magnet airspace	32
3.10	Airgap Components	32
3.11	Airgap Components shown in C-GEN	32
3.12	Circuit of the generator used for the simulation	33
4.1	Thesis results for: Current and Difference for Load 1 (Case Demag 25 13.125)	34
4.2	Thesis results for: Current and Difference for Load 1 (Case Demag 25 17.5)	34
4.3	Thesis results for: Current and Difference for Load 1 (Case Demag 25 21.875)	35
4.4	Thesis results for: Currents for 4 Coils of Phase 1 (Case Demag 25 13.125)	35
4.5	Thesis results for: Currents for 4 Coils of Phase 1 (Case Demag 25 17.5)	35
4.6	Thesis results for: Currents for 4 Coils of Phase 1 (Case Demag 25 21.875)	36
4.7	Thesis results for: Difference of Currents for 4 coils of Phase 1 (Case Demag 25 13.125)	36
4.8	Thesis results for: Difference of Currents for 4 coils of Phase 1 (Case Demag 25 17.5)	37
4.9	Thesis results for: Difference of Currents for 4 coils of Phase 1 (Case Demag 25 21.875)	37
4.10	Thesis results for: Fourier and Differences in Current of Load Between Healthy and Faulty (Case Demag 25 13.125)	38
4.11	Thesis results for: Fourier and Differences in Current of Load Between Healthy and Faulty (Case Demag 25 17.5)	38
4.12	Thesis results for: Fourier and Differences in Current of Load Between Healthy and Faulty (Case Demag 25 21.875)	38
4.13	Thesis results for: Voltage and Difference for $Coil_{11}$ of Phase 1 (Case Demag 25 13.125)	39

4.14	Thesis results for: Voltage and Difference for $Coil_{11}$ of Phase 1 (Case Demag 25 17.5)	39
4.15	Thesis results for: Voltage and Difference for $Coil_{11}$ of Phase 1 (Case Demag 25 21.875)	39
4.16	Thesis results for: Fourier for Currents of 4 Coils of Phase 1 (Case Demag 25 13.125)	40
4.17	Thesis results for: Fourier for Currents of 4 Coils of Phase 1 (Case Demag 25 17.5)	40
4.18	Thesis results for: Fourier for Currents of 4 Coils of Phase 1 (Case Demag 25 21.875)	40
4.19	Thesis results for: Current and Difference for Load 1 (Case Demag 50 13.125)	41
4.20	Thesis results for: Current and Difference for Load 1 (Case Demag 50 17.5)	41
4.21	Thesis results for: Current and Difference for Load 1 (Case Demag 50 21.875)	41
4.22	Thesis results for: Currents for 4 Coils of Phase 1 (Case Demag 50 13.125)	42
4.23	Thesis results for: Currents for 4 Coils of Phase 1 (Case Demag 50 17.5)	42
4.24	Thesis results for: Currents for 4 Coils of Phase 1 (Case Demag 50 21.875)	43
4.25	Thesis results for: Difference of Currents for 4 coils of Phase 1 (Case Demag 50 13.125)	43
4.26	Thesis results for: Difference of Currents for 4 coils of Phase 1 (Case Demag 50 17.5)	44
4.27	Thesis results for: Difference of Currents for 4 coils of Phase 1 (Case Demag 50 21.875)	44
4.28	Thesis results for: Fourier and Differences in Current of Load Between Healthy and Faulty (Case Demag 50 13.125)	44
4.29	Thesis results for: Fourier and Differences in Current of Load Between Healthy and Faulty (Case Demag 50 17.5)	45
4.30	Thesis results for: Fourier and Differences in Current of Load Between Healthy and Faulty (Case Demag 50 21.875)	45
4.31	Thesis results for: Voltage and Difference for $Coil_{11}$ of Phase 1 (Case Demag 50 13.125)	46
4.32	Thesis results for: Voltage and Difference for $Coil_{11}$ of Phase 1 (Case Demag 50 17.5)	46
4.33	Thesis results for: Voltage and Difference for $Coil_{11}$ of Phase 1 (Case Demag 50 21.875)	46
4.34	Thesis results for: Fourier for Currents of 4 Coils of Phase 1 (Case Demag 50 13.125)	47
4.35	Thesis results for: Fourier for Currents of 4 Coils of Phase 1 (Case Demag 50 17.5)	47
4.36	Thesis results for: Fourier for Currents of 4 Coils of Phase 1 (Case Demag 50 21.875)	47
4.37	Thesis results for: Current and Difference for Load 1 (Case Demag 25 50 13.125)	48
4.38	Thesis results for: Current and Difference for Load 1 (Case Demag 25 50 17.5)	48
4.39	Thesis results for: Current and Difference for Load 1 (Case Demag 25 50 21.875)	48
4.40	Thesis results for: Currents for 4 Coils of Phase 1 (Case Demag 25 50 13.125)	49
4.41	Thesis results for: Currents for 4 Coils of Phase 1 (Case Demag 25 50 17.5)	49
4.42	Thesis results for: Currents for 4 Coils of Phase 1 (Case Demag 25 50 21.875)	49
4.43	Thesis results for: Difference of Currents for 4 coils of Phase 1 (Case Demag 25 50 13.125)	50
4.44	Thesis results for: Difference of Currents for 4 coils of Phase 1 (Case Demag 25 50 17.5)	50
4.45	Thesis results for: Difference of Currents for 4 coils of Phase 1 (Case Demag 25 50 21.875)	50
4.46	Thesis results for: Fourier and Differences in Current of Load Between Healthy and Faulty (Case Demag 25 50 13.125)	51
4.47	Thesis results for: Fourier and Differences in Current of Load Between Healthy and Faulty (Case Demag 25 50 17.5)	51
4.48	Thesis results for: Fourier and Differences in Current of Load Between Healthy and Faulty (Case Demag 25 50 21.875)	52
4.49	Thesis results for: Voltage and Difference for $Coil_{11}$ of Phase 1 (Case Demag 25 50 13.125)	52
4.50	Thesis results for: Voltage and Difference for $Coil_{11}$ of Phase 1 (Case Demag 25 50 17.5)	53
4.51	Thesis results for: Voltage and Difference for $Coil_{11}$ of Phase 1 (Case Demag 25 50 21.875)	53
4.52	Thesis results for: Fourier for Currents of 4 Coils of Phase 1 (Case Demag 25 50 13.125)	53
4.53	Thesis results for: Fourier for Currents of 4 Coils of Phase 1 (Case Demag 25 50 17.5)	54
4.54	Thesis results for: Fourier for Currents of 4 Coils of Phase 1 (Case Demag 25 50 21.875)	54
4.55	Thesis results for: Current and Difference for Load 1 (Case Demag 25 Both 13.125)	54
4.56	Thesis results for: Current and Difference for Load 1 (Case Demag 25 Both 17.5)	55
4.57	Thesis results for: Current and Difference for Load 1 (Case Demag 25 Both 21.875)	55
4.58	Thesis results for: Currents for 4 Coils of Phase 1 (Case Demag 25 Both 13.125)	56
4.59	Thesis results for: Currents for 4 Coils of Phase 1 (Case Demag 25 Both 17.5)	56
4.60	Thesis results for: Currents for 4 Coils of Phase 1 (Case Demag 25 Both 21.875)	56
4.61	Thesis results for: Difference of Currents for 4 coils of Phase 1 (Case Demag 25 Both 13.125)	57
4.62	Thesis results for: Difference of Currents for 4 coils of Phase 1 (Case Demag 25 Both 17.5)	57
4.63	Thesis results for: Difference of Currents for 4 coils of Phase 1 (Case Demag 25 Both 21.875)	57
4.64	Thesis results for: Fourier and Differences in Current of Load Between Healthy and Faulty (Case Demag 25 Both 13.125)	58
4.65	Thesis results for: Fourier and Differences in Current of Load Between Healthy and Faulty (Case Demag 25 Both 17.5)	58

4.66 Thesis results for: Fourier and Differences in Current of Load Between Healthy and Faulty (Case Demag 25 Both 21.875)	58
4.67 Thesis results for: Voltage and Difference for $Coil_{11}$ of Phase 1 (Case Demag 25 Both 13.125)	59
4.68 Thesis results for: Voltage and Difference for $Coil_{11}$ of Phase 1 (Case Demag 25 Both 17.5)	59
4.69 Thesis results for: Voltage and Difference for $Coil_{11}$ of Phase 1 (Case Demag 25 Both 21.875)	59
4.70 Thesis results for: Fourier for Currents of 4 Coils of Phase 1 (Case Demag 25 Both 13.125)	60
4.71 Thesis results for: Fourier for Currents of 4 Coils of Phase 1 (Case Demag 25 Both 17.5)	60
4.72 Thesis results for: Fourier for Currents of 4 Coils of Phase 1 (Case Demag 25 Both 21.875)	60
4.73 Thesis results for: Current and Difference for Load 1 (Case Demag 50 Both 13.125)	61
4.74 Thesis results for: Current and Difference for Load 1 (Case Demag 50 Both 17.5)	61
4.75 Thesis results for: Current and Difference for Load 1 (Case Demag 50 Both 21.875)	62
4.76 Thesis results for: Currents for 4 Coils of Phase 1 (Case Demag 50 Both 13.125)	62
4.77 Thesis results for: Currents for 4 Coils of Phase 1 (Case Demag 50 Both 17.5)	62
4.78 Thesis results for: Currents for 4 Coils of Phase 1 (Case Demag 50 Both 21.875)	63
4.79 Thesis results for: Difference of Currents for 4 coils of Phase 1 (Case Demag 50 Both 13.125)	63
4.80 Thesis results for: Difference of Currents for 4 coils of Phase 1 (Case Demag 50 Both 17.5)	63
4.81 Thesis results for: Difference of Currents for 4 coils of Phase 1 (Case Demag 50 Both 21.875)	64
4.82 Thesis results for: Fourier and Differences in Current of Load Between Healthy and Faulty (Case Demag 50 Both 13.125)	64
4.83 Thesis results for: Fourier and Differences in Current of Load Between Healthy and Faulty (Case Demag 50 Both 17.5)	65
4.84 Thesis results for: Fourier and Differences in Current of Load Between Healthy and Faulty (Case Demag 50 Both 21.875)	65
4.85 Thesis results for: Voltage and Difference for $Coil_{11}$ of Phase 1 (Case Demag 50 Both 13.125)	66
4.86 Thesis results for: Voltage and Difference for $Coil_{11}$ of Phase 1 (Case Demag 50 Both 17.5)	66
4.87 Thesis results for: Voltage and Difference for $Coil_{11}$ of Phase 1 (Case Demag 50 Both 21.875)	66
4.88 Thesis results for: Fourier for Currents of 4 Coils of Phase 1 (Case Demag 50 Both 13.125)	67
4.89 Thesis results for: Fourier for Currents of 4 Coils of Phase 1 (Case Demag 50 Both 17.5)	67
4.90 Thesis results for: Fourier for Currents of 4 Coils of Phase 1 (Case Demag 50 Both 21.875)	67
4.91 Thesis results for: Torque and Difference in Time(s) (Case Demag 25 13.125)	68
4.92 Thesis results for: Torque and Difference in Time(s) (Case Demag 25 17.5)	68
4.93 Thesis results for: Torque and Difference in Time(s) (Case Demag 25 21.875)	68
4.94 Thesis results for: Fourier and Difference of Torque (Case Demag 25 13.125)	69
4.95 Thesis results for: Fourier and Difference of Torque (Case Demag 25 17.5)	69
4.96 Thesis results for: Fourier and Difference of Torque (Case Demag 25 21.875)	69
4.97 Thesis results for: Torque and Difference in Time(s) (Case Demag 50 13.125)	70
4.98 Thesis results for: Torque and Difference in Time(s) (Case Demag 50 17.5)	70
4.99 Thesis results for: Torque and Difference in Time(s) (Case Demag 50 21.875)	70
4.100 Thesis results for: Fourier and Difference of Torque (Case Demag 50 13.125)	71
4.101 Thesis results for: Fourier and Difference of Torque (Case Demag 50 17.5)	71
4.102 Thesis results for: Fourier and Difference of Torque (Case Demag 50 21.875)	72
4.103 Thesis results for: Torque and Difference in Time(s) (Case Demag 25 50 13.125)	72
4.104 Thesis results for: Torque and Difference in Time(s) (Case Demag 25 50 17.5)	72
4.105 Thesis results for: Torque and Difference in Time(s) (Case Demag 25 50 21.875)	73
4.106 Thesis results for: Fourier and Difference of Torque (Case Demag 25 50 13.125)	73
4.107 Thesis results for: Fourier and Difference of Torque (Case Demag 25 50 17.5)	73
4.108 Thesis results for: Fourier and Difference of Torque (Case Demag 25 50 21.875)	74
4.109 Thesis results for: Torque and Difference in Time(s) (Case Demag 25 Both 13.125)	74
4.110 Thesis results for: Torque and Difference in Time(s) (Case Demag 25 Both 17.5)	74
4.111 Thesis results for: Torque and Difference in Time(s) (Case Demag 25 Both 21.875)	75
4.112 Thesis results for: Fourier and Difference of Torque (Case Demag 25 Both 13.125)	75
4.113 Thesis results for: Fourier and Difference of Torque (Case Demag 25 Both 17.5)	76
4.114 Thesis results for: Fourier and Difference of Torque (Case Demag 25 Both 21.875)	76
4.115 Thesis results for: Torque and Difference in Time(s) (Case Demag 50 Both 13.125)	76
4.116 Thesis results for: Torque and Difference in Time(s) (Case Demag 50 Both 17.5)	77
4.117 Thesis results for: Torque and Difference in Time(s) (Case Demag 50 Both 21.875)	77
4.118 Thesis results for: Fourier and Difference of Torque (Case Demag 50 Both 13.125)	77
4.119 Thesis results for: Fourier and Difference of Torque (Case Demag 50 Both 17.5)	78
4.120 Thesis results for: Fourier and Difference of Torque (Case Demag 50 Both 21.875)	78
4.121 Thesis results for: Fourier and Differences of Voltage of Sensors (R_4 to R_8) Part 1 (Case Demag 25 13.125)	79

4.122	Thesis results for: Fourier and Differences of Voltage of Sensors(R_4 to R_8) Part 1 (Case Demag 25 17.5)	79
4.123	Thesis results for: Fourier and Differences of Voltage of Sensors(R_4 to R_8) Part 1 (Case Demag 25 21.875)	79
4.124	Thesis results for: Fourier and Differences of Voltage of Sensors(R_4 to R_8) Part 2 (Case Demag 25 13.125)	80
4.125	Thesis results for: Fourier and Differences of Voltage of Sensors(R_4 to R_8) Part 2 (Case Demag 25 17.5)	80
4.126	Thesis results for: Fourier and Differences of Voltage of Sensors(R_4 to R_8) Part 2 (Case Demag 25 21.875)	80
4.127	Thesis results for: Fourier and Differences of Voltage of Sensors(R_4 to R_8) Part 1 (Case Demag 50 13.125)	81
4.128	Thesis results for: Fourier and Differences of Voltage of Sensors(R_4 to R_8) Part 1 (Case Demag 50 17.5)	81
4.129	Thesis results for: Fourier and Differences of Voltage of Sensors(R_4 to R_8) Part 1 (Case Demag 50 21.875)	81
4.130	Thesis results for: Fourier and Differences of Voltage of Sensors(R_4 to R_8) Part 2 (Case Demag 50 13.125)	82
4.131	Thesis results for: Fourier and Differences of Voltage of Sensors(R_4 to R_8) Part 2 (Case Demag 50 17.5)	82
4.132	Thesis results for: Fourier and Differences of Voltage of Sensors(R_4 to R_8) Part 2 (Case Demag 50 21.875)	82
4.133	Thesis results for: Fourier and Differences of Voltage of Sensors(R_4 to R_8) Part 1 (Case Demag 25 50 13.125)	83
4.134	Thesis results for: Fourier and Differences of Voltage of Sensors(R_4 to R_8) Part 1 (Case Demag 25 50 17.5)	83
4.135	Thesis results for: Fourier and Differences of Voltage of Sensors(R_4 to R_8) Part 1 (Case Demag 25 50 21.875)	83
4.136	Thesis results for: Fourier and Differences of Voltage of Sensors(R_4 to R_8) Part 2 (Case Demag 25 50 13.125)	84
4.137	Thesis results for: Fourier and Differences of Voltage of Sensors(R_4 to R_8) Part 2 (Case Demag 25 50 17.5)	84
4.138	Thesis results for: Fourier and Differences of Voltage of Sensors(R_4 to R_8) Part 2 (Case Demag 25 50 21.875)	84
4.139	Thesis results for: Fourier and Differences of Voltage of Sensors(R_4 to R_8) Part 1 (Case Demag 25 Both 13.125)	85
4.140	Thesis results for: Fourier and Differences of Voltage of Sensors(R_4 to R_8) Part 1 (Case Demag 25 Both 17.5)	85
4.141	Thesis results for: Fourier and Differences of Voltage of Sensors(R_4 to R_8) Part 1 (Case Demag 25 Both 21.875)	85
4.142	Thesis results for: Fourier and Differences of Voltage of Sensors(R_4 to R_8) Part 2 (Case Demag 25 Both 13.125)	86
4.143	Thesis results for: Fourier and Differences of Voltage of Sensors(R_4 to R_8) Part 2 (Case Demag 25 Both 17.5)	86
4.144	Thesis results for: Fourier and Differences of Voltage of Sensors(R_4 to R_8) Part 2 (Case Demag 25 Both 21.875)	86
4.145	Thesis results for: Fourier and Differences of Voltage of Sensors(R_4 to R_8) Part 1 (Case Demag 50 Both 13.125)	87
4.146	Thesis results for: Fourier and Differences of Voltage of Sensors(R_4 to R_8) Part 1 (Case Demag 50 Both 17.5)	87
4.147	Thesis results for: Fourier and Differences of Voltage of Sensors(R_4 to R_8) Part 1 (Case Demag 50 Both 21.875)	87
4.148	Thesis results for: Fourier and Differences of Voltage of Sensors(R_4 to R_8) Part 2 (Case Demag 50 Both 13.125)	88
4.149	Thesis results for: Fourier and Differences of Voltage of Sensors(R_4 to R_8) Part 2 (Case Demag 50 Both 17.5)	88
4.150	Thesis results for: Fourier and Differences of Voltage of Sensors(R_4 to R_8) Part 2 (Case Demag 50 Both 21.875)	88
4.151	Thesis results for: PVA and EPVA (Case Demag 25 13.125)	89
4.152	Thesis results for: PVA and EPVA (Case Demag 25 17.5)	89
4.153	Thesis results for: PVA and EPVA (Case Demag 25 21.875)	89

4.154	Thesis results for: PVA and EPVA (Case Demag 50 13.125)	90
4.155	Thesis results for: PVA and EPVA (Case Demag 50 17.5)	90
4.156	Thesis results for: PVA and EPVA (Case Demag 50 21.875)	90
4.157	Thesis results for: PVA and EPVA (Case Demag 25 50 13.125)	91
4.158	Thesis results for: PVA and EPVA (Case Demag 25 50 17.5)	91
4.159	Thesis results for: PVA and EPVA (Case Demag 25 50 21.875)	91
4.160	Thesis results for: PVA and EPVA (Case Demag 25 Both 13.125)	92
4.161	Thesis results for: PVA and EPVA (Case Demag 25 Both 17.5)	92
4.162	Thesis results for: PVA and EPVA (Case Demag 25 Both 21.875)	92
4.163	Thesis results for: PVA and EPVA (Case Demag 50 Both 13.125)	93
4.164	Thesis results for: PVA and EPVA (Case Demag 50 Both 17.5)	93
4.165	Thesis results for: PVA and EPVA (Case Demag 50 Both 21.875)	93
6.1	Conclusion of the Investment in Offshore Wind Turbines in Greece	105
6.2	(a) The effect of armature reaction on ID (b) the effect of temperature on the required external DF for the NdFeB magnet.[10]	105

List of Tables

3.1	Simulation Cases	26
3.2	Characteristics of the C-GEN PM Generator	27
3.3	Comparison of testing and FEA results	27
5.1	Table with important data for each case	94
5.2	Comparison Table with increase and decrease values between healthy and faulty cases.	95
5.3	Table with the values of Joule loses of all coils in each case and the magnet loses for each simulation.	95
5.4	Table with the increase value of Joule loses of all coils in each case and the magnet loses for each simulation.	96
5.5	Table with harmonics values(dB) for each phase.	96
5.6	Table with increase values of harmonics values(dB) for each phase between healthy and faulty.	97
5.7	Table with Harmonic values(dB) for each $Coil_{1-8}$ of Phase 1.	97
5.8	Table with Rms values of Voltage and Current for 4 Parallel $Coils_{1-4}$ of Phase 1.	98
5.9	Table with increase and decrease of Rms values of Voltage and Current for 4 Parallel $Coils_{1-4}$ of Phase 1 between Healthy and Faulty.	98
5.10	Table with Amplitude of Left Sidebands of $Sensor_1$ Used for Flux Monitoring.	99

Acronyms

H_d Demagnetization Field. 15

CBA Cost Benefit Analysis. 1

CFD Computational Fluid Dynamics. 9

DF External Demagnetization Field. 15, 16

DWT Discrete Wavelet Transform. 3

ELIAMEP Hellenic Foundation for European and Foreign Policy. 1

EMF ElectroMotive Force. 14, 18, 35, 42, 48, 55, 61

EPVA Extended Park's Vector Approach. 2, 11, 12, 89, 99

ESPs Electrical Submarine Pumps. 12

FEA Finite Element Analysis. 4, 7, 8, 23, 24

FFT Fast Fourier Transform. 37, 39, 46, 53, 59, 66, 68, 71, 72, 75, 76

FSCWs Fractional Slot Concentrated Windings. 3

ID Irreversible Demagnetization. 14–17

IPTO Independent Power Transmission Operator S.A.. 1

MCSA Motor Current Signature Analysis. 2, 9, 12, 13, 20, 37, 43, 51, 56, 63, 99

MMF Magneto Motive Force. 7, 14, 17, 18

PM Permanent Magnet. 3–8, 12–17

PMG Permanet Magnet Generator. 3, 5, 6, 17

PMSG Permanent Magnet Synchronous Generator. 5, 24, 25

PVA Park Vector Approach. 2, 9, 11, 88, 99

TC Temperature Coefficients. 15

Chapter 1

Introduction

1.1 Background[1]

Offshore wind industry in Europe is on the rise with expectations of substantial growth in the coming decade. While Greece has yet to fully harness its remarkable offshore wind potential the prospect of developing offshore wind projects in the Mediterranean sea is of significant importance. Hellenic Foundation for European and Foreign Policy (ELIAMEP) commissioned Alma Economics to conduct a comprehensive social impact study shedding light on the social implications of investing in offshore wind energy in Greece.

This review employs a detailed Cost Benefit Analysis (CBA) framework, evaluating the investment's value from international, national and local perspectives. It draws on extensive evidence from social impact studies, business cases, engineering and environmental research as well as insights from key stakeholders in renewable energy and offshore wind farms. The analysis extends beyond financial costs and benefits encompassing global and local societal impacts including hard to measure social benefits. The work enables a comparison of these benefits with costs revealing the net social gains resulting from the investment. The hypothetical scenario envisions a 455 MW offshore wind farm located 10 km from the shore and 250m deep in Greek seas replacing oil and gas energy sources. The report outlines the methodological approach presents key findings and offers insights into potential benefits and geopolitical implications. The evidence from the Independent Power Transmission Operator S.A. (IPTO) (2023) shows that Greece's energy landscape is evolving. While renewable energy sources are growing they face challenges due to their intermittent nature depending on weather conditions. To fill in gaps in energy production Greece has turned to less eco-friendly options like lignite and imported natural gas increasing carbon emissions and energy dependency.

To address these issues the country is exploring innovative solutions such as energy storage. The European Parliament suggests using new battery technologies thermal storage or green hydrogen to store energy from renewables ensuring a consistent energy supply. Green hydrogen, produced via electrolysis is a promising alternative to replace lignite power plants and align with EU carbon emissions goals. The "White Dragon" proposal, with an 8 billion € investment, aims to develop a green hydrogen project in Greece. This initiative seeks to transition away from lignite, replace it with renewables and produce hydrogen for energy marking a significant step towards a more sustainable and eco-friendly energy future in Greece.

Renewable energy sources in Greek islands, particularly the non-interconnected ones, face challenges in their energy supply. While there has been progress in connecting some islands to the mainland grid there are still 29 islands with autonomous electrical systems. These islands rely on a combination of renewable energy sources and oil power plants with renewable energy accounting for 21% of the energy mix. The key concern is the lack of investment in expanding renewable energy and storage systems. These investments depend on the economic feasibility of interconnecting these islands with the mainland grid. However, there are promising examples of self-sufficiency. Tilos Island is already an energy self sufficient island with a hybrid energy system based on wind, solar power and storage. Astypalaia is on track to become "Smart Green" by installing a hybrid renewable energy system. These incidents demonstrate the potential for sustainable energy solutions on Greek islands. The future of these non-interconnected islands hinges on balancing economic considerations and the need for cleaner more reliable energy sources. Wind power in Greece is actively harnessing its wind energy potential, primarily through onshore wind farms in island regions currently contributing 4 GW of capacity to cover 12% of the country's electricity demand. To align with environmental targets Greece aims to install 7 GW of wind energy capacity by 2030. The nation's wind energy potential, especially in offshore wind, offers significant opportunities, potentially enabling islands to achieve energy self-sufficiency.

In the summer of 2021, Greece took a significant step by preparing the legislative and regulatory framework for offshore wind power following a collaborative public consultation between key wind energy associations. However, it's important to note that the acceptance of onshore wind farms faces challenges as seen in the Cyclades where residents express concerns about the impact on landscapes, biodiversity and tourism. This



issue is not unique to Greece and is part of the international "Not in My Backyard" movement driven by concerns related to noise and visual disturbances.

Internationally, the development of offshore wind energy has seen significant progress over the past three decades. Denmark led the way with the construction of the world's first offshore wind farm in 1991 providing energy to thousands of households. This groundbreaking project showed the way for numerous investments in offshore wind farms with Denmark, the UK, Germany, China and the Netherlands emerging as leaders in offshore wind markets. Europe in particular has made substantial steps boasting 25 GW of installed offshore wind capacity covering a notable 3% of its electricity demand in 2020. The United States entered the offshore wind sector in 2016 with a 150 MW capacity farm and further expansion is anticipated. China has been a key player, representing 23% of global offshore wind energy capacity by the end of 2019, with ambitious plans to add 52 GW of capacity by 2030.

While many operating wind farms currently rely on fixed-bottom turbines, the shift towards floating offshore wind turbines is becoming more prominent, especially in areas with water depths exceeding 50 meters. Notably, floating wind farms like Hywind Scotland and Windfloat Atlantic have demonstrated the feasibility of this technology. This trend is expected to continue, with more investments in floating farms worldwide, including the Hywind Tampen in Norway, signifying the bright future of offshore wind energy.

In the end, the review highlights the socio-economic benefits of investing in offshore wind farms in Greece. The choice of location and capacity of these farms plays a crucial role. International perspectives suggest substantial net social value with €1.7 generated for every €1 invested, driven by reduced CO2 emissions.

The location of these farms is essential affecting both investment costs and local impacts. Greece's commitment to carbon neutrality is greatly supported by the reduction in CO2 emissions from offshore wind. Additionally, investing in offshore wind energy can benefit local communities through various compensation mechanisms including lower energy prices and public goods provision. This research underscores the importance of offshore wind in Greece's journey toward clean and sustainable electricity generation, making it an integral part of the nation's efforts to combat climate change.

1.2 Objectives and Methodology of Work

This thesis studies the application of different well-known diagnosis methods to the C-GEN (Direct drive generator) for demagnetization purposes. Some of the thesis content, specifically some equations are adopted from previous work for better understanding of the harmonics generation mechanism in C-GEN.

The objectives of the thesis are as follows:

- Design of the 2D outline of C-GEN in AutoCAD
- Extension with electromagnetic designs and simulation in SimcenterMAGNET for 18 different cases of demagnetization with different ohmic loads of C-GEN and comparing it with experimental results taken in Edinburgh (Institute for Energy Systems, School of Engineering, University of Edinburgh).
- Obtain measurements of voltage, current, torque and magnetic flux (through measuring voltage of sensors placed in different spacial angles) from simulating C-GEN in steady state using 6kHz sampling rate.
- Fault diagnosing C-GEN's demagnetization (rotor fault) through different fault diagnosis techniques through signal processing (PVA,EPVA,MCSA, flux monitoring and torque monitoring) using MATLAB.
- Evaluation of the results of each fault detection method after signal processing through observation of the signals and via look-up tables with percentage differences between healthy and faulty cases.

1.3 Outline

Chapter 1 - Introduction: Introduces the objectives and scope of the Thesis.

Chapter 2 - Theoretical Background: Outlines the theoretical background of the thesis, with focus on fault diagnosis techniques and equations behind harmonic generation due to demagnetization in C-GEN.

Chapter 3 - Simulation Setup: Describes the simulation setup used to extract measurements.

Chapter 4 - Case Study and Results: Outlines the case study and results used in fault detection techniques. Includes a brief discussion of results as they are presented and which method is the most useful.

Chapter 5 - Conclusions and Future Work: Presents a summary of the most important conclusions of the thesis and some suggestions for future work



1.4 Related Work[2–11]

1.4.1 Demagnetization in Permanent Magnet Machines

One of the studies highlights the critical issue of demagnetization in permanent magnet machines, particularly in renewable energy applications like offshore wind, tidal and wave energy. It distinguishes between uniform and non-uniform demagnetization, focusing on shedding light on practical challenges, especially in scenarios of uniform demagnetization due to overloading or overheating. The research provides insights into the lab-induced demagnetization case of a direct-drive C-GEN permanent magnet generator, contributing to a better understanding of demagnetization faults in real-world applications

1.4.2 Partial Irreversible Demagnetization in Large-Scale PM Wind Generators

The paper addresses irreversible demagnetization in permanent magnet wind turbines, a significant cause of motor failures. Using Maxwell software, the study creates a Permanent Magnet Generator (PMG) model to simulate various demagnetization scenarios, providing key findings on the progression of irreversible demagnetization. It establishes a theoretical foundation for online monitoring and fault diagnosis, emphasizing the significance of current harmonics and flux linkage in identifying irreversible demagnetization faults.

Another review emphasizes the critical requirement of high reliability for large-scale Permanent Magnet (PM) wind generators, particularly partial irreversible demagnetization challenges, such as those occurring under short-circuit conditions. The research explores the adoption of Fractional Slot Concentrated Windings (FSCWs) to enhance fault-tolerance capabilities and torque density. It delves into the performance of partial demagnetization in a 7 MW interior PM wind generator equipped with FSCWs, using finite-element analysis to evaluate transient magnetic behavior.

1.4.3 Machine Learning for Fault Diagnosis in permanent magnet generators

To prevent costly shutdowns in the industry, a work leverages condition monitoring methods and artificial intelligence for early fault diagnosis in Permanent Magnet Generators PMG. The research utilizes the Discrete Wavelet Transform (DWT) technique and machine learning classifiers to achieve high accuracy in diagnosing eccentricity, magnet breakage and stator inter-turn short circuit faults. Notably, the study highlights the superiority of air gap flux over stator current as a diagnostic parameter.

1.4.4 New method for demagnetization fault diagnosis in axial flux permanent magnet synchronous generators

A novel method for diagnosing demagnetization faults in Axial Flux Permanent Magnet Synchronous Generators is introduced. The review proposes using a second-order Goertzel Transform combined with the estimation of permanent magnet flux to track fault signatures in calculated instantaneous power. Experimental testing validates the proposed method under different operating conditions, demonstrating its effectiveness in discriminating demagnetization faults from other types of faults.

1.4.5 Temperature Rise Analysis of Permanent Magnet Generators with Demagnetization Faults

The research investigates the temperature rise of a permanent magnet generator with demagnetization faults. Using thermal-field finite element and mathematical models, the study analyzes the temperature distribution under different demagnetization conditions. The findings provide a diagnostic analysis basis for PMSGs, offering insights into the impact of demagnetization faults on temperature and copper losses in stator windings.

1.4.6 Fault Detection in Axial Flux Coreless Permanent Magnet Synchronous Generators

The work presents an effective method for detecting demagnetization faults in axial flux coreless Permanent Magnet Synchronous Generators. The proposed method utilizes texture analysis-based feature extraction, demonstrating high success rates in fault detection through the analysis of current and voltage signals. The research highlights the effectiveness of the proposed method in detecting demagnetization faults in axial flux coreless PMG under different operating conditions.

1.4.7 The Demagnetization Harmonics Generation Mechanism in PM Machines

The analytical investigation of partial demagnetization harmonics in the stator current of permanent magnet machines provides valuable insights. It demonstrates that the characteristics of these harmonics are closely tied to the number of phase coils, with an increase in the number of coils leading to reduced signatures in the stator current spectra. This relationship is independent of the useful flux direction and applies to both radial and axial flux PM machines. Additionally, the 3-phase connection between phases results in further cancellation of fault signatures. The study's findings are reinforced through extensive Finite Element Analysis (FEA) simulations involving three different PM generators, emphasizing the reliability of the proposed methodology. Given that various rotor faults in PM machines are linked to mechanical factors such as eccentricity, misalignment and bearing faults, identifying the origin of harmonics is crucial for planning timely maintenance and preventing catastrophic machine breakdowns. An intriguing discovery is the potential association of the second stator current harmonic with demagnetization, posing a challenge in distinguishing stator faults from rotor demagnetizations.

This paper contributes to the dependable identification of demagnetization concerning a machine's manufacturing parameters and characteristics. Future research will aim to address partial demagnetization in PM machines with distributed windings, further advancing fault diagnosis and maintenance practices.

Chapter 2

Theoretical Background

2.1 Synchronous Generator [12, 13]

A synchronous generator often called an alternator or AC generator is a synchronous machine that transforms mechanical power into AC electric power using the principle of electromagnetic induction. The term "alternator" is employed because it generates AC power. The essential characteristic of a synchronous generator is its need to operate at a synchronous speed to produce AC power at the desired frequency.

2.1.1 Permanent Magnet Synchronous Generator

A Permanent Magnet Synchronous Generator (PMSG) stands out as a generator that uses Permanent Magnets for its excitation field in contrast to traditional generators that use coils. The term "synchronous" in PMSG denotes the synchronous rotation of both the rotor and the magnetic field achieved through a shaft-mounted Permanent Magnet mechanism. Current is induced into the stationary armature as the magnetic field rotates with the rotor. This design offers efficiency and reliability in power generation, making it a valuable choice in various applications.

The fundamental design of generators typically involves a central rotating component known as the "rotor," which houses the magnet responsible for generating the magnetic field, while the stationary part called the "stator" serves as the armature connected to the electrical load. The orientation of the stator field plays a crucial role in the generator's operation, influencing both torque and voltage.

The voltage output of the generator is determined by the load it supplies. When dealing with inductive loads, the angle between the rotor and stator fields exceeds 90° , resulting in an overexcited generator with increased voltage. Conversely, capacitive loads lead to an underexcited generator.

The armature winding in standard utility equipment comprises three conductors that represent the three phases of a power circuit, aligning spatially at 120° intervals on the stator. This configuration ensures a uniform force and torque applied to the generator rotor. The induced currents in these conductors combine spatially to create a magnetic field resembling that of a single rotating magnet, resulting in a steady and synchronized stator field. This stator field rotates at the same frequency as the rotor when the rotor features a single dipole magnetic field, maintaining a fixed position relative to each other during operation.

2.2 C-GEN Technology [11, 14–18]

C-GEN Permanent Magnet Generator represents an innovative approach to enhancing efficiency and reducing the overall system mass in direct drive power take-off applications. The development of the C-GEN generator involves the integration of electromagnetic and structural models to create a wide design tool. The advancement of wave and tidal renewable energy resources necessitates innovative approaches to power takeoff technology. The variable nature of power input demands highly efficient generators capable of accommodating a range of input powers. Traditional high-speed, low-force generators are ill-suited for delivering power to wave energy converters and tidal device rotors, often requiring complex gearbox or speed conversion mechanisms that introduce additional risks and maintenance requirements.

To soften the extreme cost penalties associated with maintenance in challenging operating environments, it is essential to reduce the number of stages in the power takeoff system, ultimately lowering the overall cost of energy production. The direct drive concept, which closely couples electrical power takeoff to the energy extraction mechanism, has shown promise in commercial-scale wave and tidal energy applications. However, its adoption has been hindered by the size, weight and cost of suitable generators.



Mueller and McDonald have introduced a lightweight, cost-effective generator solution that incorporates a modular air-cored Permanent Magnet Generator layout. Permanent Magnet Generator (PMG) offer improved efficiency, especially at partial loads and can lead to a notable increase in energy conversion. The choice of an air-cored machine simplifies assembly and reduces bearing loads. While it may increase the cost of magnets and frame size, the overall reduction in construction costs and structural mass outweigh these factors.

This work on the C-GEN generator, which includes modeling, optimization, prototype construction and results, represents a significant step in advancing renewable energy applications. The review aims to demonstrate the effectiveness of modeling and optimization methods for linear and rotary C-GEN machines, paving the way for more efficient and cost-effective power takeoff solutions in the wave and tidal energy sector.

The C-GEN machine derives its name from the distinctive core shape of a rotary generator, as depicted in Figures 1a and 1b. This unique arrangement places the primary structural load on the C-shaped core, which counteracts the attractive force between the magnets and also serves as the conduit for both inter-pole (Figure 2.1a) and intra-pole (Figure 2.1b) flux.

In the case of a linear generator, the C shape can be enclosed, enhancing structural rigidity and introducing an additional path for flux (Figure 2.1c). The flux pathways within the generator are effectively represented by the reluctance network illustrated in Figures(2.1d, 2.1e). This innovative core design, whether in rotary or linear form, plays a pivotal role in the efficient operation of the C-GEN machine, enabling it to harness the power of renewable energy resources while maintaining structural integrity and reliability.

2.2.1 Constructional Features of C-GEN

Intergration

The design of any generator, including the C-GEN generator, needs a delicate balance among electromagnetic, structural, thermal and manufacturing considerations. The optimal balance varies depending on the primary priorities for a given application, which may include factors like cost, efficiency, ease of construction and environmental considerations.

The C-GEN generator's straightforward design allows for cost-effective production, even in relatively low quantities, making it well-suited for optimization tailored to specific applications. The interconnected nature of electromagnetic, structural and thermal models means that alterations to the generator's design will impact each aspect differently. Consequently, an integrated modeling approach becomes imperative to identify the most suitable solution for a particular application. This approach ensures that the generator's design aligns with the unique requirements and priorities of the intended use, promoting efficiency and effectiveness in energy generation.

The phenomenon of fringing in magnetic flux occurs when the flux path travels between magnets without crossing the air gap. This fringing effect leads to a decrease in the reluctance of this particular flux path as the magnets are positioned closer together. Consequently, this introduces a constraint on the use of relatively thin magnets and a low pole pitch to enhance the rate of change of flux in a low-speed generator. The characterization of each element in the reluctance network can be accurately defined using well-established formulas. Understanding and addressing fringing in magnetic flux is a crucial aspect of designing efficient generators, particularly in scenarios where thin magnets and low pole pitch are involved, ultimately influencing the generator's performance in low-speed applications.

Each element of magnetic reluctance can be defined by:

$$R = \frac{l}{\mu A} \quad (2.1)$$

where R: magnetic reluctance, l: length of the circuit in meters(m), μ : permeability of the material ($\mu = \mu_0 \mu_r$), A: cross-sectional area of the circuit in square meters (m^2).

The reluctances are calculated from the chosen geometry of the machine and materials data.

$$S_{ag} = \frac{h_w + 2a_c}{l_m w_m \mu_0} \quad (2.2)$$

where S_{ag} : reluctance of air gap including magnets, h_w : height of the winding, a_c : air gap clearance, w_m : width of the magnet, l_m : length of the magnet, μ_0 : permeability of free space.

$$S_{PM} = \frac{h_m}{l_m w_m \mu_r \mu_0} + \frac{t}{2l_m w_m \mu_{st} \mu_0} \quad (2.3)$$

where S_{PM} : reluctance of Permanent Magnet, h_m : height of the magnet, w_m : width of the magnet, l_m : length of the magnet, μ_0 permeability of free space, μ_r relative permeability of Permanent Magnet material, μ_{st} relative permeability of core material.

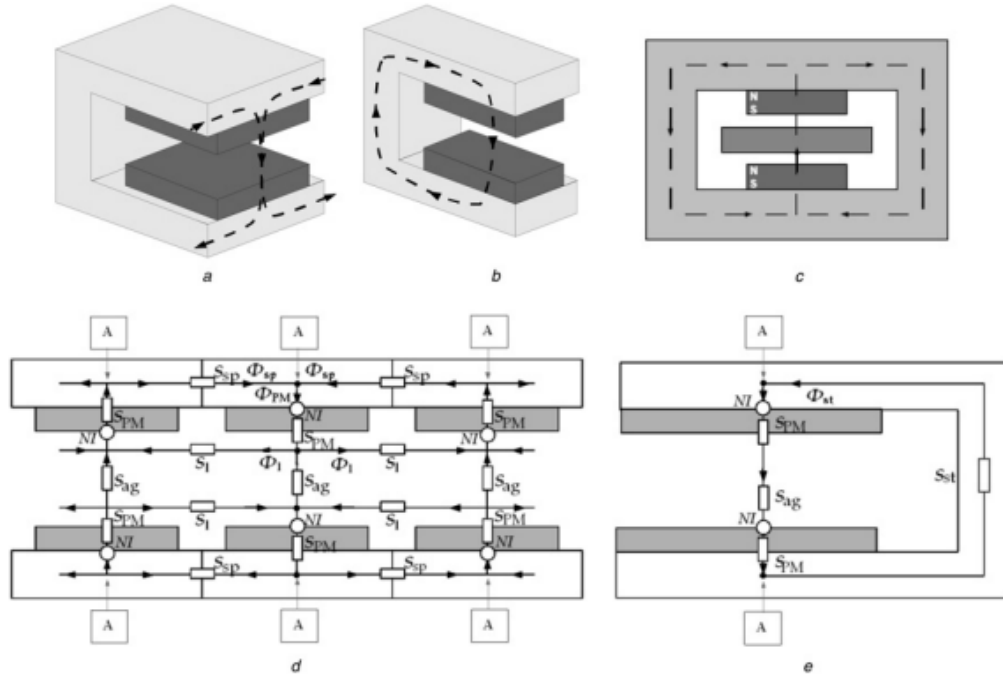


Figure 2.1: Electromagnetic Modeling where a Intermodule flux path, b Intramodule flux path, c Linear generator intramodule flux path, d Reluctance network for three C-Core modules seen end on, e Intramodule reluctance network seen side on, the common point labeled A The appendix of Figure 2.1 reluctances are, ag air gap reluctance, pm permanent magnet reluctance, sp spacer reluctance for inter-pole flux, web web steel reluctance, l fringing path reluctance. [14]

$$S_{st} = \frac{(1/2)l_m + l_{cl} + l_c}{t\tau_p\mu_{st}\mu_0} \quad (2.4)$$

where S_{st} reluctance of flux path through module back, l_m : length of the magnet, l_{cl} : clearance between magnet and steel web, l_c thickness of steel web, μ_{st} relative permeability of core material, t thickness of the core.

$$S_l = \frac{\tau_p - \tau_m}{(1/2)(h_w + 2a_c)l_m\mu_0} + \frac{\pi}{l_m\mu_0} \quad (2.5)$$

where S_l reluctance of fringing flux path between magnets, τ_p pole pitch, τ_m magnet pitch, a_c air gap clearance, h_w height of the winding, l_m : length of the magnet, μ_0 permeability of free space.

$$S_{sp} = \frac{1}{tl_m\mu_0} \left(\frac{\tau_p}{\mu_{st}} + c \right) \quad (2.6)$$

where S_{sp} reluctance of flux path from module to module, t thickness of the core, l_m : length of the magnet, μ_0 permeability of free space, τ_p pole pitch, μ_{st} relative permeability of core material.

The Magneto Motive Force (MMF) of the Permanent Magnets can be calculated using the following equation. The magnet strength is given as NI , the combined number of turns and current flow required to achieve the same Magneto Motive Force.

$$NI = \phi R \quad (2.7)$$

where Φ is the magnetic flux, R reluctance of the circuit, N number of turns in a coil, I electric current through the coil.

$$NI = B_r l_m w_m \frac{h_m}{l_m w_m \mu_0 \mu_r} = \frac{B_r h_m}{\mu_0 \mu_r} \quad (2.8)$$

where N number of turns in a coil, I electric current through the coil, B_r remnant flux density of magnet used, l_m length of the magnet, w_m width of the magnet, h_m height of the magnet, μ_0 permeability of free space, μ_r relative permeability of Permanent Magnet material.

Maximum flux density in the air gap, as determined through the analytical method, has been rigorously compared with results obtained from FEA software. The analytical findings exhibit a high degree of consistency

with the FEA results, with errors of less than 5% across all cases, well within acceptable limits. Furthermore, the visualization of flux paths in the FEA software contributes to a comprehensive understanding of the magnetic behavior within the system. This alignment between analytical and FEA results underscores the reliability of the analytical method in characterizing the flux density in the air gap, which is of paramount importance in the design and assessment of electromagnetic systems.

Structural

The primary load on the C-GEN machine is the attractive force between opposite pole magnets, a force that plays a crucial role in closing the air gap, as depicted in Figure 2.2. It is essential to ensure that the deflection of the cores remains within a safe boundary accounting for other various external factors. Notably, a positive feedback effect is at play, as the C-core deflects, the force of attraction increases leading to iterative calculations to ensure that the additional deflection does not exceed the design limitations.

The magnet force is modeled as a distributed load and with a sufficiently stiff web section, the equations for a fixed-end beam can effectively model the resulting deflection. The sizing of the back iron leverages the greater area requirement between electromagnetic and structural modeling. If the material needed for electromagnetic purposes significantly differs from the structural requirement, a non-rectangular cross-section, such as an I-beam, can be employed. Conversely, if the situation is reversed, additional material can be incorporated in the high-flux region to prevent saturation while simultaneously minimizing weight. Balancing these factors is crucial in achieving an optimal design for the C-GEN machine, considering the interplay between magnetic and structural considerations.

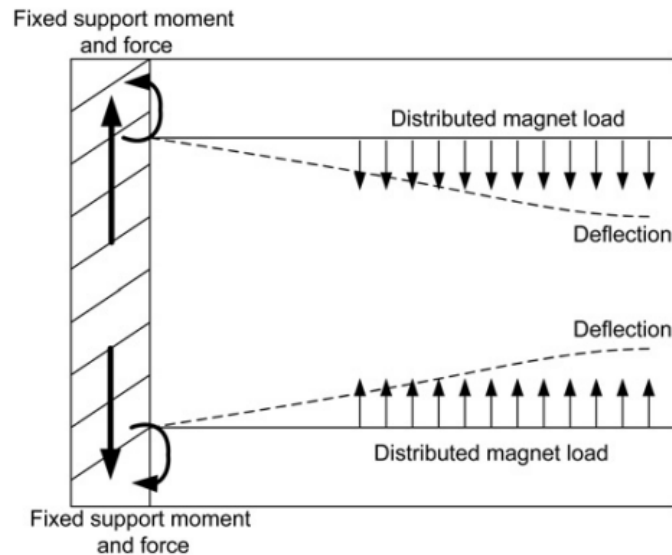


Figure 2.2: C-core under Magnet Load [14]

Thermal

In summary, the maximum sustained power output of a generator is constrained by the maximum temperature reached by critical components. The thermal model incorporates considerations for copper loss in coil resistance, eddy current, bearing and windage losses. Thermal modeling involves iterative processes to determine the final coil temperature, with a primary focus on the temperature-sensitive insulation of coil windings. The generator's components, such as Permanent Magnets and certain bearing types, are susceptible to temperature-related damage.

Utilizing appropriate correlations, geometry and measured data from existing prototypes, a thermal resistance network is constructed. This network draws an analogy between heat flow and electrical current flow, where temperature corresponds to voltage, thermal resistance equates to electrical resistance and heat represents current.

The C-GEN can function as either an axial or radial flux generator depending on the application. Thermal modeling for a radial flux generator incorporates considerations for axial heat flow to the coil support (R1), heat transfer across the air gap to the rotor (R2) and heat removal by airflow through the air gap (R3). The thermal model assumes a large thermal resistance (R3) due to the complex 'fan effect' of the magnets, which is not explicitly modeled in this work.

Additionally, the 'fan effect' of the magnets, depicted in Figure 2.3b, contributes to cooling during operation. While a comprehensive representation of this effect involves detailed Computational Fluid Dynamics (CFD) analysis, it is assumed in the thermal model that the thermal resistance R_3 is substantial, effectively disregarding the 'fan effect' of the magnets for simplicity in this review.

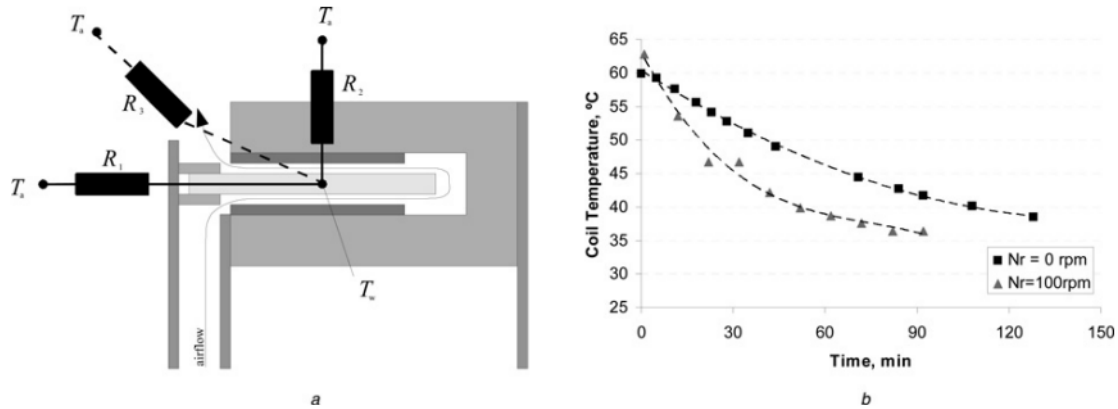


Figure 2.3: Structural Modeling of C-GEN Machine where a Main heat flow paths, b Cooling curves for rotating and steady state for radial flux machine. [14]

2.3 Electrical Testing [19–24],

Detecting faults in electric machines, particularly in the rotor or bearings, is critical for preventing severe damage and ensuring operational reliability. Various faults, such as cracks, open circuits and rotor eccentricity, can lead to accelerated aging and catastrophic failure if left undetected. Monitoring methods like electrical monitoring, specifically Motor Current Signature Analysis (MCSA), have gained popularity for their low cost, nonintrusive and remote nature.

However, challenges exist, especially in detecting mechanical defects related to bearings, eccentricity, or load, where vibration analysis is deemed more reliable. MCSA may face limitations in establishing universal fault severity thresholds and its sensitivity may be attenuated at higher frequencies in noisy environments. Additionally, interference from mechanical load defects poses challenges, leading to false indications in fault detection.

To address these challenges, ongoing research focuses on improving the reliability of MCSA. Testing under high slip conditions, such as motor standstill or starting, proves more immune to false indications, emphasizing the need for refined testing methods. Active research includes the development of new fault indicators, intelligent algorithms for simultaneous fault detection, variation of fault thresholds and statistical analysis to enhance the overall reliability and predictive capabilities of fault detection systems.

In conclusion, advancements in fault detection methods, particularly in the context of MCSA, are crucial for maintaining the integrity of electric machines, minimizing unscheduled downtime and optimizing maintenance practices. Ongoing research efforts aim to extend the capabilities of MCSA, providing more robust and accurate fault detection for improved operational efficiency.

2.4 Fault Diagnosis Methods [25–31]

Below will be described the methods that are used for fault detection in this thesis.

2.4.1 Park's Vector Approach

The utilization of Park Vector Approach emerges as a valuable diagnostic tool for electric machines and drives. By transforming the stator currents into a concise two-dimensional representation, this method provides diagnostic signs for both electrical and mechanical defects. The determination of Park's vector currents, derived from measured stator phase currents, enhances the diagnostic capabilities of this approach. The works of modern researchers collectively contribute to advancing the understanding and application of Park's vector approach in the diagnosis of electric machine elements, offering a promising avenue for effective and comprehensive fault detection.

FAULT (COMPONENT)	CHARACTERISTIC FAULT FREQUENCY
Static eccentricity	$\left[kR \left(\frac{1-s}{p} \right) \pm n \right] f_s$
Dynamic and mixed eccentricity	$\left[(kR \pm n_d) \left(\frac{1-s}{p} \right) \pm n \right] f_s$
Mixed eccentricity, PM demagnetization, SM open damper, and shorted field	$nf_s \pm kf_r = \left[n \pm k \frac{(1-s)}{p} \right] f_s$
IM broken rotor bars and end rings	$\left[\frac{k}{p} (1-s) \pm s \right] f_s$
Bearing outer race	$f_s \pm k \frac{N}{2} f_s \left(1 - \frac{D_b}{D_c} \cos \beta \right)$
Bearing inner race	$f_s \pm k \frac{N}{2} f_s \left(1 + \frac{D_b}{D_c} \cos \beta \right)$
Bearing ball element	$f_s \pm k \frac{D_c}{D_b} f_s \left[1 - \left(\frac{D_b}{D_c} \cos \beta \right)^2 \right]$

f_s : fundamental frequency, f_r : rotor rotational frequency, s : rotor slip, p : number of pole pairs, R : number of rotor slots, k : integer (= 1, 2, 3, ...), n : harmonic order (= 1, 3, 5, ...), n_d : dynamic eccentricity order, N : number of balls, D_b : ball diameter, D_c : ball pitch diameter, β : ball contact angle.

Figure 2.4: The Characteristic Fault Frequency Components Produced by Faults in Induction and Synchronous Motors [19]

The core methodology involves transforming the three-phase coordinate system of stator currents into a two-dimensional moving system represented by dq-coordinates. Diagnostic insights are derived from the trajectory described by the vector on the coordinate plane, incorporating the stator current axes (I_d and I_q), particularly as the power supply frequency changes. The approach proves effective in identifying both electrical and mechanical defects in engines. Determination of Park's Vector Currents:

The currents I_d and I_q in Park's vector approach are crucial for diagnostics and are determined through ratios based on previously measured stator phase currents I_a , I_b and I_c .

The current Park vector, using the stator reference frame, components (I_d , I_q) are a function of mains phase variables (I_a , I_b , I_c) calculated as:

$$I_d = \sqrt{\frac{2}{3}} I_a - \sqrt{\frac{1}{6}} I_b - \sqrt{\frac{1}{6}} I_c \quad (2.9)$$

$$I_q = \sqrt{\frac{1}{2}} I_b - \sqrt{\frac{1}{2}} I_c \quad (2.10)$$

Under ideal conditions, the three-phase currents lead to a Park vector with the following components:

$$I_d = \frac{\sqrt{6}}{2} I_M \sin(\omega t) \quad (2.11)$$

$$I_q = \frac{\sqrt{6}}{2} I_M \sin(\omega t - \frac{\pi}{2}) \quad (2.12)$$

where I_M : peak value of phase current, ω : angular frequency,

Then, in the dq-coordinate system, Park's vector for the engine describes a Figure centered at the origin according to the equation:

$$I = I_d + j I_q \quad (2.13)$$

In the presence of a normally functioning electric machine powered by a strictly symmetrical voltage system, the Park's vector pattern exhibits a regular circle centered at the origin of the d-q system coordinates. However, when damage occurs to components such as the stator winding, rotor winding and bearings, or if there is a violation of the symmetry of the supply voltage system, the three-phase stator currents lead to a modified form of the Park's vector pattern. Despite the simplicity of detecting damage using Park's vector approach, identifying different types of damage solely from the graphical representation of off-state modes proves challenging. The vector pattern is influenced by factors such as power supply quality, engine operating mode, load type and various other elements.

Noteworthy findings include:

- Effective results in diagnosing the stator, particularly in determining the number of closed turns in the case of a turn-to-turn short circuit, considering a poor-quality power supply system.
- Development of an algorithm for practical use within the built-in diagnostic system to establish the state and degree of the stator winding.
- Application of Park's vector method for precise determination of defects in the rotor winding of an induction motor, accounting for factors like rotor damage, magnetic poles and rotor grooves.
- Utilization of signal processing methods and spectral analysis to assess rotor defects, with a focus on monitoring the width of Park's vector patterns.

While some challenges exist, such as the difficulty in the operational determination of damage types, especially during poor power supply conditions, ongoing research aims to refine and enhance the applicability of Park's vector approach in automated control modes. This comprehensive overview underscores the method's potential in diagnosing diverse faults in electric machines, paving the way for further advancements in condition monitoring and fault detection.

2.4.2 Extended Park Vector Approach

The Extended Park's Vector Approach is based on the Park Vector Approach. In this section, the theory of Park's vector method will be introduced. The ideal three-phase currents I_a, I_b, I_c are converted to I_α, I_β by transformation. Since only a positive sequence component is contained in the three-phase current, we can obtain the following equations:

$$I_\alpha = \frac{\sqrt{6}}{2} I_p \cos(\omega t) \quad (2.14)$$

$$I_\beta = \frac{\sqrt{6}}{2} I_p \sin(\omega t) \quad (2.15)$$

where I_p is the positive sequence current of the stator.

Based on (2.14 and 2.15), if i_α is selected as the horizontal axis and i_β is selected as the vertical axis, the trajectory is the regular circle in the ideal operation condition, as shown in Figure 2.4a. However, if the three-phase currents are in the non-ideal condition, in addition to the positive sequence component, there is a negative sequence component in the three-phase currents. Based on the 3s/2s transformation, the ellipse trajectory can be obtained, as shown in Figure 2.4 b.

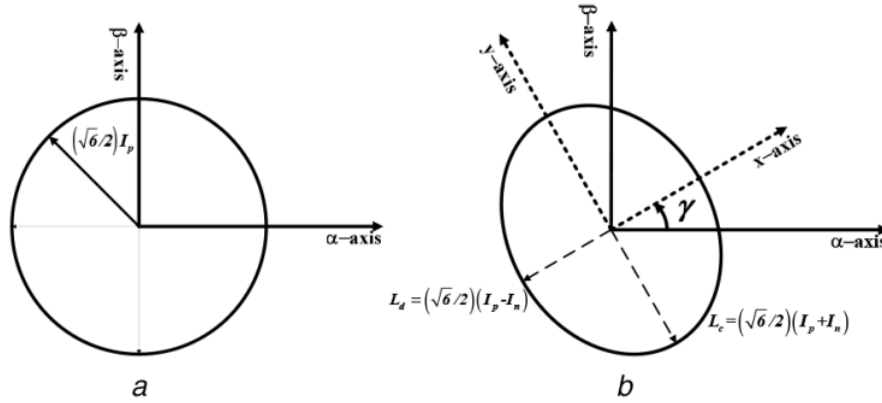


Figure 2.5: Three phase current Park's Vector where a Park's vector healthy condition, b Park's vector faulty condition.[27]

Then, we can get the expression of the Park's circle vector in the x-y axis

$$I_x = \left(\frac{\sqrt{6}}{2} \right) (I_p - I_n) \cos(\omega t) \quad (2.16)$$

$$I_y = \left(\frac{\sqrt{6}}{2} \right) (I_p + I_n) \sin(\omega t) \quad (2.17)$$

where I_n is the negative sequence current of the stator.

The transformation formulas of the coordinates are:

$$I_\alpha = I_x \cos \gamma - I_y \sin \gamma \quad (2.18)$$

$$I_\beta = I_x \sin \gamma + I_y \cos \gamma \quad (2.19)$$

Combining (2.16, 2.17, 2.18, 2.19) we get the expression of the Park's circle vector in $\alpha - \beta$ axis.

$$I_\alpha = L_d \sin(\omega t) \cos \gamma - L_c \cos(\omega t) \sin \gamma \quad (2.20)$$

$$I_\beta = L_d \sin(\omega t) \sin \gamma + L_c \cos(\omega t) \cos \gamma \quad (2.21)$$

where γ : is the angle difference between the x-y axis and $\alpha - \beta$ axis, L_d is the length of the semi-minor axis, L_c is the length of the semi-major axis.

In non-ideal operating conditions, such as voltage imbalance or load changes, asymmetrical factors disrupt the previously stable oval trajectory of the Park's vector. This deviation from the expected pattern poses challenges in fault detection using traditional Park's vector methods, especially in the presence of slight inter-turn faults or non-ideal conditions. Industrial applications encounter difficulties in accurately determining the oval trajectory due to these factors. Moreover, the reliance on image recognition in the Park's vector method introduces a vulnerability to the accuracy of image recognition systems.

To address these challenges, Extended Park's Vector Approach is introduced. This method leverages spectrum analysis of the Park's vector and quantization of fault characteristics. By utilizing the extended Park's vector method, early fault detection becomes achievable and the uncertainties associated with image recognition accuracy are diminished. This innovative approach represents a valuable advancement in fault detection methodologies, ensuring more robust and reliable performance under diverse operating conditions.

Using (2.20 and 2.21) we can find that:

$$I_e = \sqrt{I_\alpha^2 + I_\beta^2} = \frac{\sqrt{6}}{2} \sqrt{I_p^2 + I_n^2 + 2I_p I_n \cos(2\omega t)} \quad (2.22)$$

where I_e : module of the Park's Vector, I_e includes the direct current component and twice fundamental frequency component.

2.4.3 MCSA

In the field of industrial electric machines, the prevalence and challenges of Motor Current Signature Analysis (MCSA) as a fault detection method are underscored. While widely used, MCSA has acknowledged limitations in detecting mechanical defects related to bearing, eccentricity, or load, with vibration analysis considered more reliable for these issues. The review highlights challenges such as false positives and negatives, particularly in the context of load defects and interference from mechanical load defects. Ongoing research aims to enhance MCSA's reliability through intelligent algorithms, fault indicators and statistical analysis. Continued efforts in developing new fault indicators are deemed essential for improving reliability and fault severity determination.

Motor Current Signature Analysis (MCSA) emerges as a crucial tool for fault detection in electric motors. The method, based on processing the current signal's frequency spectrum, proves effective in identifying various faults, including bearing faults, broken rotor bars and air-gap eccentricity. The review emphasizes MCSA's transformative role in the condition monitoring industry, particularly in applications like Electrical Submarine Pumps (ESPs). MCSA's ability to provide continuous, high-quality data and its effectiveness in anomaly detection algorithms make it a valuable asset for predictive maintenance, risk mitigation and optimization of industrial operations.

The work underscores the significance of Motor Current Signature Analysis (MCSA) in diagnosing faults in Permanent Magnet (PM) Machines with concentrated non-overlapping windings. Monitoring the harmonic index of stator current at steady state, MCSA proves to be a powerful tool for detecting eccentricity and demagnetization in PM synchronous machines. The spatial distribution of coils and circulating currents in machines with parallel path winding plays a crucial role in generating fault signatures. The cancellation effects in Y-connected and Δ -connected machines, as well as fractional slot motors, are discussed. The review differentiates between static and dynamic eccentricity, showcasing the impact on air-gap uniformity and fault-severity-dependent harmonic components.



2.5 Torque Monitoring [32, 33]

Torque monitoring is a crucial aspect of various industrial processes and mechanical systems, particularly those involving rotating machinery. Torque refers to the rotational force applied to an object and monitoring this force is essential for ensuring the efficient operation and safety of many engineering applications. In the context of your thesis, I'll provide a general overview of torque monitoring and methods for torque measurement. Torque monitoring involves the continuous measurement and analysis of the torque applied to a rotating shaft or component. This monitoring is essential in numerous industries, including manufacturing, automotive, aerospace and energy production, where precise control over torque is critical for optimal performance and safety.

2.5.1 Methods of Torque Measurement

Several methods are employed to measure torque accurately. The choice of method depends on factors such as the application, accuracy requirements and the type of machinery involved. Here are some common methods:

Strain Gauges

Strain gauges are devices that measure the deformation of a material under stress. These gauges are often bonded to a shaft or other rotating component and torque-induced strain is measured to determine torque.

Rotary Torque Sensors

Rotary torque sensors are specialized devices designed to measure torque in rotating applications. These sensors can be installed between the power source (e.g., motor) and the load (e.g., shaft), providing direct measurements. Optical Torque Sensors:

Optical torque sensors use optical methods to measure the twist or rotation in a shaft. They are contactless and can be suitable for high-speed or high-precision applications.

Magnetic Torque Sensors

Magnetic torque sensors use the principles of magnetism to measure torque. Changes in magnetic fields caused by the rotation of a shaft are detected and translated into torque values. Surface Acoustic Wave (SAW) Sensors:

SAW sensors measure the propagation of acoustic waves on the surface of a material. Torque-induced deformations affect the wave propagation, allowing torque to be determined.

2.6 Flux Monitoring [19, 34–40]

The analysis of airgap or stray flux emerges as a potent diagnostic method, offering direct insights into the machine's radial or axial flux asymmetry induced by fault-related anomalies. Airgap flux monitoring, utilizing components like radial leakage flux and axial leakage flux, proves superior in detecting faults such as shorted field winding turns, rotor conductor issues and airgap eccentricity, showcasing heightened sensitivity compared to vibration analysis or Motor Current Signature Analysis (MCSA).

Notably, airgap flux monitoring remains unaffected by load defects, setting it apart from other diagnostic methods relying on the indirect detection of rotor faults indirectly. Despite its effectiveness, the requirement for sensor installation inside the machine presents a limitation. However, recent interest in flux monitoring, driven by the pursuit of a low-cost complement to existing monitoring techniques, suggests a potential shift in its adoption for advanced warning of failures in reliability-critical applications.

While flux monitoring, especially stray flux measurement, has gained less attention than MCSA, ongoing research focuses on improving reliability, fault detection classification and overcoming limitations. The exploration of detection and sensitivity capabilities, comparative evaluations with MCSA and vibration analysis and field test results are crucial for validating and refining flux monitoring in real-world applications. Unexplored areas such as sensor size, location and design present opportunities for further advancements in this under-researched domain. The effectiveness of flux monitoring, particularly in identifying rotor-related defects in various motor types, holds promise for enhancing the reliability of fault detection in critical applications.

2.7 Demagnetization [10, 41–58]

In recent years, Permanent Magnet (PM) motors have gained widespread adoption across industries, owing to their exceptional performance attributes—high power-torque density, efficiency, ease of construction and

reliability. However, the phenomenon of Irreversible Demagnetization (ID) poses a significant challenge, particularly in applications like Electric Vehicles where elevated working temperatures and higher Magneto Motive Force (MMF) are common. Addressing ID becomes pivotal for enhancing the reliability and durability of PM machines.

This work emphasizes the importance of considering ID in the forefront of design and control parameters, as ID weakens the electromagnetic performance of PM machines, necessitating higher currents for constant output torque. Existing literature provides valuable insights into ID, offering guidance on accurate modeling, design optimization and strategies to mitigate ID.

Notably, this study contributes a systematic survey focusing on four key aspects crucial for proper PM machine design concerning ID—non-linear modeling of the PM demagnetization curve, analysis methods accounting for local ID, geometry optimization considering ID and the selection of accurate experimental test setups to evaluate fault-tolerant capabilities. The comprehensive comparison of methods in these areas offers valuable insights into their advantages and disadvantages.

In addition to summarizing design tips for ID fault-tolerant PM machines, the study identifies research opportunities aimed at further enhancing PM machine reliability. By presenting a holistic perspective on ID and its impact on PM machines, this study serves as a valuable resource for researchers, designers and engineers navigating the complexities of PM machine development.

2.7.1 Demagnetization Principles

Irreversible Demagnetization (ID) in permanent magnet (PM) machines can be defined as the loss of remnant flux density (B_r) or the ElectroMotive Force (EMF) of the PM machine. This phenomenon results in a performance decline of PM machines, impacting their overall efficiency. Under nominal conditions, PMs exhibit a specific value of remnant flux density (B_r) and the induced open voltage (E_{oc}) at the machine's terminal is well-defined. However, exposure to severe temperature conditions or high external demagnetizing fields leads to ID, causing a loss in the initial magnetic properties of PMs. Consequently, there is a relative drop in E_{oc} , significantly affecting the machine's performance.

The occurrence of ID is linked to the working point of the PM and the demagnetization curve, typically found in the second quadrant of the B-H or M-H curves. The normal B-H curve describes the relationship between magnetic flux density B and magnetic field intensity H, incorporating both the applied field and the PM's contribution. On the other hand, the intrinsic M-H curve illustrates the relationship between magnetization M and H, showcasing only the magnetic field of the magnet itself. In the case of ID, the PM operates on a minor loop of the B-H curve, approximated by a recoil line constructed based on the original major/minor B-H curve as we can see in Figure 2.6.

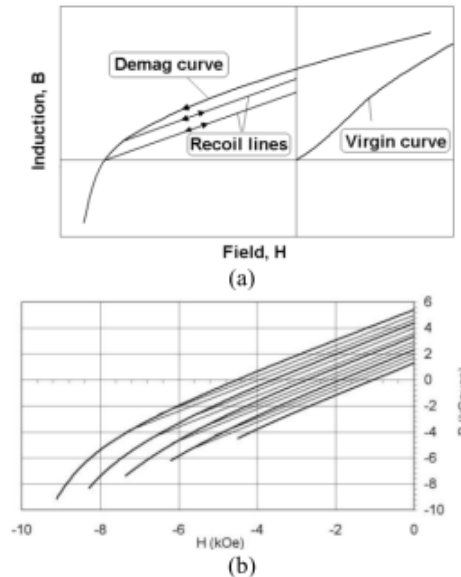


Figure 2.6: (a) Demagnetization Curve and Recoil Lines of the Permanent Magnet and (b) Major and minor B-H curve[42]

Several parameters influence ID, including working temperature, external demagnetizing fields, the load line of the PM and self-demagnetization. A critical criterion for ID analysis is the comparison of the working point with the knee point of the PM. The working point below the knee point corresponds to ID and it is determined

by the intersection of the demagnetization curve and the PM's load line. Understanding the influential factors on ID is crucial for comprehensively assessing and mitigating the impact of demagnetization in PM machines.

Temperature

Investigating the impact of temperature on Irreversible Demagnetization (ID) requires categorizing permanent magnets (PMs) into two groups based on their Temperature Coefficients (TC). PMs with a negative TC, such as NdFeB and SmCo magnets, exhibit an increased risk of ID with rising temperatures, while those with a positive TC including Alnico and Ferrite magnets, experience the opposite effect. Figure 2.7 illustrates the actual B-H curve of both groups and a simplified curve at two temperatures: T_1 (room temperature) and T_2 (high temperature for negative TC PMs and low temperature for positive TC PMs).

At room temperature, the knee point is not evident in the B-H curve of both groups. For negative TC magnets (Figure 2.7(a)), an increase in temperature leads to the appearance of the knee point on the B-H curve. Conversely, for positive TC magnets (Figure 2.7(b)), a decrease in temperature results in the appearance of the knee point on the B-H curve. To investigate ID under the worst working conditions, the review considers the highest and lowest temperatures for negative and positive TC magnets, respectively. This approach ensures a comprehensive examination of ID in varying thermal scenarios, providing valuable insights into the temperature-dependent behavior of different types of permanent magnets.

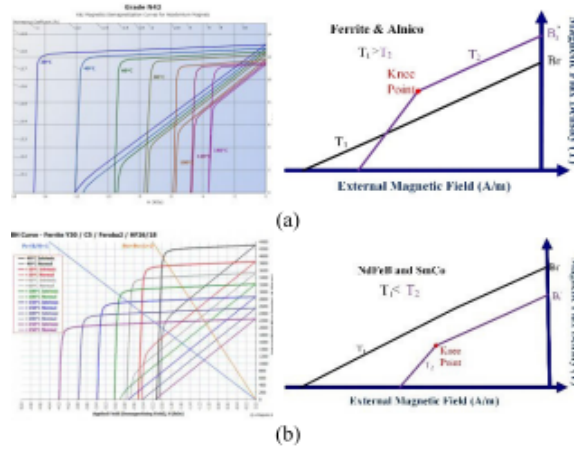


Figure 2.7: The Effect of Temperature on the B-H curve of the PMs (a) Ferrite and Alnico (b) NdFeB and SmCo [41]

External Demagnetization Field

The analysis presented in Figure 2.8(a) demonstrates the critical influence of an External Demagnetization Field (DF) on the working point of a Permanent Magnet (PM), emphasizing two distinct conditions:

- **EXTERNAL DF < H_d (Reversible Demagnetization):** When the external DF is less than the demagnetization threshold H_d , as depicted in Figure 2.8(a), the magnetic flux density can recover to its initial remnant value B_r after the DF is removed. This condition is termed reversible demagnetization.
- **EXTERNAL DF > H_d (Irreversible Demagnetization (ID)):** Conversely, if the external DF exceeds the threshold H_d , the working point shifts to P_2 and the PM cannot fully recover its initial B_r . Instead, it returns to a recoil line with a slope like the demagnetization curve above the knee point, resulting in a lower residual flux density (B_r'') and the loss of some magnetic properties. This state is known as Irreversible Demagnetization (ID).

Figure 2.8(b) extends this analysis to consider temperature variations (T_1 to T_2) and their impact on the risk of ID for NdFeB and SmCo magnets. At lower temperatures (T_2), the risk of ID is significantly reduced as the required DF increases and the knee point value decreases.

Furthermore, the work relates dynamic operations in PM machines, such as over-load conditions, acceleration in electric vehicle applications and cooling system failures, to the risk of ID:

Higher Current due to Over-load or Acceleration: The applied external demagnetization field due to over-load and acceleration current exceeding the acceptable H_d criteria can lead to ID, as illustrated in Figure 2.8(a).

High Working Temperature due to Over-load, Acceleration and Cooling System Failure: Figure 2.8(b) highlights that an increase in the working temperature reduces the acceptable criteria for external demagnetization

field, potentially leading to ID if the load line intersects the second quadrant of the curve below the knee point. The study emphasizes that despite dynamic operations causing high working temperatures, the difference may not be substantial, considering the high thermal inertia of PM machines.

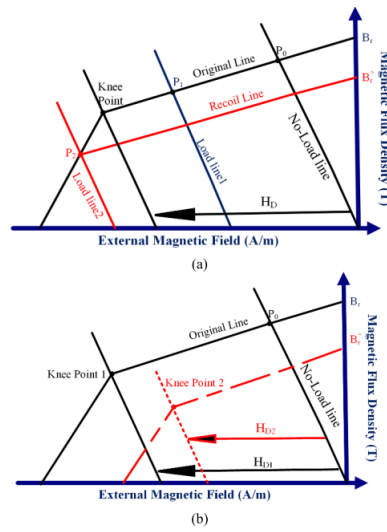


Figure 2.8: (a) The Effect of Armature Reaction on ID (b) The Effect of Temperature on the Required External DF for the NdFeB Magnet.[41]

Load Line of the Magnet

In summary, the slope of the Permanent Magnet's PM load line emerges as a pivotal factor influencing the risk of Irreversible Demagnetization (ID) in PM machines. As depicted in Figure 2.9, the conditions are delineated based on the relationship between the load line slope and a critical parameter, m_D :

THE SLOPE OF THE LOAD LINE $< m_D$: If the slope of the load line (illustrated by L_1 in Figure 2.9) is less than the critical parameter m_D , the working point of the magnet P_0 remains above the knee point. In this scenario, ID does not occur.

THE SLOPE OF THE LOAD LINE $> m_D$: Conversely, if the slope of the load line exceeds m_D , the working point of the magnet shifts to P_1 , below the knee point, leading to the occurrence of ID.

Figure 2.9 underscores the significance of PM machine design considerations, emphasizing the importance of designing PM machines with a meticulous view of the load-line slope. Motor designers should carefully select design parameters, considering the highest working temperature, to mitigate the risk of ID. It is crucial to note that even in the absence of external Demagnetization Fields DF, improper selection of design parameters can induce ID at elevated working temperatures. This underscores the necessity for precision in parameter selection to ensure the robust performance of PM machines under varying operational conditions.

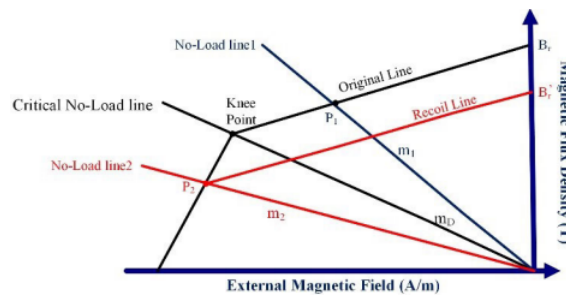


Figure 2.9: The Effect of Load Line on the ID[41]

Self-Demagnetization

Beyond the influence of external magnetic fields and temperature, self-demagnetization emerges as a noteworthy factor contributing to the degradation of magnetic properties in magnet materials. Self-demagnetization occurs when the magnetic field generated by the magnet can permeate back through the magnet itself.



It's important to note that while all magnets in free space exert a self-demagnetizing field to some extent, its impact is particularly pronounced in magnets with very low working points and/or low coercive force values. Notably, rare-earth magnets and Ferrite magnets, under normal operating conditions, exhibit resilience against self-demagnetization. Consequently, for these types of magnets, self-demagnetization is not a significant factor impacting their magnetic properties.

Understanding the interplay between external factors, temperature and self-demagnetization is crucial in the comprehensive assessment of Irreversible Demagnetization (ID) risks in Permanent Magnet (PM) machines. This multifaceted consideration is vital for designing resilient PM machines that can maintain optimal performance across diverse operating conditions.

2.7.2 Demagnetization Harmonics in PM Machines With Concentrated Windings

Magnetic Flux Density due to Demagnetization

The initial stage involves determining the magnetic flux density within the air gap of the PM machine. This calculation necessitates two key components: the air gap permeance and the Magneto Motive Force (MMF). Once these parameters are known, the air gap flux density is computed as the product of the air gap permeance and the MMF. This approach enables a comprehensive understanding of the magnetic characteristics within the machine, laying the groundwork for subsequent analyses and optimizations in the design and performance of the Permanent Magnet Generator.

$$B_{AG} = \Lambda F_m \quad (2.23)$$

where B_{AG} : magnetic flux density in the air gap, Λ : air gap permeance, F_m :Magneto Motive Force (MMF). The Magneto Motive Force equation is given below:

$$F_m(\theta, t) = \sum_{n=2m+1}^{\infty} F_{PM} \cos(np\theta - n\omega_s t - \phi_n) \quad (2.24)$$

where F_m : the Magneto Motive Force (MMF), F_{PM} : the MMF amplitude, n: harmonic order, p: pole pair number, θ : space angle, ω_s : the synchronous radial frequency, ϕ_n : the phase angle of the n^{th} harmonic component.

Furthermore, the permeance equation is given as follows in the case of a single magnet demagnetization where the magnet is considered as a pulse rotating with the rotor speed:

$$\Lambda_{dmg}(\theta, t) = \alpha + \beta(D) + \gamma(D) \sum_{k=1}^{\infty} \cos(k\theta - k\omega_r t) \quad (2.25)$$

where α : constant related to the design parameters, β : constant related to the design parameters and demagnetization, D: demagnetization severity, γ : constant related to design parameters and demagnetization, k: pulse wave series index, θ : space angle, ω_r : the rotor radial frequency.

where

$$\alpha = \frac{\mu_0}{2h_{PM}} \left(1 - \frac{g}{h_{PM}} - \frac{t_w}{2h_{PM}} + \frac{g^2}{h_{PM}^2} + \frac{gt_w}{h_{PM}^2} + \frac{t_w^2}{4h_{PM}^2} \right) \quad (2.26)$$

where α : constant related to the design parameters, μ_0 : permeability of free space, h_{PM} : permanent-magnet height, t_w : winding thickness, g: air gap length.

$$\beta(D) = \frac{\mu_0 D}{2h_{PM}} \left(\frac{g}{2h_{PM}^2 p} + \frac{t_w}{4h_{PM} p} - \frac{1}{2h_{PM} p} \right) \quad (2.27)$$

where β : constant related to the design parameters and demagnetization, D: demagnetization severity, μ_0 : permeability of free space, h_{PM} : permanent-magnet height, p: pole pair number, g: air gap length, t_w : winding thickness.

$$\gamma(D) = \frac{\mu_0}{2h_{PM}} \left\{ \left(\frac{D}{2h_{PM} p} + \frac{2g}{h_{PM}} + \frac{t_w}{h_{PM}} - 1 \right) \sum_{k=1}^{\infty} \frac{D}{k\pi h_{PM}} \sin\left(\frac{k\pi}{2p}\right) \right\} \quad (2.28)$$

where γ : constant related to design parameters and demagnetization, D: demagnetization severity, μ_0 : permeability of free space, h_{PM} : permanent-magnet height, p: pole pair number, g: air gap length, t_w : winding thickness, k: pulse wave series index.

The magnetic flux density due to demagnetization is given after substitution of (2.24) and (2.25) into (2.23) as follows:

$$\begin{aligned}
B(\theta, t) = & ak \sum_{n=2m+1}^{\infty} F_{PM} \cos(np\theta - n\omega_s t - \phi_n) \\
& + \beta_k \sum_{n=2m+1}^{\infty} \sum_{k=1}^{\infty} F_{PM} A_k \left\{ \cos \left[(np - k)\theta - \left(n - \frac{k}{p}\right)\omega_s t - \phi_n \right] \right. \\
& \left. + \cos \left[(np + k)\theta - \left(n + \frac{k}{p}\right)\omega_s t - \phi_n \right] \right\} \quad (2.29)
\end{aligned}$$

where

$$\alpha_k = \alpha + \beta(D) \quad (2.30)$$

$$\beta_k = \frac{\gamma(D)}{2} \quad (2.31)$$

where B : magnetic flux density, A_k : the sum between α and β , α : constant related to the design parameters, β : constant related to the design parameters and demagnetization, F_{PM} : the MMF amplitude, n : harmonic order, p : pole pair number, θ : space angle, ω_s : the synchronous radial frequency, ϕ_n : the phase angle of the n^{th} harmonic component, γ : constant related to design parameters and demagnetization, D : demagnetization severity, k : pulse wave series index.

Furthermore, the magnetic flux is given below:

$$\Phi = \oiint B dS \quad (2.32)$$

where Φ : the magnetic flux, B : magnetic flux density.

Because the magnetic flux is changing, the voltage will be induced in the stator coils due to Faraday's Law of Induction:

$$\varepsilon = -N \frac{d\Phi}{dt} \quad (2.33)$$

where ε : the ElectroMotive Force (EMF), N : turn number of an armature coil, n : harmonic order, Φ : the magnetic flux.

Putting (2.29), (2.32) and (2.33) together, the induced voltage in the stator coils due to demagnetization is given below:

$$\begin{aligned}
V_{dmg} = & \sum_{n=2m+1}^{\infty} V_n \cos(np\theta - n\omega_s t - \phi_n) \\
& + \sum_{n=2m+1}^{\infty} \sum_{k=1}^{\infty} V_{nk} \left\{ \cos \left[(np - k)\theta - \left(n - \frac{k}{p}\right)\omega_s t - \phi_n \right] \right. \\
& \left. + \cos \left[(np + k)\theta - \left(n + \frac{k}{p}\right)\omega_s t - \phi_n \right] \right\} \quad (2.34)
\end{aligned}$$

where V_{dmg} : voltage in the stator coils due to the demagnetization, V_n : Voltage amplitudes, n : harmonic order, p : pole pair number, θ : space angle, ω_s : the synchronous radial frequency, ϕ_n : the phase angle of the n^{th} harmonic component, V_{nk} : voltage of n^{th} harmonic in the k^{th} term, k : pulse wave series index.

Harmonics Cancellation Within a Single Phase With Pairs of Coils at 180 Degrees

The analysis presented earlier shows that demagnetization induces voltage harmonics in a single stator coil, as per equation (2.34). This implies the anticipation of sidebands of frequencies, integer multiples of the mechanical frequency, around the fundamental voltage harmonic in every coil. The following section looks into the revelation of the expected harmonics in a single phase, taking into account the number of phase coils and poles. Additionally, the case of two coils of the same phase, positioned with a 180-degree spatial phase difference is explored. The examination primarily focuses on the left sidebands of (2.34), showing the relationship between demagnetization and voltage harmonics.

The left sidebands of (2.34) are described by the term:

$$\sum_{n=2m+1}^{\infty} \sum_{k=1}^{\infty} V_{nk} \cos \left[(np - k)\theta - \left(n - \frac{k}{p}\right)\omega_s t - \phi_n \right] \quad (2.35)$$

where V_{nk} : voltage of n^{th} harmonic in the k^{th} term, n: harmonic order, p: pole pair number, k: pulse wave series index, θ : space angle, ω_s : the synchronous radial frequency, ϕ_n : the phase angle of the n^{th} harmonic component.

The investigation shows the critical influence of the number of magnetic pole pairs on the detailed analysis. When the number of pole pairs p is even, both opposing coils exhibit identical electromotive forces (EMF). Consequently, the total voltage due to demagnetization will be:

$$V_{2c_dmg} = \sum_{n=2m+1}^{\infty} \sum_{k=1}^{\infty} V_{nk} \cos \left[- \left(n - \frac{k}{p} \right) \omega_s t - \phi_n \right] + \sum_{n=2m+1}^{\infty} \sum_{k=1}^{\infty} V_{nk} \cos \left[(np - k)\pi - \left(n - \frac{k}{p} \right) \omega_s t - \phi_n \right] \quad (2.36)$$

where V_{2c_dmg} : voltage summation between two coils, V_{nk} : voltage of n^{th} harmonic in the k^{th} term, n: harmonic order, k: pulse wave series index, p: pole pair number, ω_s : the synchronous radial frequency, ϕ_n : the phase angle of the n^{th} harmonic component.

We can distinct patterns in demagnetization signatures based on the number of magnetic pole pairs p and the arrangement of opposing coil pairs. When p is odd the opposing coil pairs need to be wound in opposite directions to prevent the cancellation of electromotive forces (EMFs) for this scenario, the two voltage components of equation (2.36) are subtracted and not added as we can see below:

$$V_{2c_dmg} = \sum_{n=2m+1}^{\infty} \sum_{k=1}^{\infty} V_{nk} \cos \left[- \left(n - \frac{k}{p} \right) \omega_s t - \phi_n \right] - \sum_{n=2m+1}^{\infty} \sum_{k=1}^{\infty} V_{nk} \cos \left[(np - k)\pi - \left(n - \frac{k}{p} \right) \omega_s t - \phi_n \right] \quad (2.37)$$

where V_{2c_dmg} : voltage summation between two coils, V_{nk} : voltage of n^{th} harmonic in the k^{th} term, n: harmonic order, k: pulse wave series index, p: pole pair number, ω_s : the synchronous radial frequency, ϕ_n : the phase angle of the n^{th} harmonic component.

Also, when p is odd then the np is always odd. Due to the subtraction as we can see in the equation above when k is even then the two coil components are in phase and when k is odd the coil components are opposite leading to cancelation. In case which p is even the product np is always even because n is odd. For this reason, the cases are examined concerning k. The outcome which depends on k is the same as described above. Examining the right-hand side sidebands of equation (2.34) gives us outcomes analogous to those observed for the left-hand side sidebands. When a single pair of phase coils is positioned 180° apart, the demagnetization signatures are as follows:

$$f_{dmg} = \left(n \pm \frac{2l}{p} \right) f_s \quad (2.38)$$

where f_{dmg} : frequency locations of demagnetization harmonics, n: harmonic order, l: integer numbers, p: pole pair number, f_s : synchronous frequency.

Expanding the number of stator coils amplifies the cancellation of fault signatures, particularly in machines characterized by power-of-two quantities of phase coils. To analyze this phenomenon, let's consider a phase winding comprising 4 coils, strategically positioned 90° apart one from another. Building upon the earlier analysis, we'll first explore the grouping of the 4 coils into pairs: The first pair includes the coils at 0° and 180° and the second pair at 90° and 270° . Due to (2.36) and (2.38) the two pairs of coils will get the following voltages induced on the left-hand side of the fundamental:

- Pair 1(0° and 180°)

$$\sum_{n=2m+1}^{\infty} \sum_{l=1}^{\infty} V_{nl} \cos \left[- \left(n - \frac{2l}{p} \right) \omega_s t - \phi_n \right] \quad (2.39)$$

- Pair 2(90° and 270°)

$$\sum_{n=2m+1}^{\infty} \sum_{l=1}^{\infty} V_{nl} \times \cos \left[(np - 2l) \frac{\pi}{2} - \left(n - \frac{2l}{p} \right) \omega_s t - \phi_n \right] \quad (2.40)$$

where V_{nl} : voltage amplitudes, n : harmonic orders, l : integer number, p : pole pair number, ω_s : the synchronous radial frequency, ϕ_n : the phase angle of the n^{th} harmonic component, $k = 2l$ and $V_{nl} = 2V_{kl}$.

In the case of an even pole pair number $p = 2b$. Depending on whether b is even or odd, p is expressed as below:

$$p = \begin{cases} 4c, & b = \text{even} \\ 2(2c+1), & b = \text{odd} \end{cases} \quad (2.41)$$

Also, l can be even ($=2q$) or odd ($=2q+1$) as well. which leads us to four different combinations to be considered:

1. if $p=4c$ and $l=2q$
2. if $p=4c$ and $l=2q+1$
3. if $p=2(2c+1)$ and $l=2q$
4. if $p=2(2c+1)$ and $l=2q+1$

Bearing in mind that the two voltage components (2.39) and (2.40) need to be added together for even pole pair numbers and subtracted for odd pole pair numbers, it is clear that:

Combinations 1 and 3 make the signals (2.39) and (2.40) to be in phase. Combinations 2 and 4 lead to cancellation.

To condense, when there are 4 phase coils at 90° apart, the demagnetization signatures are identified as follows:

$$f_{dmg} = \left(n \pm \frac{4q}{p} \right) f_s \quad (2.42)$$

where f_{dmg} : frequency locations of demagnetization harmonics, n : harmonic order, q : integer number, p : pole pair number, f_s : synchronous frequency.

Following the same approach, if 8 coils of a single phase are considered with 45° spatial phase difference, we have the following equation:

$$f_{dmg} = \left(n \pm \frac{8r}{p} \right) f_s, \quad q = 2r \quad (2.43)$$

f_{dmg} : frequency locations of demagnetization harmonics, n : harmonic order, r : integer number, p : pole pair number, f_s : synchronous frequency

Taking into consideration the analysis from above, it is now clear that the more pairs of coils in the machine, the more the cancellation of the demagnetization signatures leading to the general rule identified here is the following:

$$f_{dmg1} = \left(n \pm \frac{2^\delta \varepsilon}{p} \right) f_s \quad (2.44)$$

where f_{dmg1} : frequency locations of demagnetization harmonics, n : harmonic order, ε : any integer number, δ : equal to the binary logarithm of the number of phase coils, p : pole pair number, f_s : synchronous frequency.

It is of significant importance to mention that, if $2^\delta = p$ then the machine does not produce any demagnetization signatures in the stator current around the fundamental frequency leading MCSA to a false negative diagnostic outcome.

Harmonic Cancellation due to the Three-phase System With Pairs of Coils at 180 Degrees

The analysis has demonstrated that specific arrangements result in the cancellation of certain fault signatures. In the context of permanent magnet (PM) machines, which inherently have three phases with a 120-degree spatial phase difference, the interconnected phases introduce a new layer of complexity. This paragraph aims to unravel how, in a 3-phase winding, the spatial phase difference between coils of different phases contributes to the cancellation of additional fault signatures.

The exploration starts with a system of 3 coils strategically positioned with a spatial phase difference of 120° , each associated with a distinct phase and the phases interconnected in either Y or Δ configuration. Each phase supplies an equal resistive load, leading to a sum of three voltages equal to zero. Accordingly, each phase voltage is equivalent to the negative sum of the other two. Notably, due to the 120-degree spatial phase difference, the induced voltages in the two phases exhibit opposite signs. This results in the left-hand side demagnetization components of the first phase being equal to the difference between the other two phases as we can see below:



$$V_{3ph_dmg_1c} = \sum_{n=2m+1}^{\infty} \sum_{k=1}^{\infty} V_{nk} \left\{ \cos \left[(np - k) \frac{2\pi}{3} - \left(n - \frac{k}{p} \right) \omega_s t - \phi_n \right] - \cos \left[(np - k) \left(-\frac{2\pi}{3} \right) - \left(n - \frac{k}{p} \right) \omega_s t - \phi_n \right] \right\} \quad (2.45)$$

where $V_{3ph_dmg_1c}$: voltage demagnetization signatures due to three phases and 1 coil/phase, V_{nk} : voltage of n^{th} harmonic in the k^{th} term, n: harmonic order, p: pole pair, k: pulse wave series index, ω_s : the synchronous radial frequency, ϕ_n : the phase angle of the n^{th} harmonic component.

After changing the signs in the second term and applying trigonometric identities, equation (2.45) is transformed into:

$$(2.45) = 2 \sum_{n=2m+1}^{\infty} \sum_{k=1}^{\infty} V_{nk} \sin \left[(np - k) \frac{2\pi}{3} \right] \times \sin \left[- \left(n - \frac{k}{p} \right) \omega_s t - \phi_n \right] \quad (2.46)$$

where V_{nk} : voltage of n^{th} harmonic in the k^{th} term, n: harmonic order, p: pole pair, k: pulse wave series index, ω_s : the synchronous radial frequency, ϕ_n : the phase angle of the n^{th} harmonic component.

We can see that the first sinusoidal term is zero when:

$$(np - k) \frac{2\pi}{3} = \lambda\pi, \lambda \in \mathbb{Z} \rightarrow k = np - \frac{3\lambda}{2} \quad (2.47)$$

λ : integer number, n: harmonic order, p: pole pair, k: pulse wave series index

It's significant to see that, λ can be any integer number. Despite that, $k \in \mathbb{N}$ therefore we take into consideration the values only when λ is even. So, if $\lambda = 2\lambda'$:

$$k = np - 3\lambda' \quad (2.48)$$

where λ : integer number, n: harmonic order, p: pole pair, k: pulse wave series index.

When k satisfies (2.48), equation(2.45) is equal to zero leading the respective demagnetization signatures cancel out from the reference phase at 0° . In detail, after the substitution of equation (2.48) into equation (2.35) we get:

$$\sum_{n=2m+1}^{\infty} \sum_{k=1}^{\infty} V_{nk} \cos \left[- \left(n - \frac{np - 3\lambda'}{p} \right) \omega_s t - \phi_n \right] = \sum_{n=2m+1}^{\infty} \sum_{k=1}^{\infty} V_{nk} \cos \left(\frac{3\lambda'}{p} \omega_s t + \phi_n \right) \quad (2.49)$$

where V_{nk} : voltage of n^{th} harmonic in the k^{th} term, n: harmonic order, p: pole pair, k: pulse wave series index, ω_s : the synchronous radial frequency, ϕ_n : the phase angle of the n^{th} harmonic component, λ : integer number.

Equation (2.49) shows that signatures that are triple multiples of the mechanical frequency cancel out in the stator current when all three phases are considered in a PM machine, where each phase consists of a single coil.

Expanding the analysis to scenarios where each phase has multiple coils follows a similar formula. The key principle remains the electrical phase difference of 120° between the phases, regardless of the number of coils within each phase. If γ represents the number of coils in each phase, the demagnetization impact on each phase can be expressed as follows:

$$V_{3ph_dmg} = \sum_{n=2m+1}^{\infty} \sum_{k=1}^{\infty} V_{nk} \left\{ \cos \left[(np - k) \frac{2\pi}{3\gamma} - \left(n - \frac{k}{p} \right) \omega_s t - \phi_n \right] - \cos \left[(np - k) \left(-\frac{2\pi}{3\gamma} \right) - \left(n - \frac{k}{p} \right) \omega_s t - \phi_n \right] \right\} \quad (2.50)$$

where V_{3ph_dmg} : voltage summation of phases under demagnetization, V_{nk} : voltage of n^{th} harmonic in the k^{th} term, n: harmonic order, p: pole pair number, k: pulse wave series index, γ : number of each phase coil = 8 in my generator, ω_s : the synchronous radial frequency, ϕ_n : the phase angle of the n^{th} harmonic component.

Following a similar approach to the case of a single coil, equation (2.50) leads to the deduction that the number of phase coils leads to the cancellation of demagnetization signatures located at:

$$f_{3ph_null} = \frac{3\gamma\lambda'}{p} f_s \quad (2.51)$$

where γ : number of each phase coil = 8 in my generator, λ' :integer, p : pole pair number, f_s : synchronous frequency.

In practical terms, Equation (2.51) implies that in a 3-phase PM generator experiencing demagnetization, certain harmonics, specifically the sixth multiples of the mechanical frequency, will not be present if the machine has 2 coils per phase. Similarly, if the number of phase coils is increased to 4, the twelfth multiples of the mechanical frequency will cancel out and so on. So in the generator used, the 24th multiples of the mechanical frequency cancel out leading to the following equation:

$$\frac{24\lambda'}{16}26.6 = 40\lambda' \quad (2.52)$$

2.8 False Negative Diagnosis [3]

Direct drive permanent magnet (PM) generators, prevalent in renewable power applications, offer advantages like reduced maintenance and operating costs. However, faults such as stator inter-turn short circuits, rotor eccentricity and rotor demagnetization can still occur, with demagnetization being particularly concerning due to its progressive severity. The relationship between demagnetization, dynamic eccentricity and increased stator current is highlighted, leading to hotspot formation and potential inter-turn faults.

Demagnetization, a fault in permanent magnet machines, poses risks of increased vibrations, noise and efficiency reduction in the short term. If not detected early, it can lead to higher currents, temperature increases and eventual catastrophic failure, particularly impactful in direct drive applications like offshore energy harvesting. The urgency for prompt diagnosis is emphasized. Stator's current analysis, despite its non-intrusive, low-cost and online capabilities, is shown in this study to be unreliable due to its dependence on the geometrical and manufacturing characteristics of the permanent magnet generator. This work uncovers multiple instances leading to false negative diagnostic alarms, highlighting the need for further research and exploration of alternative diagnostic methods to ensure accurate and timely fault detection in permanent magnet machines.

Various diagnostic methods, including stator current analysis, have been explored for demagnetization detection, often applied to high-speed machines. This study, focusing on low-speed and high-pole PM machines, challenges the reliability of using the stator current spectrum for demagnetization detection in such generators. Through analytical calculations, finite element simulations and experimental testing, the study unveils scenarios where demagnetization faults could be masked, resulting in false-negative diagnostic conclusions, indicating a healthy machine when it suffers from demagnetization.

It's crucial to note that demagnetization conditions are not uniform and a single magnet defect is possible, especially in NdFeB magnets prone to irreversible demagnetization. This research urges further exploration of alternative diagnostic methods for the accurate detection of demagnetization faults in low-speed PM generators.

Demagnetization Misdiagnosis Cases

Firstly, equation (2.34) leads to the following rules regarding the production or cancellation of demagnetization harmonics in the stator current.

$$f_{dmg1} = \left(n \pm \frac{2^\delta \varepsilon}{p} \right) f_s, \text{ produced due to coils at } \frac{\pi}{2} \quad (2.53)$$

where f_{dmg1} : frequency locations of demagnetization harmonics, n : harmonic order, ε : any integer number, δ : equal to the binary logarithm of the number of phase coils, p : pole pair number, f_s : synchronous frequency

$$f_{3ph_null} = \left(\frac{3\gamma_{ph}\lambda'}{p} \right) f_s, \text{ cancelled due to 3-phase} \quad (2.54)$$

where γ : number of each phase coil = 8 in my generator, λ' :integer, p : pole pair number, f_s : synchronous frequency.

$$f_{dmg2} = \left(n \pm \frac{3\kappa}{p} \right) f_s, \text{ produces due to 3x coils} \quad (2.55)$$

where f_{dmg2} : frequency locations of demagnetization harmonics, p : pole pair number, f_s : synchronous frequency, n : harmonic order, κ integer number.

Extending the investigation to scenarios involving multiple faulty magnets around the circumference unveiled a noteworthy consideration. The potential cancellation of previously identified signatures was highlighted, particularly when two demagnetized magnets were studied to illustrate this principle. While the analysis focused on this specific case, it is essential to recognize that the principles elucidated could readily be applied to scenarios featuring multiple faulty magnets.

By isolating the second term of equation (2.34), the examination zeroed in on the left sidebands of the fault surrounding the stator current fundamental, with $n=1$. Introducing a spatial phase difference θ between the two magnets, where the position of the first magnet served as the reference at 0° , facilitated a more nuanced understanding of the fault characteristics. This nuanced analysis lays the groundwork for a comprehensive exploration of fault scenarios involving various spatial configurations and sets the stage for future research endeavors in this domain.

$$\sum_{k=1}^{\infty} V_{1k} \left\{ \cos \left[- \left(1 - \frac{k}{p} \right) \omega_s t - \phi_1 \right] + \cos \left[(p - k) \theta - \left(1 - \frac{k}{p} \right) \omega_s t - \phi_1 \right] \right\} \quad (2.56)$$

θ : space angle, ω_s : the synchronous radial frequency, ϕ_n : the phase angle of the n^{th} harmonic component, V_{1k} : voltage of 1^{st} harmonic in the k^{th} term, k : pulse wave series index, p : pole pair

In seeking the condition for the sum of infinite terms to be zero in the above scenario, a crucial insight emerged. The spatial component of the second part was identified to necessitate equality to an odd multiple of π . This revelation marks a pivotal understanding, indicating a specific criterion for achieving a null sum in the context of the infinite terms under consideration. This finding serves as a foundational element for further exploration and theoretical developments within this mathematical framework, offering a clear condition for a particular spatial arrangement that yields a zero-sum.

$$(p - k)\theta = (2d + 1)\pi \rightarrow \theta = \frac{(2d + 1)\pi}{(p - k)} \quad (2.57)$$

where k : pulse wave series index, p : pole pair, θ : space angle, d : integer number.

False Negative due to Machine Geometry

The simulation of the generator, featuring a single demagnetized magnet under the actual geometry with 8 coils/phase and 16 pole pairs, provided valuable insights. Modification of the generator's model by doubling the stator coils/phase allowed for the study of the impact of winding configuration on demagnetization harmonics production. Specifically, the machine was simulated with one phase and all three phases to analyze the influence of stator coil numbers.

Demagnetization of one outer rotor magnet was simulated and the cross sections of the machine with 8 and 16 coils per phase, having one and three phases, were examined. Frequency spectra of the stator current for these configurations were presented, showcasing two signatures of demagnetization at $0.5f_s$ and $1.5f_s$ in each phase current when 8 coils per phase were used. However, the connection of three phases led to the cancellation of the second signature, leaving only the $0.5f_s$ component to indicate the fault. Interestingly, when the number of phase coils equaled the number of pole pairs, no signatures of the fault were observed, aligning with analytical predictions.

The Finite Element Analysis (FEA) unequivocally confirmed a clear case of false-negative diagnosis for the demagnetization fault, emphasizing the importance of considering winding configuration in diagnostic assessments. Further exploration is warranted to refine diagnostic methods and enhance accuracy in identifying demagnetization faults.

False Negative due to non-Adjacent Faulty Magnets

Equation (2.56) introduces a compelling hypothesis, suggesting that non-adjacent demagnetized magnets possess the potential to annul their magnetic asymmetries, resulting in the cancellation of demagnetization signatures. This theoretical proposition underwent rigorous testing through finite element simulations, validating its applicability.

Upon substitution of machine parameters into equation (2.56), an estimated minimum angle of 22.5° emerged, denoting a critical spatial disposition for the demagnetized magnets. Simulation results affirmed this concept, showcasing that two non-adjacent demagnetized magnets, despite facing different phase coils of the stator, exhibited a similar magnetic polarity.

The simulations further demonstrated that the fault's existence led to a marginal increase in the maximum magnetic flux density, with stator current spectra confirming a significant rise in the $0.5f_s$ component in the machine with a single magnet defect. Crucially, the predicted harmonic cancellation was evident in the case of non-adjacent demagnetized permanent magnets, emphasizing the potential for false negative assessments due to the absence of fault-relevant signatures. This comprehensive analysis underscores the complex interplay of spatial factors in demagnetization fault diagnostics.



2.9 Finite Element Analysis [59, 60]

2.9.1 Introduction

In the steady state of a Permanent Magnet Synchronous Generator (PMSG), voltages and currents exhibit sinusoidal functions while the speed remains constant. In such cases, it is well-established that an equivalent circuit of the PMSG can be constructed, allowing for the calculation of desired parameters.

However, when dealing with the specific problem at hand—investigating electrical machines—we encounter challenges in providing an analytical solution for the equations. Our objective is to transform the continuous model of the problem into a discrete one, making it amenable to computer-based solutions. Numerous arithmetic methods are employed in electromagnetism, with noteworthy techniques including the finite difference method, Finite Element Analysis (FEA) and the Torque method. These methods play a crucial role in enabling the computational study of electrical machines, where analytical solutions may not be readily attainable.

Since with numerical methods the real space (which is continuous) is approximated by a finite set of points, these methods are also called approximate. This name is somewhat misleading since it is possible to increase the accuracy as much as we want at the cost of computational time. These digital approximate solutions may indeed be less accurate than analytical ones for simple geometry problems. In the real world, however, we often encounter much more complex geometries, such as that of an electric motor, which through analytical methods are impossible to solve without making significant simplifications to the whole problem. As a consequence of the simplifications, the resulting analytical formula is not completely accurate, whereas a numerical method comparatively offers more accurate results. For the study of models of electrical machines, we make use of the finite element method.

The finite element method, in the study of electrical machines, may be approximate, but can give more reliable results compared to the equivalent circuit analysis and can also be applied to all problems. The disadvantages of the method are various. Not all of the geometric characteristics of the model we want to study may be available and also the characteristics of some materials and data necessary for solving the method. Finally, with the increase in complexity of our problem, corresponding computational time is needed. This fact establishes the computer as a key tool for the solving of electrical machine problems with the finite element method. The success of the method in complex electromechanical problems is so great that today it is widely used in research and industry for the calculation and study of various structures.

2.9.2 Equations Used in FEA

The nature of the problem suggests the usage of the appropriate equations for the right solution. There are two basic categories of the problems, magnetostatic and harmonic. In the first category, the variables are time-invariant, in contrast with the second category which is time-variant and we presume that they are sinusoidal for the solution of the problem. In the case of the magnetostatic problem the magnetic field strength, also called magnetic intensity H and the magnetic induction B are connected with Maxwell equations:

$$\nabla \times H = J \quad (2.58)$$

where H : magnetic intensity, J : total electric current density.

$$\nabla B = 0 \quad (2.59)$$

where B : magnetic induction.

The magnetic intensity H and the magnetic induction B are connected for every material through magnetic permeability μ

$$B = \mu H \quad (2.60)$$

where B : magnetic induction, μ : magnetic permeability, H magnetic intensity.

At this point, we define the magnetic vector potential:

$$B = \nabla \times A \quad (2.61)$$

where B : magnetic induction, A : vector potential.

With the substitution of 2.58 in the above equation, we have:

$$\nabla \times \left(\frac{1}{\mu(B)} \nabla \times A \right) = J \quad (2.62)$$

where B : magnetic induction, A : vector potential, J : total electric current density, μ : magnetic permeability.

If the material is linear and isotropic we take the following equation:

$$-\frac{1}{\mu}\nabla^2 A = J \quad (2.63)$$

where A: vector potential, J: total electric current density, μ : magnetic permeability.

In the case of harmonic problems, the magnetic fields are time variants. For this reason, there will be induced eddy currents in every material that is characterized by their electrical conductivity σ

$$J = \sigma E \quad (2.64)$$

where J: total electric current density, σ : electrical conductivity of the material, E: electric field.

Also:

$$\nabla \times E = -\frac{\partial B}{\partial t} \quad (2.65)$$

where E: electric field, B: magnetic induction.

With the substitution of 2.63 to the above equation we take the following equation :

$$\nabla \times E = -\nabla \times \frac{\partial A}{\partial t} \quad (2.66)$$

where E: electric field, A: vector potential.

Now if we substitute the equation in 1.6 we take:

$$-\frac{1}{\mu}\nabla^2 A = J - \sigma \frac{\partial A}{\partial t} \quad (2.67)$$

where A: vector potential, J: total electric current density, μ : magnetic permeability.

For 2D problems, only the axial component of the magnetic vector potential is used. In the case of studying the generator when the rotor is rotating under load, we are taking into consideration the equation of motion:

$$T = J \frac{\partial^2 \theta}{\partial t^2} \quad (2.68)$$

where J: a moment of inertia, θ : the angle, T: Torque.

The torque T is described below:

$$T = T_{E_m} + T_L + T_F \quad (2.69)$$

where T_{E_m} : Electromagnetic Torque, T_L : Torque of Load, T_F :Torque of friction.

2.9.3 Application of FEA in SimcenterMagnet

The simulation analysis can take on either a linear or non-linear approach. In linear analysis, the program solves the models using a specific value for relative permeability defined by the user for each material. On the other hand, in non-linear analysis, the program tackles the models by utilizing the B-H curve of each material.

An essential requirement for the simulation involves the incorporation of an external circuit that mirrors the model's circuit (see Figure 3.12).

The steps for utilizing Finite Element Analysis (FEA) are outlined below:

- **Insert Geometry:** Begin by introducing the geometry of the Permanent Magnet Synchronous Generator (PMSG) into a graphical environment and create the 2D or 3D model.
- **Mesh Creation:** Divide the model into finite elements. After creating the mesh, select the type of solution and input additional necessary data. This step is typically performed using pre-processors.
- **Solver Execution:** Once the data is prepared for the solution, input it into a program that acts as a solver. Solvers are designed to execute arithmetic methods and resolve the defined problem.
- **Post-Processing:** After the problem is solved, utilize a post-processor to process and interpret the results effectively.

These stages collectively form the process of utilizing FEA for the analysis of the Permanent Magnet Synchronous Generator.

Chapter 3

Simulation Setup

In this chapter, the description of the case study system and the modeling of the C-GEN generator are discussed. The simulation results compared to the experimental are also presented. The cases that are simulated are shown below:

1.)	Healthy 17.5
2.)	Healthy 13.125
3.)	Healthy 21.875
4.)	Demag 25 13.125
5.)	Demag 25 17.5
6.)	Demag 25 21.875
7.)	Demag 50 13.125
8.)	Demag 50 17.5
9.)	Demag 50 21.875
10.)	Demag 25 50 13.125
11.)	Demag 25 50 17.5
12.)	Demag 25 50 21.875
13.)	Demag 25 both 13.125
14.)	Demag 25 both 17.5
15.)	Demag 25 both 21.875
16.)	Demag 50 both 13.125
17.)	Demag 50 both 17.5
18.)	Demag 50 both 21.875

Table 3.1: Simulation Cases

Each simulation corresponds to a specific demagnetization scenario. There are 5 cases of demagnetization for 3 different loads. The idea behind the simulations was to simulate the 5 different cases with 17.5 Ω load and then increase the load by 25% and decrease it by 25% to see the differences.

- Healthy 17.5 Healthy model with 17.5 Ω load.
- Healthy 13.125 Healthy model with 13.125 Ω load (25% load decreased).
- Healthy 21.875 Healthy model with 21.875 Ω load (25% load increased).
- Demag 25 13.125 Faulty model with one magnet demagnetized at 25% with 13.125 Ω load.
- Demag 25 17.5 Faulty model with one magnet demagnetized at 25% with 17.5 Ω load.
- Demag 25 21.875 Faulty model with one magnet demagnetized at 25% with 21.875 Ω load.
- Demag 50 13.125 Faulty model with one magnet demagnetized at 50% with 13.125 Ω load.
- Demag 50 17.5 Faulty model with one magnet demagnetized at 50% with 17.5 Ω load.
- Demag 50 21.875 Faulty model with one magnet demagnetized at 50% with 21.875 Ω load.
- Demag 25 50 13.125 Faulty model with two non-adjacent magnets demagnetized (22.5° apart) at 25% and 50% with 13.125 Ω load.



- Demag 25 50 17.5 Faulty model with two non-adjacent magnets demagnetized (22.5° apart) at 25% and 50% with 17.5 Ω load.
- Demag 25 50 21.875 Faulty model with two non-adjacent magnets demagnetized (22.5° apart) at 25% and 50% with 21.875 Ω load.
- Demag 25 both 13.125 Faulty model with two non-adjacent magnets demagnetized (22.5° apart) at 25% and 25% with 13.125 Ω load.
- Demag 25 both 17.5 Faulty model with two non-adjacent magnets demagnetized (22.5° apart) at 25% and 25% with 17.5 Ω load.
- Demag 25 both 21.875 Faulty model with two non-adjacent magnets demagnetized (22.5° apart) at 25% and 25% with 21.875 Ω load.
- Demag 50 both 13.125 Faulty model with two non-adjacent magnets demagnetized (22.5° apart) at 50% and 50% with 13.125 Ω load.
- Demag 50 both 17.5 Faulty model with two non-adjacent magnets demagnetized (22.5° apart) at 50% and 50% with 17.5 Ω load.
- Demag 50 both 21.875 Faulty model with two non-adjacent magnets demagnetized (22.5° apart) at 50% and 50% with 21.875 Ω load.

3.1 Model Description

In this section, there will be described C-GEN's characteristics and the process used for the creation of the model.

Rated power	21.5 kW
Rated speed	100 rpm
Stator	Coreless
Frequency	26.67
Pole pairs	16
Stator Coils	24 x single concentrated
Stator coil turns	205
Magnet material	N42

Table 3.2: Characteristics of the C-GEN PM Generator

Variable	FEA	Experiment
Phase Voltage (V)	292.4	306.7
Stator Current (A)	16.71	17.41
Torque (Nm)	1494	1575
Output Power (kW)	14.65	15.4
Input Power (kW)	15.64	16.5
Efficiency	0.936	0.933

Table 3.3: Comparison of testing and FEA results

Simulation and experimental results have difference less than 5% so they simulation is reliable.

3.1.1 AutoCAD

Below there is the model outline Figure 3.1 that was designed in AutoCAD. The difficult part of this design was that the generator geometry didn't have round borders. Also, Simcenter Magnet works with motion components airgap between motion components. For this reason, the airgap must be firm because we will have collisions between the motion components and the simulation could not run. Furthermore, because the magnets are square the design of the airgap layers was challenging. All the measurements for all the components of the design were given to simulate a real C-GEN.

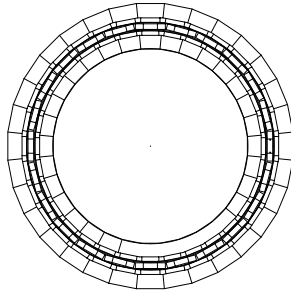


Figure 3.1: Outline of C-GEN with layers of airgap and sensors

3.1.2 Model Creation in SimcenterMagnet

Coils

For each phase, we have 8 coils each coil was created separately. For Phase 1 the Coils are named $Coil_{11x}$ for input of the coil and $Coil_{11y}$ for output up to $Coil_{18x}$ and $Coil_{18y}$. The material used for Phase 1 has the same characteristics as Copper: $5.77e7$ Siemens/meter and it is named Copper A as depicted in the Figure below (Figure 3.2):

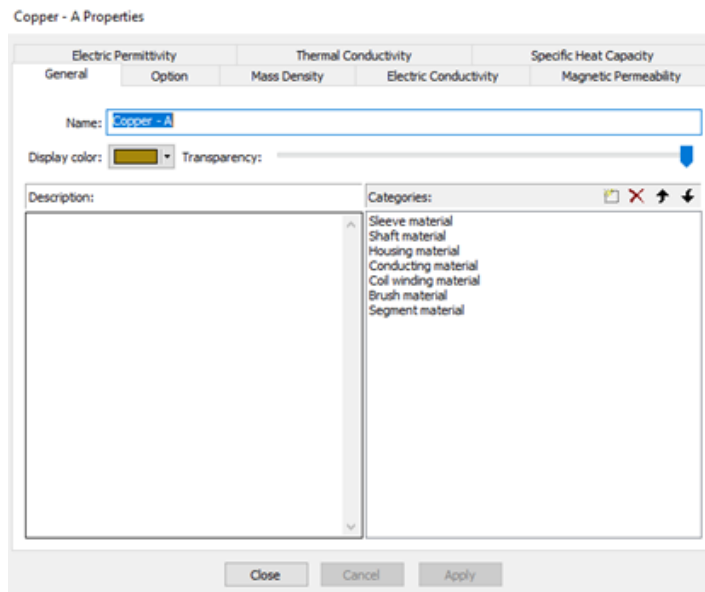


Figure 3.2: Properties of Copper A used in Coils of Phase 1

For phase 2 the Coils are named $Coil_{31x}$ for input of the coil and $Coil_{31y}$ for output up to $Coil_{38x}$ and $Coil_{38y}$. The material used for Phase 2 has the same characteristics as Copper: $5.77e7$ Siemens/meter and it is named Copper B as depicted in the Figure below (Figure 3.3):

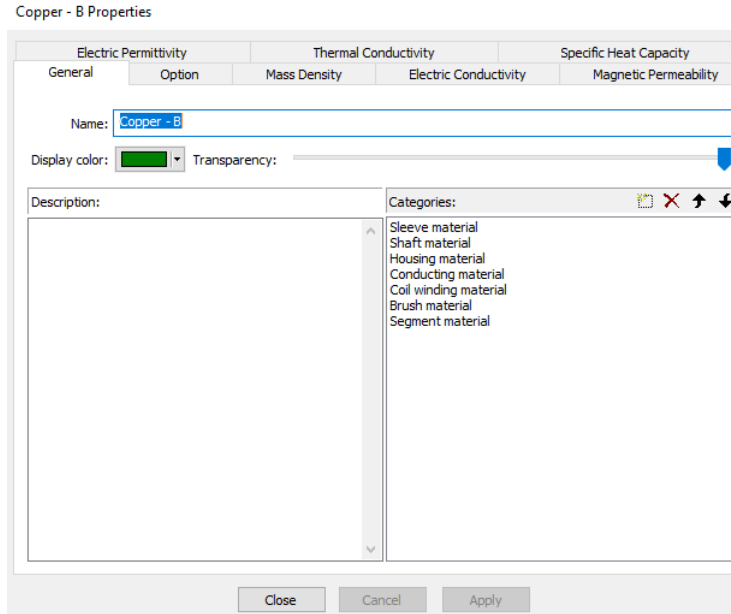


Figure 3.3: Properties of Copper B used in Coils of Phase 2

For phase 3 the Coils are named $Coil_{51x}$ for input of the coil and $Coil_{51y}$ for output up to $Coil_{58x}$ and $Coil_{58y}$. The material used for Phase 3 has the same characteristics as Copper: $5.77e7$ Siemens/meter and it is named Copper C as depicted in the Figure below (Figure 3.4):

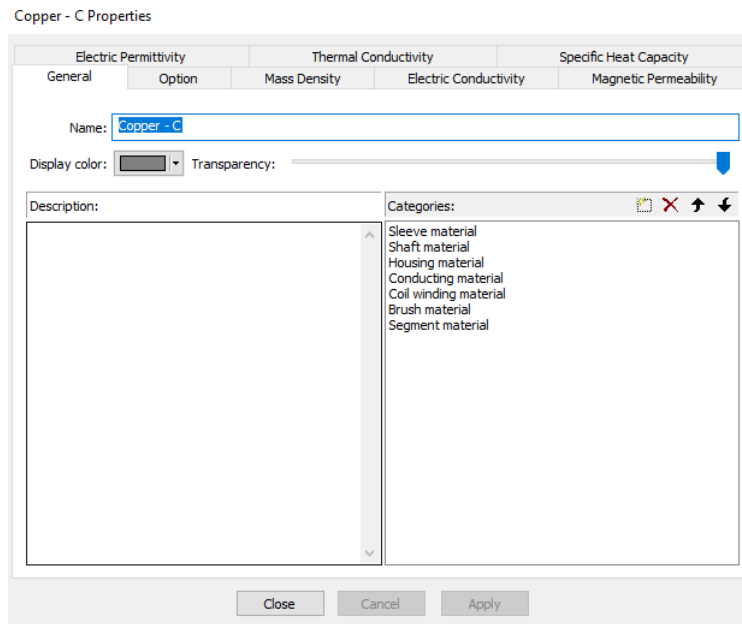


Figure 3.4: Properties of Copper C used in Coils of Phase 3

Rotor Outer and Rotor Inner

Rotor outer and Rotor Inner are the components shown in Figure 3.5 and the material that was used is named rotor steel

Airtooth

As you can see in Figure 3.6 it is the air gap between the input and output of a coil. We have 24 Airtooth components because we have 24 coils. The material used in Airtooth is Air.

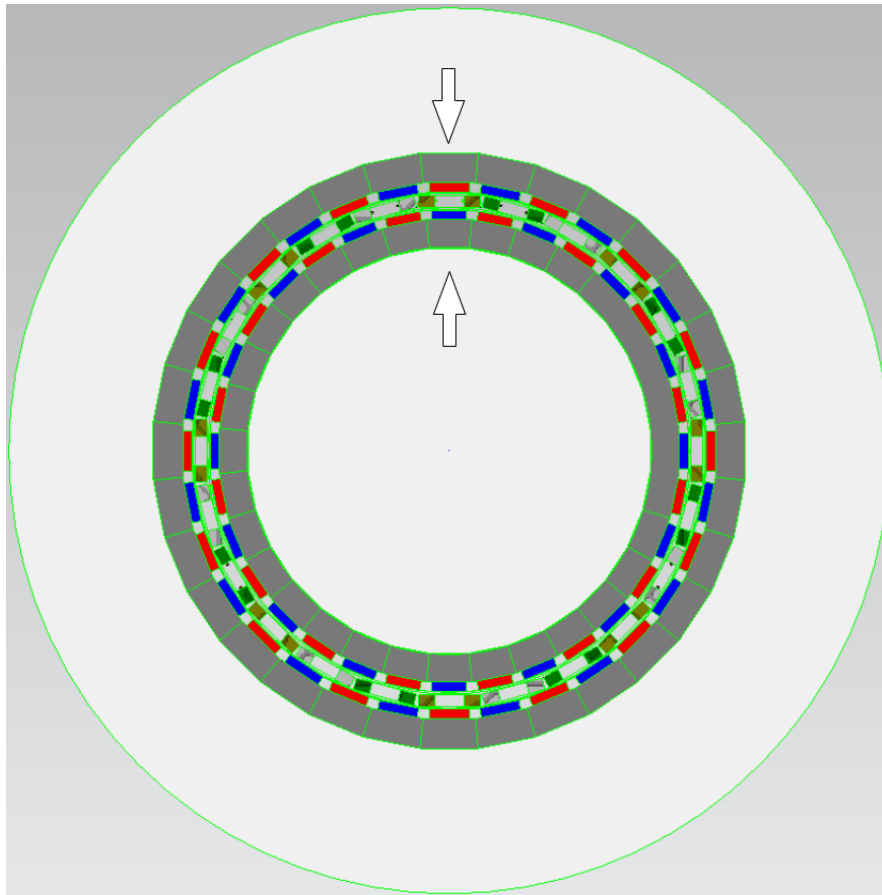


Figure 3.5: Inner and Outer Rotor made by Rotor Steel (Gray color)

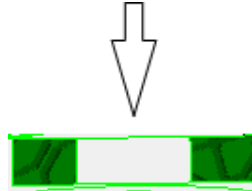


Figure 3.6: Airtooth

Inner Airspace

It is the white circle created inside the inner rotor. The material used is Air

Outer Airspace

Is the white circle created out of the generator and it simulates the environment in which the generator is placed. The material used is Air.

Inner Magnet and Outer Magnet

We have 32 Inner magnets and 32 Outer magnets that are created from 2 materials depending if it is a north or south pole.

The materials are named N42 South (blue) and N42 North (red) and they have the same characteristics as N42 material (Figures 3.7 and 3.8).

Inner and Outer Magnet Airspace

As depicted in Figure 3.9 the air gap between the inner magnets and outer magnets the material used is Air. Below we will describe each airgap. You can see all the airgaps together in Figure 3.11

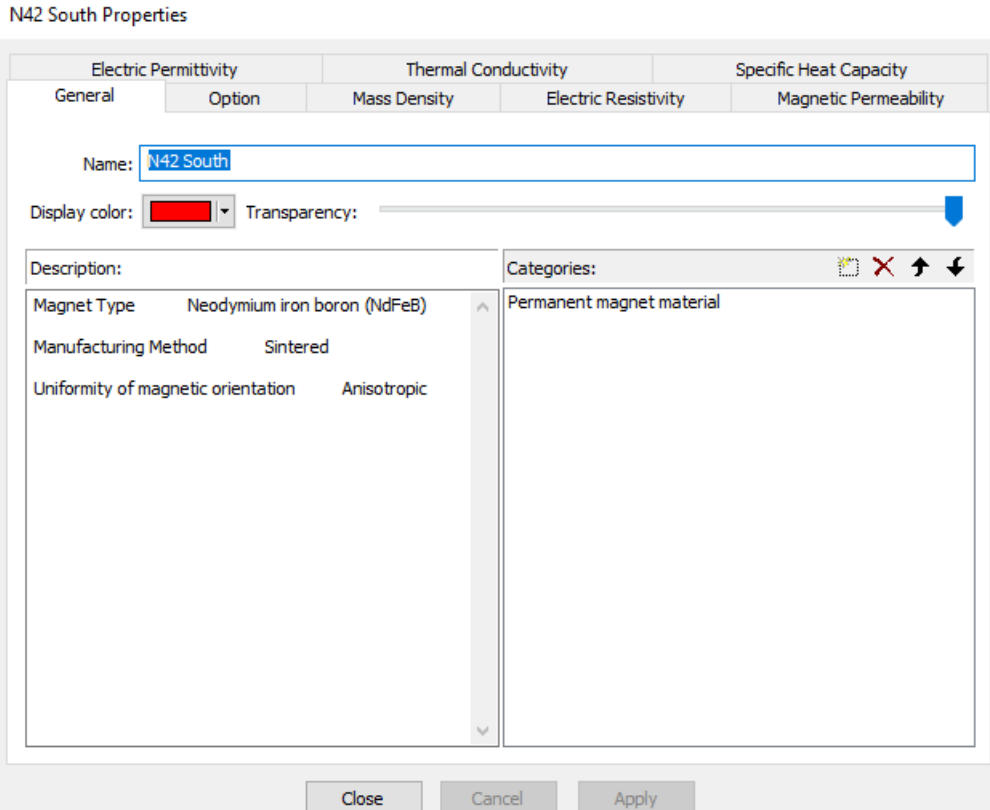


Figure 3.7: N42 south

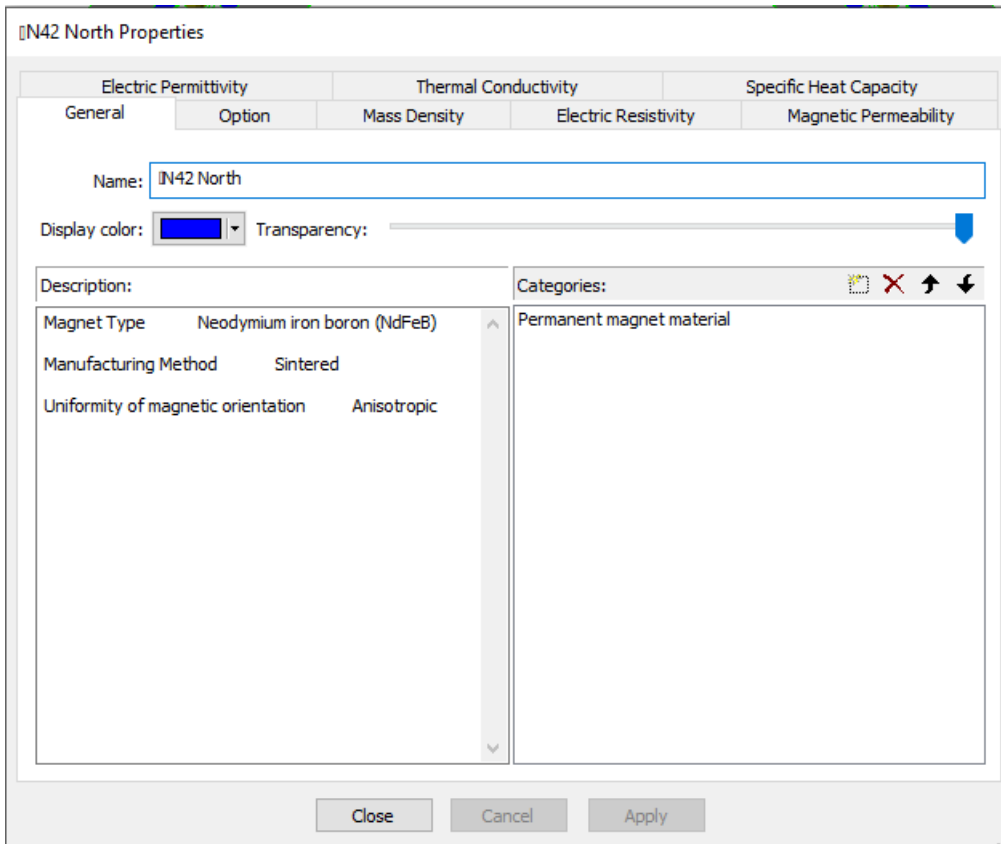


Figure 3.8: N42 north

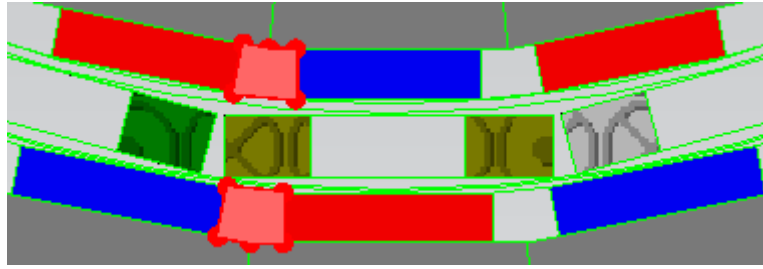


Figure 3.9: Inner and outer magnet airspace

Outer Airgap

Is a layer between the Outer Rotor airgap and Stator airgap.

Outer Rotor Airgap

Is a layer of air between upper magnets and outer airgap.

Stator Airgap

Is the stator airgap between the Inner and Outer airgap (It could be split in 2 components one between the upper part of the stator and the outer airgap and the other between the Inner airgap and the lower part of the stator).

Inner Airgap

Is a layer of air between the Inner rotor airgap and the stator airgap.

Inner Rotor Airgap

Is a layer of air between Inner Magnets and Inner airgap.

As described above the material used for each one of the airgap layers is Air.



Figure 3.10: Airgap Components

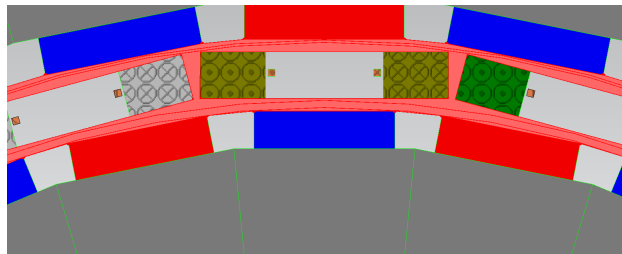


Figure 3.11: Airgap Components shown in C-GEN

Motion Components

We have 3 motion components for each one of the moving parts. The motion components include some of the components that are described above to determine the motion of each group.

- *Rotor#1* This motion component includes: The 32 Inner Rotor Magnets, Inner Airspace, Inner Rotor airgap, Rotor inner and Inner Magnet Airspace (32 components)
- *Stator#1* This motion component includes: $Coil_{11x} - Coil_{58y}$ (all the coils), Airtooth1-Airtooth24 and Stator Airgap.
- *Rotor#2* This motion component includes: The 32 Outer Rotor Magnets, Outer Rotor airgap, Rotor Outer and Outer Magnet Airspace (32 components)

Rotors 1 and 2 are velocity-driven components that use Rotary motion and they are both rotating at 100rpm. The stator components are not moving which equals 0 rpm.

Sensors

We have 5 Sensors placed inside coil Airtooths with 100 number of turns each in different positions. We used them to calculate the magnetic flux through voltage

- *Sensor#1* is a sensor placed at 0° .
- *Sensor#2* is a sensor placed at 120° .
- *Sensor#3* is a sensor placed at 240° .
- *SensorLeft* is a sensor placed at the left coil (11.25°).
- *SensorRight* is a sensor placed at the right coil (-11.25°).

Circuit

Below we will describe the circuit used for the simulation: First of all, we have 3 Resistors at 17.5Ω representing the ohmic load of each phase. As depicted below in Figure 3.12 we have 24 coils, 4 of them are in parallel connection and in series connection with another 4 parallel coils. This connection is used in each phase.

The sensors are open-circuited because they are connected with $1 \text{ G}\Omega$.

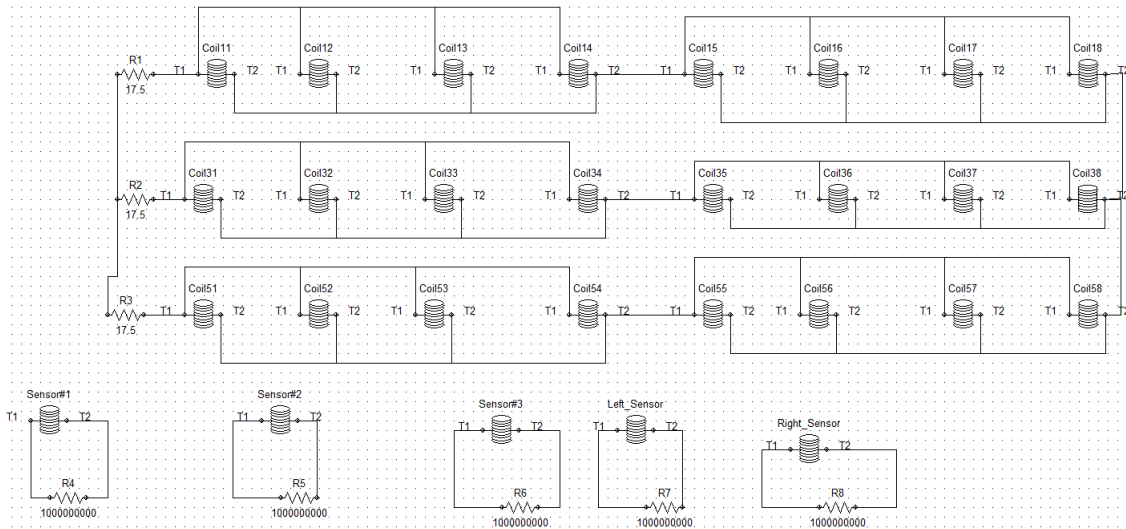


Figure 3.12: Circuit of the generator used for the simulation

Chapter 4

Case Study and Results

4.1 Voltage and Current Analysis for All Cases

4.1.1 Demagnetization 25%

Current and Difference for Load 1

The examination of the time domain signals, as depicted in Figures (4.1, 4.2 and 4.3), reveals minimal distinctions between the current patterns of healthy and faulty cases. The subtle nature of these differences, coupled with the presence of an ohmic load, results in a consistent pattern in voltage. Consequently, the presentation of voltage patterns is excluded, as it gives the same characteristics due to the ohmic load. For a more distinct understanding of fault signatures, the focus shifts to alternative diagnostic approaches, such as the Fourier transforms discussed later.

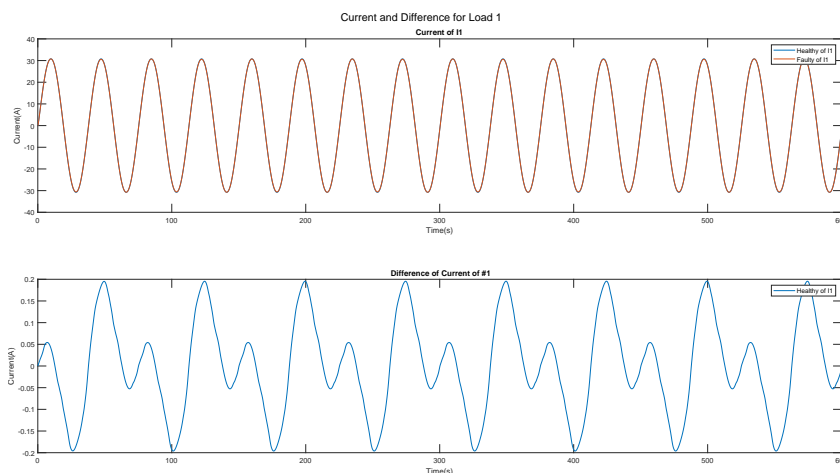


Figure 4.1: Thesis results for: Current and Difference for Load 1 (Case Demag 25 13.125)

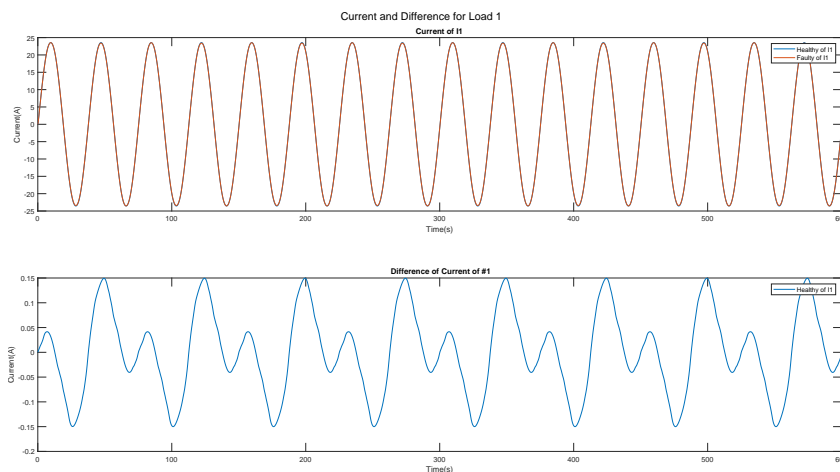


Figure 4.2: Thesis results for: Current and Difference for Load 1 (Case Demag 25 17.5)

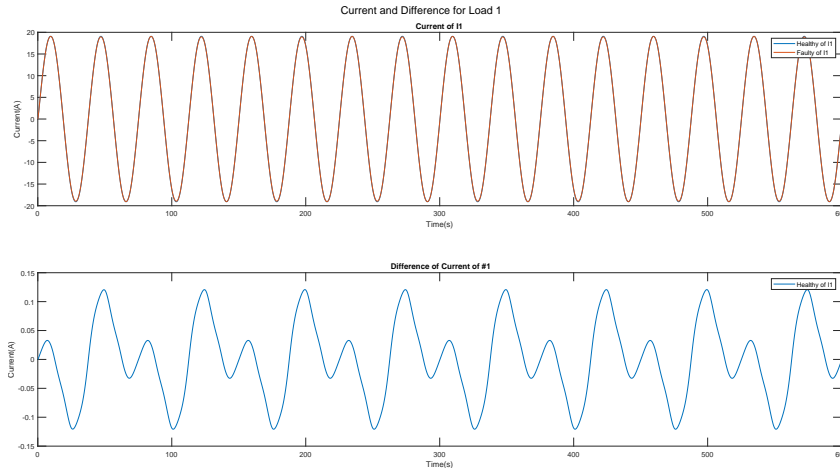


Figure 4.3: Thesis results for: Current and Difference for Load 1 (Case Demag 25 21.875)

Currents for 4 Coils of Phase 1

In the coils of the machine, the effects of demagnetization are much more obvious as depicted in Figures (4.4, 4.5 and 4.6). The observed phenomenon where the magnet undergoes demagnetization, results in a diminished magnetic field compared to its healthy state. This demagnetization, in turn, leads to a lower inductance and a subsequent reduction in the induced electromotive force (EMF) according to Faraday’s law.

Despite the demagnetization-induced changes in the individual electromotive forces across the four coils in the parallel circuit, the overall voltage remains nearly constant. This stability is maintained by the dynamic adjustment of currents in each coil, ensuring that the required values are attained to keep the voltage stable. Consequently, while the four coils exhibit different currents due to the variations in their electromotive forces caused by demagnetization, the parallel circuit’s voltage remains almost identical to its healthy state. This complex interplay between demagnetization, Faraday’s law and circuit dynamics highlights the complexity involved in under-

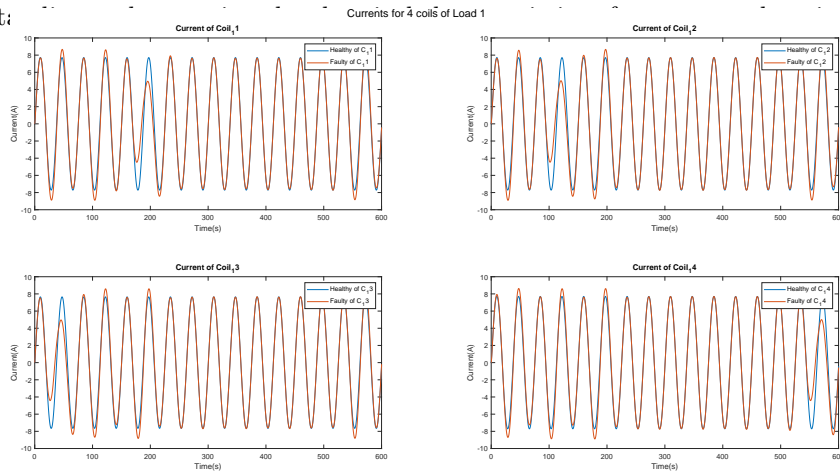


Figure 4.4: Thesis results for: Currents for 4 Coils of Phase 1 (Case Demag 25 13.125)

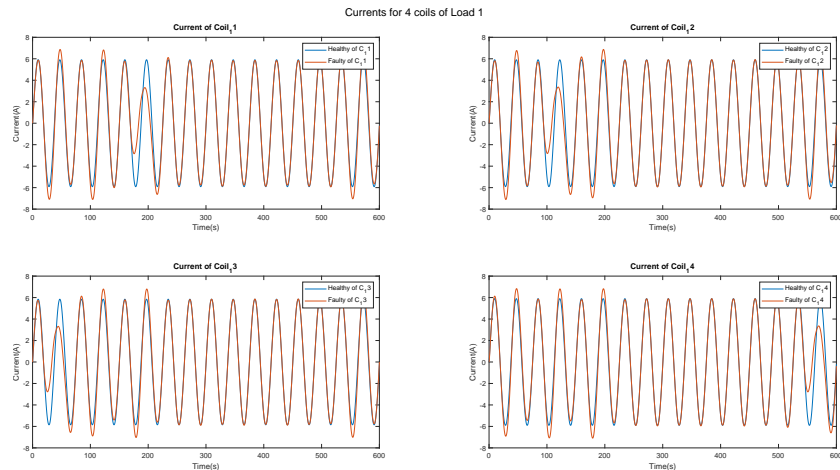


Figure 4.5: Thesis results for: Currents for 4 Coils of Phase 1 (Case Demag 25 17.5)

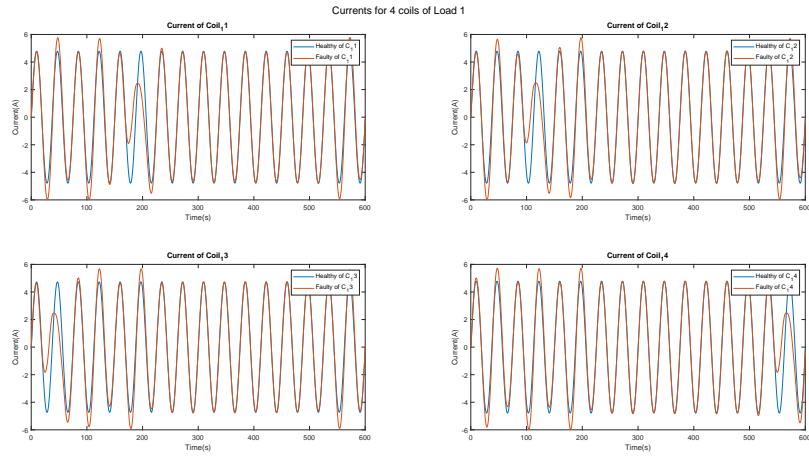


Figure 4.6: Thesis results for: Currents for 4 Coils of Phase 1 (Case Demag 25 21.875)

Difference of Currents for 4 coils

Intriguing patterns emerge in the time domain when comparing healthy and faulty cases as we can see in Figures (4.7, 4.8 and 4.9), revealing substantial differences at specific time steps. Surprisingly, these variations may not be evident when observing the load directly. The thermal implications within the generator become a crucial aspect to consider, given the considerable differences observed, signifying substantial thermal stress on the generator.

Furthermore, the distinct currents in each coil, arising from the demagnetization-induced differences in electromotive forces, contribute to diverse thermal stresses. Despite these differences, the system dynamically manages the currents to ensure a constant voltage output. This underscores the complex relationship between demagnetization, electrical behavior and thermal dynamics, emphasizing the necessity of a comprehensive understanding of effective diagnosis and mitigation strategies.

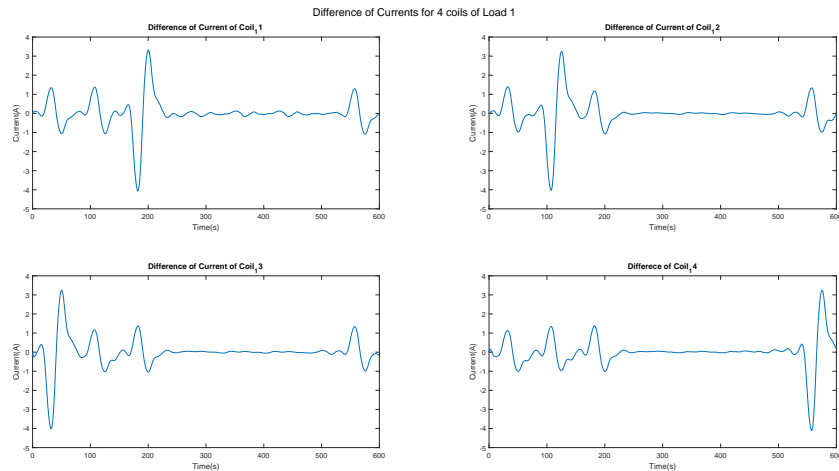


Figure 4.7: Thesis results for: Difference of Currents for 4 coils of Phase 1 (Case Demag 25 13.125)

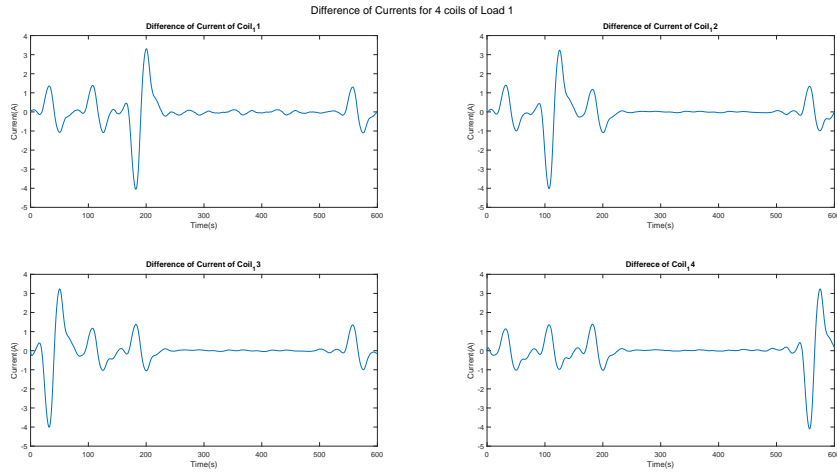


Figure 4.8: Thesis results for: Difference of Currents for 4 coils of Phase 1 (Case Demag 25 17.5)

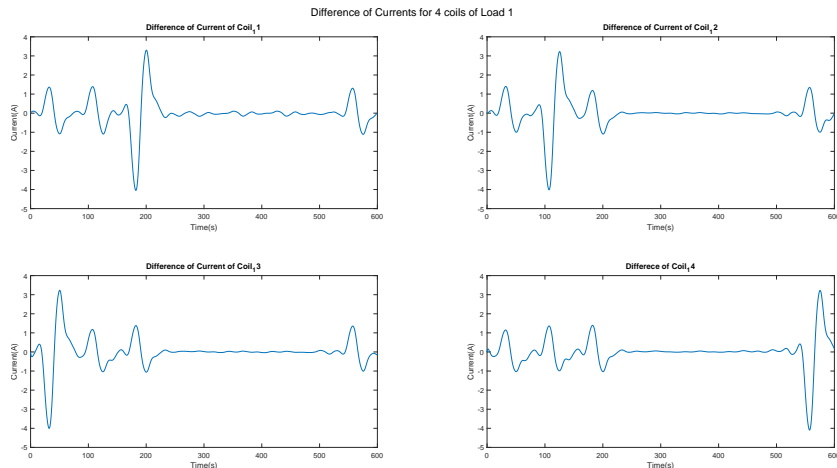


Figure 4.9: Thesis results for: Difference of Currents for 4 coils of Phase 1 (Case Demag 25 21.875)

Fourier and Differences in Current of Load Between Healthy and Faulty Cases

In the realm of Motor Current Signature Analysis (MCSA), demagnetization signatures are sought by examining the left sideband of the frequencies. A notable observation arises in the $2f_s$ harmonic, where the amplitude in faulty cases increases, contradicting the expected cancellation phenomenon. Disparities between simulation and experimental results, particularly in the second harmonic, raise concerns. While the second harmonic is usually associated with asymmetry in healthy conditions, variations in real-world scenarios, such as slight resistance errors, challenge its reliability.

Moreover, the linkage of fault indications in the second harmonic with stator faults, while the present case involves a rotor fault, adds complexity. Combining this with the potential cancellation of the left sideband $\frac{f_s}{2}$ due to the demagnetization of non-adjacent magnets emphasizes the need for a distinct interpretation of diagnostic indicators. The risk of misdiagnosing the machine is large if such difficulties are overlooked, reinforcing the importance of considering experimental results for a more accurate fault diagnosis. The cancellation phenomenon, particularly evident in the case of demagnetization affecting two non-adjacent magnets, further underscores the complexities in fault analysis.

A comprehensive analysis of Fourier transforms at $\frac{f_s}{2}$ in the left sideband reveals a consistent trend of rising amplitudes in most demagnetization cases, providing valuable diagnostic insight in Figures (4.10, 4.11 and 4.12). Notably, when demagnetization impacts two non-adjacent magnets at 25% or 50%, a cancellation phenomenon in the left sideband $\frac{f_s}{2}$ is observed, as detailed in Chapter 2 (see Figures 4.64, 4.65, 4.66, 4.82, 4.83 and 4.84). This phenomenon underscores the complexity of fault detection mechanisms in demagnetization scenarios.

Furthermore, leveraging Fast Fourier Transform (FFT) the difference signals proves beneficial, highlighting frequencies crucial for fault detection with higher amplitudes. This method offers a distinct perspective, aiding in the identification of demagnetization-induced faults.

Interestingly, the MCSA results for identical demagnetization under three different loads demonstrate a consistency that defies significant variation. This finding suggests that the load conditions may not exert a pronounced influence on the MCSA outcomes in demagnetization scenarios, emphasizing the robustness of the diagnostic approach across diverse operational conditions.

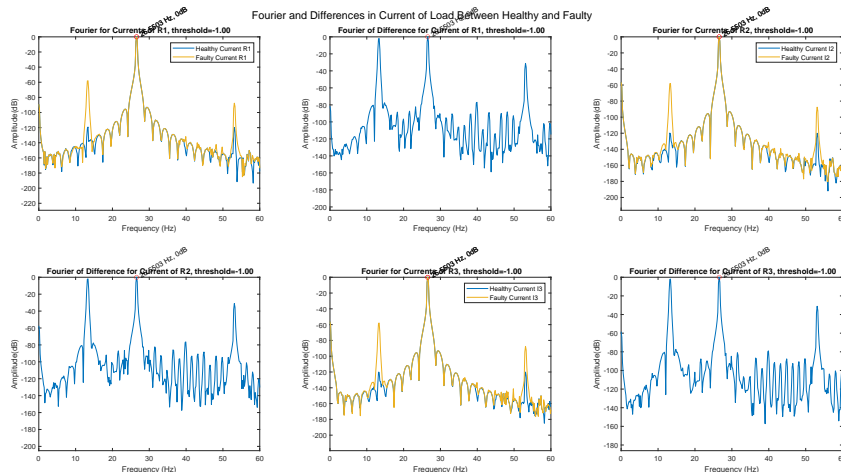


Figure 4.10: Thesis results for: Fourier and Differences in Current of Load Between Healthy and Faulty (Case Demag 25 13.125)

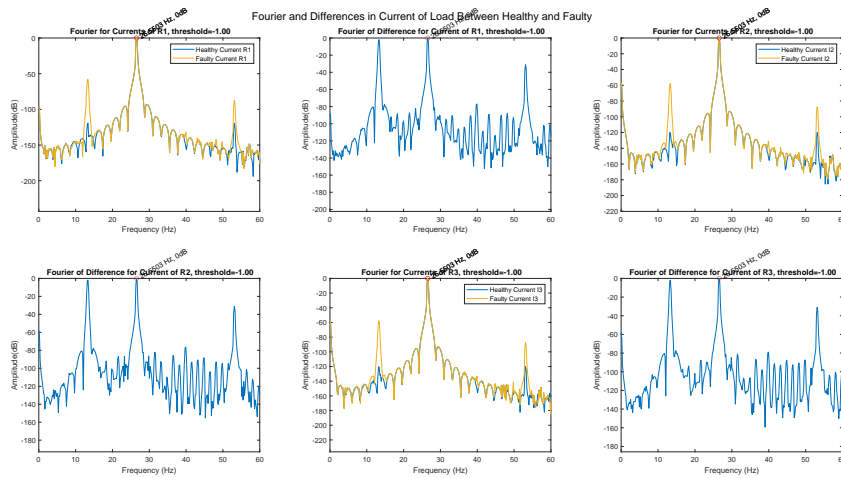


Figure 4.11: Thesis results for: Fourier and Differences in Current of Load Between Healthy and Faulty (Case Demag 25 17.5)

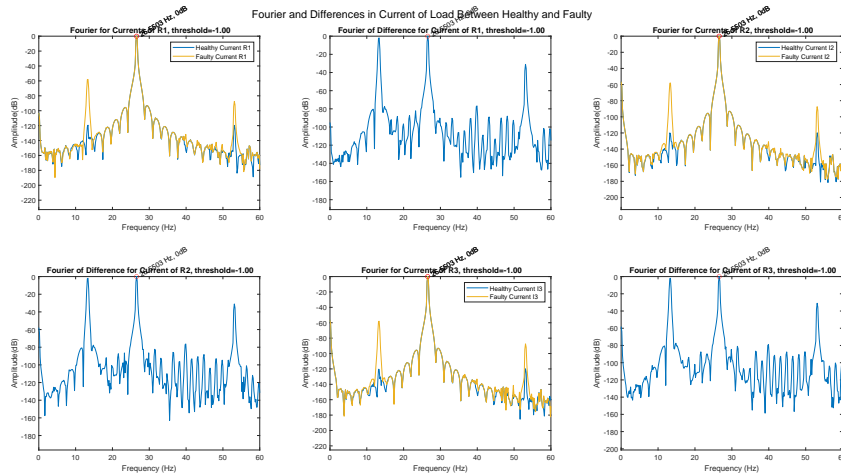


Figure 4.12: Thesis results for: Fourier and Differences in Current of Load Between Healthy and Faulty (Case Demag 25 21.875)

Voltage and Difference for $Coil_{11}$ of Phase 1

As we previously analyzed the theory behind the currents of the coils, it is noteworthy that the voltage remains nearly constant, exhibiting only a marginal decrease, as illustrated below in Figures (4.13, 4.14 and 4.15). The difference is less than 1.5% between the two signals which raises concerns about its reliability as an indicator of a fault. In light of this, additional diagnostic techniques, such as frequency domain analyses, may provide more robust insights into potential demagnetization faults. Interestingly, the time domain results for

identical demagnetization under three different loads demonstrate a consistency that defies significant variation. This finding suggests that the load conditions may not exert a pronounced influence on the voltage pattern outcomes in demagnetization scenarios, emphasizing the robustness of the diagnostic approach across diverse operational conditions.

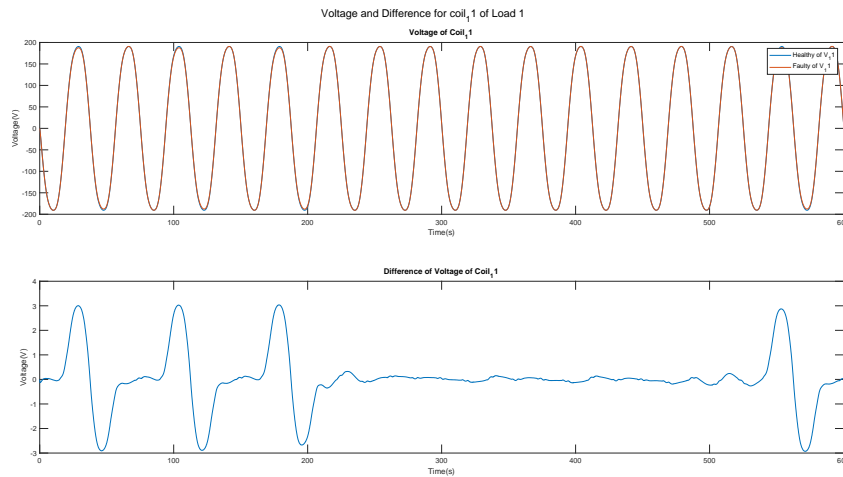


Figure 4.13: Thesis results for: Voltage and Difference for $Coil_{11}$ of Phase 1 (Case Demag 25 13.125)

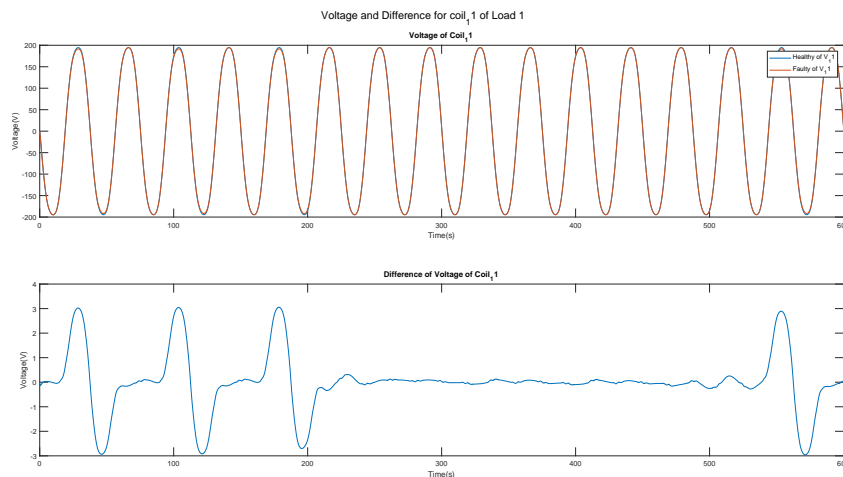


Figure 4.14: Thesis results for: Voltage and Difference for $Coil_{11}$ of Phase 1 (Case Demag 25 17.5)

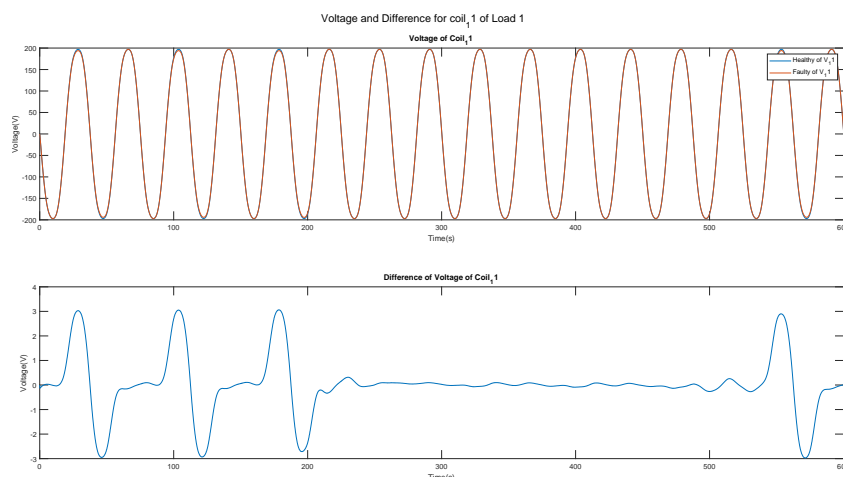


Figure 4.15: Thesis results for: Voltage and Difference for $Coil_{11}$ of Phase 1 (Case Demag 25 21.875)

Fourier for Currents of 4 Coils of Phase 1

Utilizing Fast Fourier Transform (FFT) on the signals from the four coils reveals a substantial increase in amplitude across almost every frequency in the case of demagnetization as shown below in Figures (4.16, 4.17 and

4.18), providing a clear indication of the demagnetization phenomenon. However, a practical limitation arises as measuring the current of each coil in real-life scenarios is often unfeasible, restricting the direct applicability of this method. Consequently, alternative approaches or complementary diagnostic techniques may be necessary for effective demagnetization fault detection.

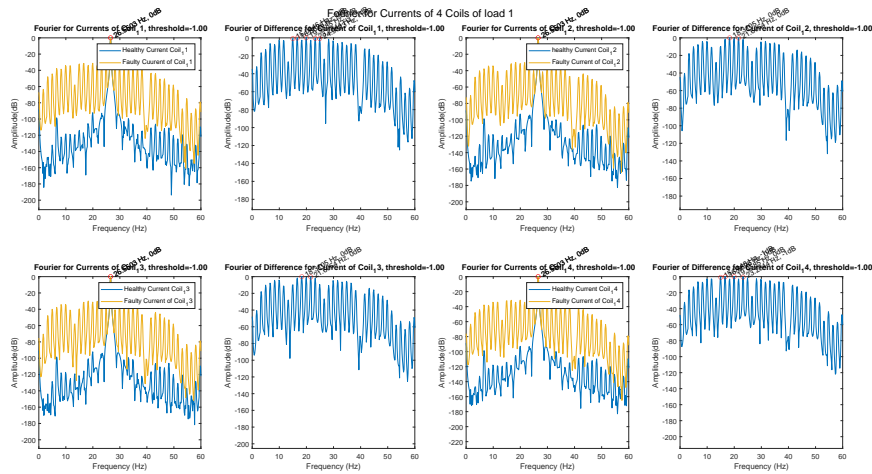


Figure 4.16: Thesis results for: Fourier for Currents of 4 Coils of Phase 1 (Case Demag 25 13.125)

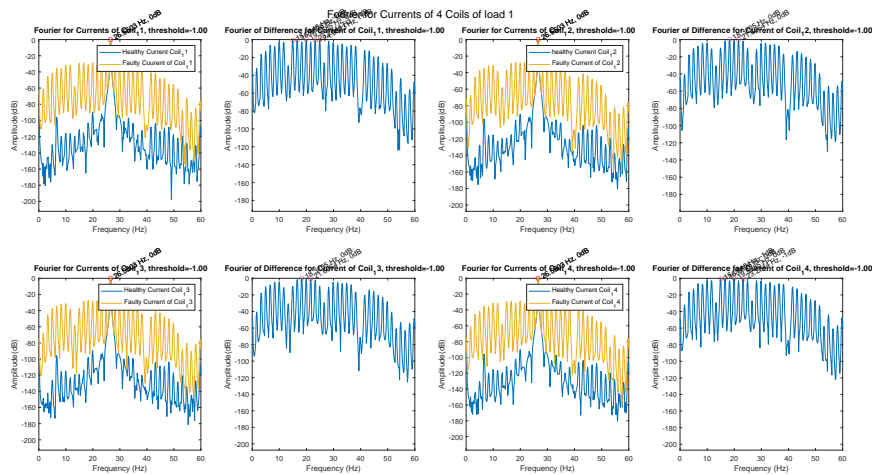


Figure 4.17: Thesis results for: Fourier for Currents of 4 Coils of Phase 1 (Case Demag 25 17.5)

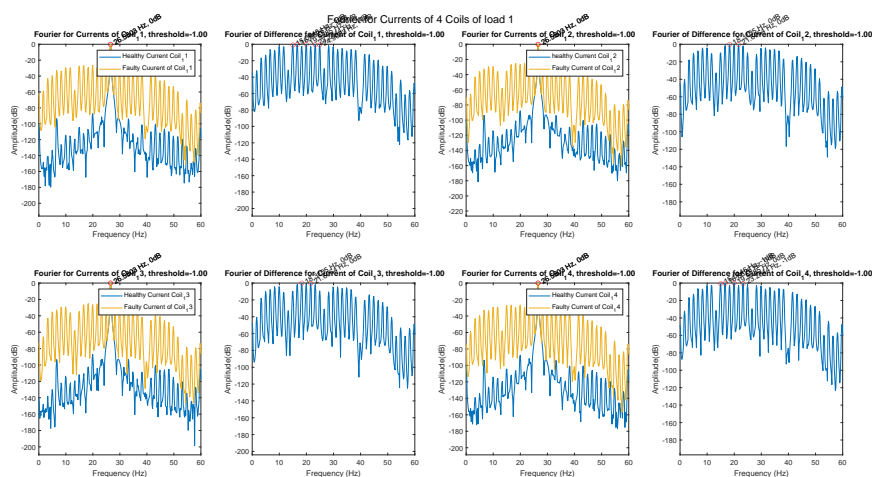


Figure 4.18: Thesis results for: Fourier for Currents of 4 Coils of Phase 1 (Case Demag 25 21.875)



4.1.2 Demagnetization 50%

Current and Difference for Load 1

Analysis of the data reveals consistent patterns as described in case of 25% demagnetization as shown below in Figures (4.19, 4.20 and 4.21), consistent characteristics and comparable attributes across various measurements. The observed similarities are grounded in rigorous scientific principles, including the repeatability of results, statistical analyses indicating non-significant differences and the presence of shared qualitative features. Even the pattern of difference is almost identical.

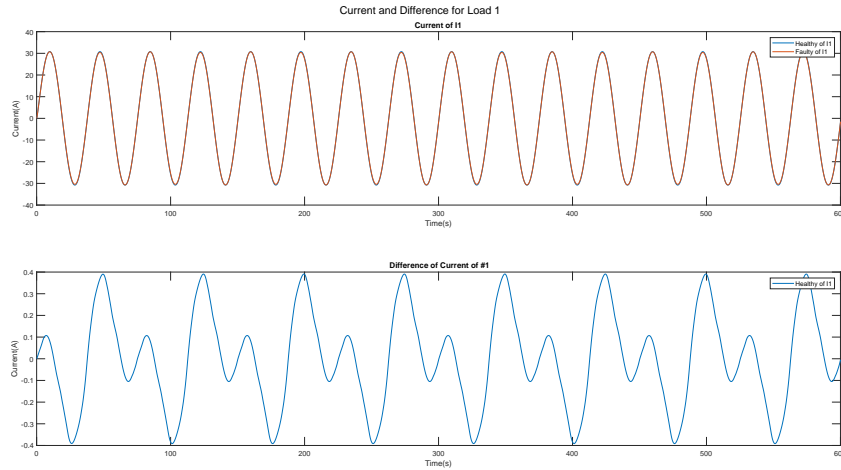


Figure 4.19: Thesis results for: Current and Difference for Load 1 (Case Demag 50 13.125)

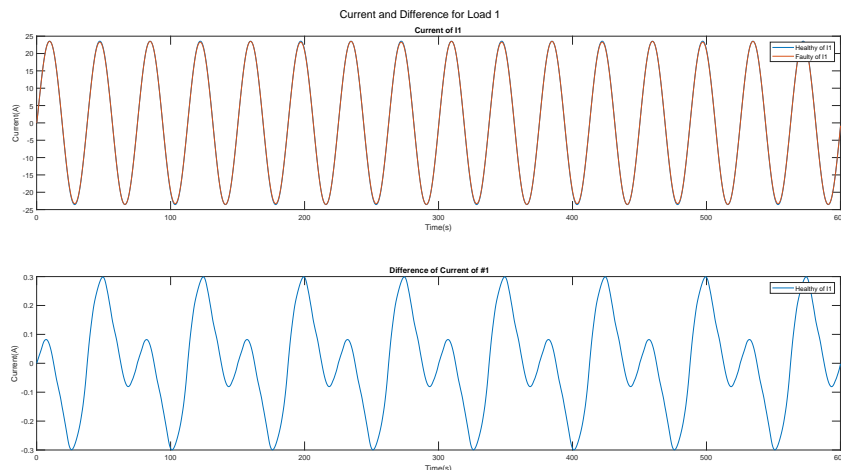


Figure 4.20: Thesis results for: Current and Difference for Load 1 (Case Demag 50 17.5)

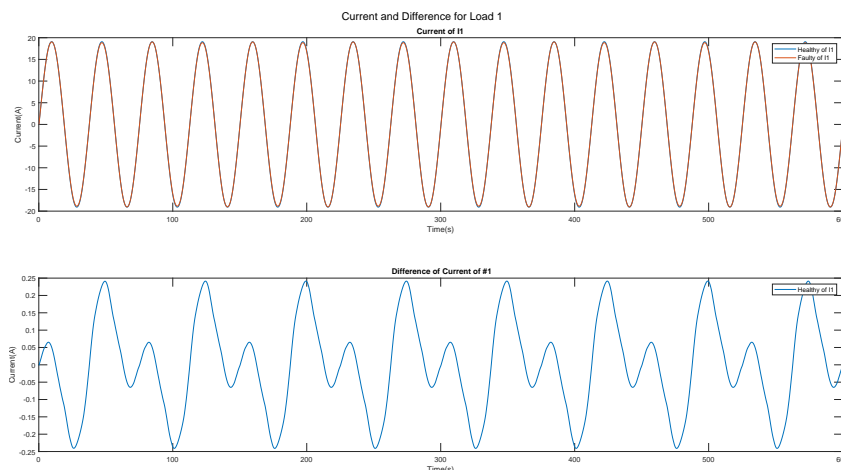


Figure 4.21: Thesis results for: Current and Difference for Load 1 (Case Demag 50 21.875)



Currents for 4 Coils of Phase 1

Qualitatively, the theory is consistently applied across this case as explained in case of 25% demagnetization as depicted below in Figures (4.22, 4.23 and 4.24). In the context of coil demagnetization within the machine, the visible effect involves the magnet undergoing demagnetization, resulting in a weakened magnetic field compared to its healthy state. This demagnetization, subsequently, lowers the inductance, leading to a reduction in the induced electromotive force (EMF) as dictated by Faraday's law.

Despite the alterations in individual electromotive forces across the four coils within the parallel circuit due to demagnetization, the overall voltage maintains a constant value. This stability is achieved through the dynamic adjustment of currents in each coil, ensuring that the required values are achieved to sustain voltage stability. Consequently, although the four coils exhibit distinct currents due to variations in their electromotive forces EMF caused by demagnetization, the voltage across the parallel circuit remains nearly identical to its healthy state.

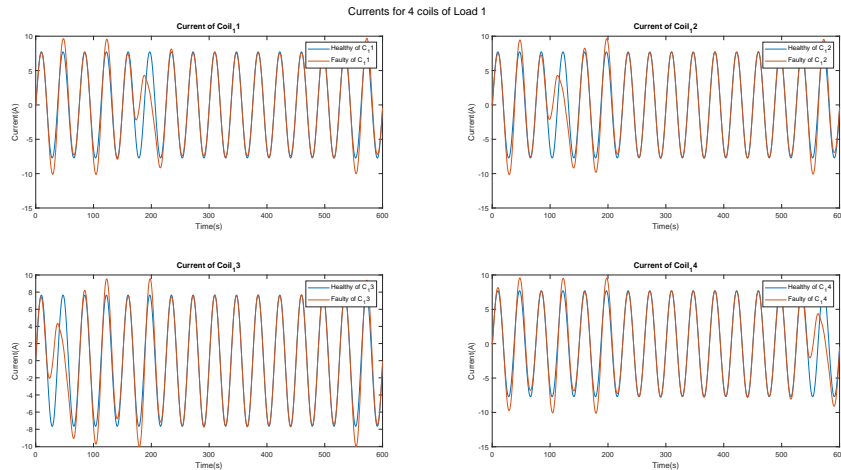


Figure 4.22: Thesis results for: Currents for 4 Coils of Phase 1 (Case Demag 50 13.125)

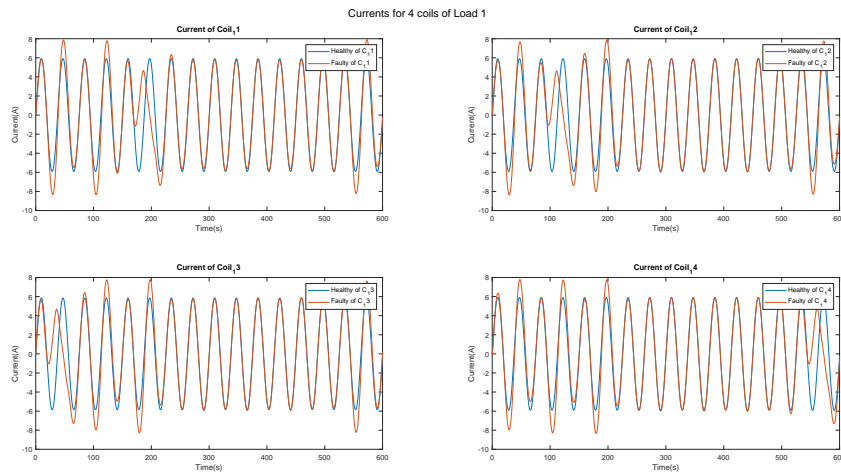


Figure 4.23: Thesis results for: Currents for 4 Coils of Phase 1 (Case Demag 50 17.5)

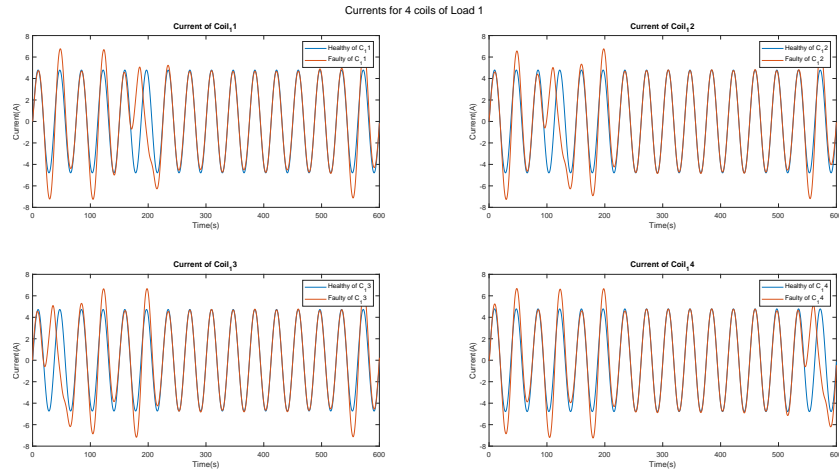


Figure 4.24: Thesis results for: Currents for 4 Coils of Phase 1 (Case Demag 50 21.875)

Difference of Currents for 4 coils

Presenting complicated time-related patterns in the time domain when contrasting healthy and faulty scenarios reveals noteworthy differences at specific time intervals. Interestingly, these variations could be undetected with the direct observation of the load. The thermal issue within the generator emerge as pivotal, considering the marked distinctions observed, indicating significant thermal stress on the generator. It is important to note that this is qualitatively the same theory as explained for the case of 25% demagnetization as depicted below in Figures (4.25, 4.26 and 4.27).

Additionally, the unique currents coursing through each coil, arising from the demagnetization-induced disparities in electromotive forces, contribute to varied thermal stresses. Despite these distinctions, the system adapts the currents to maintain a steadfast voltage output.

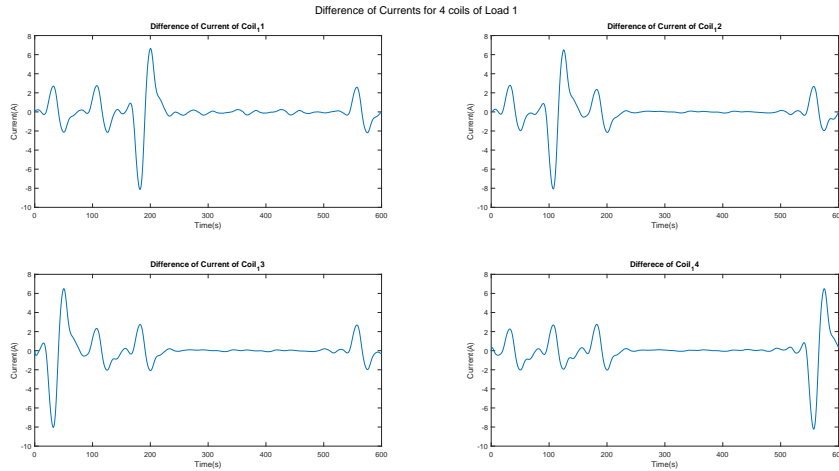


Figure 4.25: Thesis results for: Difference of Currents for 4 coils of Phase 1 (Case Demag 50 13.125)

Fourier and Differences in Current of Load Between Healthy and Faulty Cases

In the domain of Motor Current Signature Analysis (MCSA), the pursuit of demagnetization signatures involves studying the left sideband of frequencies. An interesting correlation is noted in the $2f_s$ harmonic, where faulty cases exhibit an unexpected increase in amplitude, challenging the anticipated cancellation phenomenon. The disparities observed in the second harmonic between simulations and experimental results, raise valid concerns. Typically associated with asymmetry in healthy conditions, the reliability of the second harmonic is put to the test due to real-world variations, such as slight resistance errors.

It is imperative to acknowledge the difficulties associated with fault indications in the second harmonic, primarily linked with stator faults in healthy conditions. However, in the current scenario involving a rotor fault, this conventional association adds a layer of complexity. When combined with the potential cancellation of the left sideband $\frac{f_s}{2}$ due to demagnetization of non-adjacent magnets, the interpretation of diagnostic indicators becomes difficult. Overlooking these difficulties poses a substantial risk of misdiagnosing the machine, reinforcing the critical role of incorporating experimental results for precise fault diagnosis. The cancellation phenomenon,

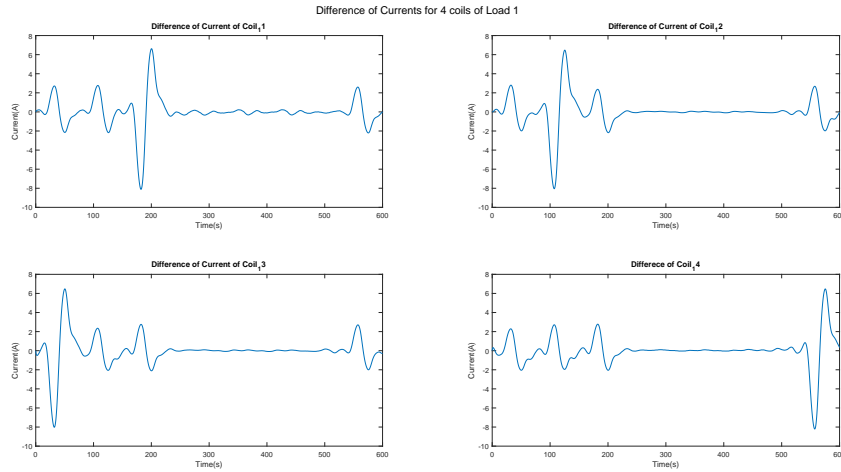


Figure 4.26: Thesis results for: Difference of Currents for 4 coils of Phase 1 (Case Demag 50 17.5)

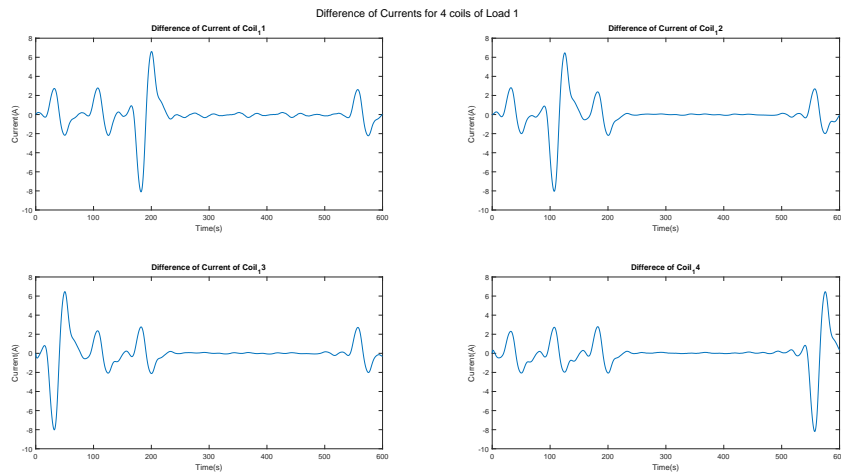


Figure 4.27: Thesis results for: Difference of Currents for 4 coils of Phase 1 (Case Demag 50 21.875)

prominently observed in the demagnetization of two non-adjacent magnets, further underscores the multifaceted nature of fault analysis.

A detailed Fourier analysis at $\frac{f_s}{2}$ in the left sideband consistently reveals escalating amplitudes in most demagnetization cases as shown below in Figures (4.28, 4.29 and 4.30), offering valuable diagnostic insights. Particularly noteworthy is the cancellation phenomenon in the left sideband $\frac{f_s}{2}$ when demagnetization affects two non-adjacent magnets at 25% or 50%, as explained in Chapter 2 (Figures 4.64, 4.65, 4.66, 4.82, 4.83 and 4.84).

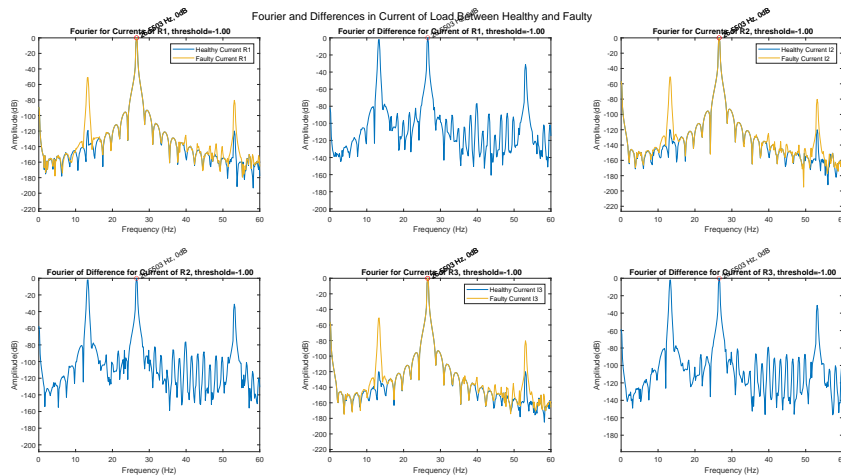


Figure 4.28: Thesis results for: Fourier and Differences in Current of Load Between Healthy and Faulty (Case Demag 50 13.125)

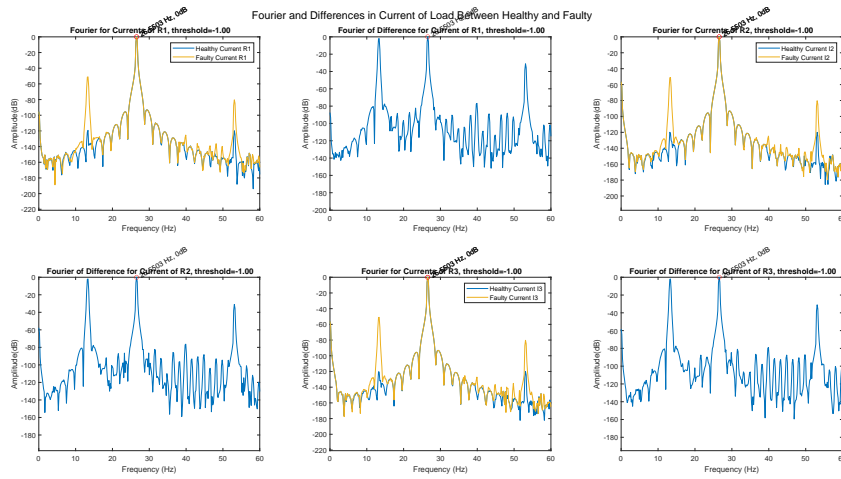


Figure 4.29: Thesis results for: Fourier and Differences in Current of Load Between Healthy and Faulty (Case Demag 50 17.5)

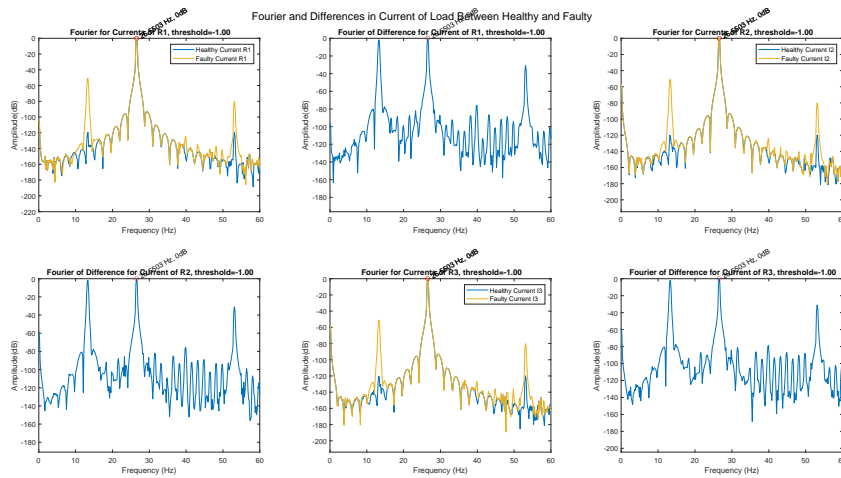


Figure 4.30: Thesis results for: Fourier and Differences in Current of Load Between Healthy and Faulty (Case Demag 50 21.875)

Voltage and Difference for $Coil_{11}$ of Phase 1

In examining the coil currents as discussed earlier, it's crucial to note that the voltage exhibits remarkable stability, showcasing only a minimal decrease, as illustrated below in Figures (4.31, 4.32 and 4.33). The negligible difference of less than 1.5% between the two signals raises doubts about its reliability as a fault indicator. Given this concern, it becomes appropriate to explore additional diagnostic methods, such as frequency domain analyses, to gain more reliable insights into potential demagnetization faults. Importantly, this qualitative observation aligns with the theory explained for the case of 25% demagnetization.

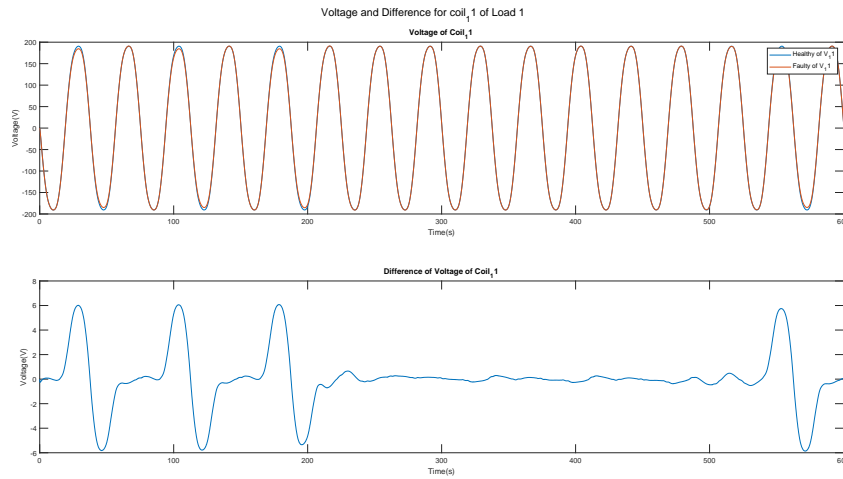


Figure 4.31: Thesis results for: Voltage and Difference for $Coil_{11}$ of Phase 1 (Case Demag 50 13.125)

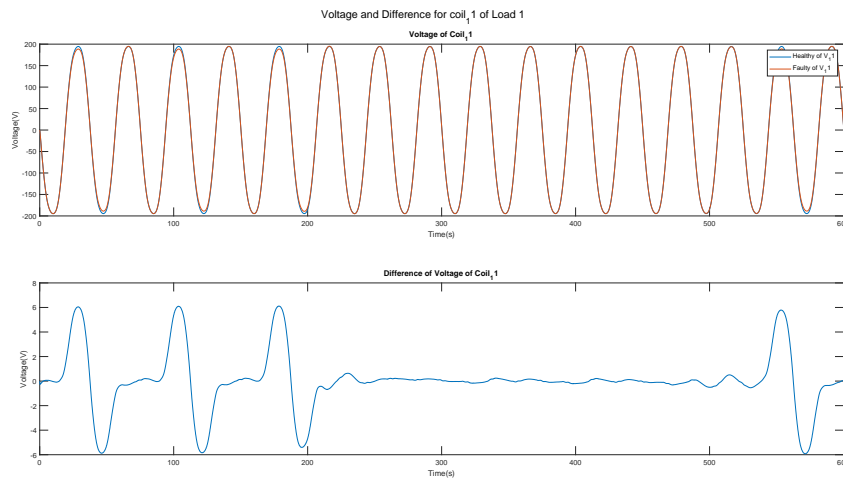


Figure 4.32: Thesis results for: Voltage and Difference for $Coil_{11}$ of Phase 1 (Case Demag 50 17.5)

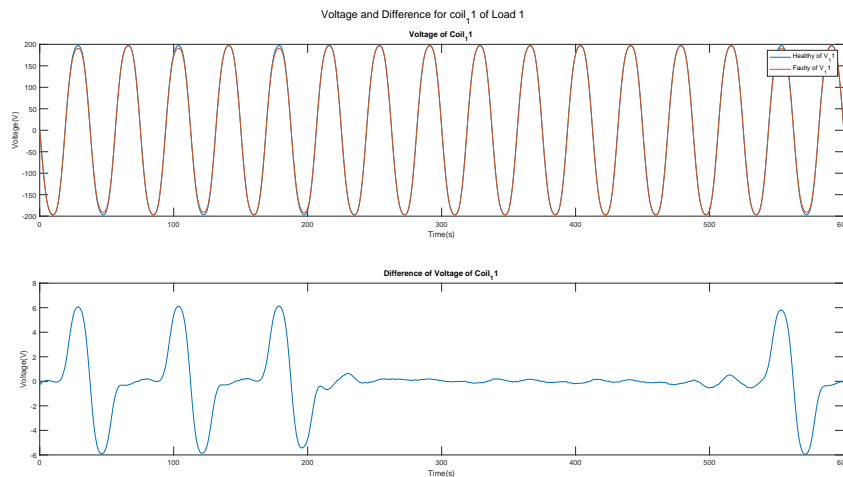


Figure 4.33: Thesis results for: Voltage and Difference for $Coil_{11}$ of Phase 1 (Case Demag 50 21.875)

Fourier for Currents of 4 Coils of Phase 1

In the exploration of Fast Fourier Transform (FFT) applied to the signals from the four coils, a significant rise in amplitude across nearly all frequencies is observed in instances of demagnetization. This conspicuous increase serves as a reliable marker for detecting demagnetization phenomena, mirroring the qualitative findings observed in the case of 25% demagnetization as depicted in Figures (4.34, 4.35 and 4.36). However, the practical challenge of measuring individual coil currents in real-world situations hinders the direct implementation of this method.

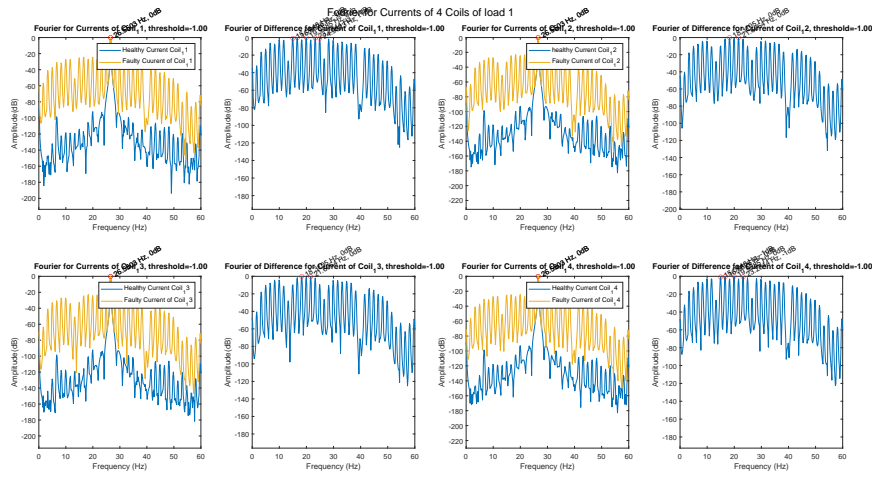


Figure 4.34: Thesis results for: Fourier for Currents of 4 Coils of Phase 1 (Case Demag 50 13.125)

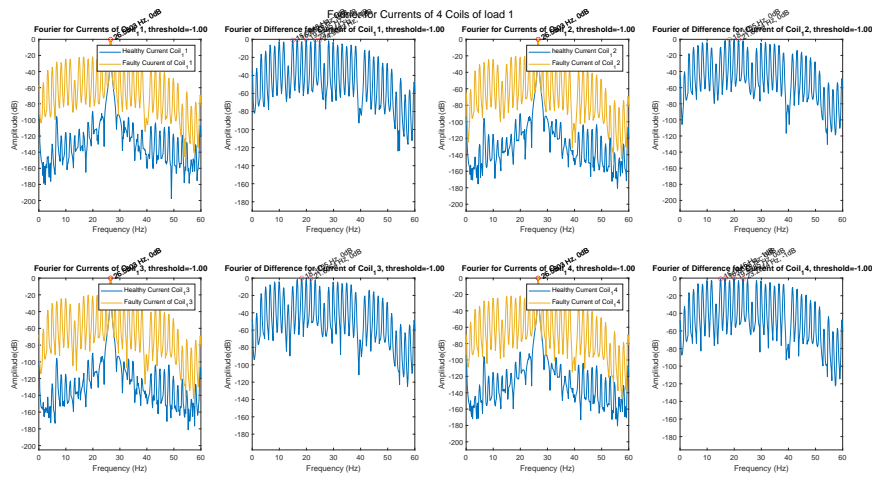


Figure 4.35: Thesis results for: Fourier for Currents of 4 Coils of Phase 1 (Case Demag 50 17.5)

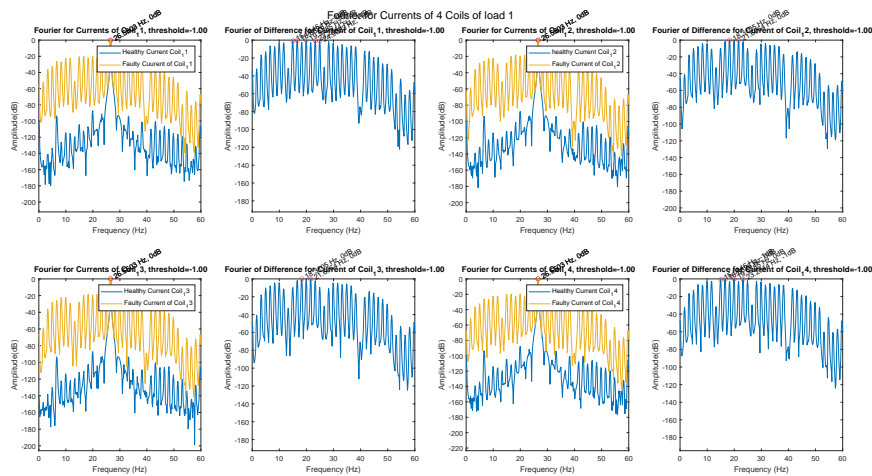


Figure 4.36: Thesis results for: Fourier for Currents of 4 Coils of Phase 1 (Case Demag 50 21.875)

4.1.3 Demagnetization 25% 50 %

Current and Difference for Load 1

Analysis of the data reveals consistent patterns as described in case of 25% demagnetization as depicted below in Figures (4.37, 4.38 and 4.39), consistent characteristics and comparable attributes across various measurements. The observed similarities are grounded in rigorous scientific principles, including the repeatability of results, statistical analyses indicating non-significant differences and the presence of shared qualitative features. In the time domain, the disparity between the healthy and faulty cases is marginal. Due to the similarity in the values of both signals, a substantial difference is not observed. Additionally, since the values of both signals are comparable, the patterns remain consistent across different load conditions.

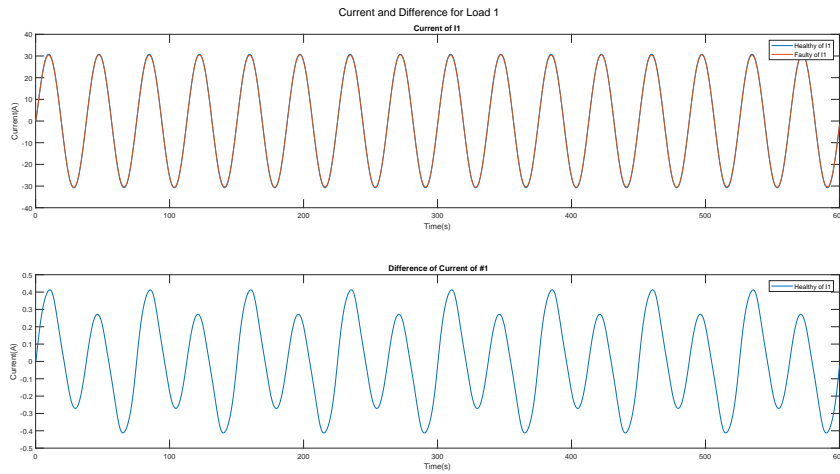


Figure 4.37: Thesis results for: Current and Difference for Load 1 (Case Demag 25 50 13.125)

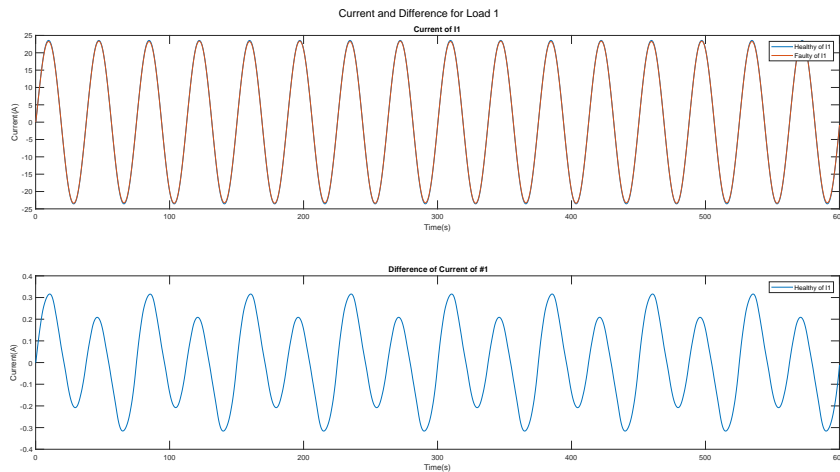


Figure 4.38: Thesis results for: Current and Difference for Load 1 (Case Demag 25 50 17.5)

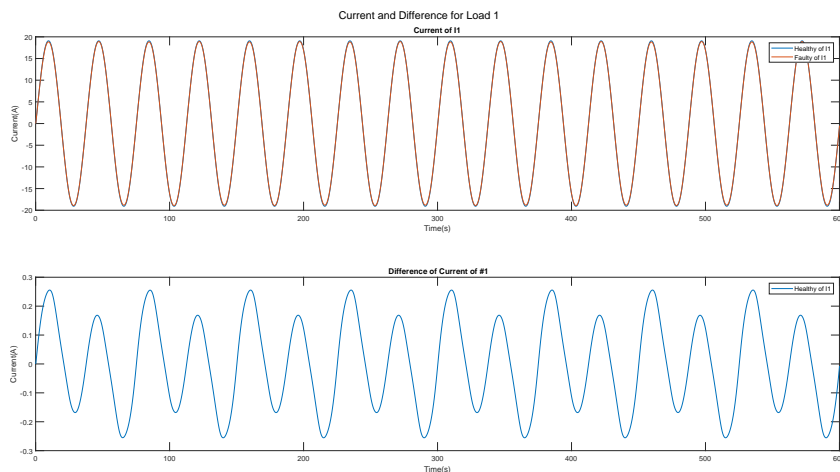


Figure 4.39: Thesis results for: Current and Difference for Load 1 (Case Demag 25 50 21.875)

Currents for 4 Coils of Phase 1

Qualitatively, the theory is consistently applied across this case as explained in case of 25% demagnetization as depicted below in Figures (4.40, 4.41 and 4.42), each illustrating the pronounced effect of demagnetization in the coils of the machine. The observable phenomenon entails the demagnetization of the magnet, leading to a weakened magnetic field compared to its healthy state. This demagnetization results in a reduced inductance and consequently a decline in the induced electromotive force (EMF) in accordance with Faraday’s law.

Despite variations in the individual electromotive forces EMF across the four coils in the parallel circuit due to demagnetization, the overall voltage remains consistently stable. This stability is maintained through the



dynamic adjustment of currents in each coil, ensuring that the necessary values are achieved to keep the voltage stable. Therefore, while each of the four coils exhibits different currents due to the diverse electromotive forces caused by demagnetization, the voltage across the parallel circuit remains nearly identical to its healthy state.

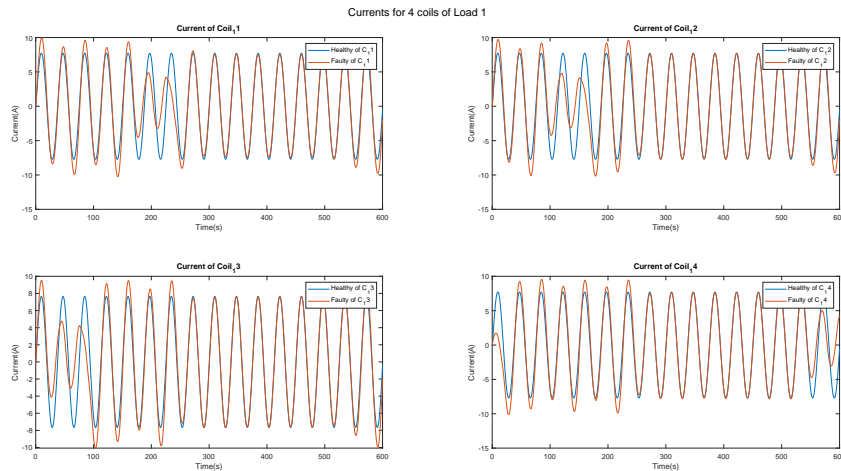


Figure 4.40: Thesis results for: Currents for 4 Coils of Phase 1 (Case Demag 25 50 13.125)

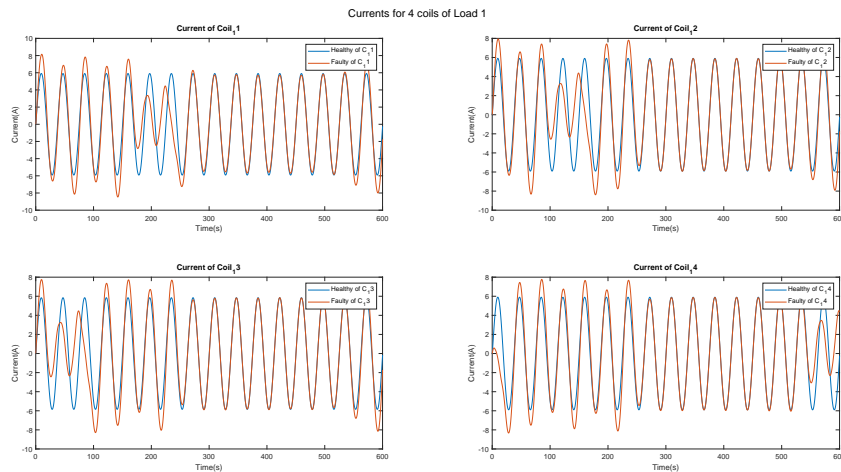


Figure 4.41: Thesis results for: Currents for 4 Coils of Phase 1 (Case Demag 25 50 17.5)

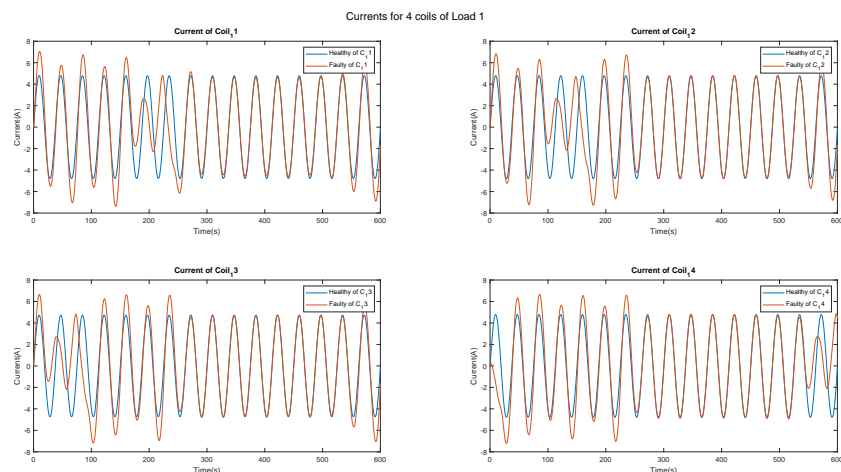


Figure 4.42: Thesis results for: Currents for 4 Coils of Phase 1 (Case Demag 25 50 21.875)

Difference of Currents for 4 coils

Time-domain analysis unravels interesting patterns when contrasting the temporal evolution of healthy and faulty states, unveiling substantial differences at specific time junctures. Curiously, these disparities may

remain inconspicuous when directly observing the load. The thermal impacts within the generator take center stage, given the marked variations observed, indicating notable thermal stress on the generator. It is crucial to emphasize that this is qualitatively the same theory as explained for the case of 25% demagnetization as depicted below in Figures (4.43, 4.44 and 4.45).

Moreover, the distinct currents passing through each coil, coming from demagnetization-induced variations in electromotive forces, contribute to diverse thermal stresses. Despite these differences, the system adeptly modulates the currents to maintain a consistent voltage output.

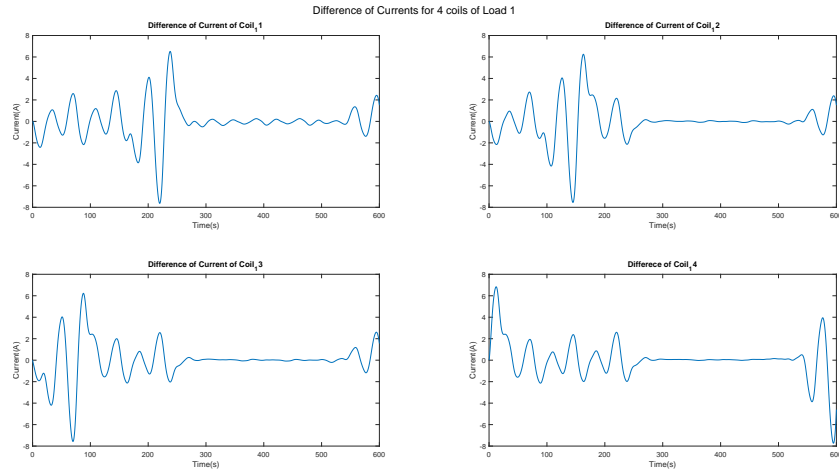


Figure 4.43: Thesis results for: Difference of Currents for 4 coils of Phase 1 (Case Demag 25 50 13.125)

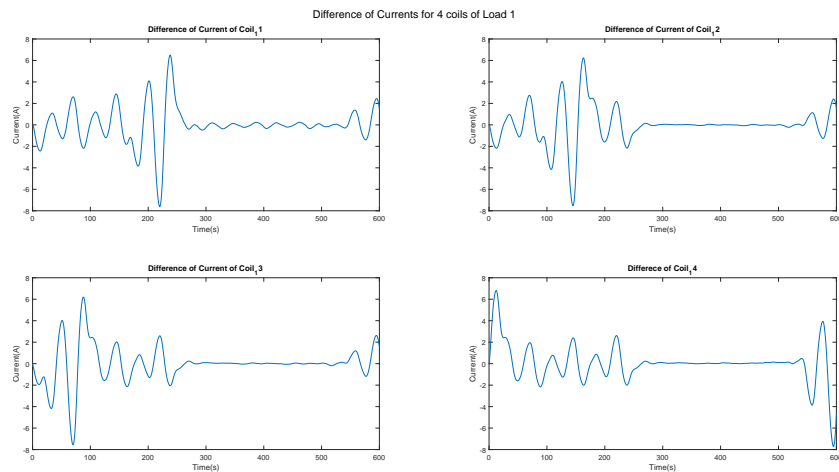


Figure 4.44: Thesis results for: Difference of Currents for 4 coils of Phase 1 (Case Demag 25 50 17.5)

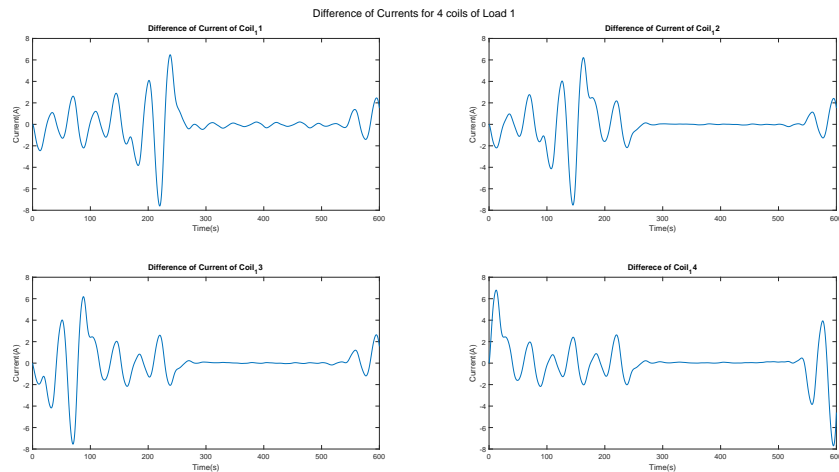


Figure 4.45: Thesis results for: Difference of Currents for 4 coils of Phase 1 (Case Demag 25 50 21.875)



Fourier and Differences in Current of Load Between Healthy and Faulty Cases

Within the domain of Motor Current Signature Analysis (MCSA), the search for demagnetization signatures involves a meticulous examination of the left sideband of frequencies as depicted below in Figures (4.46, 4.47 and 4.48). An intriguing phenomenon is observed in the $2f_s$ harmonic, where faulty cases exhibit an unexpected increase in amplitude, challenging the anticipated cancellation phenomenon. Differences between simulations and experimental results, particularly in the second harmonic, prompt valid concerns. Typically associated with asymmetry in healthy conditions, the reliability of the second harmonic is questioned due to real-world variations, such as slight resistance errors.

It is crucial to recognize the difficulties associated with fault indications in the second harmonic, primarily linked with stator faults in healthy conditions. However, in the present scenario involving a rotor fault, this conventional association adds a layer of complexity. When combined with the potential cancellation of the left sideband $\frac{f_s}{2}$ due to demagnetization of non-adjacent magnets, the interpretation of diagnostic indicators becomes difficult. Overlooking these difficulties poses a substantial risk of misdiagnosing the machine, emphasizing the critical role of incorporating experimental results for precise fault diagnosis. The cancellation phenomenon, prominently observed in the demagnetization of two non-adjacent magnets, further underscores the multifaceted nature of fault analysis.

A detailed Fourier analysis at $\frac{f_s}{2}$ in the left sideband consistently reveals escalating amplitudes in most demagnetization cases, offering valuable diagnostic insights. Particularly noteworthy is the cancellation phenomenon in the left sideband $\frac{f_s}{2}$ when demagnetization affects two non-adjacent magnets at 25% or 50%, as explained in Chapter 2 (Figures 4.64, 4.65, 4.66, 4.82, 4.83 and 4.84).

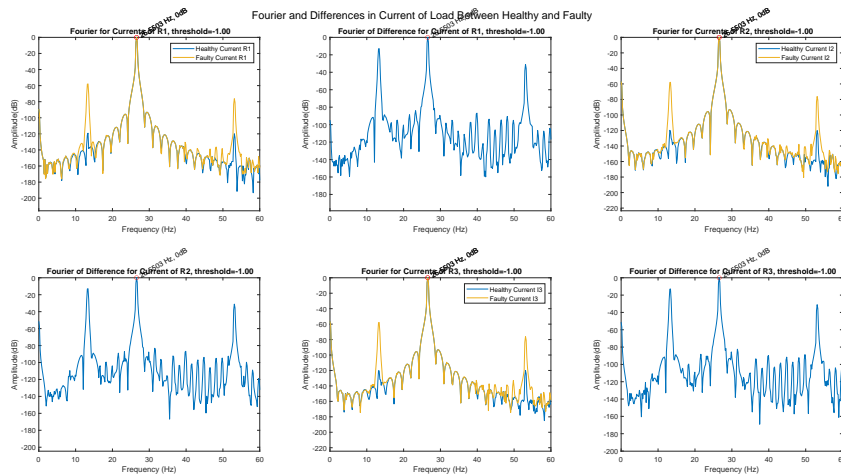


Figure 4.46: Thesis results for: Fourier and Differences in Current of Load Between Healthy and Faulty (Case Demag 25 50 13.125)

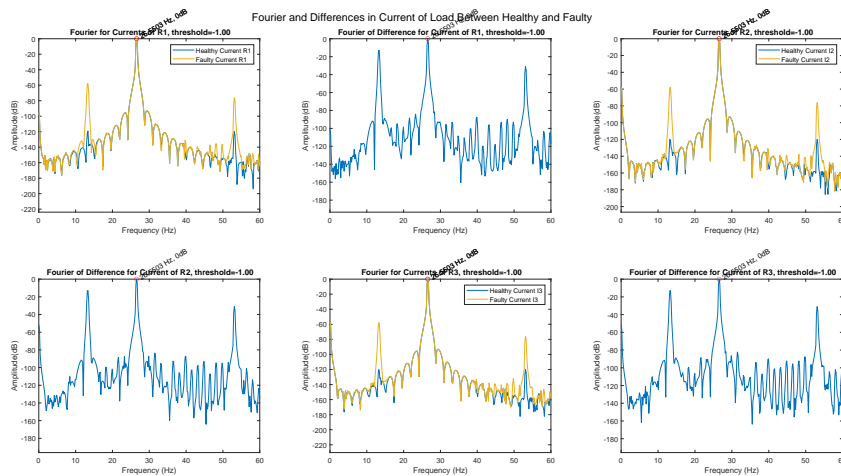


Figure 4.47: Thesis results for: Fourier and Differences in Current of Load Between Healthy and Faulty (Case Demag 25 50 17.5)

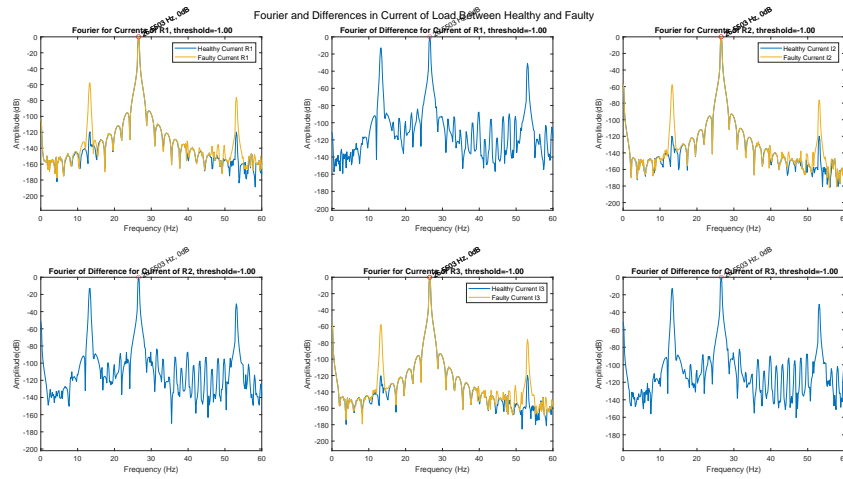


Figure 4.48: Thesis results for: Fourier and Differences in Current of Load Between Healthy and Faulty (Case Demag 25 50 21.875)

Voltage and Difference for $Coil_{11}$ of Phase 1

Upon studying the coil currents as outlined previously, it’s crucial to highlight the voltage’s noteworthy stability, showcasing only a slight decrease, as demonstrated below. The marginal difference, measuring less than 1.5%, between the two signals raises questions about its dependability as a fault indicator. Considering this concern, it becomes imperative to explore supplementary diagnostic techniques, such as frequency domain analyses, for more robust insights into potential demagnetization faults. Importantly, this qualitative observation aligns with the theory explained for the case of 25% demagnetization, as depicted in Figures (4.49, 4.50 and 4.51).

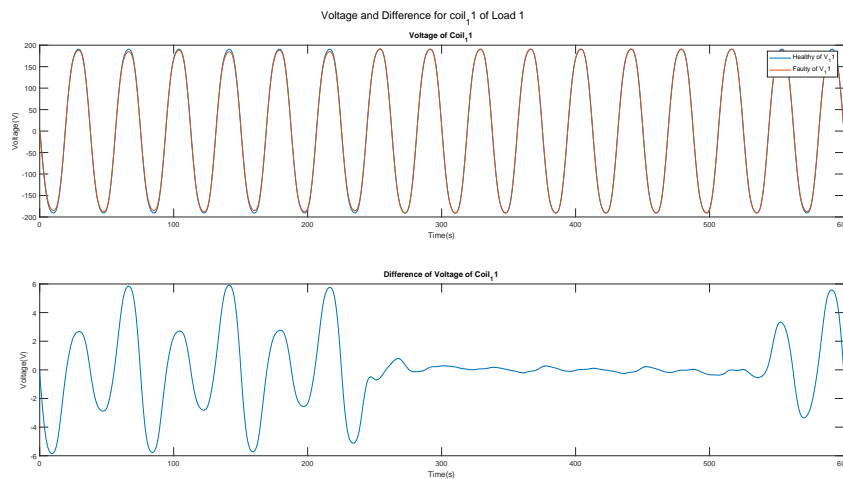


Figure 4.49: Thesis results for: Voltage and Difference for $Coil_{11}$ of Phase 1 (Case Demag 25 50 13.125)

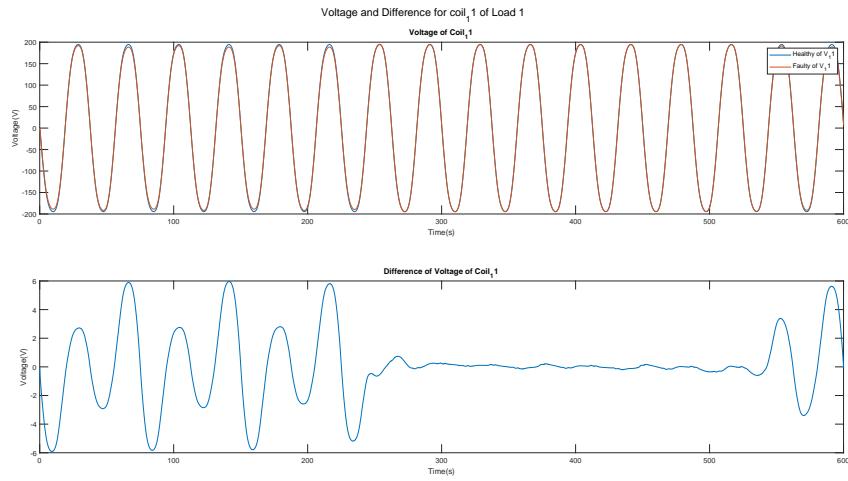


Figure 4.50: Thesis results for: Voltage and Difference for $Coil_{11}$ of Phase 1 (Case Demag 25 50 17.5)

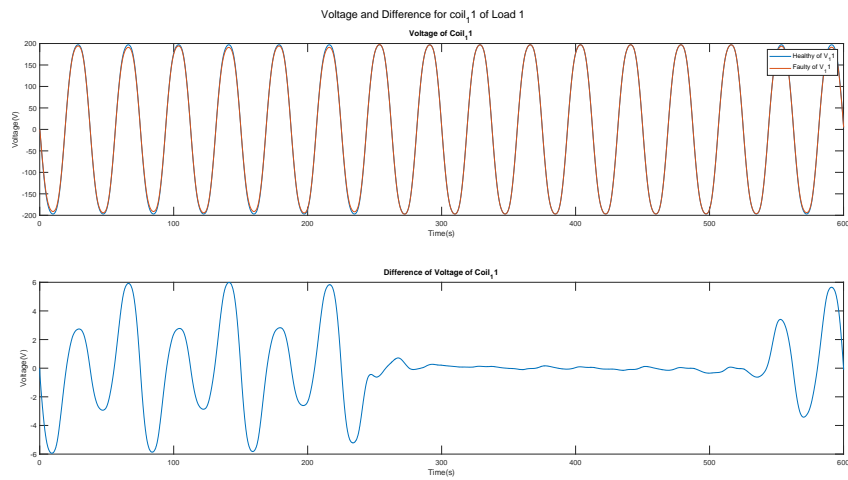


Figure 4.51: Thesis results for: Voltage and Difference for $Coil_{11}$ of Phase 1 (Case Demag 25 50 21.875)

Fourier for Currents of 4 Coils of Phase 1

By subjecting the signals from the four coils to Fast Fourier Transform (FFT), a marked increase in amplitude is discerned across nearly all frequencies in the presence of demagnetization. This conspicuous rise stands out as a reliable indicator of demagnetization phenomena, qualitatively aligning with the observations made in the case of 25% demagnetization as portrayed in Figures (4.52, 4.53 and 4.54). However, the pragmatic challenge of measuring individual coil currents in practical scenarios limits the direct application of this method.

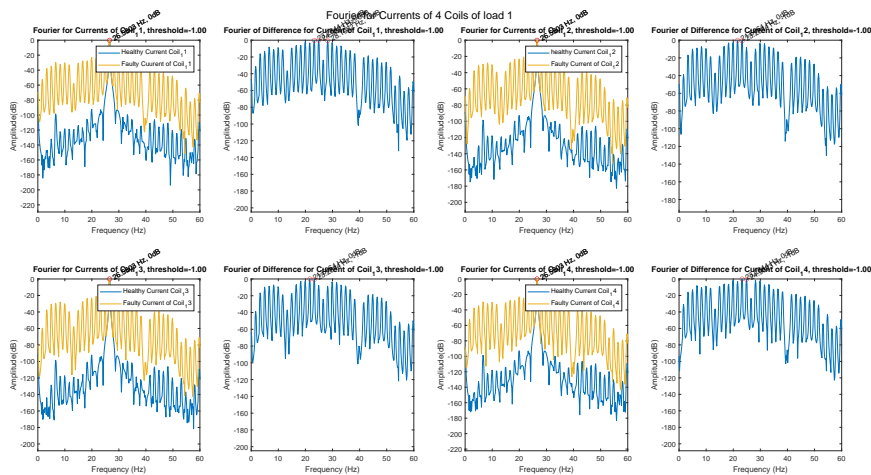


Figure 4.52: Thesis results for: Fourier for Currents of 4 Coils of Phase 1 (Case Demag 25 50 13.125)

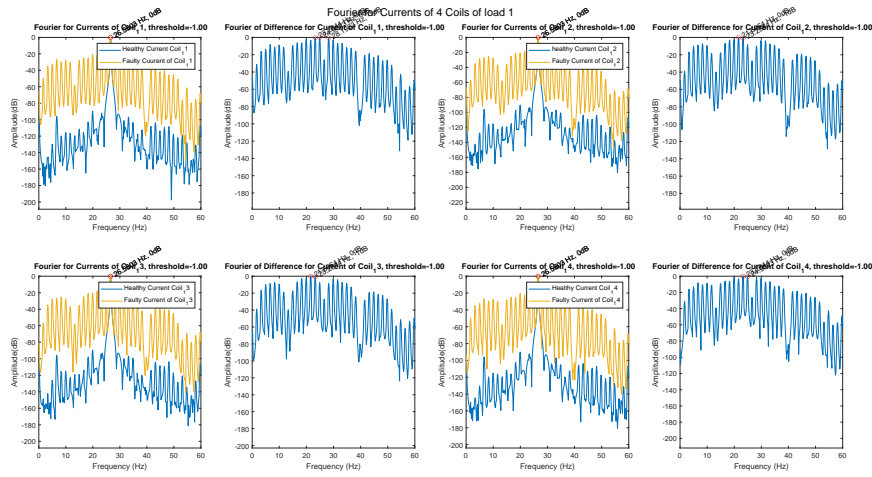


Figure 4.53: Thesis results for: Fourier for Currents of 4 Coils of Phase 1 (Case Demag 25 50 17.5)

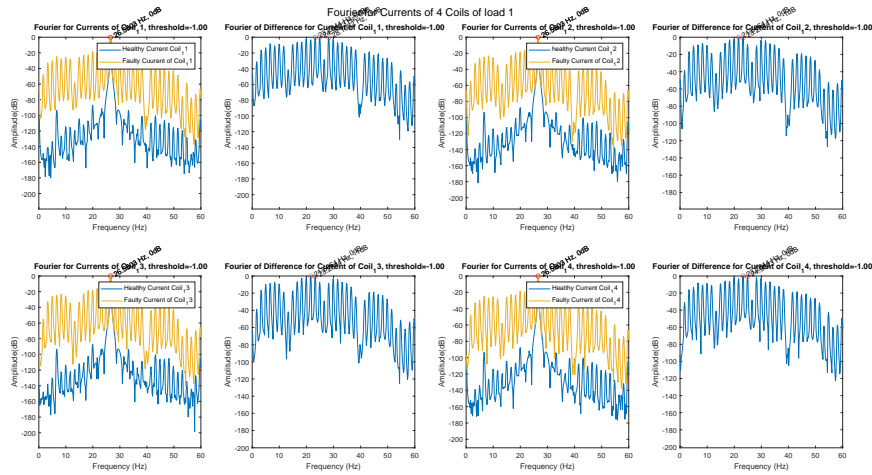


Figure 4.54: Thesis results for: Fourier for Currents of 4 Coils of Phase 1 (Case Demag 25 50 21.875)

4.1.4 Demagnetization 25% Both

Current and Difference for Load 1

Analysis of the data reveals consistent patterns as described in case of 25% demagnetization as portrayed in Figures (4.55, 4.56 and 4.57), consistent characteristics and comparable attributes across various measurements. The observed similarities are grounded in rigorous scientific principles, including the repeatability of results, statistical analyses indicating non-significant differences and the presence of shared qualitative features. In the time domain, the disparity between the healthy and faulty cases is marginal. Due to the similarity in the values of both signals, a substantial difference is not observed. Additionally, since the values of both signals are comparable, the patterns remain consistent across different load conditions.

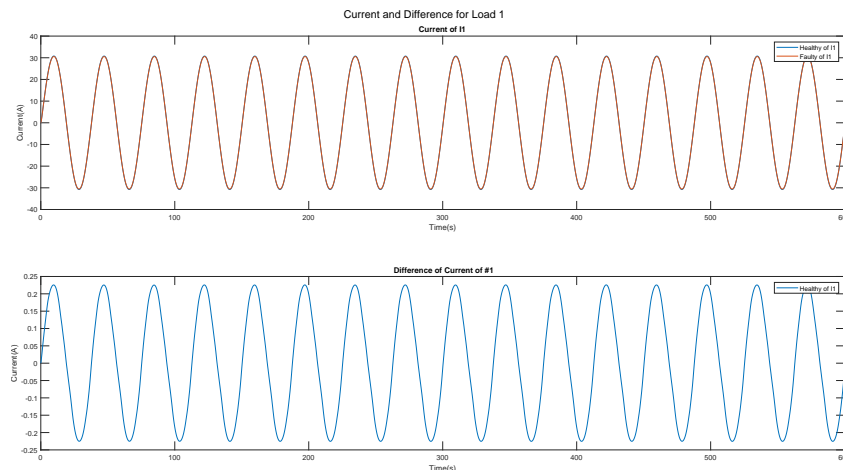


Figure 4.55: Thesis results for: Current and Difference for Load 1 (Case Demag 25 Both 13.125)

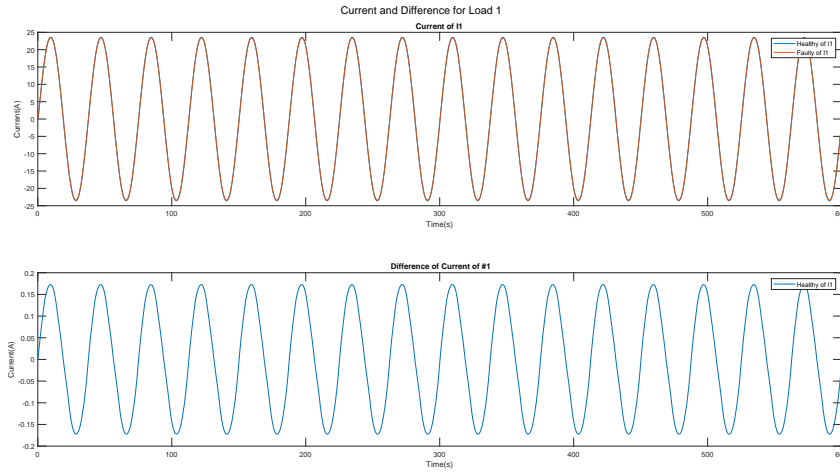


Figure 4.56: Thesis results for: Current and Difference for Load 1 (Case Demag 25 Both 17.5)

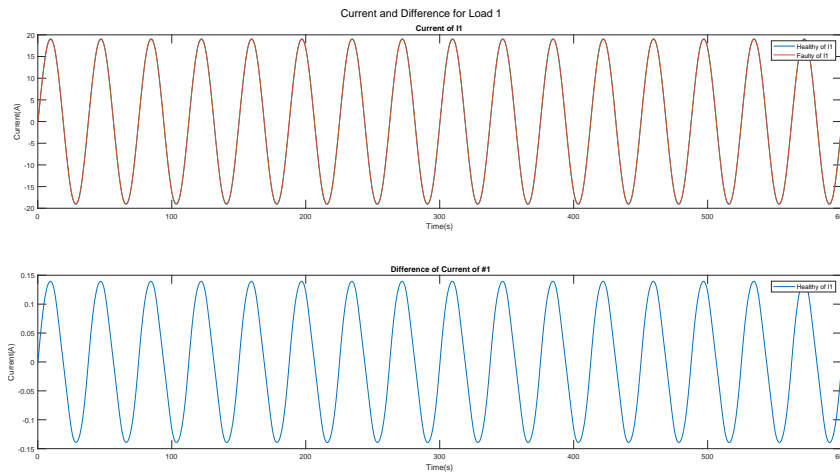


Figure 4.57: Thesis results for: Current and Difference for Load 1 (Case Demag 25 Both 21.875)

Currents for 4 Coils of Phase 1

Qualitatively, the theory is consistently applied across this case as explained in case of 25% demagnetization as portrayed in Figures (4.58, 4.59 and 4.60), explaining the distinct manifestations of demagnetization within the coils of the machine. The observable outcome involves the demagnetization of the magnet, leading to a diminished magnetic field in contrast to its healthy state. This demagnetization induces a reduction in inductance, subsequently causing a decline in the induced electromotive force (EMF) as per Faraday's law.

Despite variations in individual electromotive forces across the four coils in the parallel circuit due to demagnetization, the overall voltage exhibits remarkable stability. This stability is managed through dynamic adjustments in the currents of each coil, ensuring the voltage stability. Consequently, despite distinct currents in each of the four coils due to variations in electromotive forces caused by demagnetization, the voltage across the parallel circuit remains almost identical to its healthy state.

Difference of Currents for 4 coils

Intriguing temporal patterns surface in the time domain when contrasting healthy and faulty scenarios, uncovering substantial disparities at specific temporal intervals. Interestingly, these variations might be undetected with direct observation of the load. The thermal consequences within the generator assume paramount importance, given the considerable differences observed, indicating significant thermal strain on the generator. It is essential to highlight that this is qualitatively the same theory as explained for the case of 25% demagnetization as portrayed in Figures (4.61, 4.62 and 4.63).

Additionally, the discrete currents flowing through each coil, arising from demagnetization-induced distinctions in electromotive forces, contribute to varied thermal stresses. Despite these variations, the system adapts the currents to sustain a steadfast voltage output.

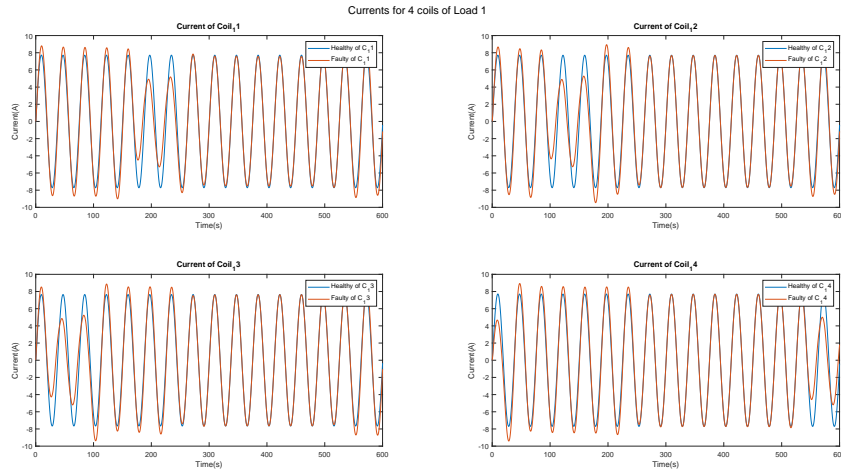


Figure 4.58: Thesis results for: Currents for 4 Coils of Phase 1 (Case Demag 25 Both 13.125)

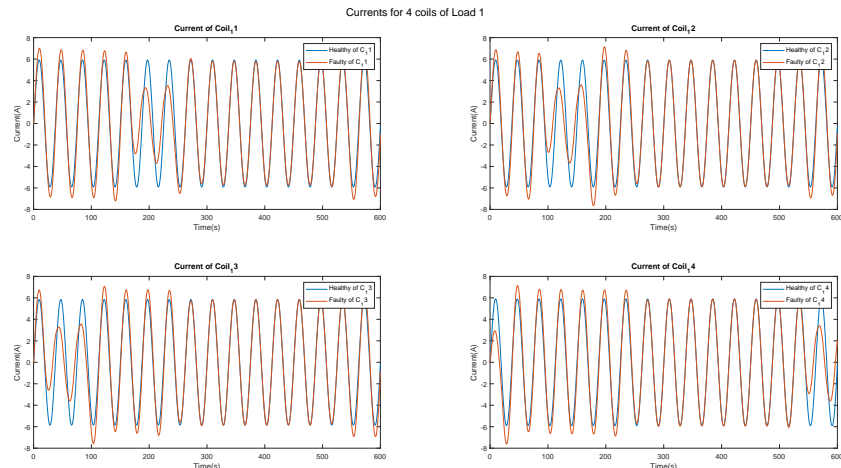


Figure 4.59: Thesis results for: Currents for 4 Coils of Phase 1 (Case Demag 25 Both 17.5)

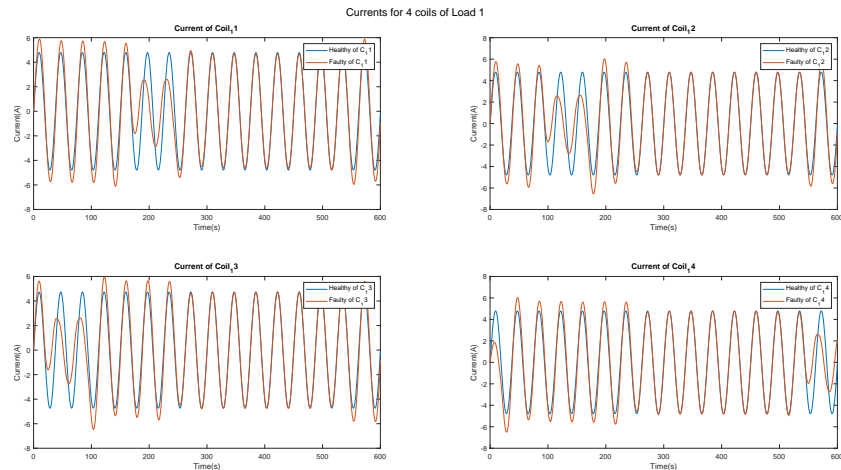


Figure 4.60: Thesis results for: Currents for 4 Coils of Phase 1 (Case Demag 25 Both 21.875)

Fourier and Differences in Current of Load Between Healthy and Faulty Cases

In the realm of Motor Current Signature Analysis (MCSA), demagnetization signatures are pursued through a meticulous examination of the left sideband of frequencies. A peculiar observation surfaces in the $2f_s$ harmonic, where faulty cases exhibit an unexpected surge in amplitude, challenging the expected cancellation phenomenon. Differences between simulations and experimental results, particularly in the second harmonic, give rise to valid concerns. Typically associated with asymmetry in healthy conditions, the reliability of the second harmonic comes under scrutiny due to real-world variations, such as slight resistance errors.

Recognizing the complexities linked with fault indications in the second harmonic, primarily associated with stator faults in healthy conditions, adds complexity to the current scenario involving a rotor fault. Combined

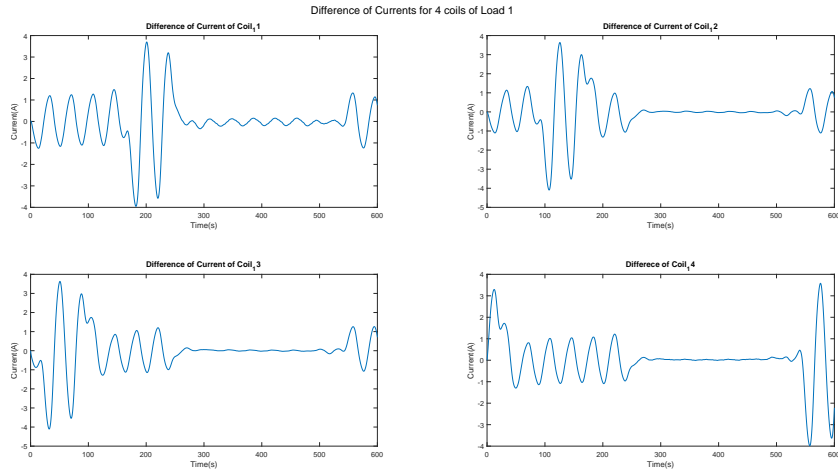


Figure 4.61: Thesis results for: Difference of Currents for 4 coils of Phase 1 (Case Demag 25 Both 13.125)

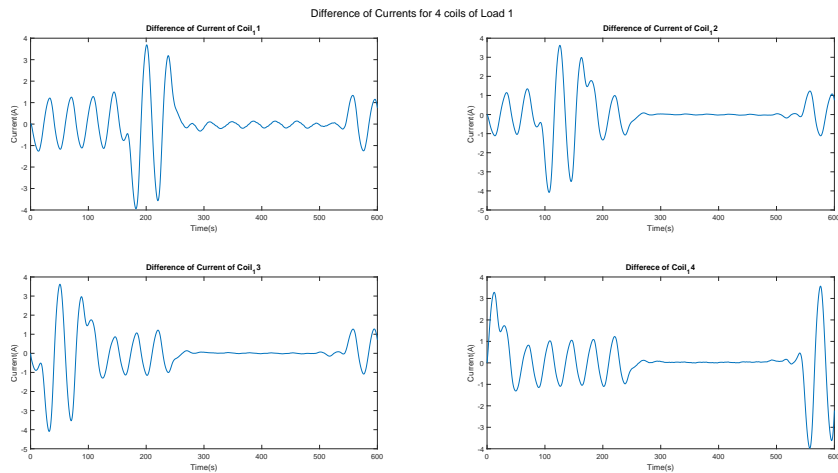


Figure 4.62: Thesis results for: Difference of Currents for 4 coils of Phase 1 (Case Demag 25 Both 17.5)

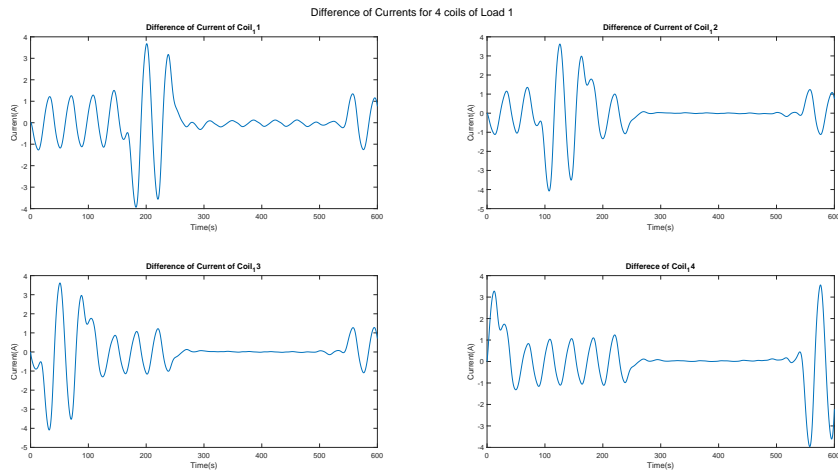


Figure 4.63: Thesis results for: Difference of Currents for 4 coils of Phase 1 (Case Demag 25 Both 21.875)

with the potential cancellation of the left sideband $\frac{f_s}{2}$ due to the demagnetization of non-adjacent magnets, interpreting diagnostic indicators becomes difficult. Overlooking these difficulties poses a substantial risk of misdiagnosing the machine, emphasizing the crucial role of incorporating experimental results for precise fault diagnosis. The cancellation phenomenon, prominently observed in the demagnetization of two non-adjacent magnets, further underscores the multifaceted nature of fault analysis.

A detailed Fourier analysis at $\frac{f_s}{2}$ in the left sideband consistently reveals escalating amplitudes in most demagnetization cases, providing valuable diagnostic insights. Particularly noteworthy is the cancellation phenomenon in the left sideband $\frac{f_s}{2}$ when demagnetization affects two non-adjacent magnets at 25% or 50% as explained in Chapter 2 and depicted below in Figures (4.64, 4.65 and 4.66). Also, the same cancellation phenomenon is depicted in Figures (4.82, 4.83 and 4.84).

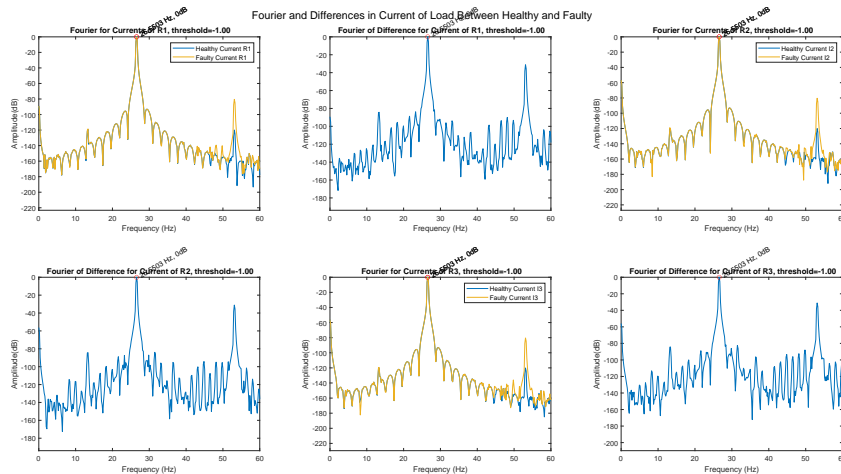


Figure 4.64: Thesis results for: Fourier and Differences in Current of Load Between Healthy and Faulty (Case Demag 25 Both 13.125)

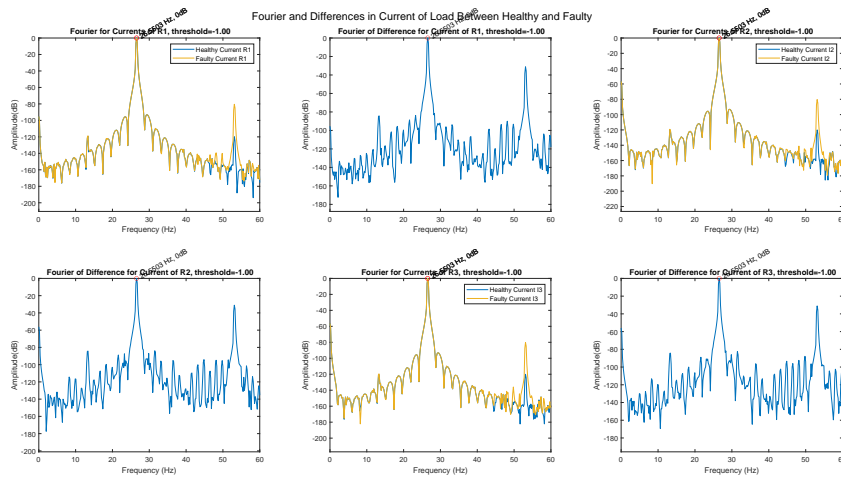


Figure 4.65: Thesis results for: Fourier and Differences in Current of Load Between Healthy and Faulty (Case Demag 25 Both 17.5)

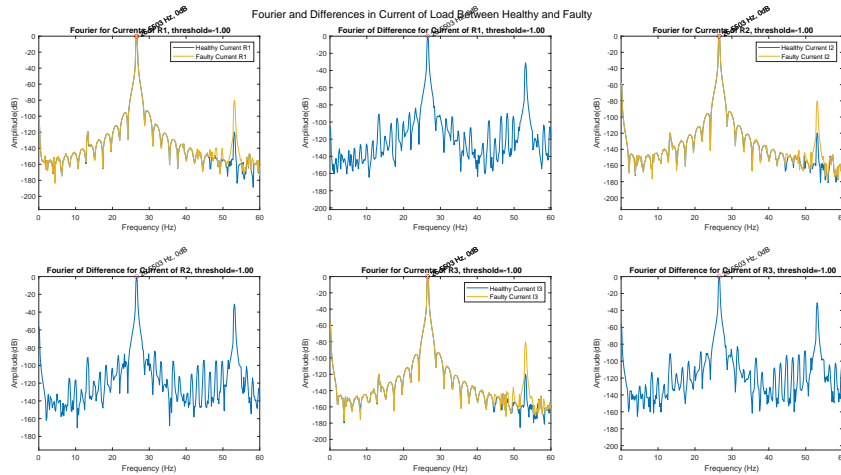


Figure 4.66: Thesis results for: Fourier and Differences in Current of Load Between Healthy and Faulty (Case Demag 25 Both 21.875)

Voltage and Difference for $Coil_{11}$ of Phase 1

Upon closer examination of the coil currents as discussed earlier, it becomes apparent that the voltage maintains a nearly constant level, experiencing only a marginal decrease, as depicted in the illustration below. The minimal difference, less than 1.5%, between the two signals raises concerns regarding its reliability as a fault indicator. In response to this, it becomes essential to explore supplementary diagnostic techniques, such as frequency domain analyses, to obtain more dependable insights into potential demagnetization faults.



Importantly, this qualitative observation aligns with the theory explained for the case of 25% demagnetization, as depicted in Figures (4.67, 4.68 and 4.69). Moreover, the time domain results for identical demagnetization under three different loads reveal a consistency that remains unaffected by significant variation, emphasizing the robustness of the diagnostic approach.

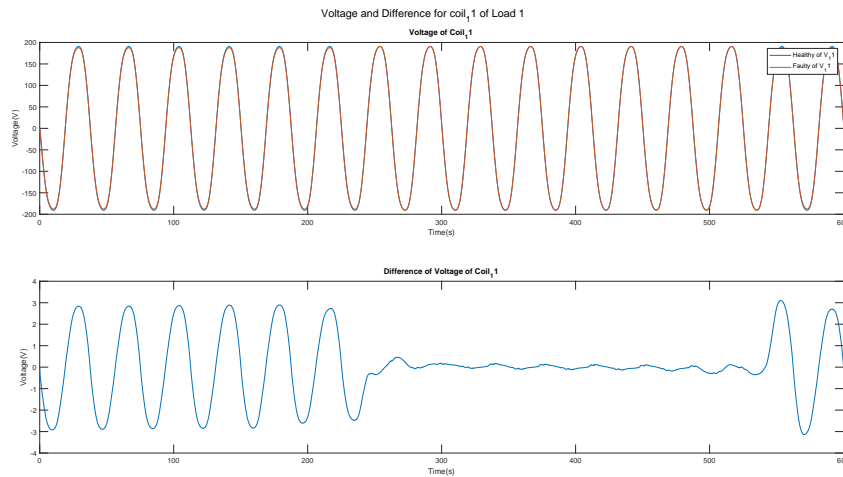


Figure 4.67: Thesis results for: Voltage and Difference for $Coil_{11}$ of Phase 1 (Case Demag 25 Both 13.125)

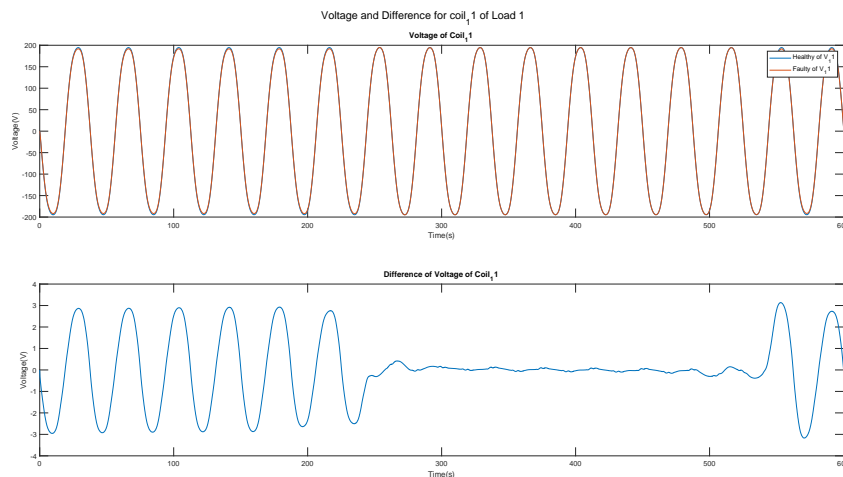


Figure 4.68: Thesis results for: Voltage and Difference for $Coil_{11}$ of Phase 1 (Case Demag 25 Both 17.5)

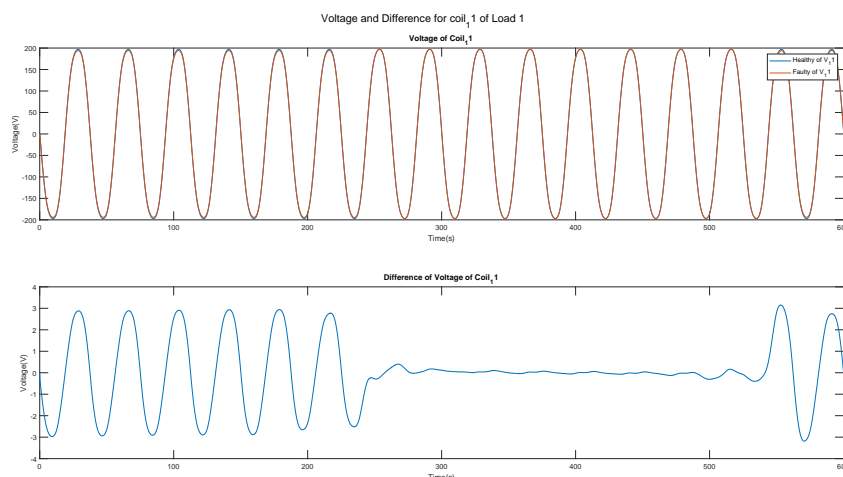


Figure 4.69: Thesis results for: Voltage and Difference for $Coil_{11}$ of Phase 1 (Case Demag 25 Both 21.875)

Fourier for Currents of 4 Coils of Phase 1

The application of Fast Fourier Transform (FFT) to the signals from the four coils uncovers a noteworthy surge in amplitude across almost every frequency when demagnetization occurs. This distinctive escalation

serves as a clear and dependable indication of the demagnetization phenomenon, aligning with the qualitative observations made in the case of 25% demagnetization as illustrated in Figures (4.70, 4.71 and 4.72). Yet, the practical difficulty of measuring the current in each coil under real-world conditions poses a constraint on the direct utility of this method.

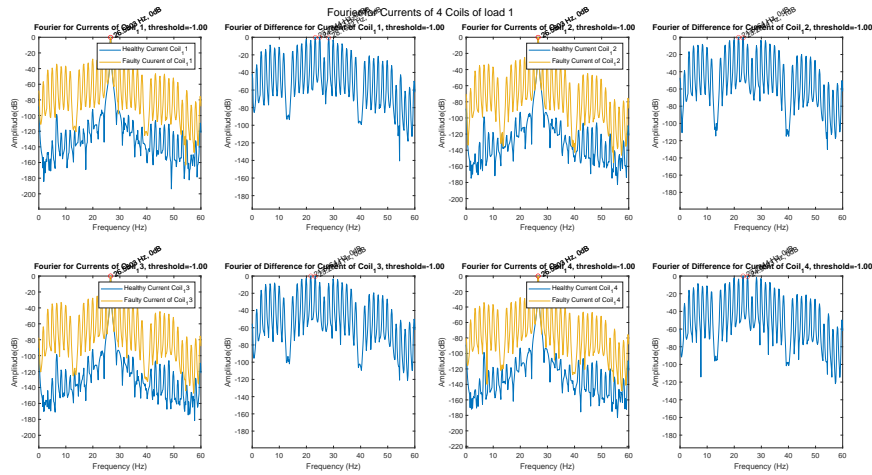


Figure 4.70: Thesis results for: Fourier for Currents of 4 Coils of Phase 1 (Case Demag 25 Both 13.125)

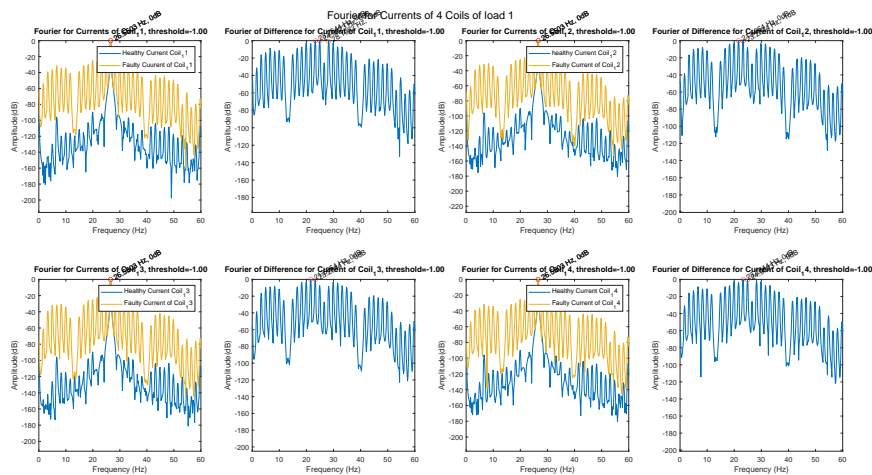


Figure 4.71: Thesis results for: Fourier for Currents of 4 Coils of Phase 1 (Case Demag 25 Both 17.5)

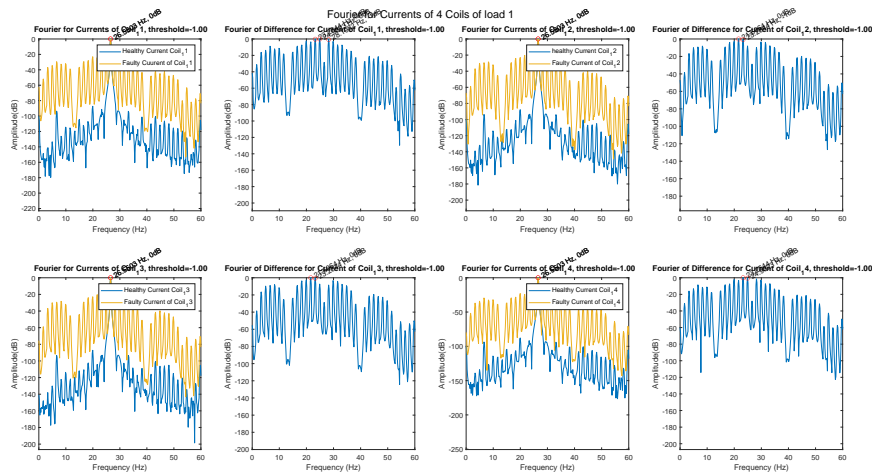


Figure 4.72: Thesis results for: Fourier for Currents of 4 Coils of Phase 1 (Case Demag 25 Both 21.875)



4.1.5 Demagnetization 50% Both

Current and Difference for Load 1

Analysis of the data reveals consistent patterns as described in case of 25% demagnetization as depicted in Figures (4.73, 4.74 and 4.75), consistent characteristics and comparable attributes across various measurements. The observed similarities are grounded in rigorous scientific principles, including the repeatability of results, statistical analyses indicating non-significant differences and the presence of shared qualitative features. In the time domain, the disparity between the healthy and faulty cases is marginal. Due to the similarity in the values of both signals, a substantial difference is not observed. Additionally, since the values of both signals are comparable, the patterns remain consistent across different load conditions.

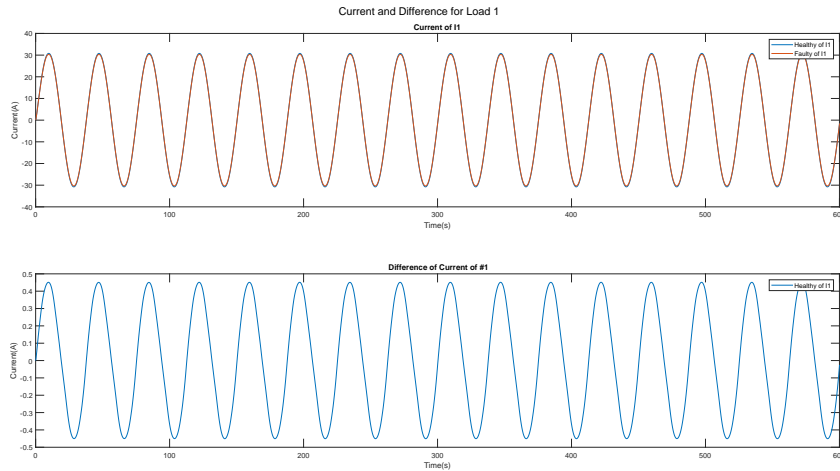


Figure 4.73: Thesis results for: Current and Difference for Load 1 (Case Demag 50 Both 13.125)

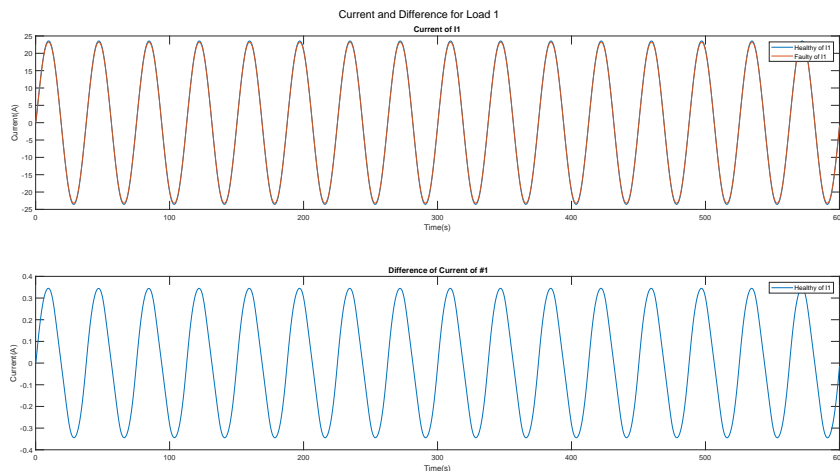


Figure 4.74: Thesis results for: Current and Difference for Load 1 (Case Demag 50 Both 17.5)

Currents for 4 Coils of Phase 1

Qualitatively, the theory is consistently applied across this case as explained in case of 25% demagnetization as depicted in Figures (4.76, 4.77 and 4.78). There is an observable impact of demagnetization in the coils of the machine. The phenomenon is characterized by the demagnetization of the magnet, resulting in a weakened magnetic field compared to its healthy state. This demagnetization initiates a decrease in inductance, leading to a subsequent reduction in the induced electromotive force (EMF) in accordance with Faraday's law.

Despite fluctuations in individual electromotive forces across the four coils in the parallel circuit due to demagnetization, the overall voltage maintains a distinct stability. This stability is achieved through dynamic adjustments in the currents of each coil, ensuring voltage stability. Thus, while each of the four coils exhibits varying currents due to diverse electromotive forces caused by demagnetization, the voltage across the parallel circuit remains nearly identical to its healthy state.

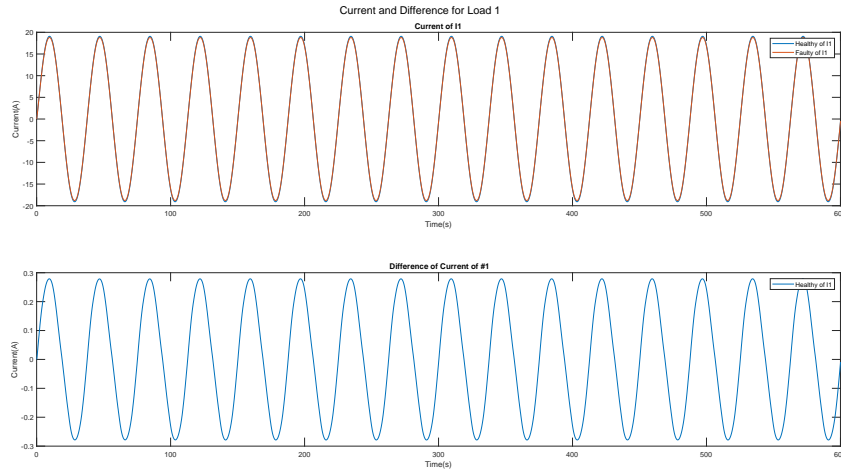


Figure 4.75: Thesis results for: Current and Difference for Load 1 (Case Demag 50 Both 21.875)

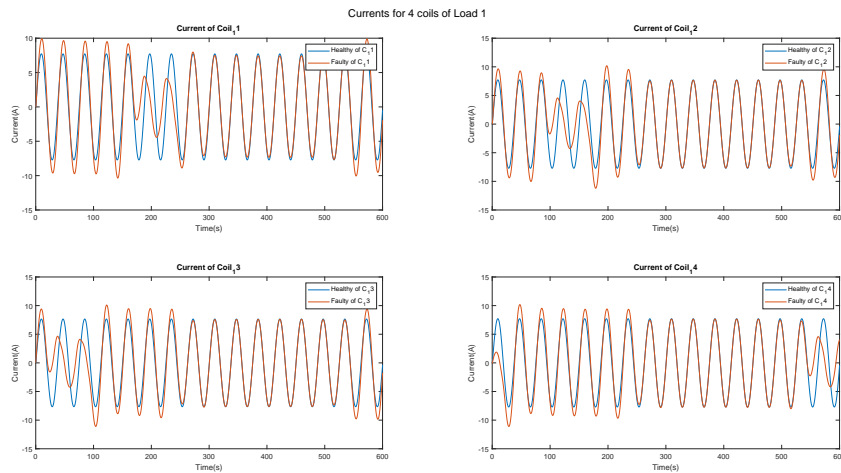


Figure 4.76: Thesis results for: Currents for 4 Coils of Phase 1 (Case Demag 50 Both 13.125)

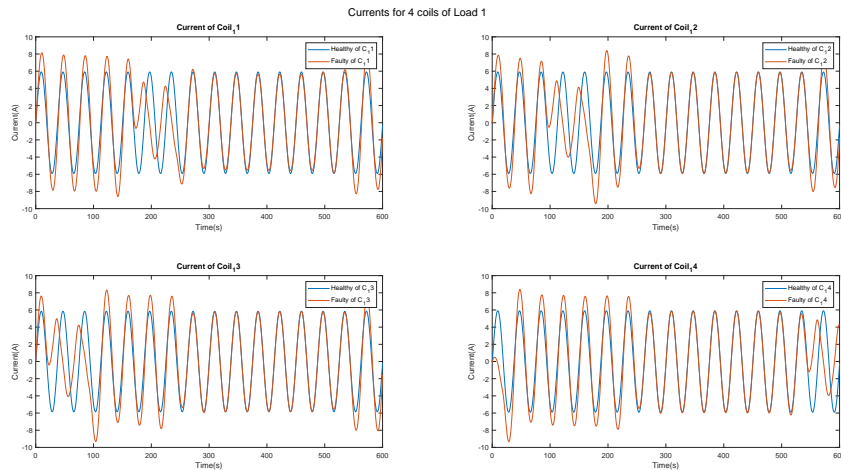


Figure 4.77: Thesis results for: Currents for 4 Coils of Phase 1 (Case Demag 50 Both 17.5)

Difference of Currents for 4 coils

Compelling patterns materialize in the time domain when juxtaposing healthy and faulty scenarios, divulging noteworthy deviations at specific time intervals. Strikingly, these variations may evade direct observation of the load. The thermal consequences within the generator assume critical significance, given the marked differences observed, signifying considerable thermal stress on the generator. It is crucial to note that this is qualitatively the same theory as explained for the case of 25% demagnetization as depicted in Figures (4.79, 4.80 and 4.81).

Moreover, the distinct currents traversing each coil, coming from demagnetization-induced variations in electromotive forces, contribute to diverse thermal stresses. Despite these differences, the system adeptly adjusts the currents to maintain a consistent voltage output.

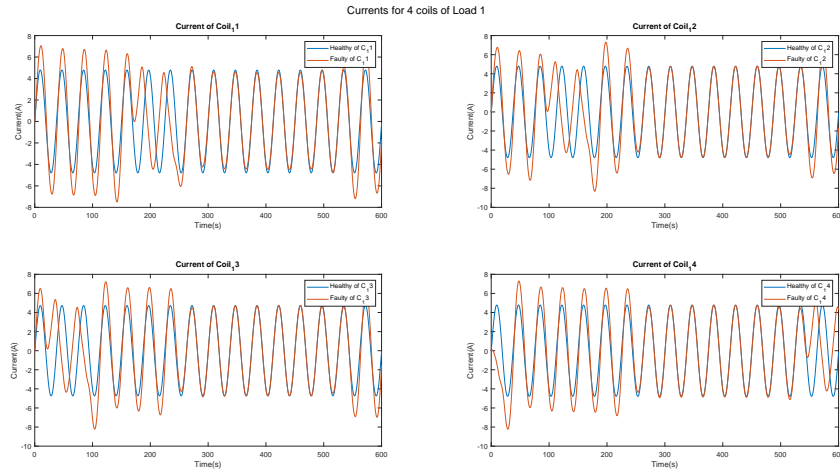


Figure 4.78: Thesis results for: Currents for 4 Coils of Phase 1 (Case Demag 50 Both 21.875)

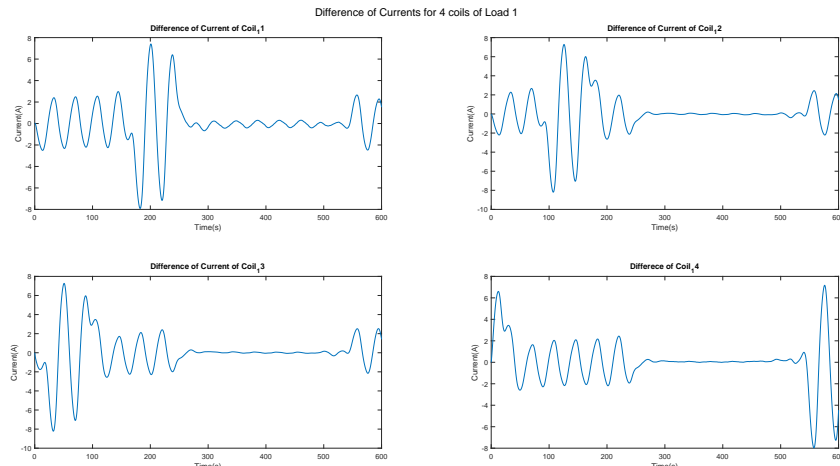


Figure 4.79: Thesis results for: Difference of Currents for 4 coils of Phase 1 (Case Demag 50 Both 13.125)

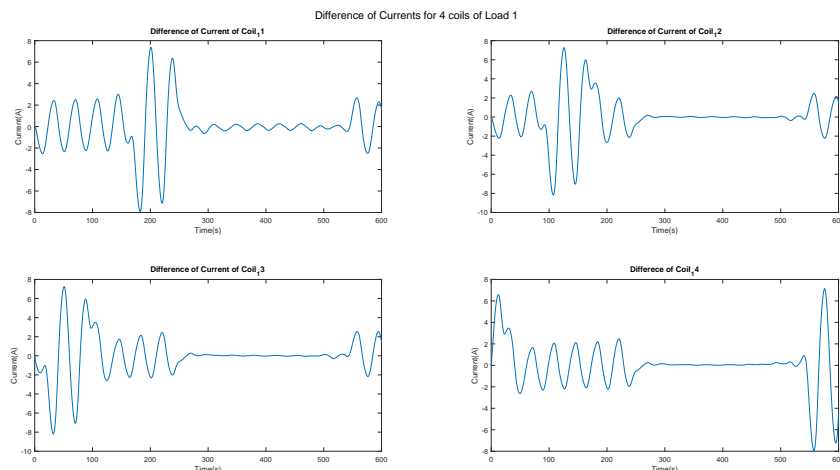


Figure 4.80: Thesis results for: Difference of Currents for 4 coils of Phase 1 (Case Demag 50 Both 17.5)

Fourier and Differences in Current of Load Between Healthy and Faulty Cases

Delving into the domain of Motor Current Signature Analysis (MCSA), the quest for demagnetization signatures involves a meticulous examination of the left sideband of frequencies. An intriguing observation materializes in the $2f_s$ harmonic, where faulty cases exhibit an unexpected surge in amplitude, challenging the anticipated cancellation phenomenon. Disparities between simulations and experimental results, particularly in the second harmonic, prompt valid concerns. Typically associated with asymmetry in healthy conditions, the reliability of the second harmonic comes under scrutiny due to real-world variations, such as slight resistance errors.

Acknowledging the complexities linked with fault indications in the second harmonic, primarily associated

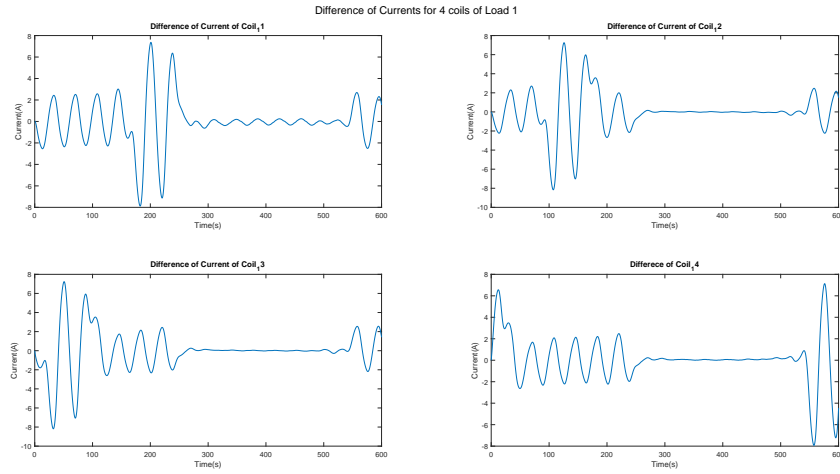


Figure 4.81: Thesis results for: Difference of Currents for 4 coils of Phase 1 (Case Demag 50 Both 21.875)

with stator faults in healthy conditions, adds complexity to the present scenario involving a rotor fault. Combined with the potential cancellation of the left sideband $\frac{f_s}{2}$ due to the demagnetization of non-adjacent magnets, interpreting diagnostic indicators becomes difficult. Overlooking these complexities poses a substantial risk of misdiagnosing the machine, emphasizing the crucial role of incorporating experimental results for precise fault diagnosis. The cancellation phenomenon, prominently observed in the demagnetization of two non-adjacent magnets, further underscores the multifaceted nature of fault analysis.

A detailed Fourier analysis at $\frac{f_s}{2}$ in the left sideband consistently reveals escalating amplitudes in most demagnetization cases, providing valuable diagnostic insights. Particularly noteworthy is the cancellation phenomenon in the left sideband $\frac{f_s}{2}$ when demagnetization affects two non-adjacent magnets at 25% or 50%, as explained in Chapter 2 and depicted below in Figures (4.82, 4.83 and 4.84). Also the same cancellation phenomenon is depicted above in Figures (4.64, 4.65 and 4.66).

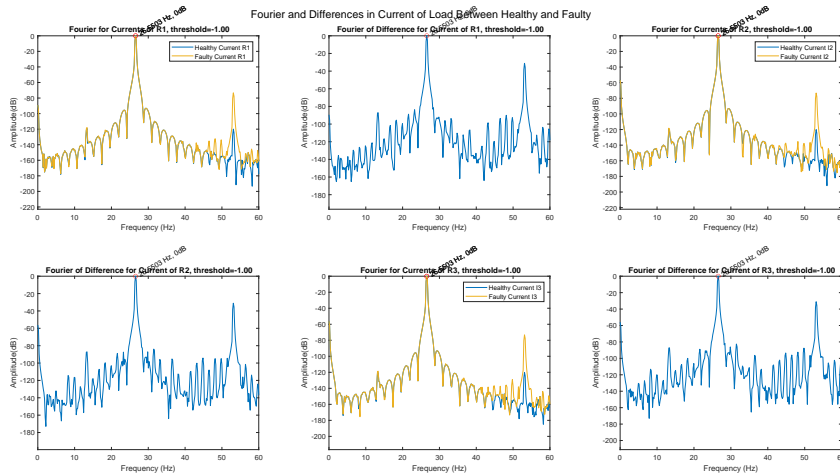


Figure 4.82: Thesis results for: Fourier and Differences in Current of Load Between Healthy and Faulty (Case Demag 50 Both 13.125)

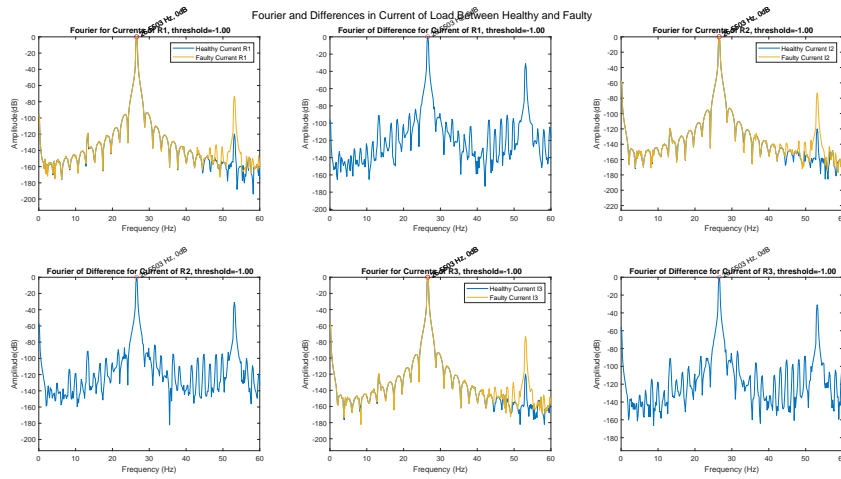


Figure 4.83: Thesis results for: Fourier and Differences in Current of Load Between Healthy and Faulty (Case Demag 50 Both 17.5)

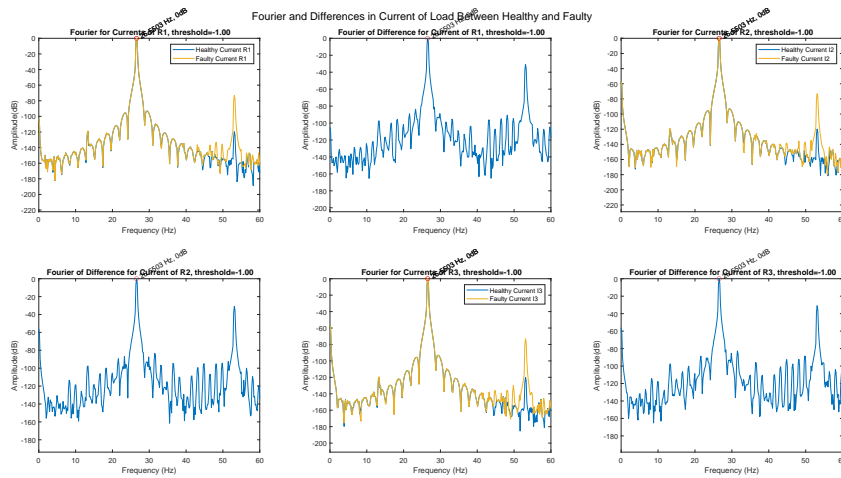


Figure 4.84: Thesis results for: Fourier and Differences in Current of Load Between Healthy and Faulty (Case Demag 50 Both 21.875)

Voltage and Difference for $Coil_{11}$ of Phase 1

Upon analyzing the coil currents as discussed earlier, a crucial observation emerges – the voltage remains remarkably constant, exhibiting only a slight decrease, as illustrated below. The marginal difference, measuring less than 1.5%, between the two signals raises skepticism about its reliability as a fault indicator. Considering this, it becomes imperative to explore additional diagnostic techniques, such as frequency domain analyses, for more robust insights into potential demagnetization faults. Importantly, this qualitative observation aligns with the theory explained for the case of 25% demagnetization, as depicted in Figures (4.85, 4.86 and 4.87). Additionally, the time domain results for identical demagnetization under three different loads showcase a consistency that defies significant variation, underscoring the diagnostic approach’s resilience across diverse operational conditions.

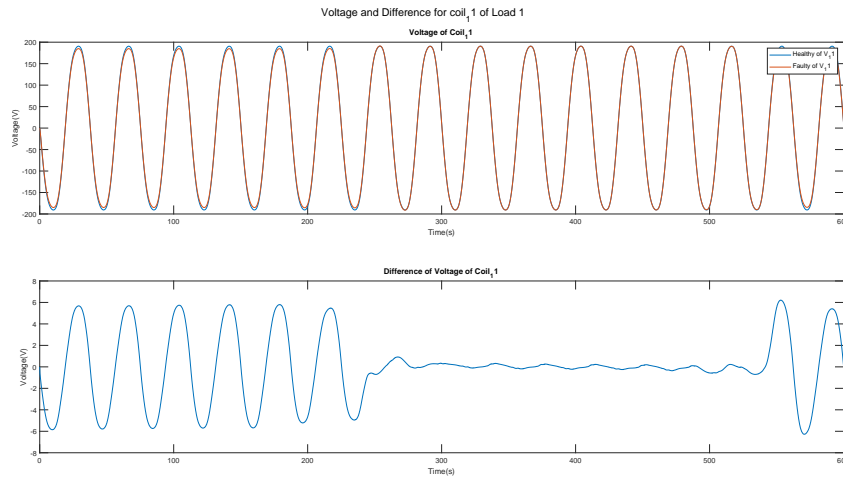


Figure 4.85: Thesis results for: Voltage and Difference for $Coil_{11}$ of Phase 1 (Case Demag 50 Both 13.125)

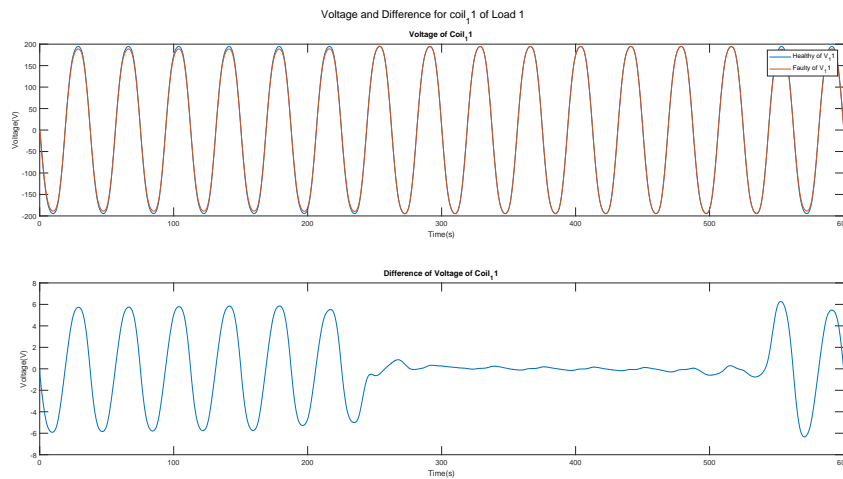


Figure 4.86: Thesis results for: Voltage and Difference for $Coil_{11}$ of Phase 1 (Case Demag 50 Both 17.5)

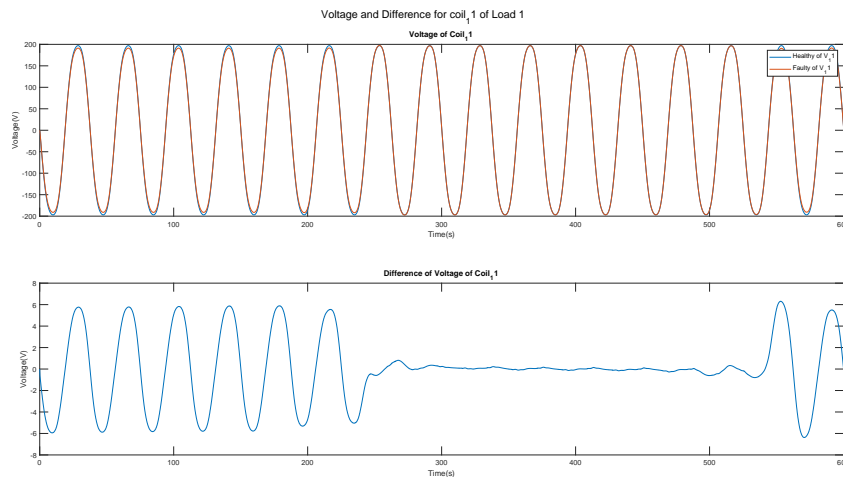


Figure 4.87: Thesis results for: Voltage and Difference for $Coil_{11}$ of Phase 1 (Case Demag 50 Both 21.875)

Fourier for Currents of 4 Coils of Phase 1

Utilizing Fast Fourier Transform (FFT) on signals from the four coils brings to light a significant amplification in amplitude across almost every frequency during demagnetization. This prominent elevation serves as a clear and trustworthy sign of the demagnetization phenomenon, in line with the qualitative findings observed in the case of 25% demagnetization as demonstrated in Figures (4.88, 4.89 and 4.90). Nevertheless, the practical complexity of measuring the current in each coil within real-world contexts imposes constraints on the direct implementation of this method.

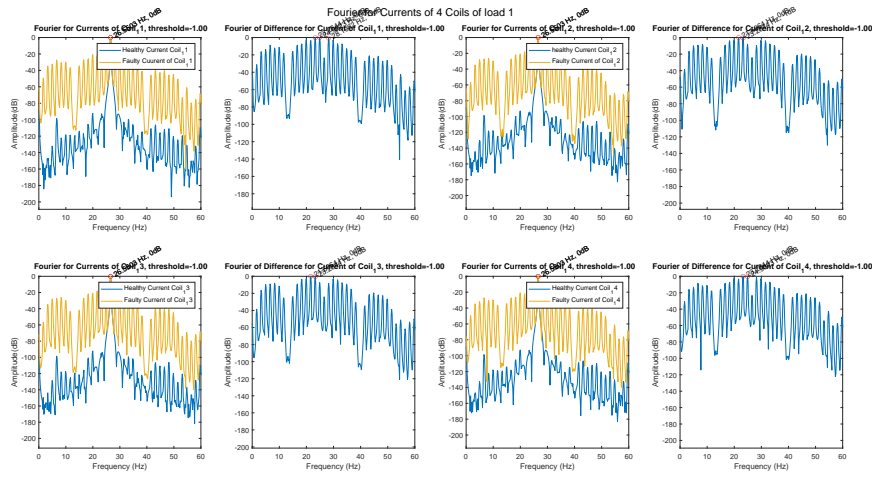


Figure 4.88: Thesis results for: Fourier for Currents of 4 Coils of Phase 1 (Case Demag 50 Both 13.125)

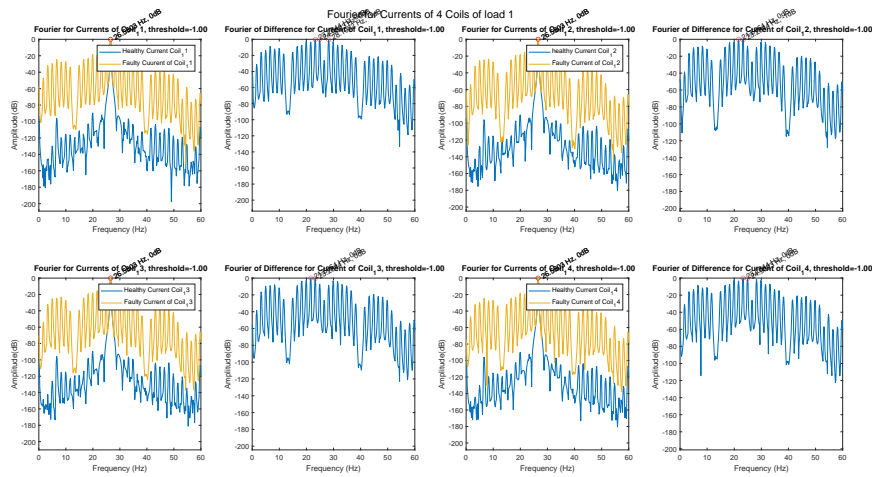


Figure 4.89: Thesis results for: Fourier for Currents of 4 Coils of Phase 1 (Case Demag 50 Both 17.5)

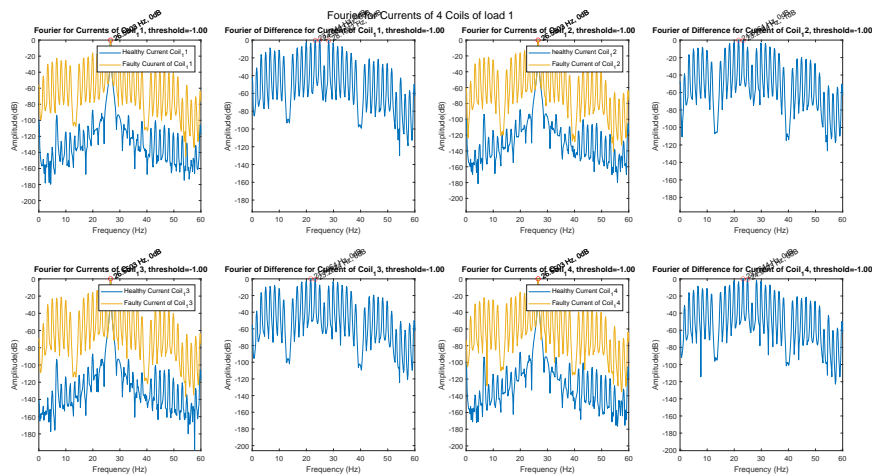


Figure 4.90: Thesis results for: Fourier for Currents of 4 Coils of Phase 1 (Case Demag 50 Both 21.875)

4.2 Torque Monitoring All Cases

4.2.1 Demagnetization 25%

Torque and Difference of Torque

In the time domain analysis, the difference between healthy and faulty cases is minimal and the patterns remain consistent across various loads, as depicted in Figures (4.91, 4.92 and 4.93). The most notable distinction with varying loads is the direct correlation between decreasing ohmic load and an increase in current, resulting in higher power and, consequently, greater torque. This observation underscores the importance of load conditions in understanding the operational characteristics and performance of the system.

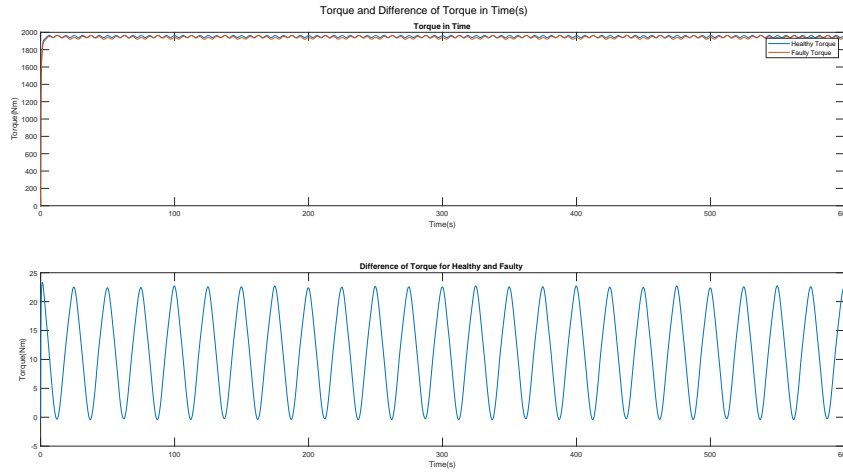


Figure 4.91: Thesis results for: Torque and Difference in Time(s) (Case Demag 25 13.125)

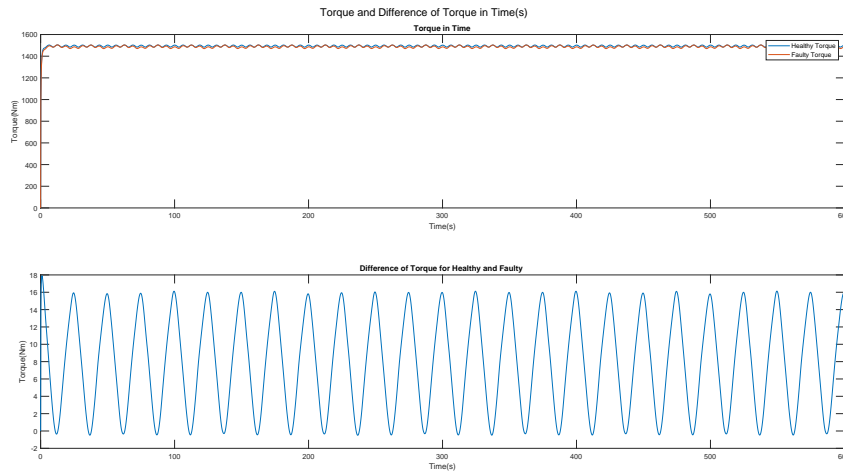


Figure 4.92: Thesis results for: Torque and Difference in Time(s) (Case Demag 25 17.5)

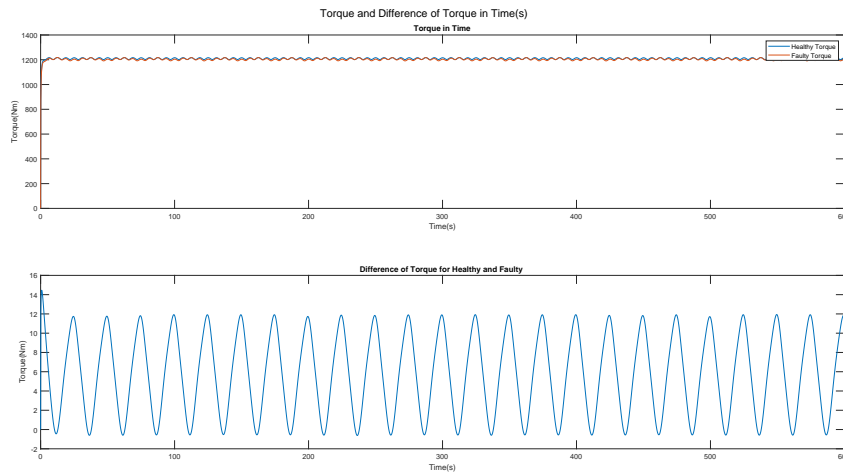


Figure 4.93: Thesis results for: Torque and Difference in Time(s) (Case Demag 25 21.875)

Fourier and Difference of Torque

As we operate in a steady state and torque behaves akin to a DC signal, it was anticipated that the highest value would occur at 0 Hz as depicted in Figures (4.94, 4.95 and 4.96). Notably, at $k=8$, corresponding to the formula $f = fs(1 + \frac{k}{p})$, there is a substantial increase in amplitude and a pronounced difference between the healthy and faulty cases. Additionally, a significant amplitude rise is observed in the 6th harmonic.

It's essential to recognize that this phenomenon is inherent and doesn't result from a fault but rather from the interaction between the 5th and 1st harmonic of the stator and rotor. The observable difference in the third harmonic, escalating at $3f_s$, is evident in the Fast Fourier Transform (FFT) analysis used to compare healthy



and faulty cases.

Understanding these harmonic interactions and variations is vital for accurate fault diagnosis and interpretation of spectral analyses in the context of steady-state operations.

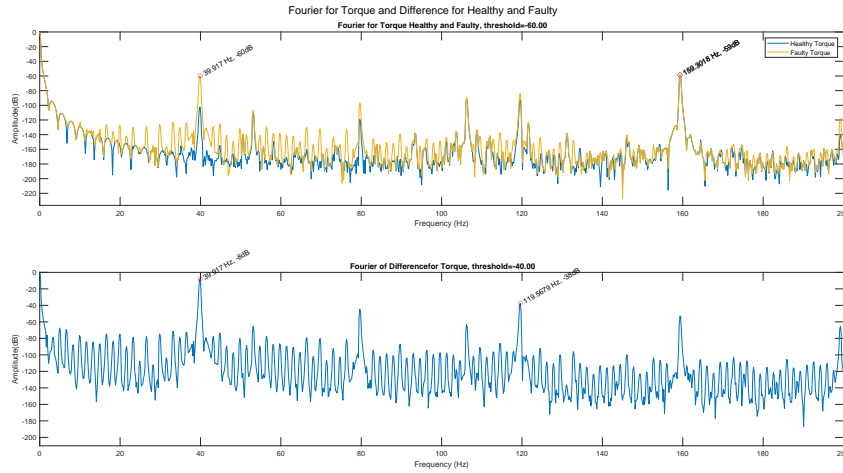


Figure 4.94: Thesis results for: Fourier and Difference of Torque (Case Demag 25 13.125)

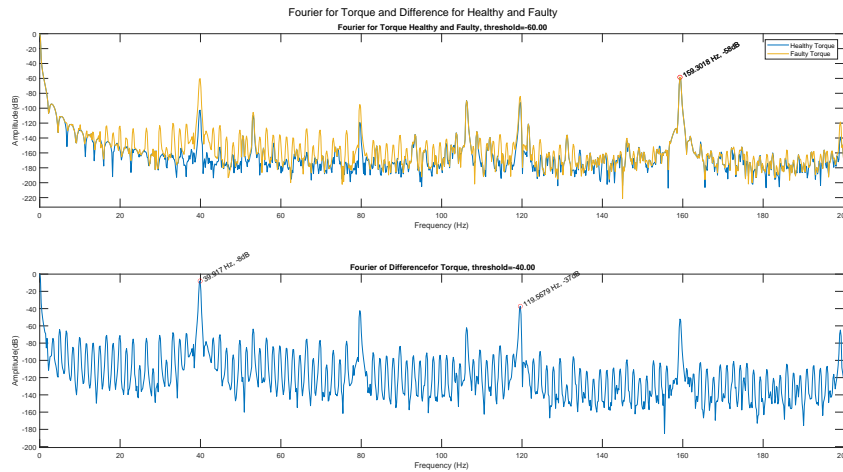


Figure 4.95: Thesis results for: Fourier and Difference of Torque (Case Demag 25 17.5)

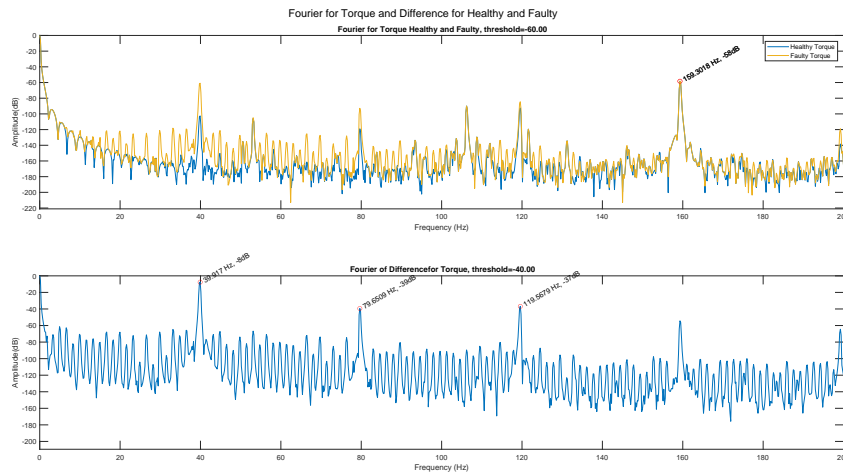


Figure 4.96: Thesis results for: Fourier and Difference of Torque (Case Demag 25 21.875)



4.2.2 Demagnetization 50%

Torque and Difference of Torque

The temporal examination of healthy and faulty cases reveals negligible differences in the time domain analysis, with consistent patterns persisting across different loads. Interestingly, the most discernible variation occurs in the relationship between decreasing ohmic load and an augmented current, leading to elevated power and subsequent torque. It is important to note that this observation aligns qualitatively with the case of 25% demagnetization, as demonstrated in Figures (4.97, 4.98 and 4.99).

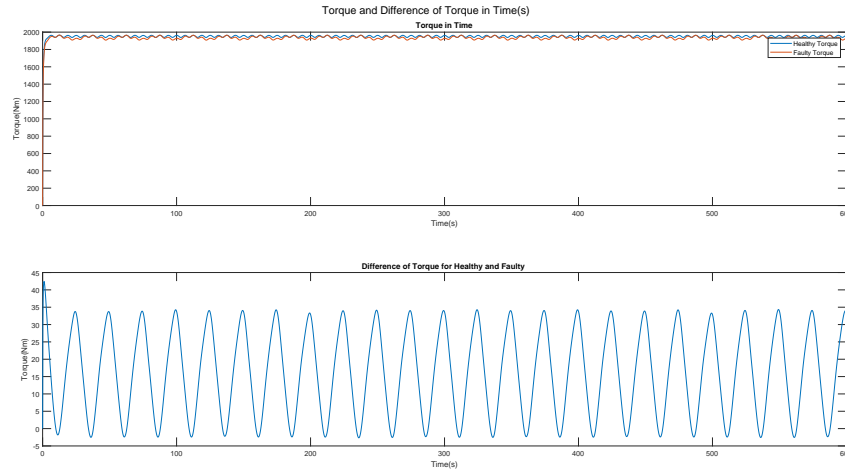


Figure 4.97: Thesis results for: Torque and Difference in Time(s) (Case Demag 50 13.125)

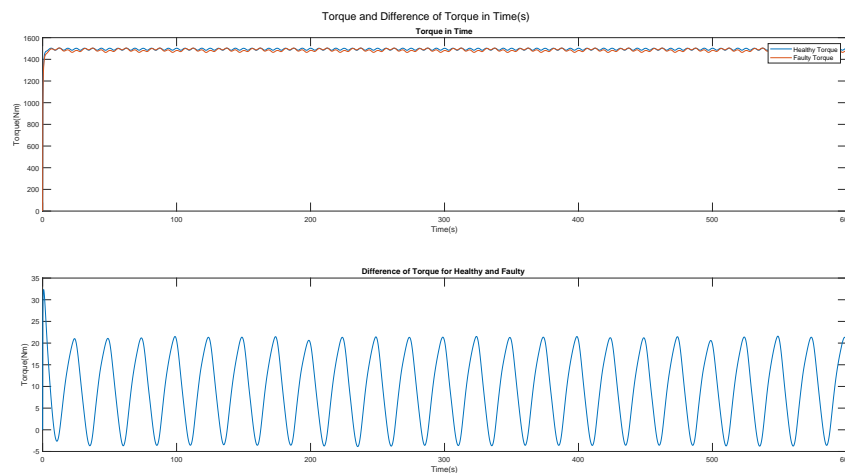


Figure 4.98: Thesis results for: Torque and Difference in Time(s) (Case Demag 50 17.5)

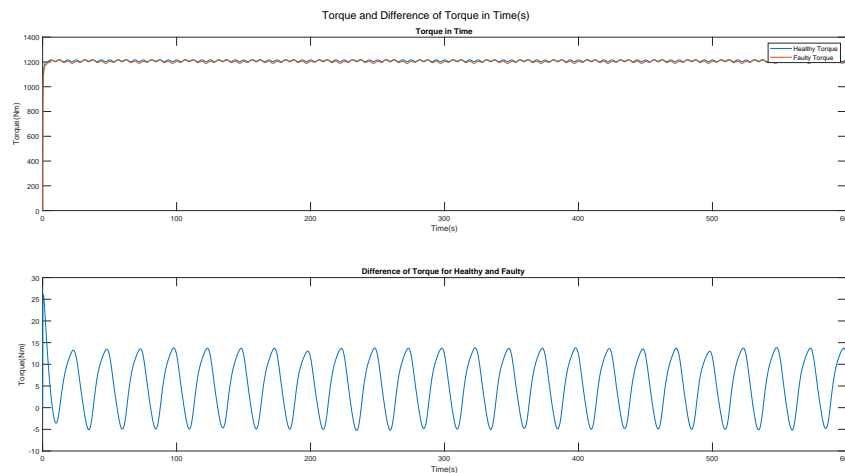


Figure 4.99: Thesis results for: Torque and Difference in Time(s) (Case Demag 50 21.875)



Fourier and Difference of Torque

In our steady-state operation, where torque behaves like a DC signal, we expected the highest value to occur at 0 Hz as depicted in Figures (4.100, 4.101 and 4.102). Notably, at $k=8$, as indicated by the formula $f = fs(1 + \frac{k}{p})$, there is a substantial increase in amplitude, highlighting a significant difference between healthy and faulty cases. Additionally, a pronounced rise in amplitude is observed in the 6th harmonic.

It's crucial to acknowledge that this phenomenon is inherent and doesn't come from a fault but rather emerges from the interaction between the 5th and 1st harmonic of the stator and rotor. The observable difference in the third harmonic, escalating at $3f_s$, becomes apparent in the Fast Fourier Transform (FFT) analysis used to compare healthy and faulty cases. This qualitative theory aligns with the observations made for a 25% demagnetization.

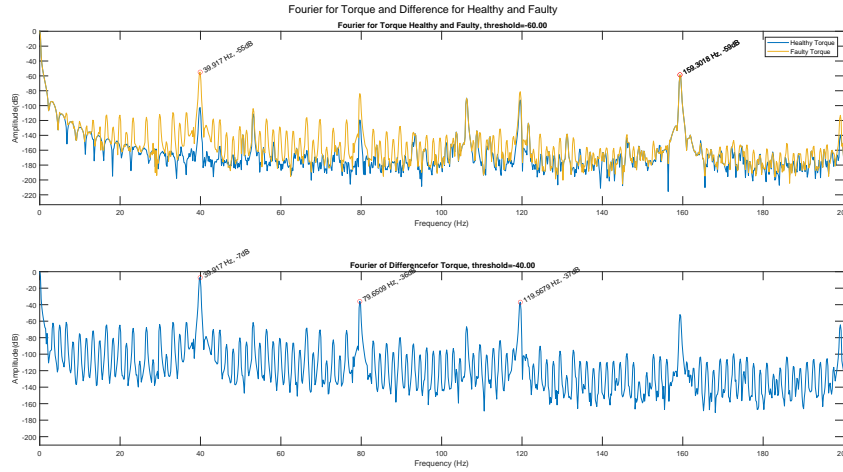


Figure 4.100: Thesis results for: Fourier and Difference of Torque (Case Demag 50 13.125)

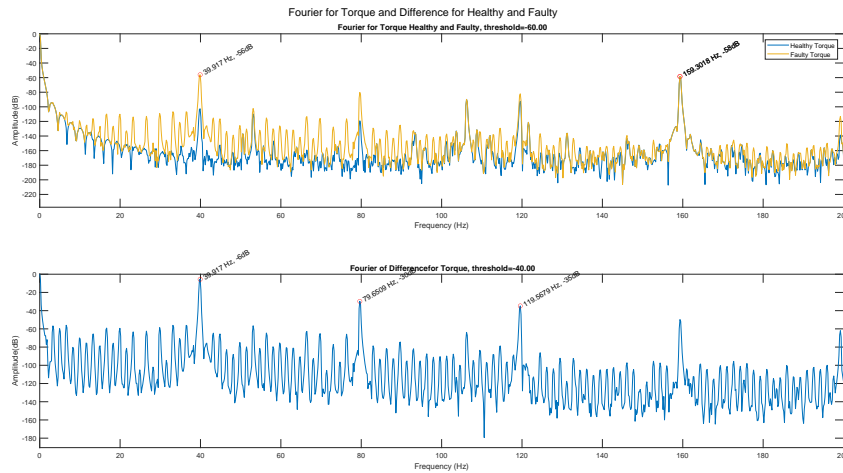


Figure 4.101: Thesis results for: Fourier and Difference of Torque (Case Demag 50 17.5)

4.2.3 Demagnetization 25% 50%

Torque and Difference of Torque

The comparison between healthy and faulty cases in the time domain illustrates minimal disparities, maintaining a consistent pattern under varying loads. Notably, the decrease in ohmic load correlates with an upsurge in current, resulting in heightened power and, consequently, increased torque. It is worth mentioning that this finding corresponds qualitatively with the case of 25% demagnetization, as depicted in Figures (4.103, 4.104 and 4.105).

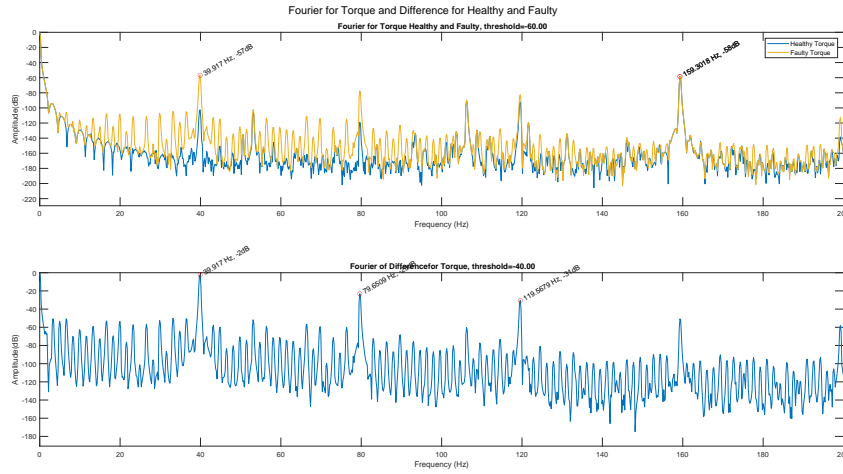


Figure 4.102: Thesis results for: Fourier and Difference of Torque (Case Demag 50 21.875)

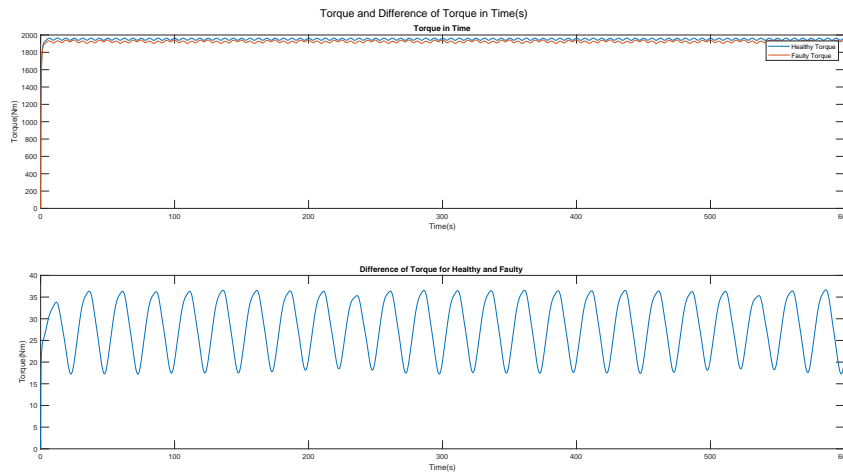


Figure 4.103: Thesis results for: Torque and Difference in Time(s) (Case Demag 25 50 13.125)

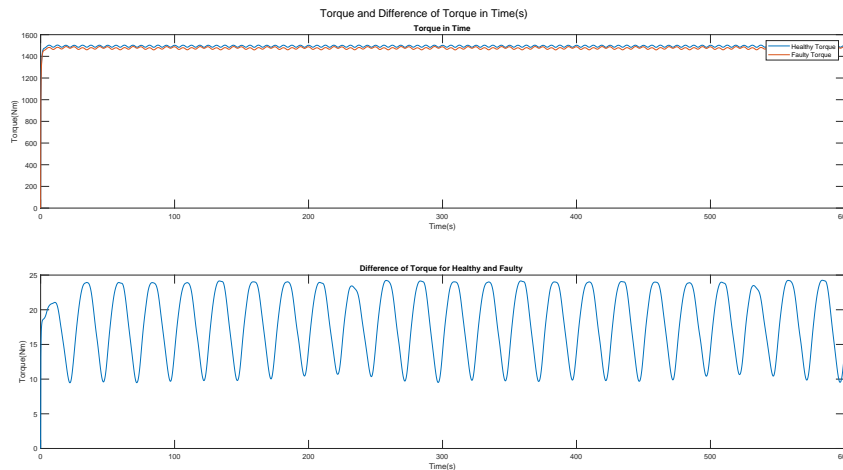


Figure 4.104: Thesis results for: Torque and Difference in Time(s) (Case Demag 25 50 17.5)

Fourier and Difference of Torque

In the realm of our steady-state operation, where torque exhibits characteristics similar to a DC signal, we initially expected the highest amplitude at 0 Hz. A noteworthy deviation from this expectation occurs at $k=8$, denoted by the formula $f = fs(1 + \frac{k}{p})$, revealing a significant increase in amplitude and a conspicuous contrast between healthy and faulty cases. Additionally, a marked elevation in amplitude is detected in the 6th harmonic.

It's crucial to emphasize that this phenomenon is natural and doesn't arise from a fault but rather emerges from the interaction between the 5th and 1st harmonic of the stator and rotor. The discernible difference in the third harmonic, intensifying at $3f_s$, is clearly visible in the Fast Fourier Transform (FFT) analysis applied

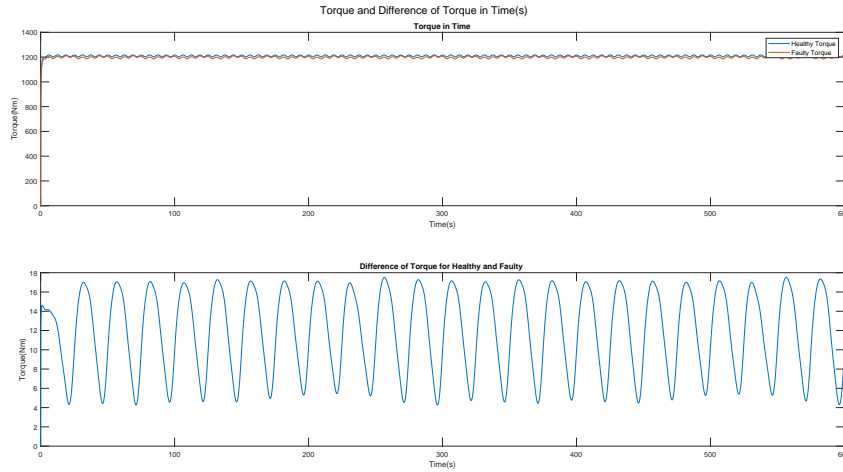


Figure 4.105: Thesis results for: Torque and Difference in Time(s) (Case Demag 25 50 21.875)

to compare healthy and faulty cases. This qualitative theory aligns with the observations made for a 25% demagnetization case and depicted in Figures (4.106, 4.107 and 4.108).

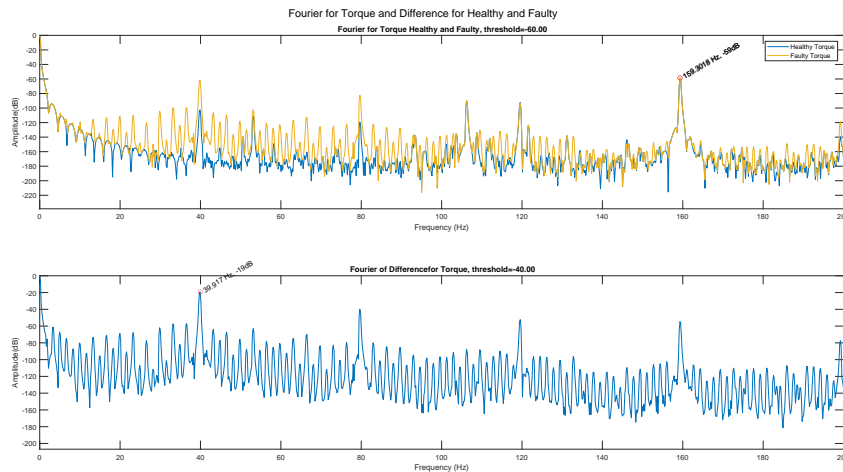


Figure 4.106: Thesis results for: Fourier and Difference of Torque (Case Demag 25 50 13.125)

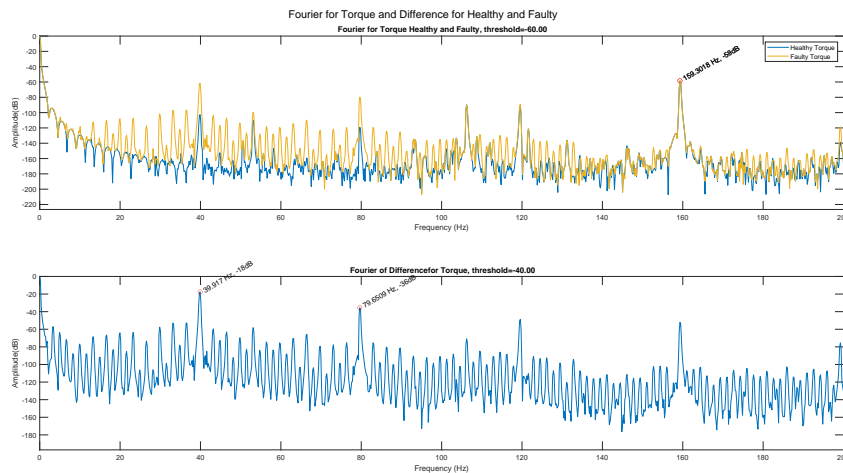


Figure 4.107: Thesis results for: Fourier and Difference of Torque (Case Demag 25 50 17.5)

4.2.4 Demagnetization 25% Both

Torque and Difference of Torque

Examining the time domain for both healthy and faulty scenarios indicates marginal distinctions, with patterns holding steady across diverse loads. Of particular interest is the inverse relationship observed between

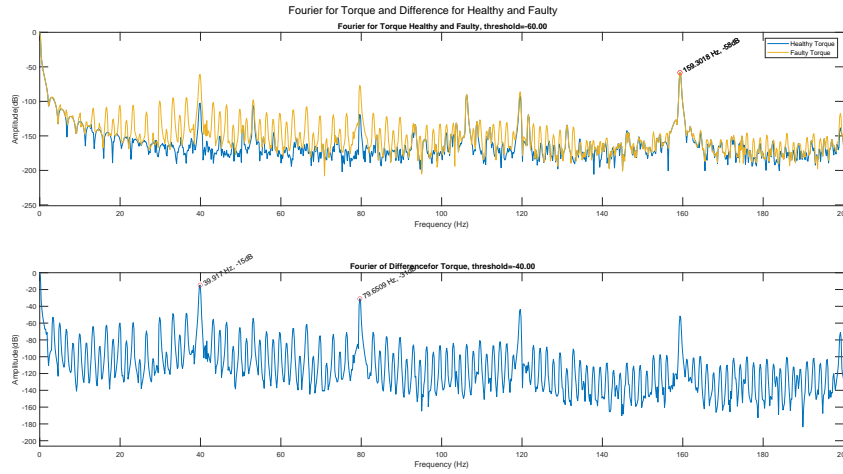


Figure 4.108: Thesis results for: Fourier and Difference of Torque (Case Demag 25 50 21.875)

diminishing ohmic load and an amplification in current, leading to augmented power and, subsequently, greater torque. This correlation highlights the influential role of load conditions in shaping the operational characteristics of the system. Importantly, this observation aligns qualitatively with the case of 25% demagnetization, as demonstrated in Figures (4.109, 4.110 and 4.111).

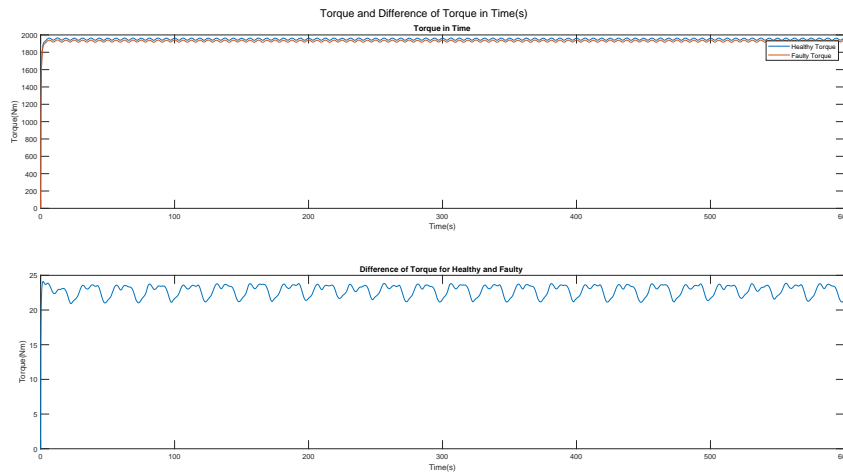


Figure 4.109: Thesis results for: Torque and Difference in Time(s) (Case Demag 25 Both 13.125)

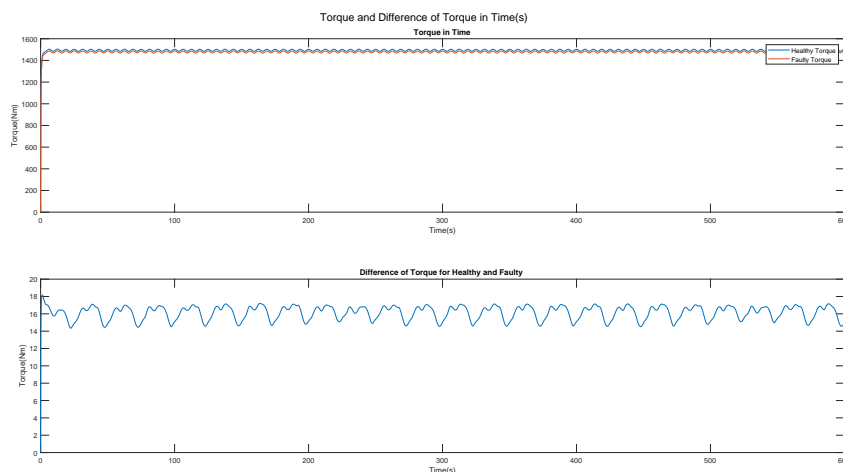


Figure 4.110: Thesis results for: Torque and Difference in Time(s) (Case Demag 25 Both 17.5)

Fourier and Difference of Torque

In the context of our steady-state operation, where torque acts akin to a DC signal, the initial expectation was for the highest amplitude at 0 Hz. Notably, at $k=8$, signifying the formula $f = fs(1 + \frac{k}{p})$, there

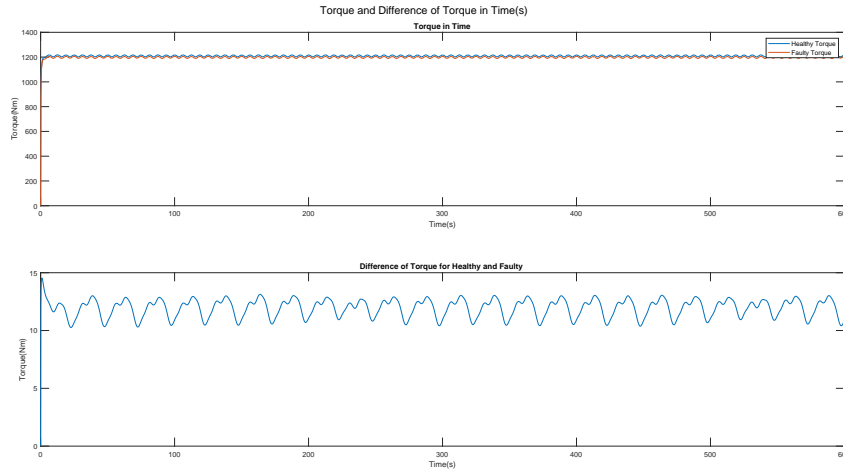


Figure 4.111: Thesis results for: Torque and Difference in Time(s) (Case Demag 25 Both 21.875)

emerges a substantial increase in amplitude, delineating a marked distinction between healthy and faulty cases. Furthermore, a pronounced surge in amplitude characterizes the 6th harmonic.

It's pivotal to acknowledge that this phenomenon is inherent and doesn't come from a fault but rather manifests from the interaction between the 5th and 1st harmonic of the stator and rotor. The evident difference in the third harmonic, intensifying at $3f_s$, is clearly discerned in the Fast Fourier Transform (FFT) analysis employed to compare healthy and faulty cases.

Understanding these harmonic interactions and variations is fundamental for precise fault diagnosis and the insightful interpretation of spectral analyses in the context of steady-state operations. This qualitative theory aligns with the observations made for a 25% demagnetization, as demonstrated in Figures (4.112, 4.113 and 4.114).

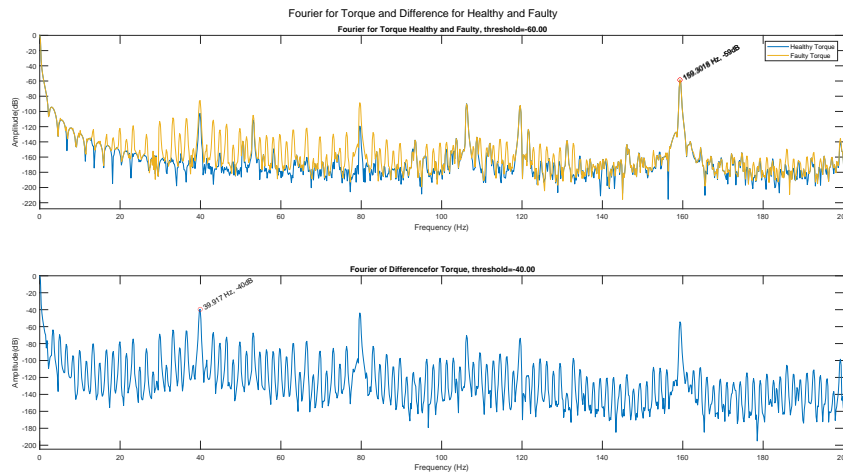


Figure 4.112: Thesis results for: Fourier and Difference of Torque (Case Demag 25 Both 13.125)

4.2.5 Demagnetization 50% Both

Torque and Difference of Torque

Within the time domain analysis, the contrast between healthy and faulty instances showcases subtle differences, with consistent patterns evident across different loads. Noteworthy is the direct correlation identified between a reduction in ohmic load and an increase in current, yielding higher power and, consequently, elevated torque. Additionally, it's worth noting that this observation is qualitatively consistent with the case of 25% demagnetization, as shown in Figures (4.115, 4.116 and 4.117).

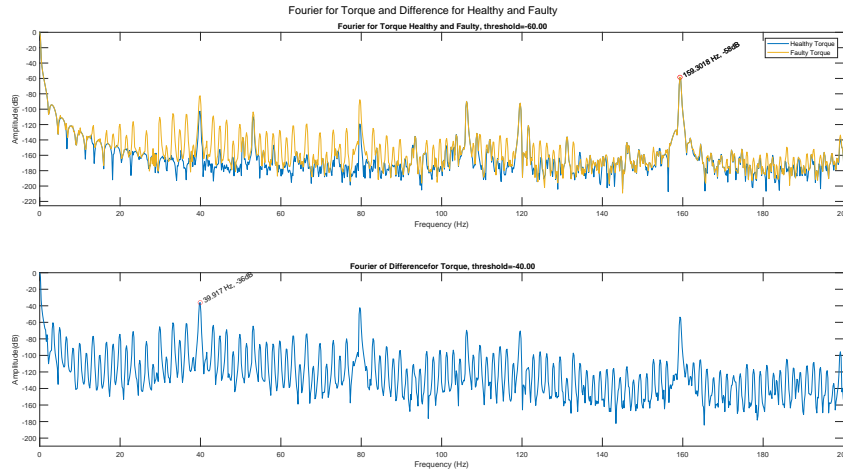


Figure 4.113: Thesis results for: Fourier and Difference of Torque (Case Demag 25 Both 17.5)

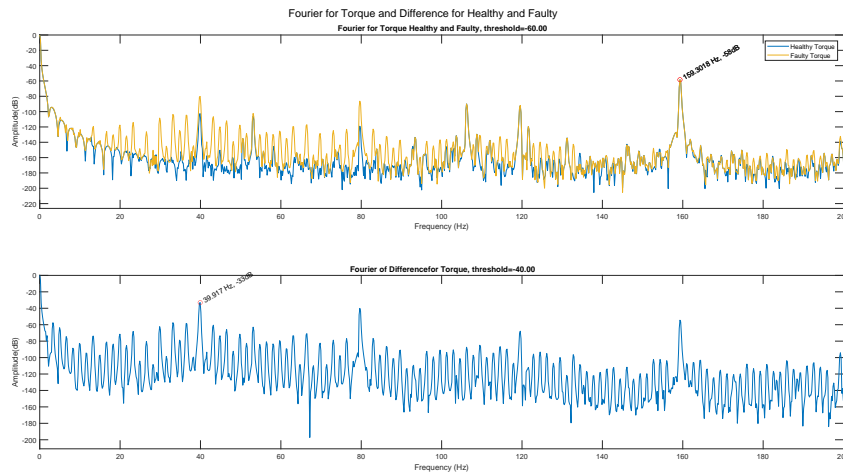


Figure 4.114: Thesis results for: Fourier and Difference of Torque (Case Demag 25 Both 21.875)

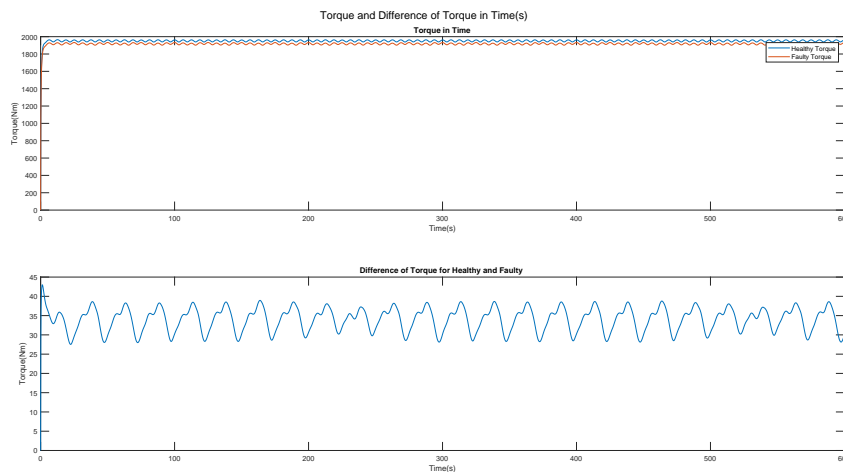


Figure 4.115: Thesis results for: Torque and Difference in Time(s) (Case Demag 50 Both 13.125)

Fourier and Difference of Torque

Within the framework of our steady-state operation, where torque mirrors the characteristics of a DC signal, the initial anticipation was for the highest amplitude at 0 Hz. Significantly, at $k=8$, denoted by the formula $f = fs(1 + \frac{k}{p})$, a substantial increase in amplitude becomes apparent, outlining a distinct contrast between healthy and faulty cases. Additionally, a marked escalation in amplitude characterizes the 6th harmonic.

It's crucial to underscore that this phenomenon is intrinsic and doesn't arise from a fault but rather evolves from the interaction between the 5th and 1st harmonic of the stator and rotor. The evident difference in the third harmonic, intensifying at $3f_s$, is prominently visible in the Fast Fourier Transform (FFT) analysis utilized to compare healthy and faulty cases. This qualitative theory aligns with the observations made for a 25%

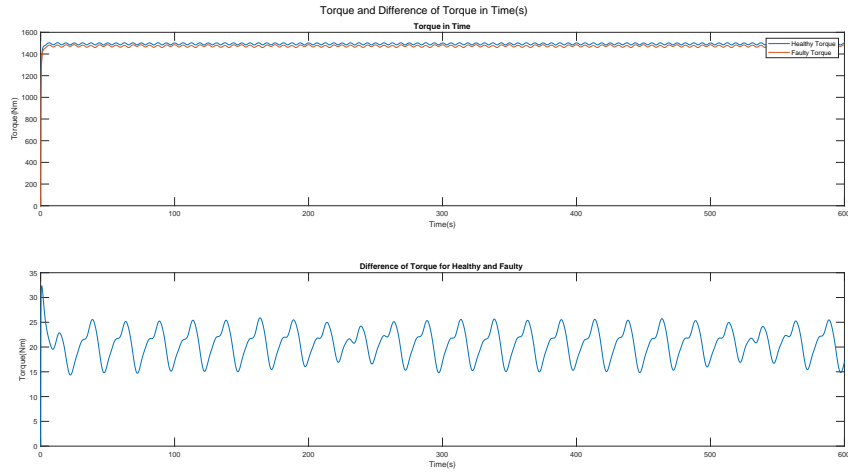


Figure 4.116: Thesis results for: Torque and Difference in Time(s) (Case Demag 50 Both 17.5)

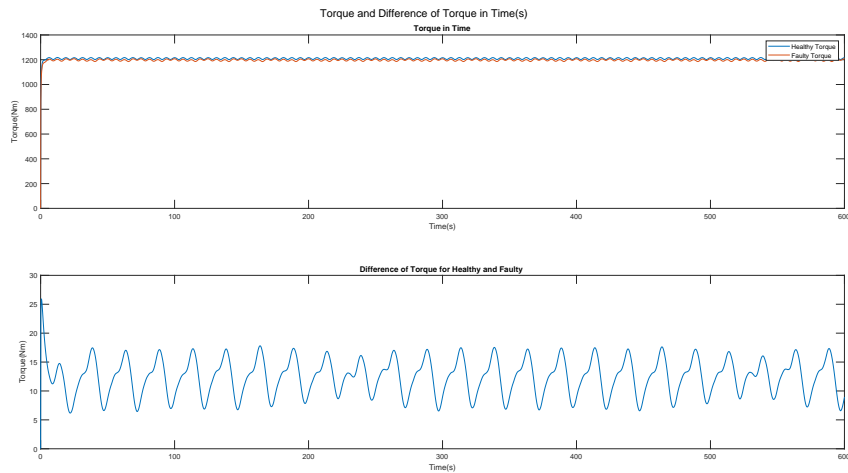


Figure 4.117: Thesis results for: Torque and Difference in Time(s) (Case Demag 50 Both 21.875)

demagnetization, as demonstrated in Figures (4.118, 4.119 and 4.120).

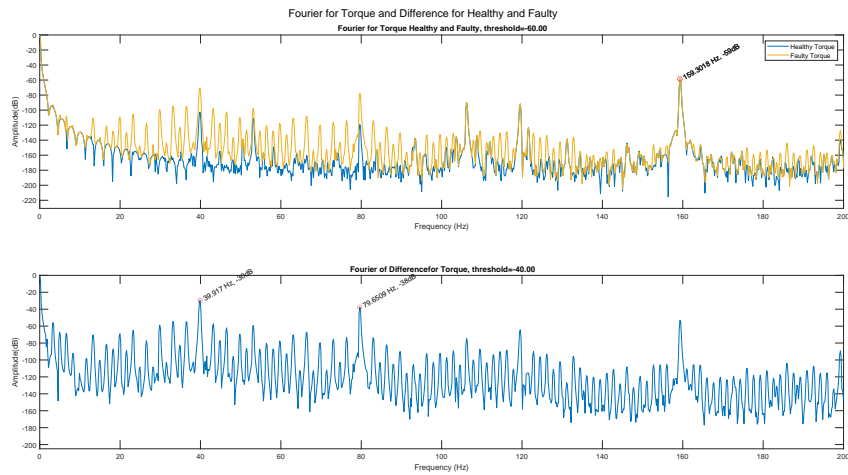


Figure 4.118: Thesis results for: Fourier and Difference of Torque (Case Demag 50 Both 13.125)

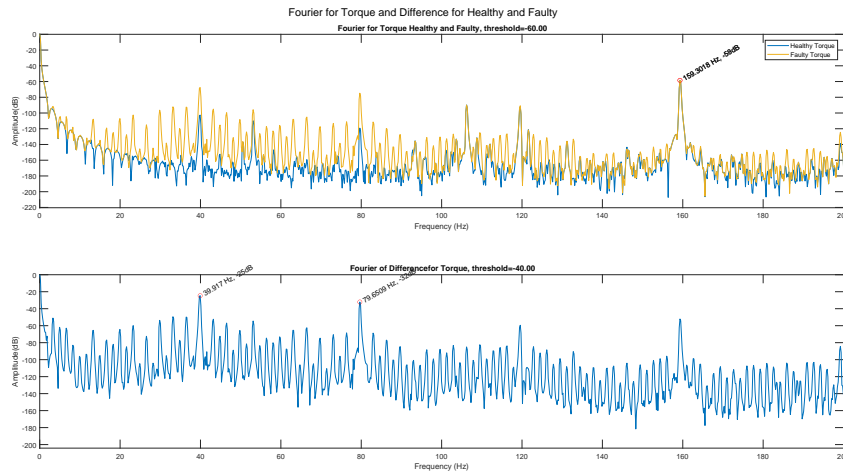


Figure 4.119: Thesis results for: Fourier and Difference of Torque (Case Demag 50 Both 17.5)

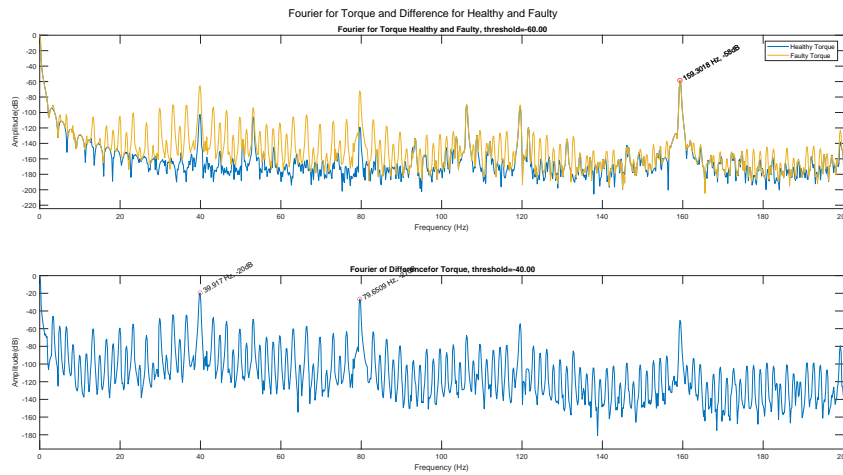


Figure 4.120: Thesis results for: Fourier and Difference of Torque (Case Demag 50 Both 21.875)

4.3 Flux Monitoring via Sensor Voltage for All Cases

4.3.1 Demagnetization 25%

Fourier and Differences of Voltage of Sensors(R_4 to R_8)

This section underscores the advantages of monitoring the amplitude-frequency components of the specific flux sensor in comparison to the stator current. The frequency spectra of the stator current was depicted above and the flux sensor voltage are depicted in Figures (4.121 - 4.150), respectively, for all studied cases during steady-state operation.

Previous literature suggested monitoring demagnetization at frequencies $f_s \pm k \frac{f_s}{p}$ or even narrowing it down to $f_s - \frac{f_s}{p}$. However, the results in Figures (4.121 - 4.150) debunk this notion. The current spectra reveal that only the component $f_s - \frac{f_s}{p}$ increases in amplitude to detect the fault. This phenomenon arises due to the generator having a number of poles that are multiples of 16, along with 8 stator coils per phase. The Y connection impact leads to the cancellation of all other signatures described as $f_s \pm k \frac{f_s}{p}$. A different number of stator coils would yield a different signature pattern identification. Despite this, the amplitude increase of this signature is monotonically proportional to the fault severity level increase.

Conversely, most of the family of mechanical speed-related sidebands $f_s \pm k \frac{f_s}{p}$ increases with the fault severity level in the flux Figures (4.121 - 4.150). The amplitudes of various signatures are detailed in Table 5.10. Notably, the harmonic $f_s - \frac{f_s}{p}$, between 25% 50% demagnetization (non-adjacent magnets) and 50% both demagnetization, exhibits tremendous increase. Furthermore, for instances of both 25% and 50% demagnetization in non-adjacent magnets as depicted in Figures (4.139 - 4.150), we have a cancellation phenomenon at $k=8$.

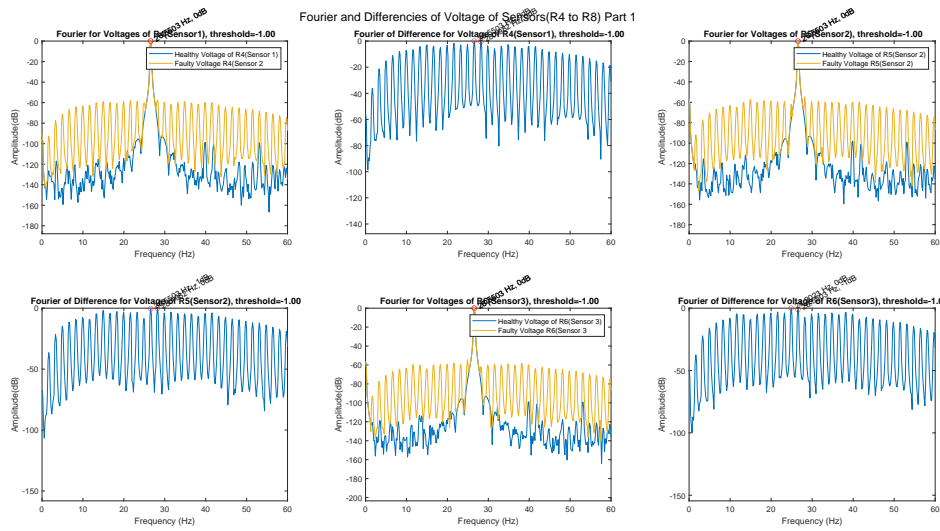


Figure 4.121: Thesis results for: Fourier and Differences of Voltage of Sensors(R_4 to R_8) Part 1 (Case Demag 25 13.125)

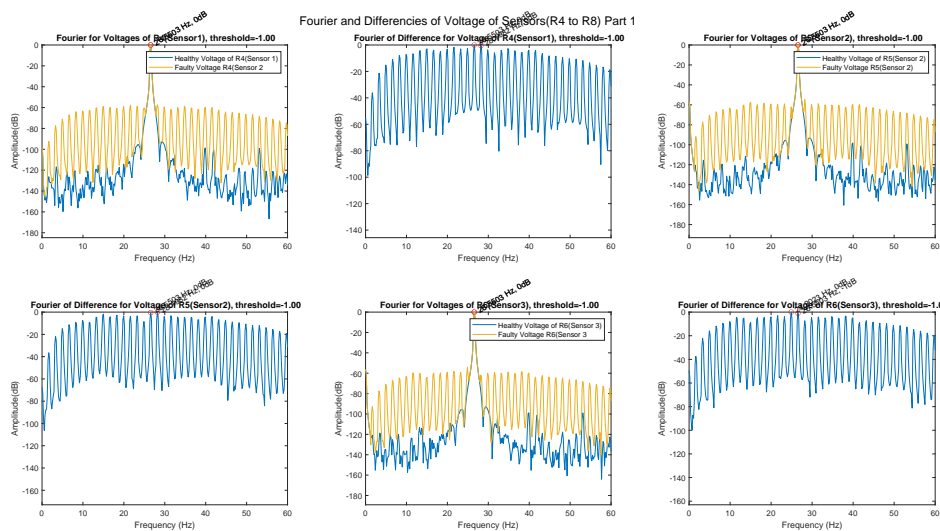


Figure 4.122: Thesis results for: Fourier and Differences of Voltage of Sensors(R_4 to R_8) Part 1 (Case Demag 25 17.5)

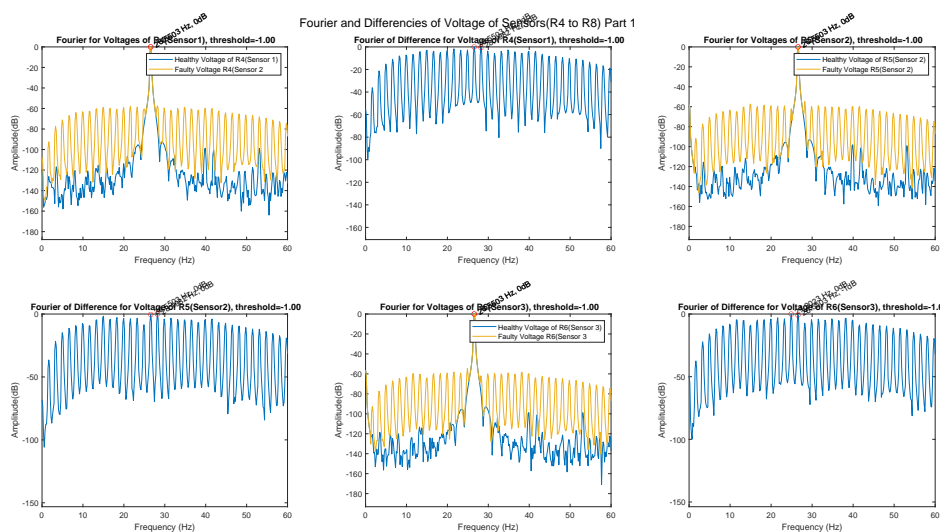


Figure 4.123: Thesis results for: Fourier and Differences of Voltage of Sensors(R_4 to R_8) Part 1 (Case Demag 25 21.875)

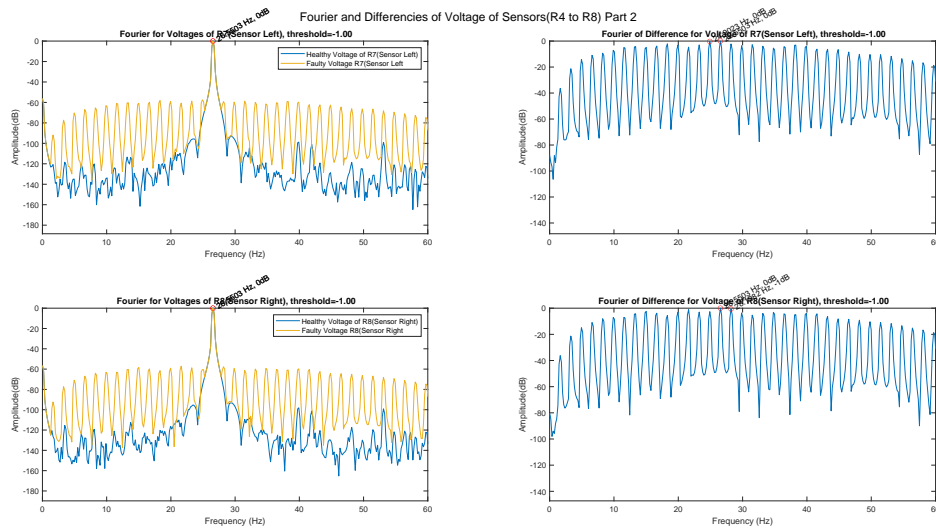


Figure 4.124: Thesis results for: Fourier and Differences of Voltage of Sensors(R_4 to R_8) Part 2 (Case Demag 25 13.125)

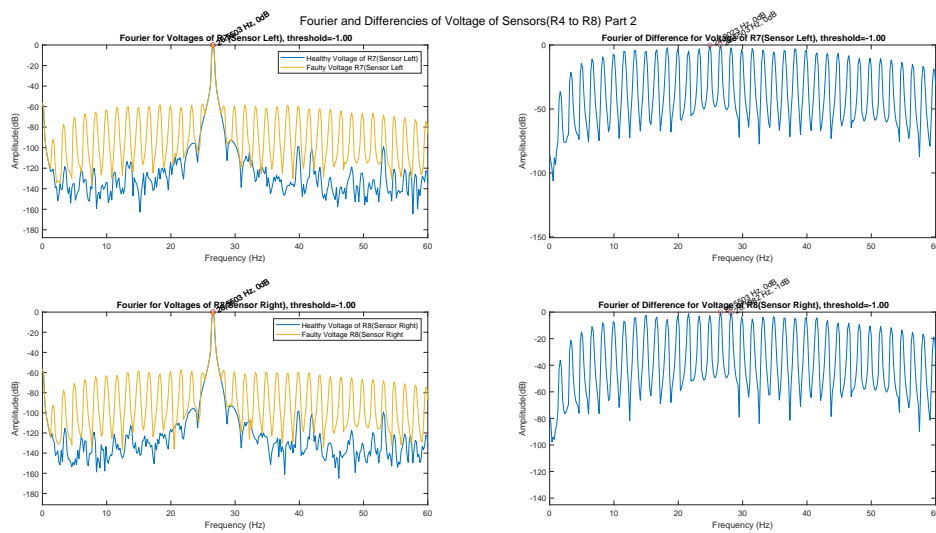


Figure 4.125: Thesis results for: Fourier and Differences of Voltage of Sensors(R_4 to R_8) Part 2 (Case Demag 25 17.5)

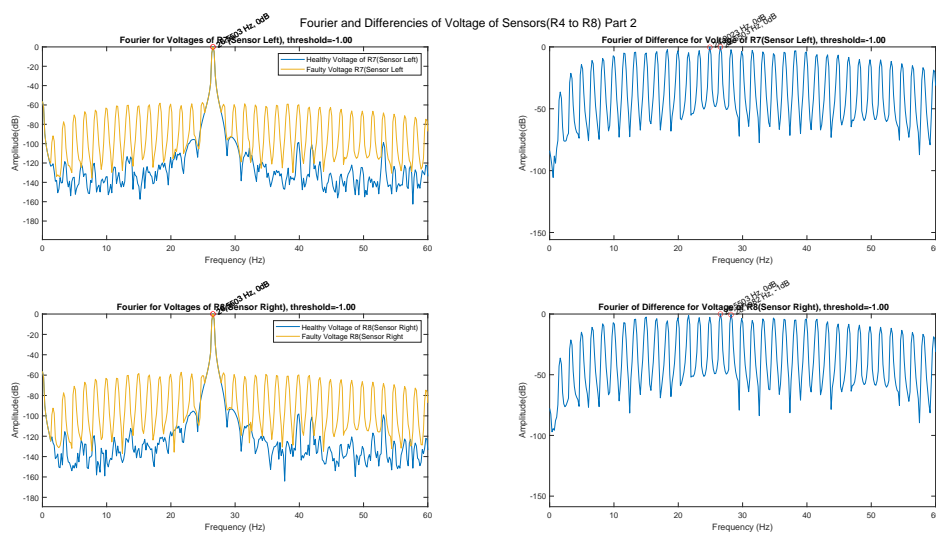


Figure 4.126: Thesis results for: Fourier and Differences of Voltage of Sensors(R_4 to R_8) Part 2 (Case Demag 25 21.875)

4.3.2 Demagnetization 50%

Fourier and Differences of Voltage of Sensors(R_4 to R_8)

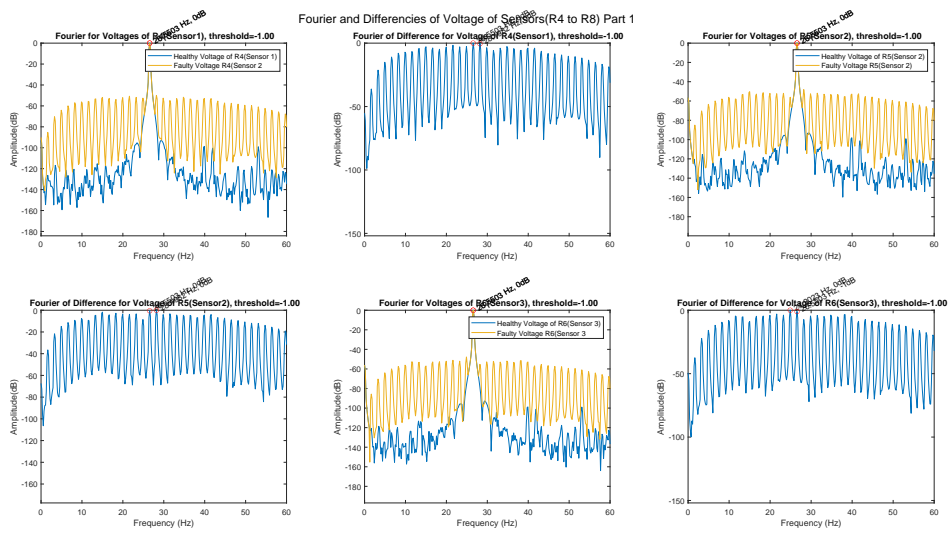


Figure 4.127: Thesis results for: Fourier and Differences of Voltage of Sensors(R_4 to R_8) Part 1 (Case Demag 50 13.125)

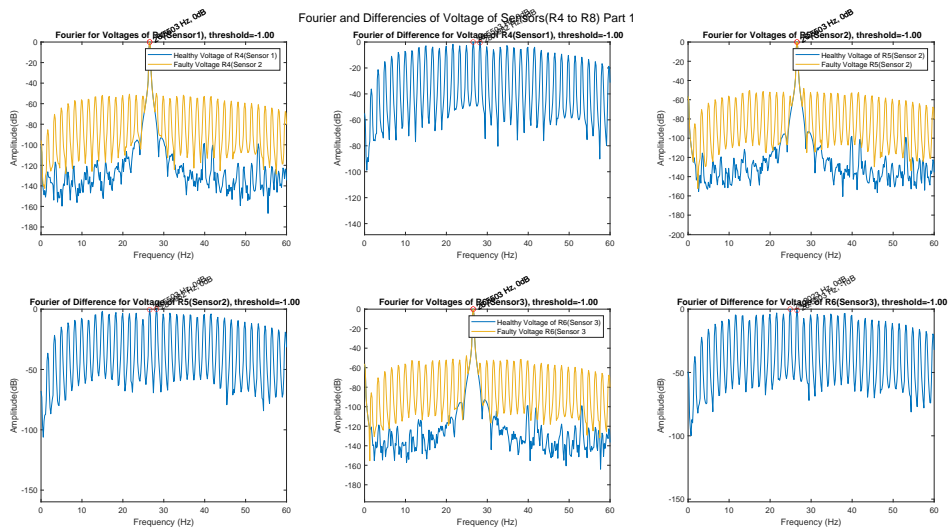


Figure 4.128: Thesis results for: Fourier and Differences of Voltage of Sensors(R_4 to R_8) Part 1 (Case Demag 50 17.5)

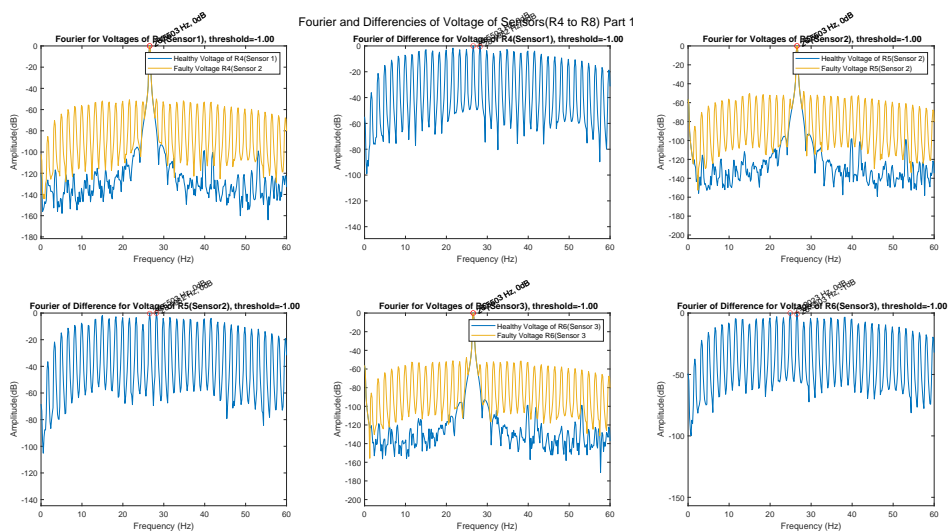


Figure 4.129: Thesis results for: Fourier and Differences of Voltage of Sensors(R_4 to R_8) Part 1 (Case Demag 50 21.875)

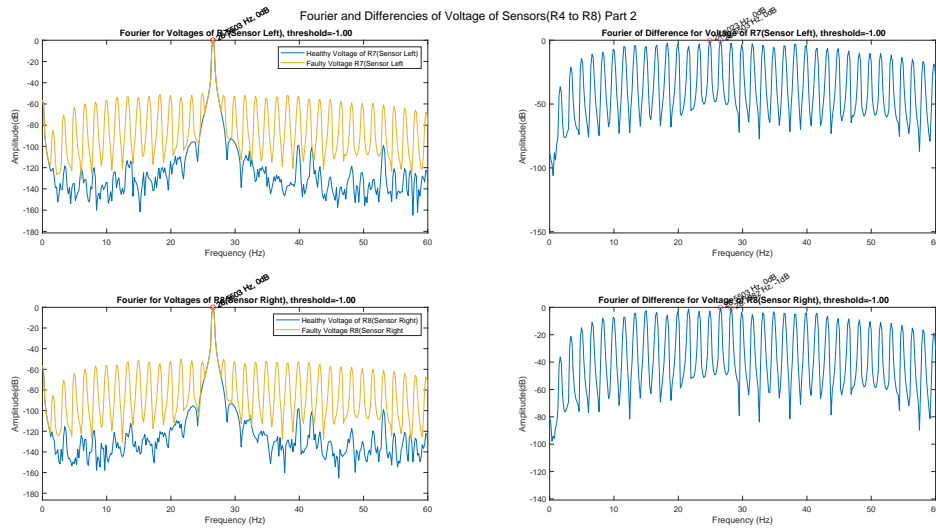


Figure 4.130: Thesis results for: Fourier and Differences of Voltage of Sensors(R_4 to R_8) Part 2 (Case Demag 50 13.125)

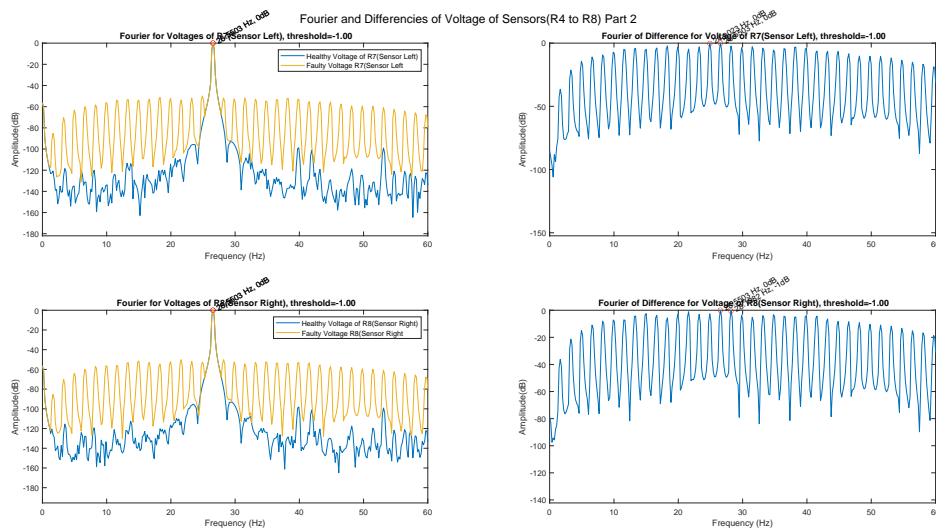


Figure 4.131: Thesis results for: Fourier and Differences of Voltage of Sensors(R_4 to R_8) Part 2 (Case Demag 50 17.5)

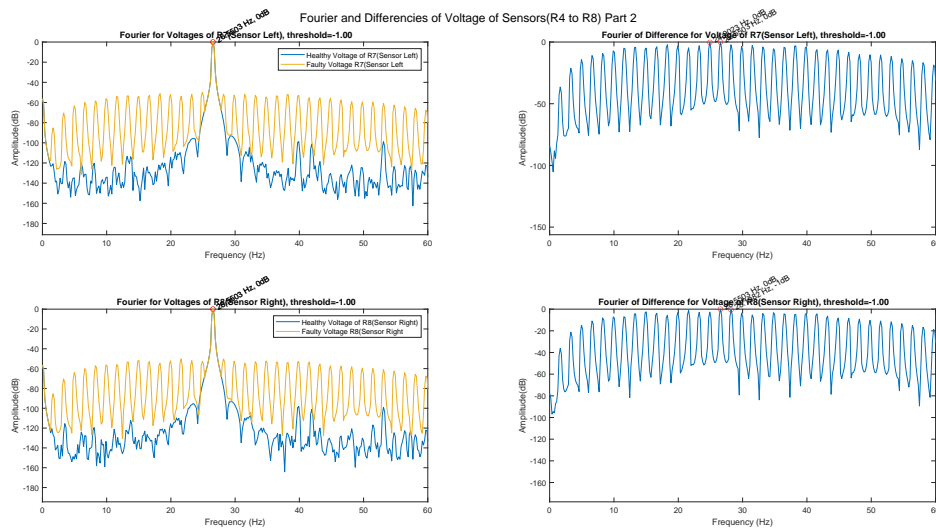


Figure 4.132: Thesis results for: Fourier and Differences of Voltage of Sensors(R_4 to R_8) Part 2 (Case Demag 50 21.875)

4.3.3 Demagnetization 25% 50%

Fourier and Differences of Voltage of Sensors(R_4 to R_8)

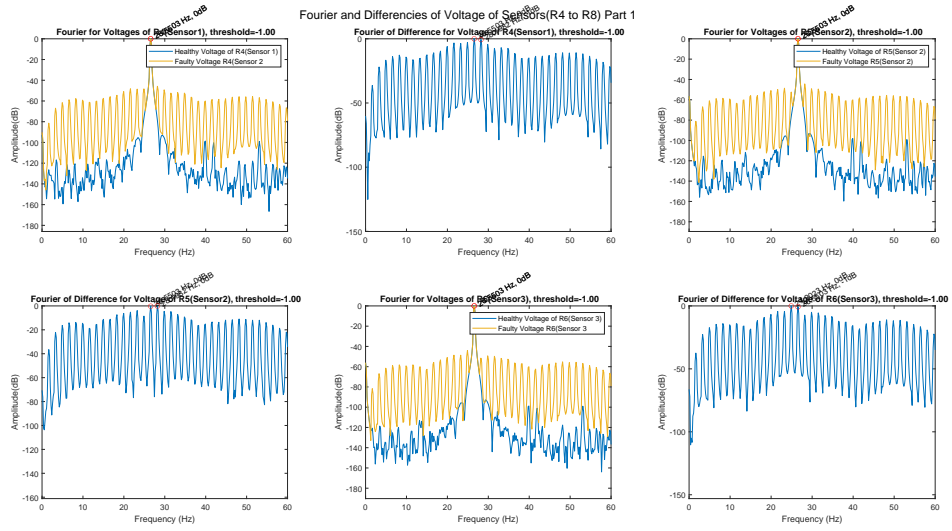


Figure 4.133: Thesis results for: Fourier and Differences of Voltage of Sensors(R_4 to R_8) Part 1 (Case Demag 25 50 13.125)

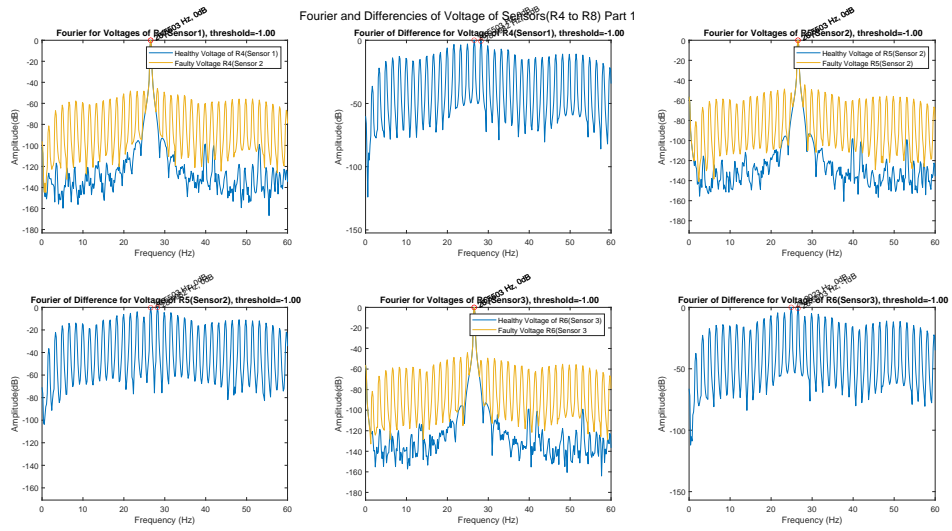


Figure 4.134: Thesis results for: Fourier and Differences of Voltage of Sensors(R_4 to R_8) Part 1 (Case Demag 25 50 17.5)

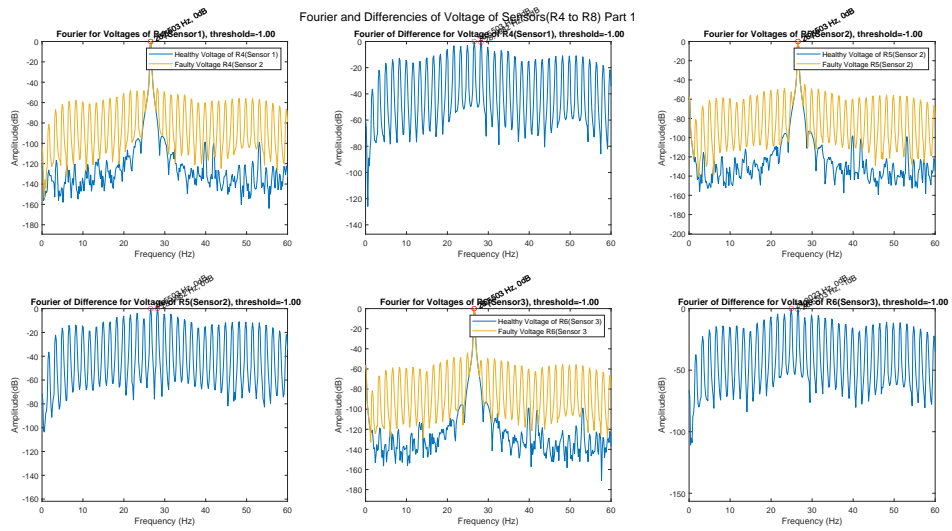


Figure 4.135: Thesis results for: Fourier and Differences of Voltage of Sensors(R_4 to R_8) Part 1 (Case Demag 25 50 21.875)

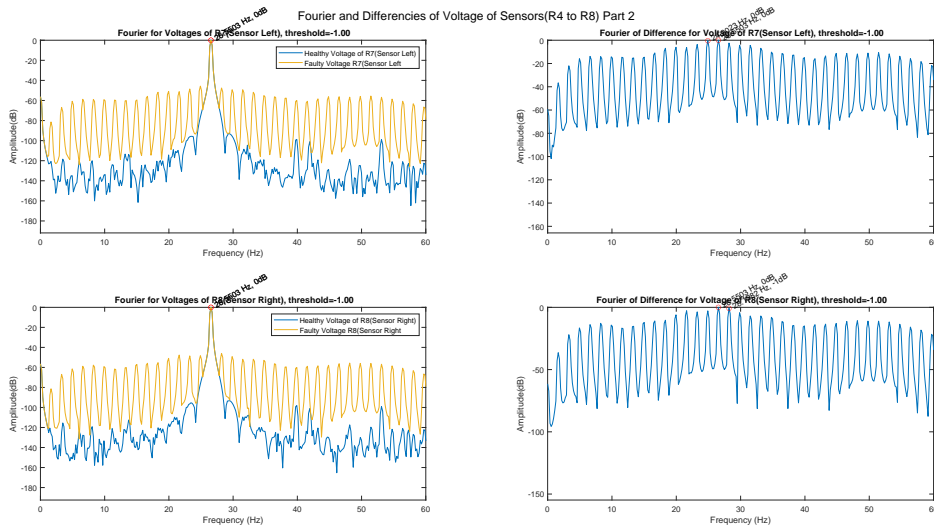


Figure 4.136: Thesis results for: Fourier and Differences of Voltage of Sensors(R_4 to R_8) Part 2 (Case Demag 25 50 13.125)

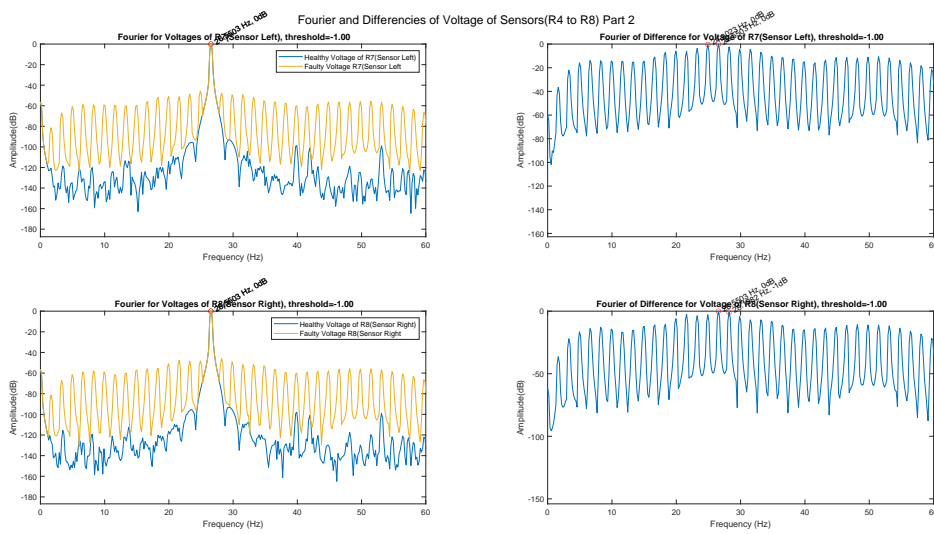


Figure 4.137: Thesis results for: Fourier and Differences of Voltage of Sensors(R_4 to R_8) Part 2 (Case Demag 25 50 17.5)

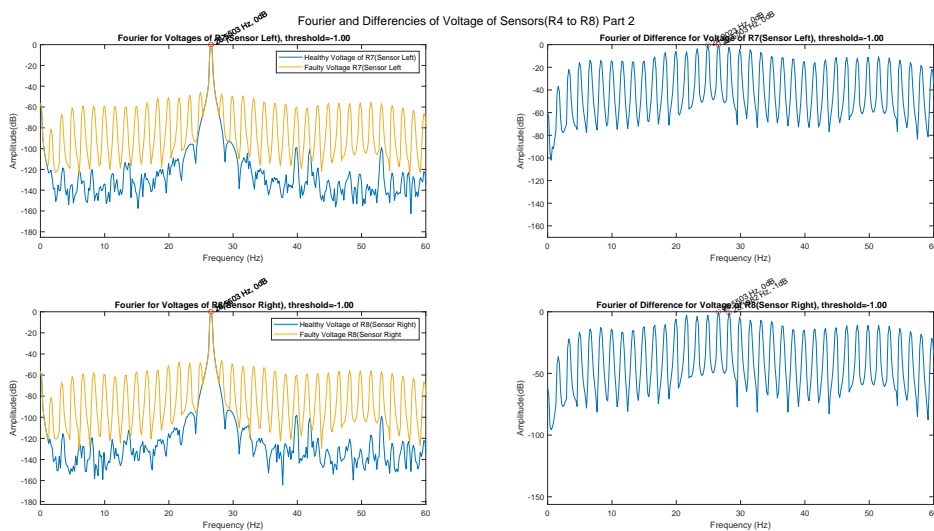


Figure 4.138: Thesis results for: Fourier and Differences of Voltage of Sensors(R_4 to R_8) Part 2 (Case Demag 25 50 21.875)

4.3.4 Demagnetization 25% Both

Fourier and Differences of Voltage of Sensors(R_4 to R_8)

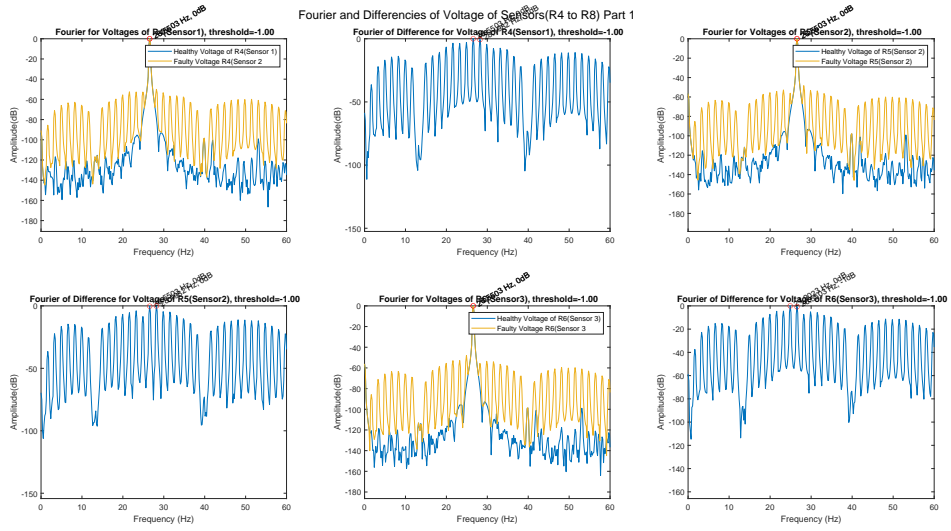


Figure 4.139: Thesis results for: Fourier and Differences of Voltage of Sensors(R_4 to R_8) Part 1 (Case Demag 25 Both 13.125)

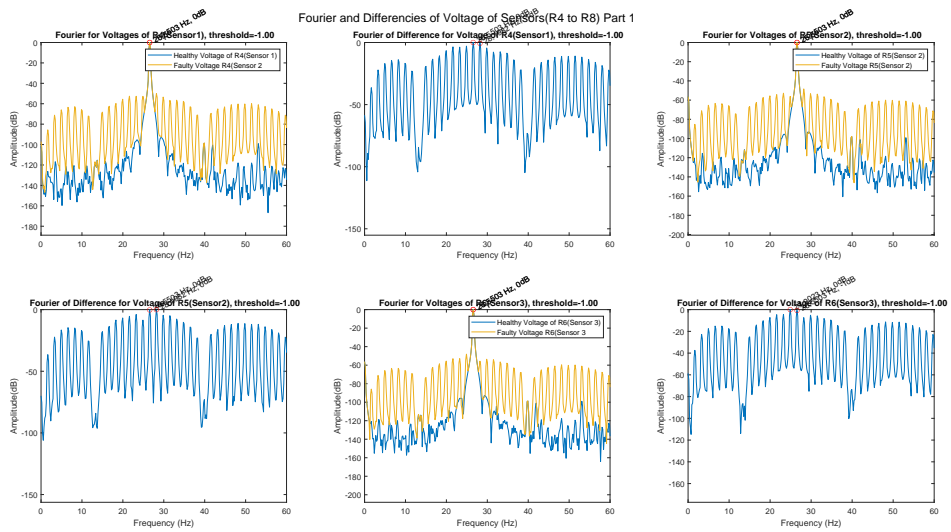


Figure 4.140: Thesis results for: Fourier and Differences of Voltage of Sensors(R_4 to R_8) Part 1 (Case Demag 25 Both 17.5)

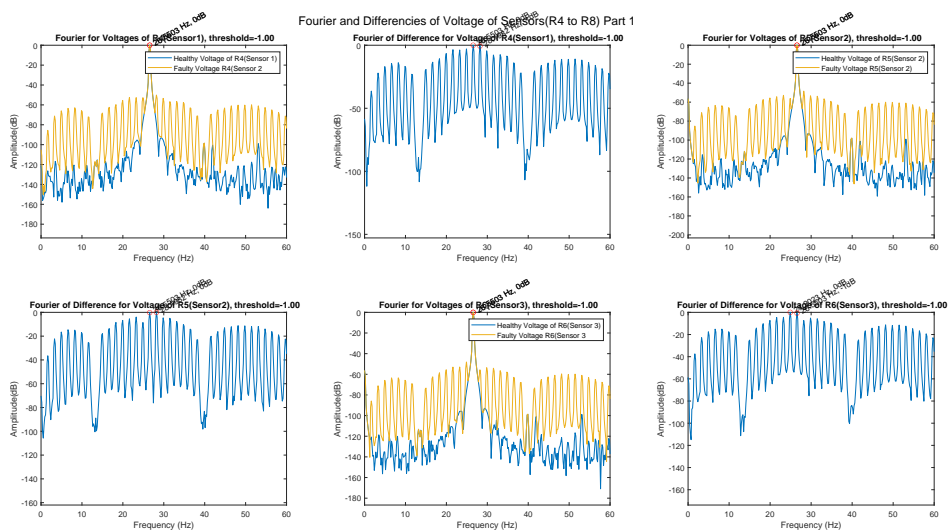


Figure 4.141: Thesis results for: Fourier and Differences of Voltage of Sensors(R_4 to R_8) Part 1 (Case Demag 25 Both 21.875)

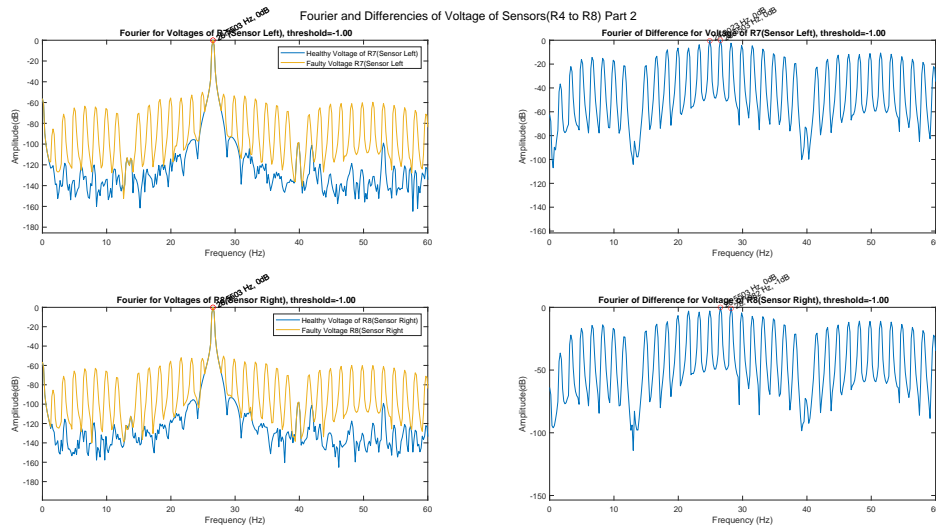


Figure 4.142: Thesis results for: Fourier and Differences of Voltage of Sensors(R_4 to R_8) Part 2 (Case Demag 25 Both 13.125)

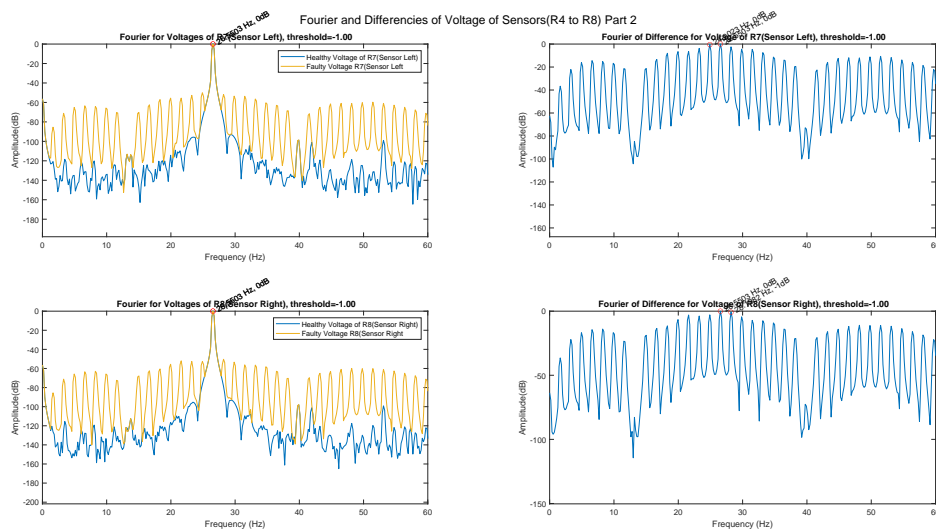


Figure 4.143: Thesis results for: Fourier and Differences of Voltage of Sensors(R_4 to R_8) Part 2 (Case Demag 25 Both 17.5)

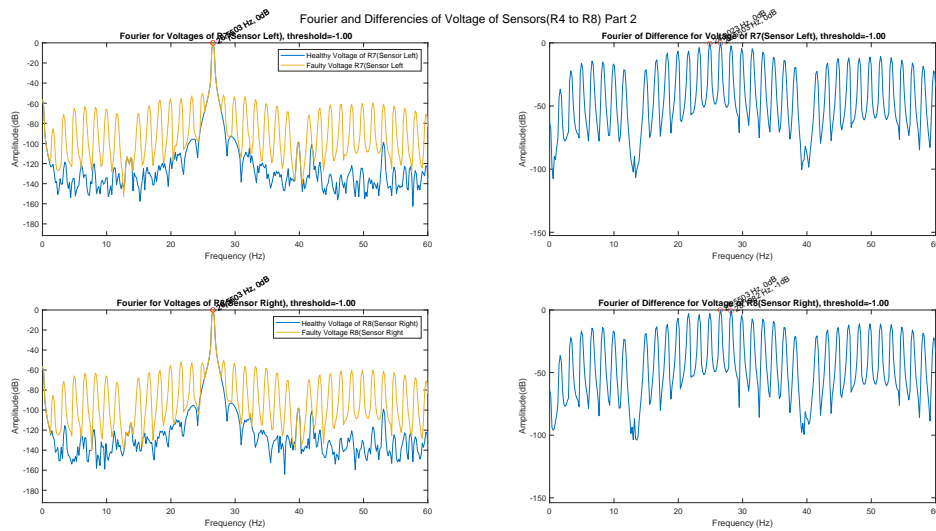


Figure 4.144: Thesis results for: Fourier and Differences of Voltage of Sensors(R_4 to R_8) Part 2 (Case Demag 25 Both 21.875)

4.3.5 Demagnetization 50% Both Fourier and Differences of Voltage of Sensors(R_4 to R_8)

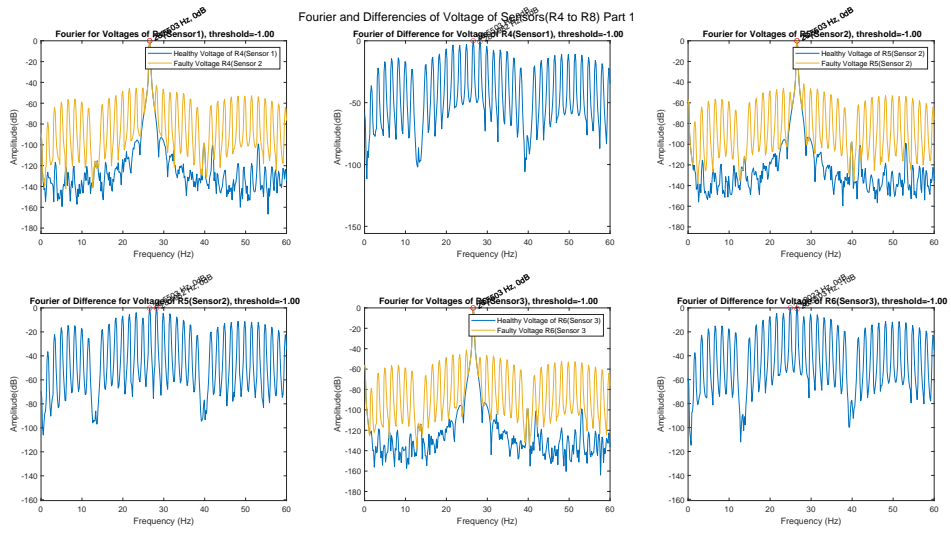


Figure 4.145: Thesis results for: Fourier and Differences of Voltage of Sensors(R_4 to R_8) Part 1 (Case Demag 50 Both 13.125)

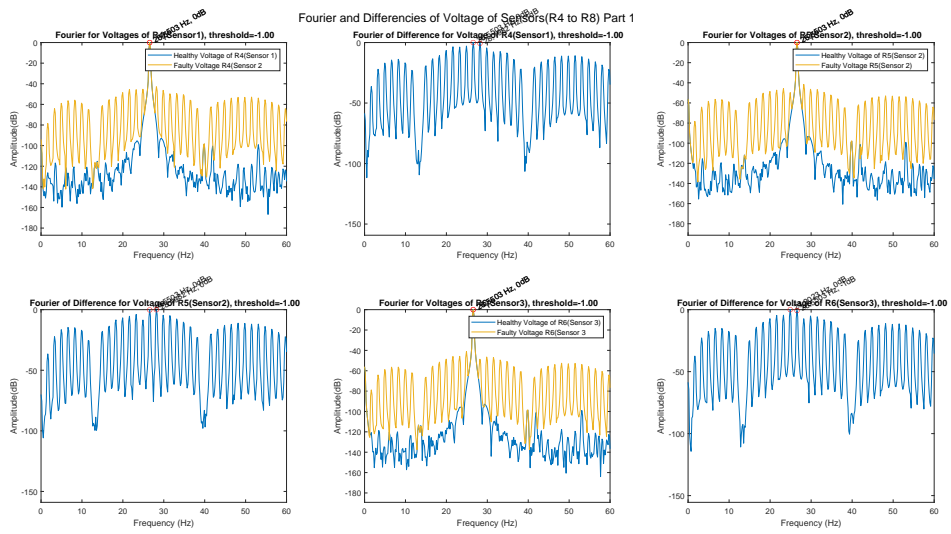


Figure 4.146: Thesis results for: Fourier and Differences of Voltage of Sensors(R_4 to R_8) Part 1 (Case Demag 50 Both 17.5)

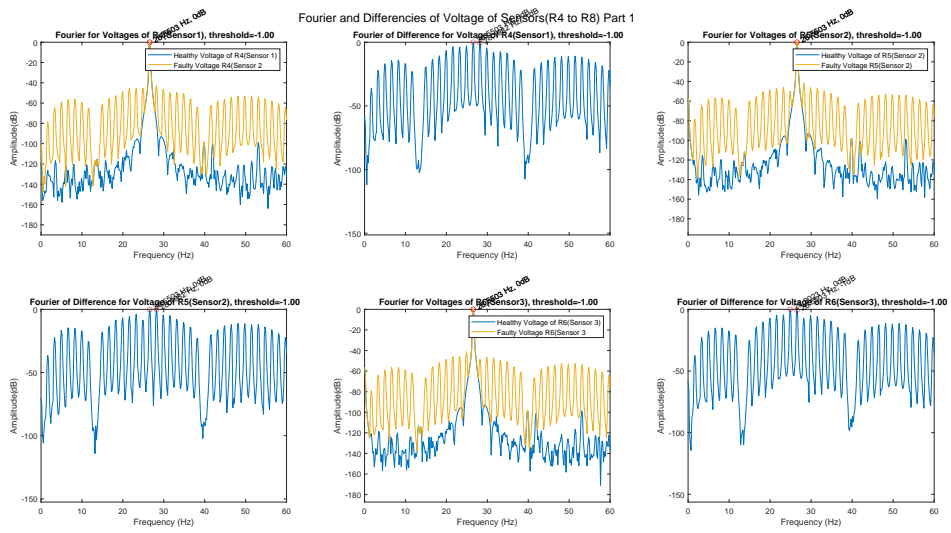


Figure 4.147: Thesis results for: Fourier and Differences of Voltage of Sensors(R_4 to R_8) Part 1 (Case Demag 50 Both 21.875)

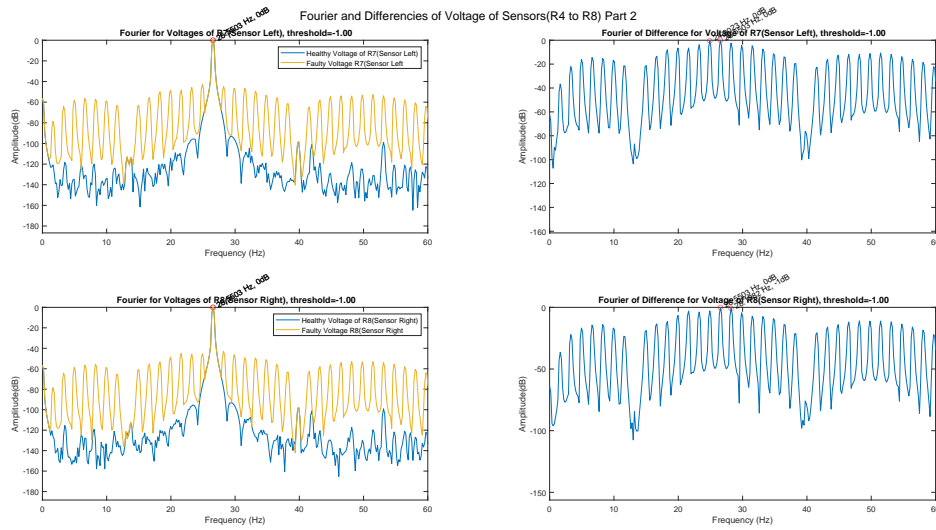


Figure 4.148: Thesis results for: Fourier and Differences of Voltage of Sensors(R_4 to R_8) Part 2 (Case Demag 50 Both 13.125)

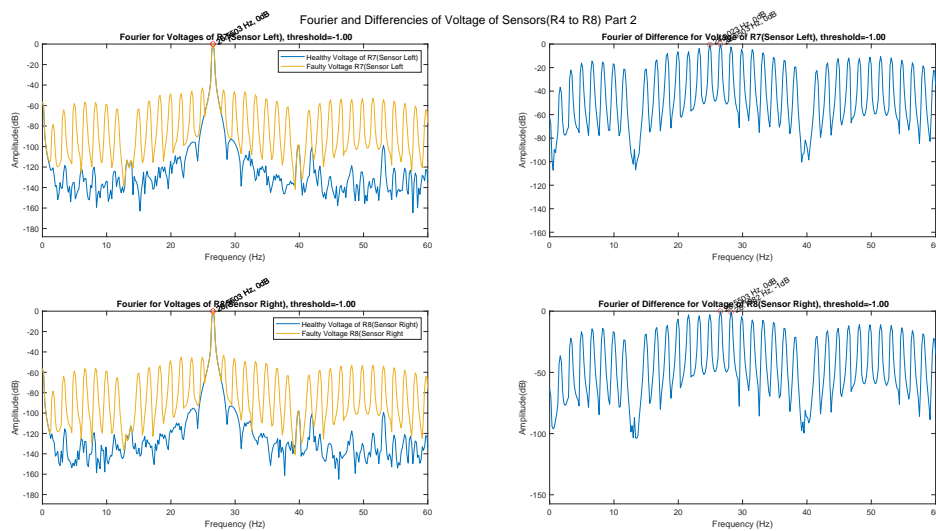


Figure 4.149: Thesis results for: Fourier and Differences of Voltage of Sensors(R_4 to R_8) Part 2 (Case Demag 50 Both 17.5)

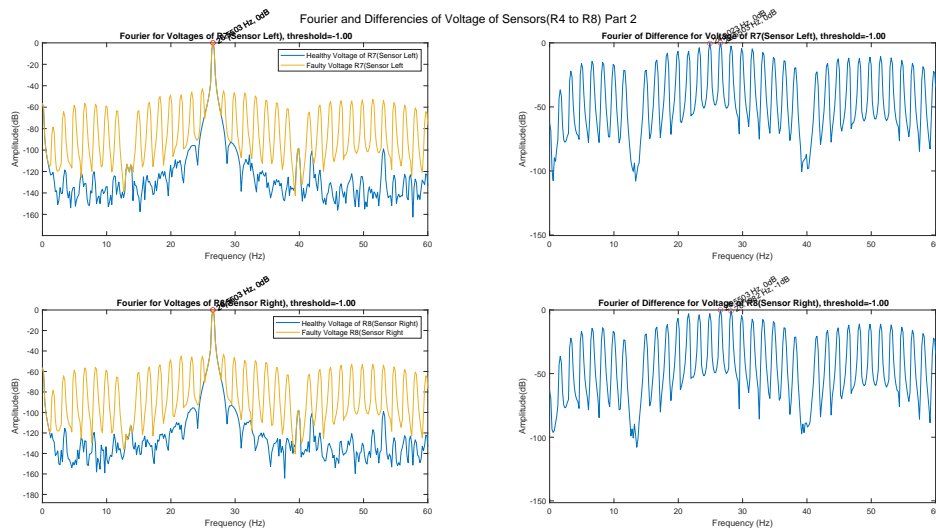


Figure 4.150: Thesis results for: Fourier and Differences of Voltage of Sensors(R_4 to R_8) Part 2 (Case Demag 50 Both 21.875)

4.4 PVA and EPVA

4.4.1 Demagnetization 25%

Each scenario of demagnetization under various loads is depicted below. Park Vector Approach (PVA) fails to provide detailed insights into the demagnetization phenomenon as portrayed below in Figures (4.151 - 4.165),

rendering it ineffective in such cases. Conversely, the Extended Park's Vector Approach (EPVA) proves more useful, offering a distinct indication at $k=8$: $f = f_s(1 + \frac{k}{p})$ in faulty cases. However, for instances of both 25% and 50% demagnetization in non-adjacent magnets as depicted in Figures (4.160 - 4.165), we have cancellation phenomenon at $k=8$ which means that the indication of the EPVA is similar with the healthy case which can lead to faulty assumptions.

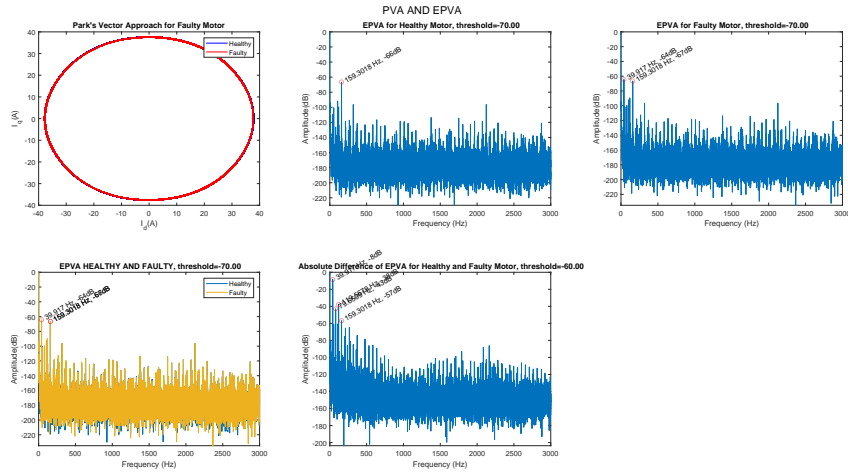


Figure 4.151: Thesis results for: PVA and EPVA (Case Demag 25 13.125)

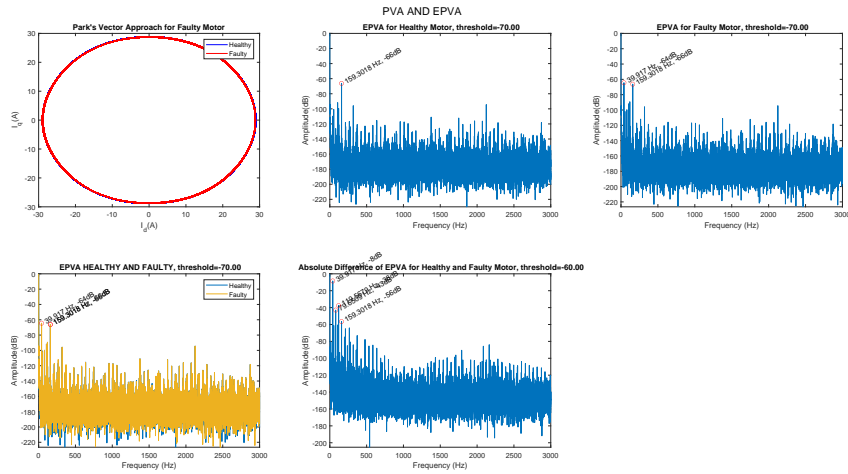


Figure 4.152: Thesis results for: PVA and EPVA (Case Demag 25 17.5)

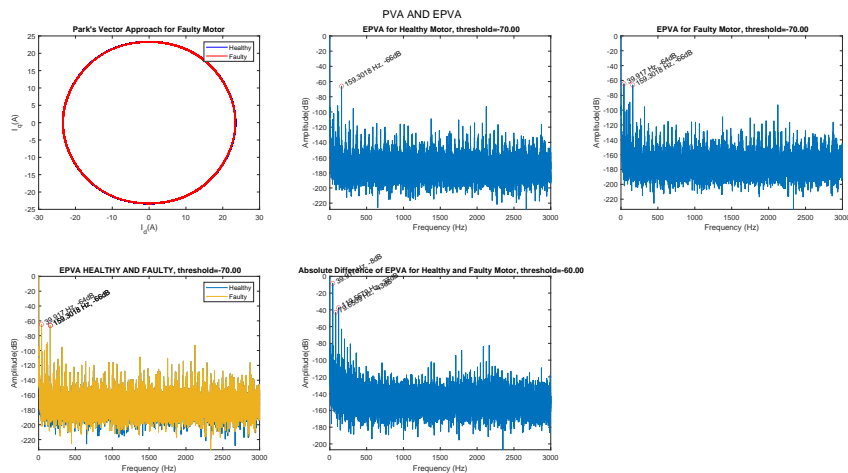


Figure 4.153: Thesis results for: PVA and EPVA (Case Demag 25 21.875)

4.4.2 Demagnetization 50%

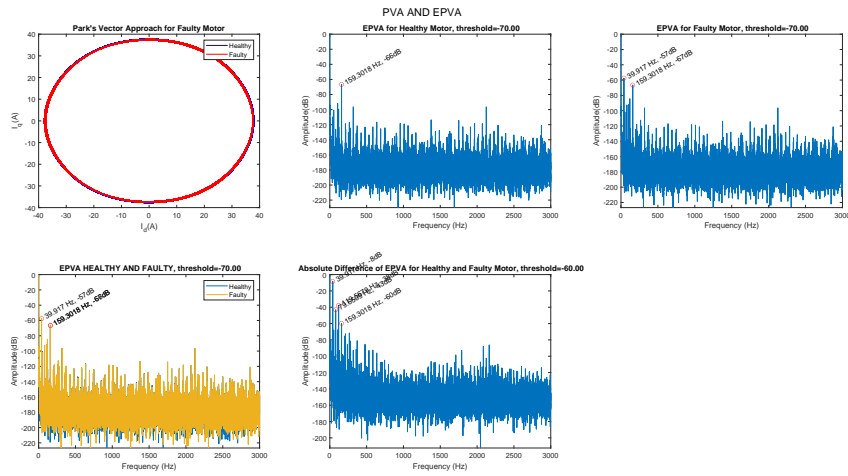


Figure 4.154: Thesis results for: PVA and EPVA (Case Demag 50 13.125)

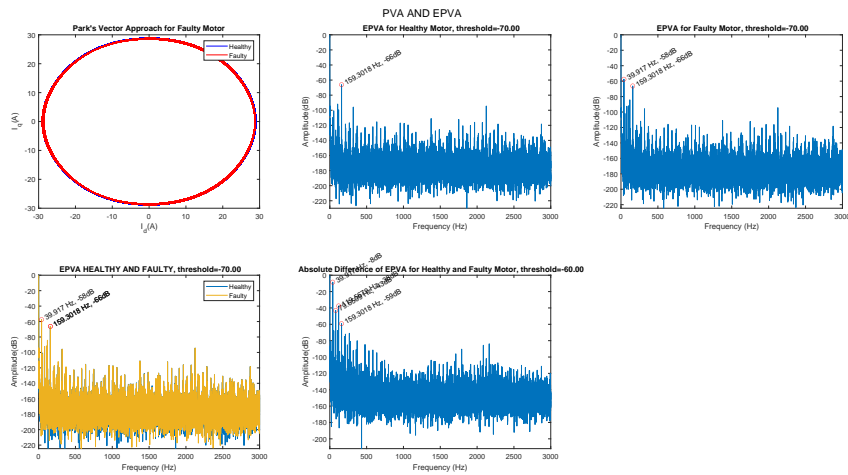


Figure 4.155: Thesis results for: PVA and EPVA (Case Demag 50 17.5)

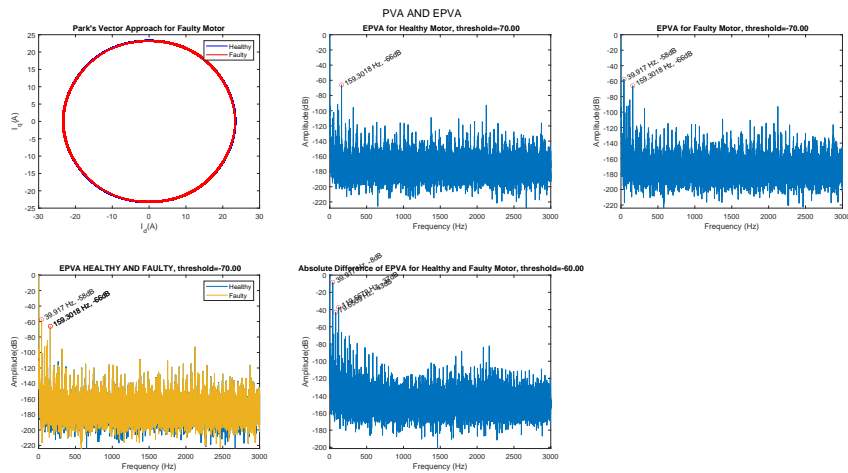


Figure 4.156: Thesis results for: PVA and EPVA (Case Demag 50 21.875)

4.4.3 Demagnetization 25% 50%

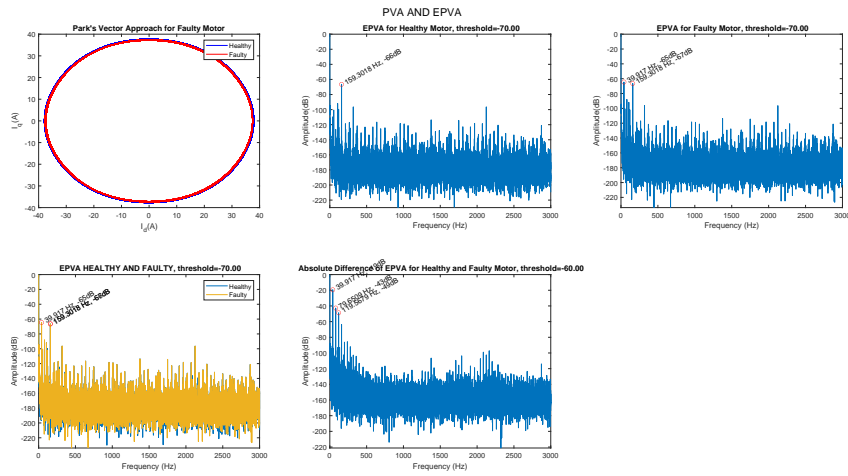


Figure 4.157: Thesis results for: PVA and EPVA (Case Demag 25 50 13.125)

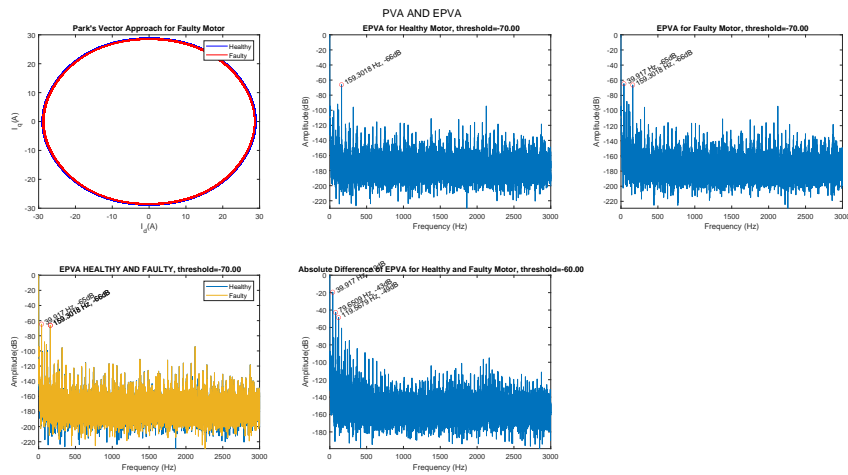


Figure 4.158: Thesis results for: PVA and EPVA (Case Demag 25 50 17.5)

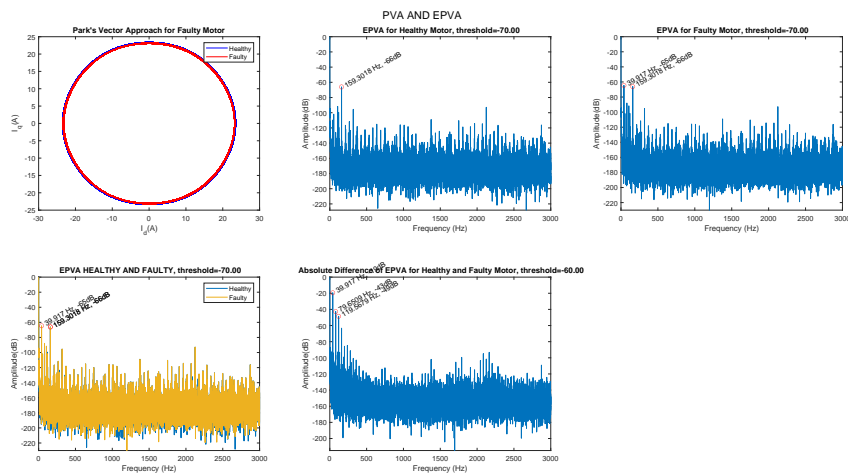


Figure 4.159: Thesis results for: PVA and EPVA (Case Demag 25 50 21.875)

4.4.4 Demagnetization 25% Both

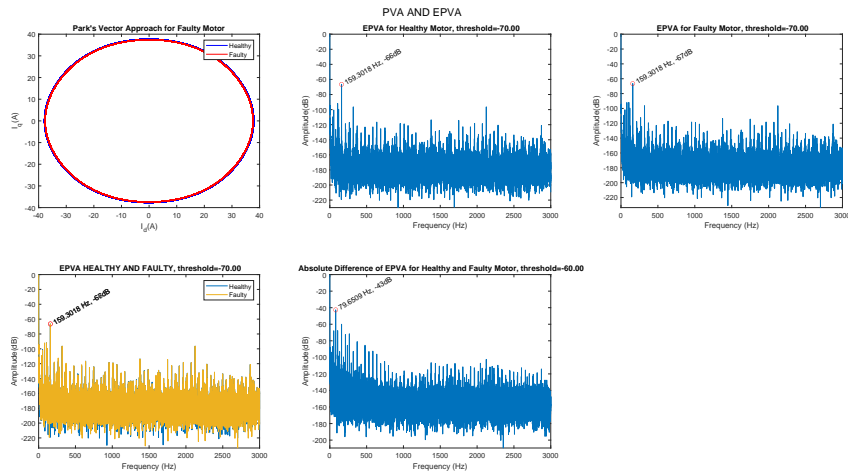


Figure 4.160: Thesis results for: PVA and EPVA (Case Demag 25 Both 13.125)

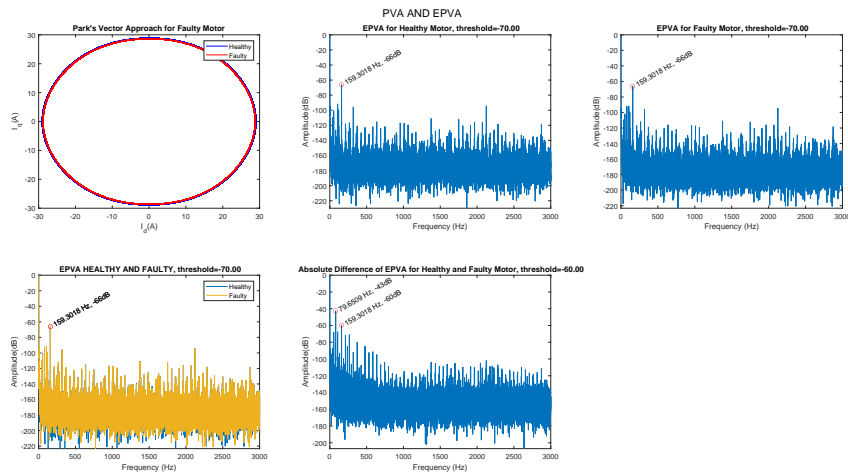


Figure 4.161: Thesis results for: PVA and EPVA (Case Demag 25 Both 17.5)

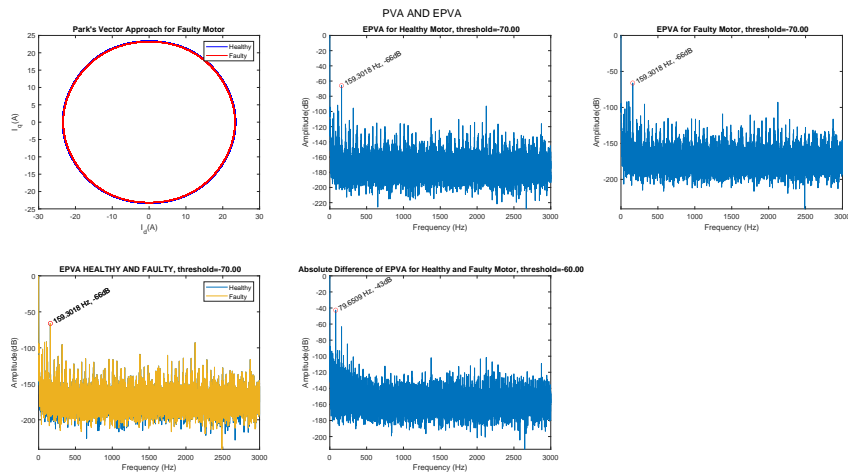


Figure 4.162: Thesis results for: PVA and EPVA (Case Demag 25 Both 21.875)

4.4.5 Demagnetization 50% Both

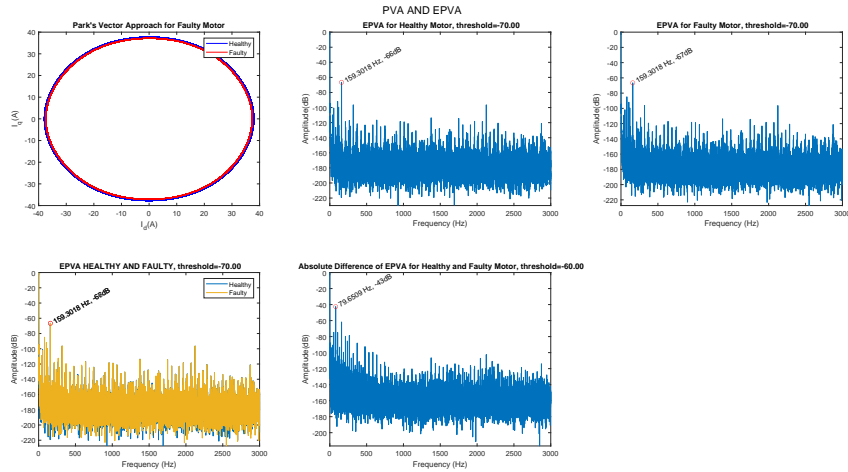


Figure 4.163: Thesis results for: PVA and EPVA (Case Demag 50 Both 13.125)

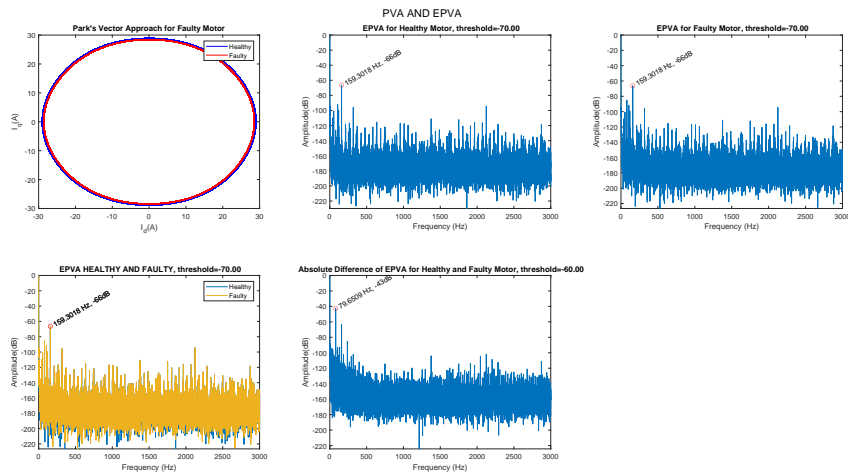


Figure 4.164: Thesis results for: PVA and EPVA (Case Demag 50 Both 17.5)

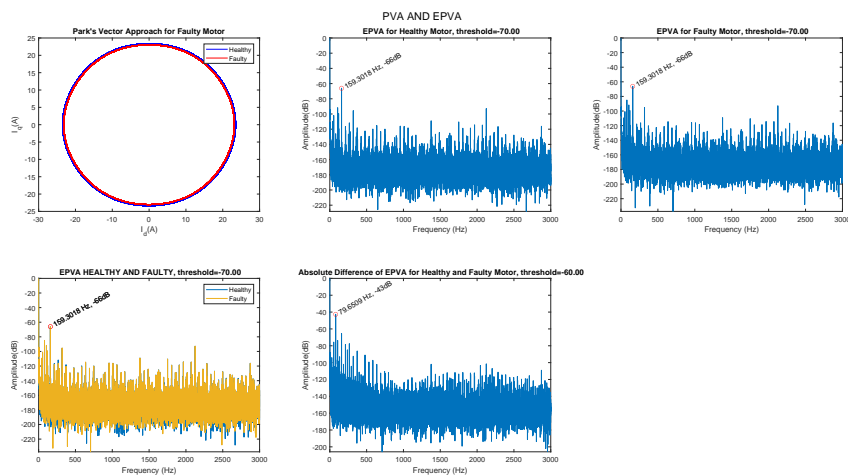


Figure 4.165: Thesis results for: PVA and EPVA (Case Demag 50 Both 21.875)

Chapter 5

Conclusions and Future Works

5.1 Discussion

Table 5.1 displays the root mean square (rms) values for each case, providing insights into the simulation results.

1.)	Simulation	V rms	I rms	Torque avg	Pmech	Pel	eff
2.)	Healthy 17.5	292.3769	16.7073	1.4938e+03	1.5643e+04	1.4654e+04	0.9368
3.)	Healthy 13.125	286.4928	21.8280	1.9517e+03	2.0438e+04	1.8761e+04	0.9179
4.)	Healthy 21.875	295.9876	13.5309	1.2097e+03	1.2668e+04	1.2015e+04	0.9485
5.)	Demag 25 13.125	285.4435	21.7481	1.9405e+03	2.0321e+04	1.8624e+04	0.9165
6.)	Demag 25 17.5	291.3060	16.6461	1.4860e+03	1.5561e+04	1.4547e+04	0.9348
7.)	Demag 25 21.875	294.9080	13.4815	1.2040e+03	1.2608e+04	1.1927e+04	0.9460
8.)	Demag 50 13.125	284.3998	21.6686	1.9356e+03	2.0270e+04	1.8488e+04	0.9121
9.)	Demag 50 17.5	290.2409	16.5852	1.4845e+03	1.5545e+04	1.4441e+04	0.9290
10.)	Demag 50 21.875	293.8343	13.4324	1.2045e+03	1.2614e+04	1.1841e+04	0.9387
11.)	Demag 25 50 13.125	283.3523	21.5888	1.9235e+03	2.0143e+04	1.8352e+04	0.9111
12.)	Demag 25 50 17.5	289.1675	16.5239	1.4757e+03	1.5453e+04	1.4334e+04	0.9276
13.)	Demag 25 50 21.875	292.7431	13.3825	1.1978e+03	1.2543e+04	1.1753e+04	0.9370
14.)	Demag 25 both 13.125	284.3951	21.6682	1.9288e+03	2.0199e+04	1.8487e+04	0.9153
15.)	Demag 25 both 17.5	290.2361	16.5849	1.4777e+03	1.5474e+04	1.4441e+04	0.9332
16.)	Demag 25 both 21.875	293.8249	13.4320	1.1977e+03	1.2543e+04	1.1840e+04	0.9440
17.)	Demag 50 both 13.125	282.2975	21.5084	1.9176e+03	2.0081e+04	1.8215e+04	0.9071
18.)	Demag 50 both 17.5	288.0998	16.4628	1.4731e+03	1.5427e+04	1.4229e+04	0.9223
19.)	Demag 50 both 21.875	291.6622	13.3331	1.1973e+03	1.2538e+04	1.1666e+04	0.9305

Table 5.1: Table with important data for each case

In Table 5.2, we observe that efficiency, voltage and current exhibit relatively stable values even with increasing faults, indicating that these parameters are not highly reliable for fault diagnosis.

1.)	Comparison	Efficiency Difference	Voltage Difference	Current Difference
2.)	Healthy 17.5 Demag 25 17.5	0.2135%	0.3670%	0.3663%
3.)	Healthy 17.5 Demag 50 17.5	0.8326%	0.7303%	0.7308%
4.)	Healthy 17.5 Demag 25 50 17.5	0.9821%	1.0974%	1.0977%
5.)	Healthy 17.5 Demag 25 both 17.5	0.3843%	0.7319%	0.7326%
6.)	Healthy 17.5 Demag 50 both 17.5	1.5478%	1.4626%	1.4634%
7.)	Healthy 13.125 Demag 25 13.125	0.1525%	0.3663%	0.3660%
8.)	Healthy 13.125 Demag 50 13.125	0.6319%	0.7306%	0.7303%
9.)	Healthy 13.125 Demag 25 50 13.125	0.7408%	1.0962%	1.0958%
10.)	Healthy 13.125 Demag 25 both 13.125	0.2833%	0.7322%	0.7321%
11.)	Healthy 13.125 Demag 50 both 13.125	1.1766%	1.4644%	1.4642%
12.)	Healthy 21.875 Demag 25 21.875	0.2636%	0.3647%	0.3651%
13.)	Healthy 21.875 Demag 50 21.875	1.0332%	0.7275%	0.7280%
14.)	Healthy 21.875 Demag 25 50 21.875	1.2124%	1.0962%	1.0967%
15.)	Healthy 21.875 Demag 25 both 21.875	0.4744%	0.7307%	0.7309%
16.)	Healthy 21.875 Demag 50 both 21.875	1.8977%	1.4613%	1.4618%

Table 5.2: Comparison Table with increase and decrease values between healthy and faulty cases.

Tables 5.3 and 5.4 emerge as better indicators for demagnetization faults in each case. The significant increase, attributed to eddy currents impacting the generator, makes them more sensitive indicators.

1.)	Simulation	Ptotal(coil losses)	P(magnet losses)
2.)	Healthy 17.5	628.0651	360.9215
3.)	Healthy 13.125	1.0721e+03	604.9414
4.)	Healthy 21.875	411.9565	240.9687
5.)	Demag 25 13.125	1.0865e+03	610.5076
6.)	Demag 25 17.5	645.7685	368.2732
7.)	Demag 25 21.875	431.2540	249.2105
8.)	Demag 50 13.125	1.1458e+03	636.2146
9.)	Demag 50 17.5	708.2721	395.7572
10.)	Demag 50 21.875	495.3439	277.5788
11.)	Demag 25 50 13.125	1.1512e+03	640.3478
12.)	Demag 25 50 17.5	716.8754	401.6632
13.)	Demag 25 50 21.875	505.4991	284.3531
14.)	Demag 25 both 13.125	1.0965e+03	615.3474
15.)	Demag 25 both 17.5	658.9415	374.8970
16.)	Demag 25 both 21.875	445.9995	256.7121
17.)	Demag 50 both 13.125	1.2013e+03	664.5413
18.)	Demag 50 both 17.5	770.2803	427.6497
19.)	Demag 50 both 21.875	560.4639	311.2102

Table 5.3: Table with the values of Joule losses of all coils in each case and the magnet losses for each simulation.



1.)	Comparison	Ptotal(Coil losses)	P(Magnet Losses)
2.)	Healthy 17.5 Demag 25 17.5	2.7414%	1.9963%
3.)	Healthy 17.5 Demag 50 17.5	11.3243%	8.8023%
4.)	Healthy 17.5 Demag 25 50 17.5	12.3885%	10.1432%
5.)	Healthy 17.5 Demag 25 both 17.5	4.6858%	3.7278%
6.)	Healthy 17.5 Demag 50 both 17.5	18.4628%	15.6035%
7.)	Healthy 13.125 Demag 25 13.125	1.3254%	0.9117%
8.)	Healthy 13.125 Demag 50 13.125	6.4322%	4.9155%
9.)	Healthy 13.125 Demag 25 50 13.125	6.8711%	5.5292%
10.)	Healthy 13.125 Demag 25 both 13.125	2.2253%	1.6911%
11.)	Healthy 13.125 Demag 50 both 13.125	10.7550%	8.9686%
12.)	Healthy 21.875 Demag 25 21.875	4.4747%	3.3072%
13.)	Healthy 21.875 Demag 50 21.875	16.8342%	13.1891%
14.)	Healthy 21.875 Demag 25 50 21.875	18.5050%	15.2572%
15.)	Healthy 21.875 Demag 25 both 21.875	7.6330%	6.1327%
16.)	Healthy 21.875 Demag 50 both 21.875	26.4972%	22.5704%

Table 5.4: Table with the increase value of Joule loses of all coils in each case and the magnet loses for each simulation.

Tables 5.5 and 5.6 present values for $\frac{f_s}{2}$ and $2f_s$. Notably, $\frac{f_s}{2}$ exhibits a substantial amplitude increase in the case of single demagnetizations. Furthermore, the tables confirm a cancellation phenomenon in the amplitude values for 2 non-adjacent demagnetizations, particularly in both 25% and 50% demagnetizations. In the case of one demagnetization at 25% and the other at 50%, the signatures resemble those of a single 25% magnet demagnetization. As for $2f_s$, there are smaller amplitude increases and the cancellation phenomenon observed in $\frac{f_s}{2}$ is not evident. However, due to the limited differentiation between healthy and faulty cases in the experimental results, $2f_s$ is deemed an unreliable harmonic for diagnosis.

1.)	Simulation	Fs/2(I1)	2Fs(I1)	Fs/2(I2)	2Fs(I2)	Fs/2(I3)	2Fs(I3)
2.)	Healthy 17.5	-119.32	-119.791	-119.94	-119.967	-120.325	-120.018
3.)	Healthy 13.125	-119.175	-119.87	-119.788	-120.044	-120.196	-120.09
4.)	Healthy 21.875	-119.378	-119.621	-119.896	-119.775	-120.46	-119.85
5.)	Demag 25 13.125	-58.0275	-87.602	-58.0236	-87.532	-58.0231	-87.5262
6.)	Demag 25 17.5	-58.3413	-87.5426	-58.3437	-87.4727	-58.0438	-87.4665
7.)	Demag 25 21.875	-58.0601	-87.5089	-58.0562	-87.4389	-58.0558	-87.4325
8.)	Demag 50 13.125	-51.0419	-80.4053	-51.0397	-80.3405	-51.0393	-80.3354
9.)	Demag 50 17.5	-51.0625	-80.3454	-51.0604	-80.2806	-51.06	-80.2753
10.)	Demag 50 21.875	-51.075	-80.306	-51.0726	-80.2476	-51.0724	-80.2341
11.)	Demag 25 50 13.125	-57.8976	-76.255	-57.9004	-76.1981	-57.9002	-76.1851
12.)	Demag 25 50 17.5	-57.9188	-76.1996	-57.9218	-76.1363	-57.9215	-76.1314
13.)	Demag 25 50 21.875	-57.9308	-76.1653	-57.9338	-76.102	-57.9336	-76.0969
14.)	Demag 25 both 13.125	-118.509	-80.4365	-118.938	-80.3713	-119.423	-80.3662
15.)	Demag 25 both 17.5	-118.719	-80.3766	-119.149	-80.3114	-119.831	-80.3062
16.)	Demag 25 both 21.875	-118.843	-80.3424	-119.269	-80.2773	-119.86	-80.2719
17.)	Demag 50 both 13.125	-117.902	-73.2991	-118.258	-73.2366	-118.616	-73.2318
18.)	Demag 50 both 17.5	-118.411	-73.2343	-118.847	-73.1783	-119.502	-73.1653
19.)	Demag 50 both 21.875	-118.534	-73.1998	-118.966	-73.1438	-119.545	-73.1309

Table 5.5: Table with harmonics values(dB) for each phase.



1.)	Comparison	Fs/2(I1)	2Fs(I1)	Fs/2(I2)	2Fs(I2)	Fs/2(I3)	2Fs(I3)
2.)	Healthy 17.5 Demag 25 17.5	51.1052%	26.9206%	51.3559%	27.0860%	51.7608%	27.1222%
3.)	Healthy 17.5 Demag 50 17.5	57.2054%	32.9287%	57.4284%	33.0811%	57.5649%	33.1139%
4.)	Healthy 17.5 Demag 25 50 17.5	51.4593%	36.3895%	51.7077%	36.5356%	51.8625%	36.5667%
5.)	Healthy 17.5 Demag 25 both 17.5	0.5037%	32.9026%	0.6588%	33.0554%	0.4106%	33.0882%
6.)	Healthy 17.5 Demag 50 both 17.5	0.7618%	38.8649%	0.9113%	39.0013%	0.6840%	39.0381%
7.)	Healthy 13.125 Demag 25 13.125	51.3090%	26.9192%	51.5614%	27.0834%	51.7263%	27.1162%
8.)	Healthy 13.125 Demag 50 13.125	57.1706%	32.9229%	57.3916%	33.0741%	57.5366%	33.1040%
9.)	Healthy 13.125 Demag 25 50 13.125	51.4180%	36.3853%	51.6643%	36.5249%	51.8285%	36.5600%
10.)	Healthy 13.125 Demag 25 both 13.125	0.5588%	32.8969%	0.7096%	33.0485%	0.6431%	33.0784%
11.)	Healthy 13.125 Demag 50 both 13.125	1.0682%	38.8512%	1.2773%	38.9919%	1.3145%	39.0192%
12.)	Healthy 21.875 Demag 25 21.875	51.3645%	26.8449%	51.5779%	26.9974%	51.8049%	27.0484%
13.)	Healthy 21.875 Demag 50 21.875	57.2157%	32.8663%	57.4026%	33.0014%	57.6022%	33.0546%
14.)	Healthy 21.875 Demag 25 50 21.875	51.4728%	36.3278%	51.6800%	36.4625%	51.9064%	36.5065%
15.)	Healthy 21.875 Demag 25 both 21.875	0.4482%	32.8359%	0.5230%	32.9766%	0.4981%	33.0230%
16.)	Healthy 21.875 Demag 50 both 21.875	0.7070%	38.8069%	0.7757%	38.9323%	0.7596%	38.9813%

Table 5.6: Table with increase values of harmonics values(dB) for each phase between healthy and faulty.

Table 5.7 reflects a similar phenomenon in diagnosing the coils of the machine as described in cases 5.5 and 5.6.

1.)	Simulation	Fs/2(Coil 11)	2Fs(Coil 11)	Fs/2(Coil 12)	2Fs(Coil 12)	Fs/2(Coil 13)	2Fs(Coil 13)	Fs/2(Coil 14)	2Fs(Coil 14)	Fs/2(Coil 15)	2Fs(Coil 15)	Fs/2(Coil 16)	2Fs(Coil 16)	Fs/2(Coil 17)	2Fs(Coil 17)	Fs/2(Coil 18)	2Fs(Coil 18)
2.)	Healthy 17.5	-119.434	-119.260	-119.22	-119.523	-119.275	-120.723	-119.323	-119.71	-119.408	-119.622	-119.330	-119.817	-119.067	-120.071	-119.461	-119.648
3.)	Healthy 13.125	-119.250	-119.440	-119.1	-119.673	-119.145	-120.580	-119.170	-119.807	-119.238	-119.735	-119.178	-119.900	-118.983	-120.001	-119.297	-119.744
4.)	Healthy 21.875	-119.376	-119.401	-119.22	-119.116	-119.388	-120.584	-119.503	-119.432	-119.384	-119.763	-119.264	-119.264	-119.64	-119.664	-119.201	-119.758
5.)	Demag 25 13.125	-58.0338	-87.4358	-58.0305	-87.5422	-57.9781	-88.2114	-58.0672	-87.2296	-58.0304	-87.3460	-58.0418	-87.5008	-58.0215	-87.9102	-58.016	-87.6546
6.)	Demag 25 17.5	-58.0558	-87.3194	-58.0512	-87.4734	-57.9846	-88.3193	-58.1004	-87.0728	-58.0523	-87.207	-58.067	-87.4193	-58.04	-87.9471	-58.0327	-87.6057
7.)	Demag 25 21.875	-58.0601	-87.2288	-58.0632	-87.4297	-57.9824	-88.4528	-58.1248	-86.9414	-58.0656	-87.0931	-58.0835	-87.363	-58.0498	-88.0105	-58.0408	-87.5821
8.)	Demag 50 13.125	-51.0484	-80.2319	-51.0419	-80.346	-50.9924	-81.0188	-51.0814	-80.0371	-51.0444	-80.1493	-51.0562	-80.3057	-51.0363	-80.7124	-51.0302	-80.4561
9.)	Demag 50 17.5	-51.0705	-80.1139	-51.0656	-80.2761	-50.9989	-81.1272	-51.1145	-79.8809	-51.0663	-80.009	-51.0815	-80.227	-51.0549	-80.7483	-51.047	-80.4064
10.)	Demag 50 21.875	-51.0904	-79.7105	-51.0754	-80.1916	-50.996	-81.2411	-51.1375	-80.1075	-51.0824	-79.9526	-51.0939	-80.1090	-51.0685	-80.7004	-51.0548	-80.4604
11.)	Demag 25 50 13.125	-57.9448	-75.8982	-57.9043	-76.1715	-57.8286	-76.8531	-57.9124	-76.1100	-57.8872	-76.0298	-57.9103	-76.1084	-57.8943	-76.5123	-57.8985	-76.3707
12.)	Demag 25 50 17.5	-57.9748	-75.9856	-57.9293	-76.1313	-57.8306	-76.9755	-57.9398	-75.7229	-57.9024	-75.858	-57.9396	-76.0694	-57.9141	-76.6089	-57.9187	-76.2819
13.)	Demag 25 50 21.875	-58	-75.8975	-57.9433	-76.0866	-57.8225	-77.1083	-57.9567	-75.5895	-57.9105	-75.7429	-57.9567	-76.01	-57.9251	-76.6732	-57.9007	-76.25
14.)	Demag 25 both 13.125	-113.448	-80.2779	-117.831	-80.376	-115.721	-81.0434	-114.911	-80.0607	-115.346	-80.1806	-117.65	-80.3303	-115.331	80.7449	-119.092	-80.4952
15.)	Demag 25 both 17.5	-111.674	-80.1639	-117.794	-80.3058	-114.437	-81.1499	-113.3667	-79.9025	-113.448	-80.0403	-117.605	-80.2457	-114.546	-80.7817	-119.431	-80.4477
16.)	Demag 25 both 21.875	-109.99	-80.0759	-117.606	-80.2609	-113.179	-81.2824	-111.937	-79.7098	-111.734	-79.9264	-117.447	-80.1866	-113.684	-80.8451	-119.548	-80.4257
17.)	Demag 50 both 13.125	-107.44	-73.1301	-116	-73.2425	-112.272	-73.9123	-110.723	-72.9244	-110.319	-73.0351	-116.127	-73.199	-111.484	-73.612	-116.731	-73.356
18.)	Demag 50 both 17.5	-105.382	-72.7572	-116.176	-73.1374	-109.781	-74.0031	-108.175	-73.06	-107.399	-72.9355	-136.414	-73.0628	-110.44	-73.5671	-116.931	-73.3728
19.)	Demag 50 both 21.875	-103.379	-72.6127	-115.506	-73.0861	-108.019	-74.1348	-106.341	-72.9932	-105.336	-72.8323	-115.989	-72.996	-109.065	-73.6063	-115.94	-73.3657

Table 5.7: Table with Harmonic values(dB) for each $Coil_{1-8}$ of Phase 1.

Tables 5.8 and 5.9 present the rms values for the 4 parallel coils of 1 phase for voltage and current. Notably, the current exhibits a more intense increase than the load current, leading to higher joule losses and, subsequently, increased temperature inside the generator. This temperature rise can be further studied through thermal diagnosis of the generator.

1.)	Simulation	Vpar rms	Ipar rms
2.)	Healthy 17.5	146.4132	4.1754
3.)	Healthy 13.125	143.4765	5.4552
4.)	Healthy 21.875	148.2143	3.3815
5.)	Demag 25 13.125	142.9733	5.4903
6.)	Demag 25 17.5	145.8992	4.2319
7.)	Demag 25 21.875	147.6971	3.4575
8.)	Demag 50 13.125	142.4787	5.6339
9.)	Demag 50 17.5	145.3939	4.4267
10.)	Demag 50 21.875	147.1886	3.6993
11.)	Demag 25 50 13.125	141.9488	5.6524
12.)	Demag 25 50 17.5	144.8498	4.4602
13.)	Demag 25 50 21.875	146.6343	3.7451
14.)	Demag 25 both 13.125	142.4566	5.5160
15.)	Demag 25 both 17.5	145.3717	4.2757
16.)	Demag 25 both 21.875	147.1630	3.5172
17.)	Demag 50 both 13.125	141.4462	5.7715
18.)	Demag 50 both 17.5	144.3429	4.6202
19.)	Demag 50 both 21.875	146.1209	3.9398

Table 5.8: Table with Rms values of Voltage and Current for 4 Parallel $Coils_{1-4}$ of Phase 1.

1.)	Comparison	Voltage Difference	Current Difference
2.)	Healthy 17.5 Demag 25 17.5	0.3511%	1.3351%
3.)	Healthy 17.5 Demag 50 17.5	0.6962%	5.6769%
4.)	Healthy 17.5 Demag 25 50 17.5	1.0678%	6.3854%
5.)	Healthy 17.5 Demag 25 both 17.5	0.7113%	2.3458%
6.)	Healthy 17.5 Demag 50 both 17.5	1.4140%	9.6273%
7.)	Healthy 13.125 Demag 25 13.125	0.3507%	0.6393%
8.)	Healthy 13.125 Demag 50 13.125	0.6954%	3.1719%
9.)	Healthy 13.125 Demag 25 50 13.125	1.0648%	3.4888%
10.)	Healthy 13.125 Demag 25 both 13.125	0.7108%	1.1022%
11.)	Healthy 13.125 Demag 50 both 13.125	1.4151%	5.4804%
12.)	Healthy 21.875 Demag 25 21.875	0.3490%	2.1981%
13.)	Healthy 21.875 Demag 50 21.87	0.6920%	8.5908%
14.)	Healthy 21.875 Demag 25 50 21.875	1.0660%	9.7087%
15.)	Healthy 21.875 Demag 25 both 21.875	0.7093%	3.8582%
16.)	Healthy 21.875 Demag 50 both 21.875	1.4124%	14.1708%

Table 5.9: Table with increase and decrease of Rms values of Voltage and Current for 4 Parallel $Coils_{1-4}$ of Phase 1 between Healthy and Faulty.

Table 5.10 presents amplitudes of various signatures of $Sensor_1$ for the mechanical speed-related sidebands $f_s \pm k \frac{f_s}{p}$. They increase with the fault severity level as depicted. The harmonic $f_s - \frac{f_s}{p}$, between 25% 50% demagnetization (non-adjacent magnets) and 50% both demagnetization, exhibits tremendous increase. Also, for instances of both 25% and 50% demagnetization in non-adjacent magnets as portrayed we have a cancellation phenomenon at $k=8$.

1.)	Cases	Healthy (dB)	25% Demag (dB)	50% Demag (dB)	25% 50% Demag (dB)	25% Both Demag (dB)	50% Both Demag (dB)
2.)	fs - 1fs/2	-76.48	-60.47	-52.58	-48.31	-52.72	-45.31
3.)	fs - 2fs/2	-96.49	-58.72	-51.85	-48.51	-52.66	-45.7
4.)	fs - 3fs/2	-118.37	-57.68	-50.7	-48.2	-52.54	-45.53
5.)	fs - 4fs/2	-114.2	-59.09	-52.11	-50.94	-55.56	-48.55
6.)	fs - 5fs/2	-122.61	-60.79	-53.82	-54.5	-59.71	-52.69
7.)	fs - 6fs/2	-126.34	-59.81	-52.83	-55.84	-62.43	-55.42
8.)	fs - 7fs/2	-147.87	-58.85	-51.88	-57.44	-68.22	-61.21
9.)	fs - 8fs/2	-122.27	-60.26	-53.28	-60.14	-122.27	-122.27
10.)	fs - 9fs/2	-138.29	-62.67	-55.69	-61.25	-72.05	-65.03
11.)	fs - 10fs/2	-134.16	-63.15	-56.18	-59.19	-65.78	-58.78
12.)	fs - 11fs/2	-136.29	-63.95	-56.98	-57.66	-62.86	-55.85
13.)	fs - 12fs/2	-126.57	-66.94	-59.97	-58.82	-63.45	-56.43
14.)	fs - 13fs/2	-143.44	-71.09	-64.11	-61.62	-65.96	-58.95
15.)	fs - 14fs/2	-125.19	-77.33	-70.33	-66.94	-71.15	-64.11
16.)	fs - 15fs/2	-126.33	-92.45	-85.34	-81.39	-85.56	-78.47

Table 5.10: Table with Amplitude of Left Sidebands of *Sensor*₁ Used for Flux Monitoring.

5.2 Conclusion [10, 61]

In this comprehensive investigation, various fault diagnosis techniques were rigorously applied to discern the most effective approach for detecting rotor demagnetization faults. Examining time domain signals revealed minimal distinctions in most cases, except for the currents in the four coils, where demagnetization was conspicuously evident, particularly with severe faults.

Notably, Motor Current Signature Analysis (MCSA) yielded intriguing insights. Traditionally associated with stator faults, the observation of rotor harmonics in multiples of the stator's frequency in C-GEN is groundbreaking. However, this discovery poses a potential misdiagnosis risk, especially in scenarios of 25% or 50% demagnetization, where a cancellation phenomenon occurs in $\frac{f_s}{2}$, leading to the observation of faults only at $2f_s$ —commonly linked with stator faults.

Fourier analysis of the current in the four coils presented promising results, although practical limitations arise due to challenges in real-life current measurement. Therefore, alternative or complementary diagnostic techniques may be imperative for robust demagnetization fault detection.

Torque monitoring showcased a substantial amplitude increase, offering a clear distinction between healthy and faulty cases at $f_s + \frac{f_s}{2}$. In flux monitoring, mechanical speed-related sidebands at $f_s \pm k\frac{f_s}{p}$ increased with the severity of demagnetization, notably in cases of 25% and 50% demagnetization in non-adjacent magnets at $\frac{f_s}{2}$.

In the final analysis, Park Vector Approach (PVA) proved insufficient for detailed insights into demagnetization phenomena. However, Extended Park's Vector Approach (EPVA) emerged as a more ideal option, providing distinct fault indications at $f_s + \frac{f_s}{2}$, except in cases of 25% and 50% demagnetization in non-adjacent magnets, where a cancellation phenomenon at this frequency could lead to a misdiagnosis of a healthy motor.

This exhaustive exploration not only enhances our understanding of rotor demagnetization diagnostics but also underscores the importance of selecting and combining diagnostic techniques judiciously for accurate fault detection in generators.

5.3 Future work

The disparities in the time domain of current differences across the four coils, underscore the urgent need for an in-depth exploration of the thermal implications within the generator. As a future work of investigation, the utilization of the generator's thermal model can provide valuable insights into the observed differences, shedding light on the extent of thermal stress on the generator. This exploration can offer a comprehensive understanding of the thermal dynamics within the generator, contributing to enhanced predictive maintenance strategies.

Furthermore, in flux monitoring, specifically focusing on right sidebands, presents a promising area for future exploration. Studying deeper into this aspect can unravel important details and patterns, providing a more comprehensive understanding of how right sidebands manifest in the context of demagnetization faults. A



detailed investigation can achieve valuable insights that contribute to refining and optimizing flux monitoring techniques for enhanced fault detection.

In the domain of torque monitoring, there is a rich potential for future research to dig into the generation mechanisms of harmonics. A detailed study can unravel the complicated processes underlying harmonic generation during demagnetization faults. Understanding the distinct characteristics of each demagnetization scenario and the corresponding harmonic signatures can show the way for more accurate fault diagnosis. This area holds the promise of refining torque monitoring techniques and advancing our capabilities in detecting and classifying demagnetization faults.

In conclusion, the identified areas for future work not only address current limitations but also present exciting opportunities to dig deeper into the complexities of thermal dynamics, flux monitoring, and torque characteristics. These investigations can significantly contribute to the advancement of fault diagnosis techniques, ultimately enhancing the reliability and effectiveness of generator health monitoring systems.

Bibliography

- [1] A. Economics, “Offshore wind energy in greece: Estimating the socio-economic impact,” 2021.
- [2] K. N. Gyftakis, G. Skarmoutsos, I. Barajas-Solano, J. Burchell, and M. Mueller, “Critical aspects of demagnetization faults in direct drive permanent magnet generators for renewables,” in *2022 IEEE Energy Conversion Congress and Exposition (ECCE)*, 2022, pp. 1–7.
- [3] K. N. Gyftakis, S. Rasid, and M. Mueller, “False negative diagnosis of demagnetization in direct drive permanent magnet generators,” in *2022 International Conference on Electrical Machines (ICEM)*, 2022, pp. 696–702.
- [4] Y. Jia, Y. Du, Y. Wang, B. Zhang, W. Cao, Y. Ren, and C. Li, “Finite element simulation on irreversible demagnetization of permanent magnet synchronous generator,” in *2022 9th International Conference on Condition Monitoring and Diagnosis (CMD)*, 2022, pp. 408–412.
- [5] H. Chen, R. Qu, J. Li, and D. Li, “Demagnetization performance of a 7 mw interior permanent magnet wind generator with fractional-slot concentrated windings,” *IEEE Transactions on Magnetics*, vol. 51, no. 11, pp. 1–4, 2015.
- [6] N. Shahbaz, Y. Chen, F. Liang, S. Zhao, S. Zhang, S. Wang, Y. Ma, Y. Zhao, and W. Deng, “Research and application of intelligent diagnosis technology in permanent magnet generator for stress demagnetization fault,” in *2022 International Conference on Sensing, Measurement Data Analytics in the era of Artificial Intelligence (ICSMD)*, 2022, pp. 1–4.
- [7] A. Lamprokostopoulos and E. Mitronikas, “Demagnetization fault diagnosis of a pmsg based on instantaneous power signatures,” in *2022 International Conference on Electrical Machines (ICEM)*, 2022, pp. 1595–1601.
- [8] L. Wang, X. Bi, H. Xing, and F. Marignetti, “Three-dimensional thermal calculation and analysis of a wind driven pmsg with different demagnetization faults,” in *2021 IEEE 4th International Electrical and Energy Conference (CIEEC)*, 2021, pp. 1–6.
- [9] M. R. Mínaz and E. Akcan, “An effective method for detection of demagnetization fault in axial flux coreless pmsg with texture-based analysis,” *IEEE Access*, vol. 9, pp. 17 438–17 449, 2021.
- [10] K. N. Gyftakis, S. A. Rasid, G. A. Skarmoutsos, and M. Mueller, “The demagnetization harmonics generation mechanism in permanent magnet machines with concentrated windings,” *IEEE Transactions on Energy Conversion*, vol. 36, no. 4, pp. 2934–2944, 2021.
- [11] M. Mueller and A. McDonald, “A lightweight low-speed permanent magnet electrical generator for direct-drive wind turbines,” *Wind Energy*, vol. 12, pp. 768 – 780, 11 2009.
- [12] M. K. Saini, “Synchronous generator construction and working principle,” 2023. [Online]. Available: <https://www.tutorialspoint.com/synchronous-generator-construction-and-working-principle>
- [13] W. Contributors, “Permanent magnet synchronous generator,” 2018. [Online]. Available: https://en.wikipedia.org/wiki/Permanent_magnet_synchronous_generator
- [14] O. Keysan, A. McDonald, M. Mueller, R. Doherty, and M. Hamilton, “C-gen, a lightweight direct drive generator for marine energy converters,” in *5th IET International Conference on Power Electronics, Machines and Drives (PEMD 2010)*, 2010, pp. 1–6.
- [15] R. Waters, M. Rahm, O. Danielsson, O. Svensson, S. Gustafsson, E. Stromstedt, M. Eriksson, J. Sundberg, and M. Leijon, “Experimental results from sea trials of an offshore wave energy system,” *Applied Physics Letters*, vol. 90, pp. 034 105–034 105, 01 2007.



- [16] N. Hodgins, A. McDonald, J. Shek, O. Keysan, and M. Mueller, “Current and future developments of the c-gen lightweight direct drive generator for wave tidal energy,” in *Proceedings of the 8th European Wave and Tidal Energy Conference, Uppsala, Sweden, 2009*, Sep. 2009, pp. 352–359.
- [17] B. S. Guru and H. R. Hiziroglu, *Electromagnetic Field Theory Fundamentals*. Cambridge University Press, 2009.
- [18] T. Judendorfer, J. Fletcher, N. Hassanain, M. Mueller, and M. Muhr, “Challenges to machine windings used in electrical generators in wave and tidal power plants,” pp. 238–241, 08 2009.
- [19] S. B. Lee, G. C. Stone, J. Antonino-Daviu, K. N. Gyftakis, E. G. Strangas, P. Maussion, and C. A. Platero, “Condition monitoring of industrial electric machines: State of the art and future challenges,” *IEEE Industrial Electronics Magazine*, vol. 14, no. 4, pp. 158–167, 2020.
- [20] S. Nandi, H. Toliyat, and X. Li, “Condition monitoring and fault diagnosis of electrical motors—a review,” *Energy Conversion, IEEE Transactions on*, vol. 20, pp. 719 – 729, 01 2006.
- [21] M. Riera-Guasp, J. Antonino-Daviu, and G.-A. Capolino, “Advances in electrical machine, power electronic, and drive condition monitoring and fault detection: State of the art,” *IEEE Transactions on Industrial Electronics*, vol. 62, pp. 1746–1759, 03 2015.
- [22] G. B. K. Hamid A. Toliyat, *Handbook of Electric Motors*. CRC Press, 2004.
- [23] W. Thomson and M. Fenger, “Current signature analysis to detect induction motor faults,” *IEEE Industry Applications Magazine*, vol. 7, no. 4, pp. 26–34, 2001.
- [24] D. Dorrell, W. Thomson, and S. Roach, “Analysis of airgap flux, current, and vibration signals as a function of the combination of static and dynamic airgap eccentricity in 3-phase induction motors,” *IEEE Transactions on Industry Applications*, vol. 33, no. 1, pp. 24–34, 1997.
- [25] O. Gubarevych, J. Gerlici, O. Kravchenko, I. Melkonova, and O. Melnyk, “Use of park’s vector method for monitoring the rotor condition of an induction motor as a part of the built-in diagnostic system of electric drives of transport,” *Energies*, vol. 16, p. 5109, 07 2023.
- [26] D. V. Spyropoulos and E. D. Mitronikas, “Induction motor stator fault diagnosis technique using park vector approach and complex wavelets,” in *2012 XXth International Conference on Electrical Machines*, 2012, pp. 1730–1734.
- [27] S. Wei, X. Zhang, Y. Xu, Y. Fu, Z. Ren, and F. Li, “Extended park’s vector method in early inter-turn short circuit fault detection for the stator windings of offshore wind doubly-fed induction generators,” *IET Generation, Transmission & Distribution*, vol. 14, no. 18, pp. 3905–3912, 2020. [Online]. Available: <https://ietresearch.onlinelibrary.wiley.com/doi/abs/10.1049/iet-gtd.2020.0127>
- [28] S. Jagers, “Motor current signature analysis (mcsa) and condition monitoring,” 2019. [Online]. Available: <https://samotics.com/blog/motor-current-signature-analysis/>
- [29] W. T. Thomson and I. Culbert, *Motor Current Signature Analysis for Induction Motors*, 2017, pp. 1–37.
- [30] M. W. Abitha and V. Rajini, “Park’s vector approach for online fault diagnosis of induction motor,” in *2013 International Conference on Information Communication and Embedded Systems (ICICES)*, 2013, pp. 1123–1129.
- [31] G. A. Skarmoutsos, K. N. Gyftakis, and M. Mueller, “Analytical prediction of the mcsa signatures under dynamic eccentricity in pm machines with concentrated non-overlapping windings,” *IEEE Transactions on Energy Conversion*, vol. 37, no. 2, pp. 1011–1019, 2022.
- [32] D. PATRANABI, *SENSORS AND TRANSDUCERS*. PHI Learning, 2003. [Online]. Available: <https://books.google.gr/books?id=7plyKXMbxgC>
- [33] G. Brooker, *Introduction to Sensors for Ranging and Imaging*, ser. Radar, Sonar and Navigation. Institution of Engineering and Technology, 2009. [Online]. Available: <https://digital-library.theiet.org/content/books/ra/sbra014e>
- [34] J. Penman, M. Dey, A. Tait, and W. Bryan, “Condition monitoring of electrical drives,” *IEE Proceedings B (Electric Power Applications)*, vol. 133, pp. 142–148(6), May 1986. [Online]. Available: <https://digital-library.theiet.org/content/journals/10.1049/ip-b.1986.0019>



- [35] A. Ceban, R. Pusca, and R. Romary, "Study of rotor faults in induction motors using external magnetic field analysis," *IEEE Transactions on Industrial Electronics*, vol. 59, no. 5, pp. 2082–2093, 2012.
- [36] L. Frosini, C. Harlișca, and L. Szabo, "Induction machine bearing fault detection by means of statistical processing of the stray flux measurement," *IEEE Transactions on Industrial Electronics*, vol. 62, pp. 1846–1854, 03 2015.
- [37] M. Irhoumah, R. Pusca, E. Lefevre, D. Mercier, R. Romary, and C. Demian, "Information fusion with belief functions for detection of interturn short-circuit faults in electrical machines using external flux sensors," *IEEE Transactions on Industrial Electronics*, vol. 65, no. 3, pp. 2642–2652, 2018.
- [38] J. Yun, S. Park, C. Yang, S. Lee, J. Antonino-Daviu, M. Sasic, and G. Stone, "Airgap search coil-based detection of damper bar failures in salient pole synchronous motors," *IEEE Transactions on Industry Applications*, vol. PP, pp. 1–1, 04 2019.
- [39] G. Mirzaeva, K. I. Saad, and M. G. Jahromi, "Comprehensive diagnostics of induction motor faults based on measurement of space and time dependencies of air gap flux," *IEEE Transactions on Industry Applications*, vol. 53, pp. 2657–2666, 2017. [Online]. Available: <https://api.semanticscholar.org/CorpusID:43756495>
- [40] Y. Park, H. Choi, S. Lee, and K. Gyftakis, "Flux-based detection of non-adjacent rotor bar damage in squirrel cage induction motors," 09 2019, pp. 7019–7026.
- [41] F. Mahmouditabar, A. Vahedi, and F. Marignetti, "The demagnetization phenomenon in pm machines: Principles, modeling, and design considerations," *IEEE Access*, vol. 11, pp. 47 750–47 773, 2023.
- [42] Y. Zhilichev, "Analysis of permanent magnet demagnetization accounting for minor $b-h$ curves," *IEEE Transactions on Magnetics*, vol. 44, no. 11, pp. 4285–4288, 2008.
- [43] P. Pietrzak and M. Wolkiewicz, "Demagnetization fault diagnosis of permanent magnet synchronous motors based on stator current signal processing and machine learning algorithms," *Sensors*, vol. 23, no. 4, 2023. [Online]. Available: <https://www.mdpi.com/1424-8220/23/4/1757>
- [44] J. Faiz and H. Nejadi Koti, "Demagnetization fault indexes in permanent magnet synchronous motors ? an overview," *IEEE Transactions on Magnetics*, vol. 52, pp. 1–1, 01 2015.
- [45] S. Ruoho, J. Kolehmainen, J. Ikaheimo, and A. Arkkio, "Interdependence of demagnetization, loading, and temperature rise in a permanent-magnet synchronous motor," *Magnetics, IEEE Transactions on*, vol. 46, pp. 949 – 953, 04 2010.
- [46] J. Mcfarland and T. Jahns, "Investigation of the rotor demagnetization characteristics of interior pm synchronous machines during fault conditions," *IEEE Transactions on Industry Applications*, vol. 50, pp. 2768–2775, 07 2014.
- [47] D. Torregrossa, A. Khoobroo, and B. Fahimi, "Prediction of acoustic noise and torque pulsation in pm synchronous machines with static eccentricity and partial demagnetization using field reconstruction method," *Industrial Electronics, IEEE Transactions on*, vol. 59, pp. 934 – 944, 03 2012.
- [48] J.-C. Urresty, R. Atashkhoei, J.-R. Riba, L. Romeral, and S. Royo, "Shaft trajectory analysis in a partially demagnetized permanent-magnet synchronous motor," *IEEE Transactions on Industrial Electronics*, vol. 60, no. 8, pp. 3454–3461, 2013.
- [49] J. Urresty, J.-R. Riba, and L. Romeral, "A back-emf based method to detect magnet failures in pmsms," *Magnetics, IEEE Transactions on*, vol. PP, pp. 1–1, 01 2012.
- [50] J.-C. Urresty, J.-R. Riba, M. Delgado, and L. Romeral, "Detection of demagnetization faults in surface-mounted permanent magnet synchronous motors by means of the zero-sequence voltage component," *IEEE Transactions on Energy Conversion*, vol. 27, no. 1, pp. 42–51, 2012.
- [51] J. De Bisschop, A. A.-E. Abdallah, P. Sergeant, and L. Dupré, "Analysis and selection of harmonics sensitive to demagnetisation faults intended for condition monitoring of double rotor axial flux permanent magnet synchronous machines," *IET Electric Power Applications*, vol. 12, no. 4, pp. 486–493, 2018. [Online]. Available: <https://ietresearch.onlinelibrary.wiley.com/doi/abs/10.1049/iet-epa.2017.0568>
- [52] W. Le Roux, R. Harley, and T. Habetler, "Detecting rotor faults in permanent magnet synchronous machines," in *4th IEEE International Symposium on Diagnostics for Electric Machines, Power Electronics and Drives, 2003. SDEMPED 2003.*, 2003, pp. 198–203.



- [53] J. Bossio, C. Ruschetti, G. Bossio, C. Verucchi, and C. De Angelo, "Rotor fault diagnosis in permanent magnet synchronous machine using the midpoint voltage of windings," *IET Electric Power Applications*, vol. 14, no. 2, pp. 256–261, 2020. [Online]. Available: <https://ietresearch.onlinelibrary.wiley.com/doi/abs/10.1049/iet-epa.2019.0428>
- [54] S. Rajagopalan, W. Roux, T. Habetler, and R. Harley, "Dynamic eccentricity and demagnetized rotor magnet detection in trapezoidal flux (brushless dc) motors operating under different load conditions," *Power Electronics, IEEE Transactions on*, vol. 22, pp. 2061 – 2069, 10 2007.
- [55] T. Goktas, M. Zafarani, and B. Akin, "Discernment of broken magnet and static eccentricity faults in permanent magnet synchronous motors," *IEEE Transactions on Energy Conversion*, vol. 31, no. 2, pp. 578–587, 2016.
- [56] T. Goktas, M. Zafarani, K. Lee, B. Akin, and T. Sculley, "A comprehensive analysis of magnet defect fault monitoring through leakage flux," *IEEE Transactions on Magnetics*, vol. PP, pp. 1–1, 10 2016.
- [57] M. Zafarani, T. Goktas, and B. Akin, "A comprehensive magnet defect fault analysis of permanent-magnet synchronous motors," *IEEE Transactions on Industry Applications*, vol. 52, pp. 1331–1339, 10 2015.
- [58] M. Kamper, A. Rix, D. Wills, and R.-J. Wang, "Formulation, finite-element modeling and winding factors of non-overlap winding permanent magnet machines," 10 2008, pp. 1 – 5.
- [59] *Introduction to Magnetostatic 2D Modeling Software Version 2022.1.*
- [60] G. Konstantinos, "Electromagnetic analysis of induction motor faults and development of new diagnostic methods to detect them," Ph.D. dissertation, University of Patras, 2015.
- [61] G. A. Skarmoutsos, K. N. Gyftakis, and M. Mueller, "Mcsa versus flux monitoring for demagnetization diagnosis in axial-flux pm generators," in *2021 IEEE 13th International Symposium on Diagnostics for Electrical Machines, Power Electronics and Drives (SDEMPED)*, vol. 1, 2021, pp. 119–125.

Chapter 6

Appendix A

Below we see a conclusion of the investment in Offshore Wind turbines in Greece

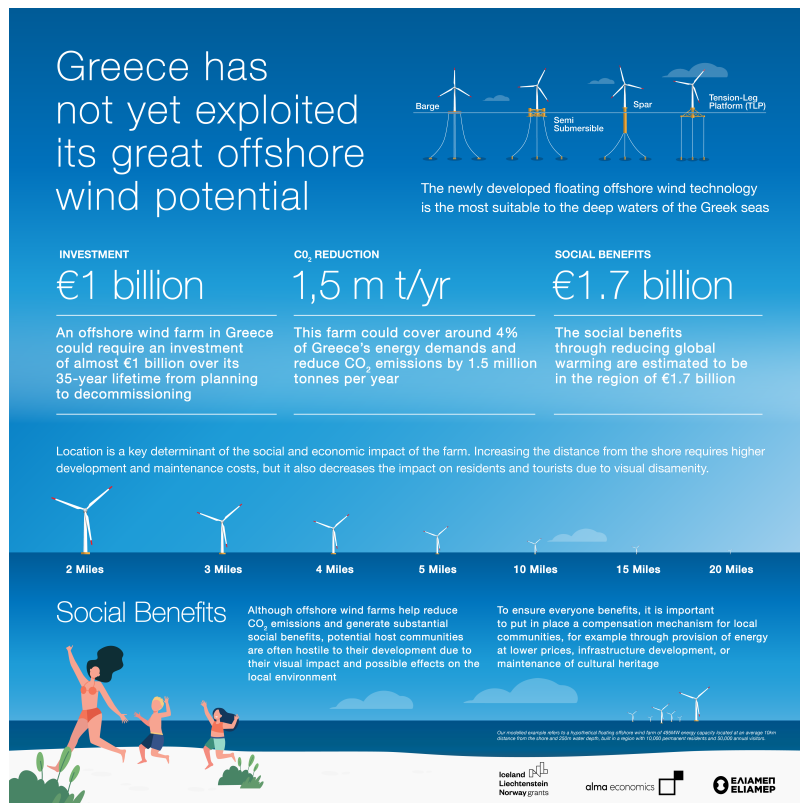


Figure 6.1: Conclusion of the Investment in Offshore Wind Turbines in Greece

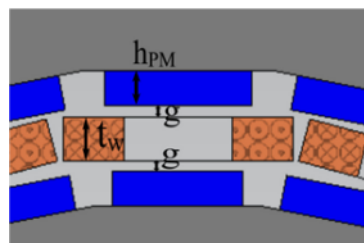


Figure 6.2: (a) The effect of armature reaction on ID (b) the effect of temperature on the required external DF for the NdFeB magnet.[10]